THE IMPACT OF MESOSCALE PROCESSES ON THE ATMOSPHERIC CIRCULATION OF MARS

Thesis by

Nicholas Gray Heavens

In Partial Fulfillment of the Requirements

for the Degree of

Doctor of Philosophy

California Institute of Technology

Pasadena, California

2010

(Defended 19 April 2010)

Maxima pars uatum, pater et iuuenes patre digni,
decipimur specie recti. Breuis esse laboro,
obscurus fio; sectantem leuia nerui
deficiunt animique; professus grandia turget;
serpit humi tutus nimium timidusque procellae;
qui uariare cupit rem prodigialiter unam,
delphinum siluis adpingit, fluctibus aprum.

The vast majority of poets, both the laureate
And the young ones some day laurelworthy,
We all are deceived by the appearance of right.
I strive to be succinct, yet I become obscure.
My mind and nerves fail in the pursuit of eloquence.
Turning epic, I merely might appear swollen.
Or fearful of such storms I could creep along
Safely upon well-trodden ground.
Since he who wants to remake a world
With overweening genius often paints
A dolphin burrowing in the woods
Or a boar at play in the rolling waves.

Quintus Horatius Flaccus, *Ars Poetica*

Acknowledgements

When I first arrived at Caltech in June of 2005, I discovered that the Registrar's Office still had my contact information from when I was admitted as an undergraduate and that the Registrar was willing to make an initial value guess of June 2010 for my graduation date. It now appears that my choice to give Caltech a second chance and the Registrar's estimate were both correct. But I do maintain that if there has been any ease or celerity in the course of my graduate career, it was not my doing.

I owe some measure of thanks to all of those who supported my vocation as a meteorologist before I came to Caltech. I fondly recall Bob Miller, Matt Zipin, Al Cope, Jim Eberwine, and Dan Vietor, who gave me the resources and encouragement to start forecasting the weather. I thank Paul Farber for deciding to publish those forecasts in the Germantown Friends School Earthquake. I am grateful to Ron Reisman and Chris McKay for letting a high school junior work for them.

At the University of Chicago, I was fortunate to be instructed by a gifted and supportive faculty inside and outside the Department of Geophysical Sciences, particularly Gidon Eshel, Noboru Nakamura, Sue Kidwell, David Archer, Carla Mazzio, Adrian Johns, and Cam Grey. The Lunar and Planetary Institute does a variety of profound services to the planetary science community, including sponsorship of a Summer Intern program. I thank Laurel Kirkland for hiring and advising me as an Intern and asking me for dust devil forecasts, starting what may be a lifelong obsession with coniometeorology. Last in this vein, I have to thank my father for first nurturing my love of weather and climate and my mother for telling me to do what I love and accept nothing on authority.

At Caltech, I have had the great privilege to serve my apprenticeship in philosophy under the tutelage of some exceptional professors and professional staff in the Division of Geological and Planetary Sciences. First in my heart are my two advisors, Mark Richardson and Yuk Yung.

Mark has advised me well under very difficult circumstances and skillfully delegated advice on purely technical matters to his valiant staff: Claire Newman, Greg Lawson, and Chris Lee. Mark has taught me much about the business and politics of planetary exploration, but most importantly he has modeled for me how a scientist both can be successful and humane. I would like to thank Yuk for taking me on as a student twice, keeping me in touch with the progress of geosciences both on and beyond Mars, and demanding surprisingly little in the bargain. I have enjoyed the conversation and hospitality of Andy Ingersoll over the years and hope he is not too disappointed that this thesis presents incomplete solutions (at best) to the very significant questions that enthrall him.

While the graduate students in Geological and Planetary Sciences often feel like a mutual querulousness society, the opportunity to complain bitterly, discuss science, or discuss anything other than science with them has made my course of study more pleasant than it would have been otherwise. The completion of this thesis owes much to Michael Busch, Joannah Metz, and Meg Schwamb, my peloton. I thank Alejandro Soto, Xin Guo, and Kevin Lewis for valuable discussions of Mars weather and climate.

Outside of Caltech, I need to thank John Wilson, Don Banfield, Francois Forget, Scot Rafkin, Tim McConnochie, Bob Sica, Jasper Kok, Nilton Renno, Luca Montabone, Mike Mischna, and Paul Hayne for deeply engaging with my research at professional conferences and on other occasions and providing interactive feedback at much shorter timescales than formal peer review.

And now at the close, I reserve the last places for those of greatest dignity. First, I would like to thank the Mars Climate Sounder Science Operations Team, especially David Kass, Armin Kleinböhl, Wedad Abdou, and Jim Shirley for providing the bulk of technical and other support necessary for this work.

And finally, I thank Daniel J. McCleese and John T. Schofield, the Principal Investigator and Deputy Principal Investigator of the Mars Climate Sounder on the Mars Reconnaissance Orbiter. When I was a cooing infant, they conceived of a multispectral, broadband limb and nadir sounder for Mars. Throughout my lifetime, they have flown such an instrument on two unsuccessful orbiters. But now (to paraphrase Vergil) after various failures of engineering and downfalls in NASA funding, an instrument of theirs successfully reached Mars. I have been most fortunate and privileged not only to analyze Mars Climate Sounder products but also to have the support and counsel of those who have dedicated much of their careers to making those products possible. This thesis is humbly dedicated to them. I think it was worth it.

Abstract

The study of the modern martian atmosphere is (1) a key to the climate of Mars's past; (2) useful for comparison with other terrestrial planets such as the Earth; and (3) can support hazard analysis and weather forecasting for future exploration and habitation of the planet. Recently, it was found that middle atmospheric downwelling near the south pole during southern winter is much more vigorous than predicted by most Mars general circulation models. This underestimate may be due to models erroneously representing the radiative forcings in the atmosphere due to aerosol and/or the mechanical forcings due to wave breaking. Errors of this kind would influence middle atmospheric dynamics and likely would result from incomplete understanding of lower atmospheric processes such as dust transport. Here, retrievals of vertical profiles of temperature, pressure, dust, and water ice from the Mars Climate Sounder (MCS) on Mars Reconnaissance Orbiter (MRO) are used to characterize the atmospheric circulation of Mars and its forcings. First, I consider the annual cycle of the thermal structure and aerosol distributions of the lower and middle atmosphere and investigate the degree of coupling between the lower and middle atmospheric mean meridional circulations. To evaluate the role of wave breaking, I look for local convective instabilities in the martian middle atmosphere: a key indicator of saturating vertically propagating waves such as the gravity waves and the thermal tides, which are important sources of wave drag in the Earth's mesosphere. I then characterize the vertical distribution of dust and its approximate radiative effects during northern spring and summer and show there is usually a maximum in dust mass mixing ratio at ~15—25 km above the tropics, which is not currently simulated by models. Next, I evaluate the relative importance of dust storm activity, pseudo-moist convection due to the solar heating of dust, orographic effects, and scavenging by water ice clouds in producing this maximum. Finally, I show that published models underestimate the thickness and altitude of water ice clouds in northern summer.

Table of Contents

List of Figures

List of Tables

Chapter 1   Introduction

The modern martian atmosphere interests the scientific community and human society in general for three fundamental reasons.

First, the environmental conditions of Mars's past are thought to have been more conducive to biological life. The current martian atmosphere is thus one outcome of the evolution of the planet from being potentially habitable, with widespread liquid water on the surface, to the cold global desert it is today. Following aktualism, the principle that the processes that occur in the present environment occurred in the past, investigations of processes in the current atmosphere can be used to develop models of the weather and climate of the Martian past that can be further constrained by evidence from the geological archives of rock and ice currently extant on the planet.

For example, Mars experiences weather systems on scales from the meter to the planetary that lift, transport, and deposit dust. Investigations of the planet's surface geology have found cyclical deposits of dust, potentially formed by variations in dust deposition on Milankovitch timescales [*Lewis et al.*, 2008]. It is impossible to observe the millions of individual events that formed these deposits. Yet if the dynamics of dust transport on the planet today are sufficiently well understood to model under different orbital parameters/atmospheric pressure etc., it may be possible to infer the formation conditions of these deposits.

In some cases, phenomena in the modern atmosphere may be relevant to the ancient atmosphere but have only indirect geological evidence to constrain them. For instance, carbon dioxide clouds sometimes form at altitudes of 50—90 km above the

tropics [e.g., *Clancy et al.*, 2007]. These clouds strongly reflect infrared radiation and so produce a modest greenhouse effect [*Forget and Pierrehumbert*, 1997]. If the carbon dioxide partial pressure (pCO$_2$) of Mars was higher in the past, these clouds may have formed lower in the atmosphere and been thicker, which may have enhanced their greenhouse effect and contributed to the warming of surface temperatures above the freezing point of water. Yet if the processes by which these clouds form in the modern system are insufficiently understood (such as the extent and efficiency with which they are nucleated by surface dust from below or meteoritic dust from above), simulations of their role in the climate of the past may be erroneous, especially since these clouds likely leave no trace in the geological record.

Second, the modern Martian atmosphere can be compared with the atmospheres of the Earth and other planetary bodies. Comparisons between the Earth and Mars generally focus on phenomena more extreme on Mars than on the Earth (such as dust storms and the thermal tides) and generally apply data, models, and assumptions developed for the Earth to Mars. Occasionally, insight gained from study of the Martian atmosphere directly informs studies of the Earth's atmosphere. While developing the LMD Mars general circulation model (GCM), *Forget et al.* [1999] determined that longwave scattering by dust aerosols could not be neglected in the radiative transfer for Mars, though most radiative transfer schemes in Earth GCMs did neglect this term. *Forget et al.* [1999] consulted Yves Fouquart about this issue. Soon *Dufresne et al.* [2002] (including Fouquart) found that longwave scattering by dust was significant in dry, dusty areas of the Earth in the "atmospheric window region" between 9 and 13 μm.

Third, the modern Martian atmosphere needs to be monitored and studied to support current robotic exploration and as a prerequisite for weather forecasting and climate modeling to support future exploration and habitation. Current methods of delivering spacecraft to the surface of Mars are affected by the density, wind, and particulate density profiles along the path of entry [*Braun and Manning*, 2007]. Once on the surface, the planet's weather creates hazards for surface operations, such as low visibility and impairment of the solar power supply. Investigations of the atmosphere from orbit also can be affected by variations in visibility and atmospheric density. And for future proposed missions that may be time sensitive and dependent on multiple spacecraft safely landing, such as the return of samples from the planet or human expeditions, the hazards of the weather for Martian exploration only will increase [*Committee on Precursor Measurements Necessary to Support Human Operations on the Surface of Mars, National Research Council*, 2002].

In the more distant future, Mars weather forecasting and climate modeling will be a necessary component of any efforts to use Mars as a base to process materials mined from the asteroids or supply asteroid mines with food and other necessities. A recent documentary on the National Geographic Channel [*Davis*, 2009] speculated that terraforming Mars through re-engineering of its volatile reservoirs and atmosphere may be a viable plan that human society will have to consider by the end of this century. This process would be analogous to the anthropogenic modification of the climate system currently taking place on the Earth (if more extreme) and would require monitoring and modeling of the martian climate system on the same scale as the Earth's climate system is modeled at present.

And while these last possible directions for martian atmospheric science seem to belong to science fiction and the unknowable future, they do seem to stimulate the imagination of wider society. The author recalls taking a cab to Richmond Airport and mentioning to the cab driver that the author just had attended a conference on the martian atmosphere. The cab driver replied, "Oh, you're planning for when we move there." Mars may be one of the next planets human beings call home, so it is worth remembering that future martian atmospheric science may be relevant to society on the basis of the contention of *Bates* [1949] that, "[Weather is] a factor that is surpassed only among sex and hunger among the stimuli to the human race."

All three of these purposes motivate understanding of the martian atmosphere and related aspects of the climate system. All three purposes require qualitative and preferably quantitative models of the atmosphere and climate that will be a summation of that understanding and in some cases directly economically useful for human society. And for all three purposes, a variety of analytical and numerical models exist and likely will be developed in the future. The most sophisticated of these are the general circulation/global climate models (GCMs), which simulate the three-dimensional structure of planetary atmospheric circulation using appropriate simplifications of the equations of fluid dynamics [e.g., *Haberle et al.*, 1993; *Wilson and Hamilton*, 1996; *Forget et al.*, 1999; *Takahashi et al.*, 2003; *Moudden and McConnell*, 2005; *Hartogh et al.*, 2005; *Kuroda et al.*, 2005; *Richardson et al.*, 2007].

While the results of these simulations have some sensitivity to the dynamical core used (the dynamical core transports heat, momentum, and tracer species such as dust within the computational space of the model), the largest uncertainties in simulations

arise from the routines broadly called, "the physics." These routines represent processes

that may not involve fluid dynamics, such as radiative transfer, or processes that occur on

scales much finer than the computational grid, such as boundary layer convection.

The latter type of process falls into the broad category of the mesoscale and so is

often simulated in more finely gridded mesoscale models. More rigorously, *Glickman*

[2000] defines "mesoscale" as

> Pertaining to atmospheric phenomena having horizontal scales ranging from a few
> to several hundred kilometers, including thunderstorms, squall lines, fronts,
> precipitation bands in tropical and extratropical cyclones, and topographically
> generated weather systems such as mountain waves and sea and land breezes.
> From a dynamical perspective, this term pertains to processes with
> timescales ranging from the inverse of the Brunt–Väisälä frequency to a
> pendulum day, encompassing deep moist convection and the full spectrum of
> inertio-gravity waves but stopping short of synoptic-scale phenomena, which have
> Rossby numbers less than 1.

The physics routines of a model can be highly parameterized, that is, they can be

empirically tuned and gross approximations to the very complex physics of the process.

In the case of Mars models, some of these parameterizations may be inherited from Earth

models, so their empirical tuning may be inappropriate for Mars. Moreover, martian

atmospheric models usually do not have the computational resources or staff support of

their Earth cousins, which are used for the societally important functions of weather and

climate prediction. Thus, in many cases, some physical processes are not represented by

the model physics for the sake of efficiency or because the modeler deems them

unimportant.

Therefore, the current range of Mars models uses a broad diversity of physics routines. For instance, dust suspended in the atmosphere is an important contributor to the radiative budget of the atmosphere. Some models represent it as a radiatively active but spatially prescribed absorber [e.g., *Forget et al.*, 1999], while other models explicitly represent its lifting, transport, and interactions with radiation [e.g., *Newman et al.*, 2002; *Kahre et al.*, 2006]. These differences usually arise from the particular interests of the investigation. *Montmessin et al.* [2004] studies water ice clouds and therefore uses a spatial prescription for dust but actively simulates water ice clouds, while *Kahre et al.* [2006] focuses on dust transport and so neglects water ice clouds altogether.

Yet terrestrial atmospheric models have an even greater diversity of dynamical cores and physics. The approach to this diversity is typically pragmatic: weather forecasters use the models that have worked well in a similar weather situation in the past or make an ensemble forecast based on the entire suite of available models. Climate forecasters/policymakers tend to follow similar procedures. Fundamentally, models are evaluated based on how well they match observations.

Observations of Mars over the last decade, however, show that the climatology of the planet's thermal structure is not simulated well by the full ensemble of Mars GCMs. For example, observations by *McCleese et al.* [2008] suggested that Mars GCMs mainly underestimate the temperature and proximity to the south pole of a temperature inversion at ~50 km above the surface during southern winter. The typical response of modelers to these kinds of discrepancies between observations and models is to tune some aspect of the model currently unconstrained by observations to match the observed thermal structure.

At present, at least three research groups are developing the capability to adjust their models to match observations in a more rigorous way, that is, by data assimilation [*Lewis et al.*, 2007] (Lawson et al., Assimilating TES radiances with the DART/Planet-WRF ensemble data assimilation system, paper presented at 1st Symposium on Planetary Atmospheres, American Meteorological Society, Atlanta, GA, 17—21 January 2010; Kalnay et al., Assimilation of TES data into a Mars general circulation model using LETKF, paper presented at 1st Symposium on Planetary Atmospheres, American Meteorological Society, Atlanta, GA, 17—21 January 2010). In data assimilation (called re-analysis in some contexts), different realizations of a model can be used to generate a model state that is consistent with observations within some uncertainties that are often explicitly provided by the data assimilation scheme. Data assimilation is an exciting and promising new avenue to understand complex and difficult to observe meteorological systems on Mars, such as the global dust storms that occasionally envelop most of the planet in a thick dust haze. It also is a way of initializing a Mars atmospheric model for purposes of numerical weather prediction. Data assimilation, however, faces some important challenges.

In some cases, a data assimilation scheme may only use temperature profiles [e.g., *Lewis et al.*, 2007]. The thermal structure, however, is a somewhat degenerate function of various atmospheric processes. For instance, at night, similar amounts of dust and water ice at the same level of the atmosphere will generate similar infrared heating to warm the atmosphere. Depending on the assimilation scheme and the physics routines of the model, this kind of degeneracy may result in a dust haze being simulated in cases in which a water ice cloud is present in the real system.

In other cases, a data assimilation scheme may assimilate observations such as the measured limb radiances that are less degenerate, but the model used may lack physics routines that simulate an important process, such as the drag of breaking gravity waves on the westerly jets (e.g., Lawson et al., 2010, *sup.*). In such cases, the model states produced by the data assimilation scheme may have such large uncertainties that they are useless for atmospheric studies or weather prediction, though the location of these uncertainties in the atmosphere may be in part diagnostic of missing processes.

Thus, the risk data assimilation poses for martian atmospheric science is very similar to the risk that the desire for originality presents for poetry (see epigraph on p. iii). In an attempt to complement an incomplete observational record, modelers may simulate the meteorological equivalent of "A dolphin burrowing in the woods/Or a playful boar in the rolling waves."

The logical remedy to this problem is to observe the forcing of the atmospheric circulation concurrently with variables indicative of the circulation such as the thermal structure, winds, or surface pressure. The analysis of the forcing in particular can be used both as a validation of the results of data assimilation schemes that use degenerate input and also as a basis for improving the physics routines of atmospheric models.

The chief forcings of interest in the martian atmosphere are some of the most uncertain forcings in the Earth's climate system, particularly because the processes involved usually are not explicitly resolved on the scale of a GCM and must be parameterized. In the lower atmosphere, suspended dust and water ice clouds are strongly seasonally and spatially variable. Due to the tenuousness of the atmosphere, these aerosols can produce significant radiative heating in relatively small amounts. In the

middle atmosphere, vertically propagating gravity waves and tides can grow to unstable amplitudes, depositing significant energy and momentum as they dissipate. While aerosol and gravity/wave tidal forcings are important at different latitudes and levels of the atmosphere, they are often controlled by similar kinds of mesoscale processes, such as the interaction of the wind with topography or convection that penetrates into highly stable atmospheric layers.

Moreover, these forcings are not just significant for atmospheric dynamics *qua* atmospheric dynamics but may be important for processes of interest to the two upcoming missions to Mars, Mars Atmosphere and Volatile Evolution (MAVEN) and the 2016 ExoMars Trace Gas Orbiter (TGO), that focus on the chemistry of the upper and lower atmospheres. Gravity waves and tides not only affect the circulation through the momentum they transport from the lower atmosphere to the middle and upper atmospheres, but their saturation also enhances the vertical diffusivity and thus the vertical exchange between the lower and upper atmospheres. Dust may affect the chemistry of the lower atmosphere through heterogeneous processes, in which adsorption of chemical species on a dust or ice particle catalyzes a variety of reactions that may be slower or even non-existent in the gas phase [e.g., *Anbar et al.*, 1993; *Usher et al.*, 2003; *Lefévre and Forget*, 2009].

This thesis develops many of the necessary observational constraints for future modeling of the circulation of the martian lower and middle atmospheres and its forcings, using simultaneous retrievals of temperature, pressure, and dust and water ice opacity from measurements of limb radiance by the Mars Climate Sounder (MCS) on Mars Reconnaissance Orbiter (MRO): a dataset with unprecedented capability for middle

atmospheric sounding and vertical aerosol profiling in the martian atmosphere. In Chapter 2, I provide a broad overview of the annual cycle of the thermal structure and aerosol distribution of the lower and middle atmospheres and infer some aspects of the mean meridional circulation. In Chapter 3, I detect and map local convective instabilities in the middle atmosphere to infer the drag in the middle atmosphere due to the saturation of gravity waves and the thermal tides. In Chapter 4, I use MCS profiles of temperature, pressure, and dust opacity to reconstruct the zonal average vertical distribution of dust and its seasonal evolution during northern spring and summer. One particular feature of the vertical dust distribution is quite unexpected from previous theory and modeling work, so the purpose of Chapter 5 is to consider what processes may be responsible for this unexpected feature and to isolate potential observational signatures of these processes. In Chapter 6, I show that the distribution of water ice clouds in the tropics during northern summer is inconsistent with published models. In Chapter 7, I summarize the results of this thesis by describing the variety of mesoscale processes identified in these studies and briefly consider the general importance of mesoscale processes for studying climate variability on Mars.

Chapters 2-6 either are published papers or papers currently in preparation for publication as part of my work for the MCS Science Team. Therefore, they often contain repetitive methodological material tailored to the particular study. In addition, the material in these Chapters will refer to more advanced versions of or more detailed information about the retrieval algorithm than currently described in the peer-reviewed literature. This material represents contributions by members of the MCS Science Team, particularly Armin Kleinböhl and Wedad Abdou. In all cases, the vast majority of the

analysis beyond the retrieval product, the interpretation, and the writing are my own.

With respect to Chapter 2, I acknowledge collaboration with Daniel J. McCleese and

Mark I. Richardson as my principal co-authors. With respect to Chapter 3, I acknowledge

collaboration with the co-authors of *Heavens et al.* [2010].

Bibliography

Anbar, A.D., M.T. Leu, H.A. Nair, and Y. L. Yung (1993), The adsorption of HO_x on aerosol surfaces: Implications for the atmosphere of Mars. *J. Geophys. Res., 98*, 10,933-10,940.

Bates, C.C. (1949), The Status of Applied Meteorology in the United States in the Post-War Period, *Bull. Amer. Met. Soc.*, *30*, 199-203.

Braun, R.D. and R.M. Manning (2007), Mars Exploration Entry, Descent, and Landing Challenges, *J. Spacecraft Rockets*, *44*(2), 310-323.

Clancy, R.T., M.J. Wolff, B.A. Whitney, B.A. Cantor, and M.D. Smith (2007), Mars equatorial mesospheric clouds: Global occurrence and physical properties from Mars Global Surveyor Thermal Emission Spectrometer and Mars Orbiter Camera limb observations, *J. Geophys. Res*., *112*, E04004, doi:10.1029/2006JE002805.

Committee on Precursor Measurements Necessary to Support Human Operations on the Surface of Mars, 2002, *Safe on Mars: Precursor Measurements Necessary to Support Human Operations on the Martian Surface*, 64 pp., National Academy Press, Washington, DC.

Davis, M., producer and director (2009), *Mars: Making The New Earth*, National Geographic Channel.

Dufresne, J.-L., C. Gautier, P. Ricchiazzi, and Y. Fouquart (2002), Longwave Scattering Effects of Mineral Aerosols, *J. Atmos. Sci.*, *59*(12), 1959-1966.

Forget, F. and R.T. Pierrehumbert (1997), Warming Early Mars with carbon dioxide clouds that scatter infrared radiation, *Science*, *278*, 1273-1276.

Forget, F., F. Hourdin, R. Fournier, C. Hourdin, O. Talagrand, M. Collins, S.R. Lewis, P.L. Read and J.-P. Huot (1999), Improved general circulation models of the Martian atmosphere from the surface to above 80 km, *J. Geophys. Res 104*, 24155–24175.

Glickman, T.S., ed. (2000), *The Glossary of Meteorology*, 2nd edition, 850 pp., American Meteorological Society, Boston, MA.

Haberle, R.M., J.B. Pollack, J.R. Barnes, R.W. Zurek, C.B. Leovy, J.R. Murphy, J. Schaeffer, and H. Lee (1993), Mars atmospheric dynamics as simulated by the NASA/Ames general circulation model I. The zonal mean circulation, *J. Geophys. Res.,* 98, 3093-3124.

Hartogh, P., A. S. Medvedev, T. Kuroda, R. Saito, G. Villanueva, A. G. Feofilov, A. A. Kutepov, and U. Berger (2005), Description and climatology of a new general circulation model of the Martian atmosphere, *J. Geophys. Res.*, *110*, E11008, doi:10.1029/2005JE002498.

Heavens, N.G., M.I. Richardson, W.G. Lawson, C. Lee, D.J. McCleese, D.M. Kass, A. Kleinböhl, J.T. Schofield, W.A. Abdou, J.H. Shirley (2010), Convective instability in the martian middle atmosphere, *Icarus*, in press, doi:10.1016/j.icarus.2010.03.023.

Kahre, M. A., J. R. Murphy, and R. M. Haberle (2006), Modeling the Martian dust cycle and surface dust reservoirs with the NASA Ames general circulation model, *J. Geophys. Res., 111*, E06008, doi:10.1029/2005JE002588.

Kuroda, T., N. Hashimoto, D. Sakai, and M. Takahashi (2005), Simulation of the Martian Atmosphere Using a CCSR/NIES AGCM, *J. Met. Soc. Japan, 83* (1), 1-19.

Lefévre, F. and F. Forget (2009), Observed variations of methane on Mars unexplained by known atmospheric chemistry and physics, *Nature, 460*, 720-723.

Lewis, K.W., O. Aharonson, J.P. Grotzinger, R.L. Kirk, A.S. McEwen, and T.-A. Suer (2008), Quasi-Periodic Bedding in the Sedimentary Rock Record of Mars, *Science, 322*(5907), 1532-1535.

Lewis, S.R., P.L. Read, B.J. Contrath, J.C. Pearl, and M.D. Smith (2007), Assimilation of thermal emission spectrometer atmospheric data during the Mars Global Surveyor aerobraking period, *Icarus, 192*(2), 327-347.

McCleese, D.J., J.T. Schofield, F.W. Taylor, W.A. Abdou, O. Aharonson, D. Banfield, S.B. Calcutt, N.G. Heavens, P.G.J. Irwin, D.M. Kass, A. Kleinböhl, W.G. Lawson, C.B. Leovy, S.R. Lewis, D.A. Paige, P.L. Read, M.I. Richardson, N. Teanby, and R.W. Zurek (2008), Intense polar temperature inversion in the middle atmosphere on Mars, *Nature Geosci., 1*, 745-749, doi:10.1038/ngeo332.

Montmessin, F., F. Forget, P. Rannou, M. Cabane, and R. M. Haberle (2004), Origin and role of water ice clouds in the Martian water cycle as inferred from a general circulation model, *J. Geophys. Res.*, *109*, E10004, doi:10.1029/2004JE002284.

Moudden, Y., and J. C. McConnell (2005), A new model for multiscale modeling of the Martian atmosphere, GM3, *J. Geophys. Res.*, *110*, E04001, doi:10.1029/2004JE002354.

Newman, C. E., S. R. Lewis, P. L. Read, and F. Forget (2002), Modeling the Martian dust cycle, 1. Representations of dust transport processes, *J. Geophys. Res.*, *107*(E12), 5123, doi:10.1029/2002JE001910.

Richardson, M. I., A. D. Toigo, and C. E. Newman (2007), PlanetWRF: A general purpose, local to global numerical model for planetary atmospheric and climate dynamics, *J. Geophys. Res.*, *112*, E09001, doi:10.1029/2006JE002825.

Takahashi, Y. O., H. Fujiwara, H. Fukunishi, M. Odaka, Y.-Y. Hayashi, and S. Watanabe (2003), Topographically induced north-south asymmetry of the meridional circulation in the Martian atmosphere, *J. Geophys. Res.*, *108*(E3), 5018, doi:10.1029/2001JE001638.

Usher, C.R., A.E. Michel, and V.H. Grassian (2003), Reactions on Mineral Dust, *Chem. Rev.*, *103*, 4883-4939.

Wilson, R.J. and K. Hamilton (1996), Comprehensive model simulation of thermal tides in the martian atmosphere, *J. Atmos. Sci.*, *54*, 1290-1326.

Chapter 2 The Mean Meridional Circulation of the Martian Atmosphere

2.1 Introduction

During some martian dust storms, atmospheric temperatures at ~15—35 km above the winter (always northern) pole warm dramatically over the course of a few martian days by up to 80 K [*Jakosky and Martin*, 1987]. While some of the warming equatorward of ~65º S can be explained by direct solar heating of dust advected from the southern hemisphere or the northern tropics, the warming within polar night ("dust storm polar warming") cannot be due to the absorption of solar radiation. Instead, dust storm polar warming is likely due to adiabatic heating from strong downwelling over the pole, in particular downwelling of the principal meridional overturning cell (PMOC), sometimes called, "the Hadley cell," which may be especially intense during strong dust storms [*Haberle et al.*, 1982; *Schneider*, 1983; *Haberle et al.*, 1993].

When the first wave-resolving, three-dimensional model of the martian general circulation was developed in the early 1990s [*Haberle et al.*, 1993], it could not simulate dust storm polar warmings, since the downwelling of the simulated PMOC never penetrated further than 65º—70º N, which *Haberle et al.* [1993] attributed to insufficiently strong eddy transport of heat and momentum. *Wilson* [1997] successfully simulated a dust storm polar warming by using a deeper vertical domain than used by *Haberle et al.* [1993] and resolving the atmospheric thermal tides. The deep vertical

domain both reduced the sensitivity of the simulation to dissipation at the model top and also improved how the PMOC (and the thermal tides) during the dust storm were resolved vertically. The atmospheric thermal tides transported sufficient easterly angular momentum to drive the PMOC downwelling closer to the north pole. Simulations of the polar warming by *Forget et al.* [1999] and *Kuroda et al.* [2009] have been successful for similar reasons.

Thus, while dust storm polar warmings are relatively brief and exceptional events within the climatology of Mars's atmospheric circulation, they do illustrate two aspects of the circulation important for modeling: (1) the PMOC can exist in the form of a nearly pole-to-pole circulation [*Schneider*, 1983] or at least one that upwells at a displacement from the pole far greater than observed on the Earth; (2) the PMOC, a feature of the lower atmosphere and whose analog on Earth is restricted to the troposphere, can penetrate to a level of the atmosphere that is in radiative equilibrium in an average sense [*Zurek et al.*, 1992], likely has a momentum budget dominated by dissipation of gravity waves and tides [e.g., *Barnes*, 1991], and thus resembles the Earth's mesosphere. This type of circulation can arise because the thermal structure of Mars lacks a highly stable atmospheric layer like the stratosphere to isolate the lower atmospheric circulation from the middle atmospheric circulation. Therefore, current martian general circulation models (GCMs) [e.g., *Wilson and Hamilton*, 1996; *Forget et al.*, 1999; *Takahashi et al.*, 2003; *Moudden and McConnell*, 2005; *Hartogh et al.*, 2005; *Kuroda et al.*, 2005; *Kahre et al.*, 2006; *Richardson et al.*, 2007] generally simulate both the lower and middle atmospheres and are now being coupled with models of the upper atmosphere [e.g., *Angelats i Coll et*

al., 2005]. These latter coupled models not only support more accurate simulation of global dust storms but also are useful for quantifying exchange of volatiles between the lower and the upper atmosphere to understand the present, past, and future history of martian atmospheric loss.

Until recently, observational constraints on simulations of the middle atmosphere were limited to ground-based microwave observations [e.g., *Deming et al.*, 1986] and retrievals from infrared limb observations by the Thermal Emission Spectrometer (TES) on Mars Global Surveyor (MGS) [*Smith et al.*, 2001]. These observations suggested that there is a thermal inversion near the winter pole (either north or south) throughout much of the year. This inversion, however, is cooler and at higher altitude than dust storm polar warmings.

New observations by the Mars Climate Sounder (MCS) [*McCleese et al.*, 2007] on Mars Reconnaissance Orbiter (MRO) [*Zurek and Smrekar*, 2007] now are providing information about the thermal structure of Mars over a greater depth of the middle atmosphere than TES and at higher spatial and temporal resolution than ground-based microwave observations. In addition, observations from MCS can be used to retrieve vertical profiles of aerosol, which provide constraints on the lower atmospheric circulation and the forcing of the circulation by radiative heating/cooling due to dust and water ice.

This paper is intended as a companion to McCleese et al. (2010, in preparation), which describes the seasonal cycle of the atmospheric thermal structure and aerosol distributions using retrievals from MCS observations. McCleese et al. (2010) (hereafter,

"P1") focuses on Mars Year (MY) 29 (according to the convention of *Clancy et al.* [2000]), a year without a global dust storm, and therefore provides important observational information that can constrain "background" simulations of the martian general circulation. Here I explore the mean meridional circulation of the lower and middle atmospheres at the equinoxes and solstices by integrating analysis of the MCS retrievals at the level presented by McCleese et al. (2010) with general results from both theory and modeling.

2.2 Data
2.2.1 Retrievals

McCleese et al. [2007] describes the MCS instrument and observing strategy. *Kleinböhl et al.* [2009] provides an in-depth description of the first generation retrieval algorithm. At present, atmospheric retrievals from MCS observations provide vertical profiles with respect to pressure, p (Pa), of temperature, T (K), dust opacity, i.e., the extinction per unit height due to dust, $d_z\tau_{dust}$ (km^{-1}) at 463 cm^{-1}, and water ice opacity $d_z\tau_{H_2Oice}$ (km^{-1}) at 843 cm^{-1}. The retrievals used here were generated using a more advanced retrieval algorithm than described in *Kleinböhl et al.* [2009], which includes the effects of aerosol scattering in the radiative transfer.

2.2.2 Zonal Averaging and Sampling

To study the zonal average circulation of the planet, the MCS retrievals and quantities

derived from them (as described later in Chapter 2.2) are averaged after being binned by

Mars Year (MY), L_s ($5°$ resolution centered at $0°$, $5°$ etc.); time of day: "dayside" (9:00-

21:00 LST) and "nightside" (21:00-9:00 LST); mean latitude ($5°$ resolution); and mean

longitude ($5.625°$ resolution). The spatial resolution of the binning is chosen to be

comparable to standard Mars general circulation model grids. Mean latitude and

longitude refer to the coordinates at the tangent point of the limb path observed by the

center of the MCS detector array at ~40 km above the surface. Zonal averages are the

average of the longitudinal averages in all longitudinal bins containing data.

Figure 2.1 plots the population of retrievals in individual latitudinal-longitudinal

bins in the L_s bins corresponding to the equinoxes and solstices (the focus of this study).

The nightside at northern summer solstice is most densely sampled (closest to optimal

given ideal operation of the instrument, spacecraft, and retrieval algorithm), while the

dayside at northern spring equinox is least densely sampled. Undersampling is usually

attributed one of two reasons: (1) operational: the instrument is powered off, or the

spacecraft is pointed significantly off-nadir; and (2) aerosol opacities are high, due to dust

storms and near the equator in all seasons, or due to water ice clouds in northern spring

and in the summer in the northern tropics [*Kleinböhl et al*, 2009]. Except for operational

impediments, sampling is likely to improve as retrieval algorithms are improved,

permitting retrievals under conditions of higher aerosol opacity than at present.
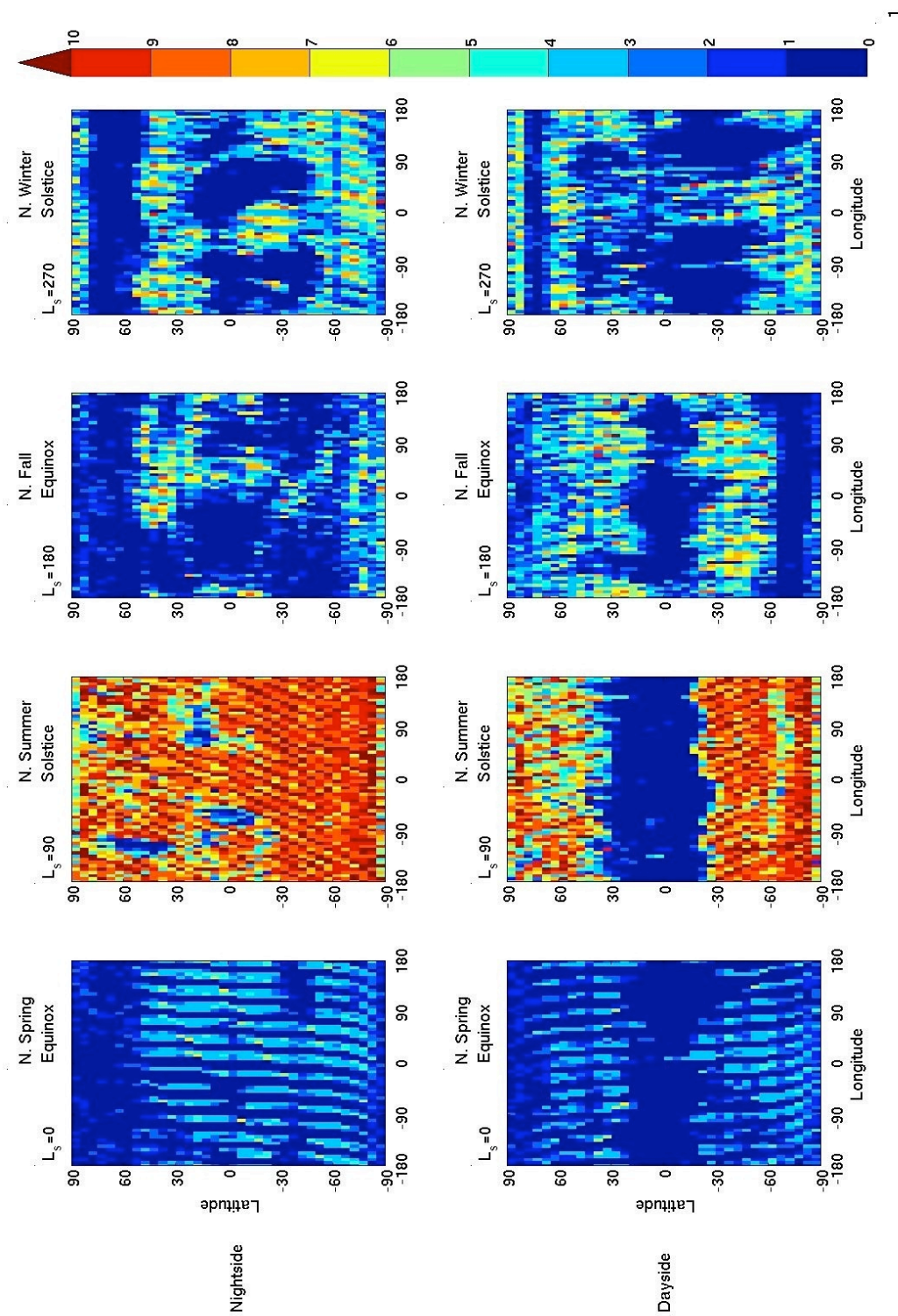
Figure 2.1. Number of retrievals per latitudinal/longitudinal bin for the labeled time of day and L_s bins during MY 29. The color scale is deepest red for 10 retrievals or more.

2.2.3 Winds

An estimate of the zonal gradient wind, $U(p)$, is derived from the zonal average

temperature by taking the lowest pressure level with retrieved temperature data in each

latitudinal bin as a level of no motion, p_{LNM}, and estimating the thermal wind, $\hat{U}(p)$:

$$\hat{U}(p) = \int\limits_{p_{LNM}}^{p} \frac{R_d}{f}\left(\frac{dT}{dy}\right)_p d\ln p'$$ (2.1)

where R_d is the specific gas constant, f is the Coriolis parameter for the latitudinal bin,

and $\left(\dfrac{dT}{dy}\right)_p$ is the temperature gradient at constant pressure. To compute the gradient wind

$U(p)$, we iteratively apply Eq. 2.2 to convergence [*Holton*, 2004].

$$U_{n+1}(p) = \frac{U_n}{1 + \dfrac{\sqrt{U_n^2}}{|fR_M|}}$$ (2.2)

where R_M is the radius of Mars. Eqs. 2.1 and 2.2 are only appropriate for winds in

approximate geostrophic balance and so cannot be used for diagnosis of zonal winds in

the tropics due to the low magnitude of the Coriolis parameter. Therefore, $U(p)$

calculated in the tropics is not plotted.

2.3 Investigative Approach

2.3.1 Use of Zonal Average Plots

Zonal average plots of temperature, zonal wind, and aerosol mass mixing ratio are often used in modeling studies [e.g., *Richardson and Wilson*, 2002] to illustrate aspects of the simulated circulation, particularly the mean meridional circulation. Figures 2.2, 2.3, 2.4, and 2.5 show respectively: the zonal average temperature, the estimated zonal wind, the zonal average dust density scaled opacity (a proxy for dust mass mixing ratio), and the zonal average water ice density scaled opacity (a proxy for water ice mass mixing ratio) on the nightside and dayside at the solstices and equinoxes.

Since longitudinal sampling is minimal in some seasons (Figure 2.1), the zonal averages in Figures 2.2—2.5 are not necessarily accurate. Zonal temperature averages based on even a small number of longitudinal bins should be accurate under most conditions: a consequence of the relative weakness of eddies in comparison to planetary-scale circulations like the non-migrating thermal tides [*Zurek et al.*, 1992]. Dust storm conditions may be an exception. Dust heating aloft may occur faster than the planetary circulation can adjust, while temperatures near the surface are suppressed relative to less dusty areas. Another exception may be the northern hemisphere during the winter, where baroclinic eddy amplitudes are known to be large [*Barnes,* 1980, 1981; *Wilson et al.,* 2002], but this region is better sampled longitudinally. Especial caution is required for analyzing the zonal average aerosol distributions, which are biased toward the dust and water ice distributions over regions with successful retrievals. The high airmass factor of
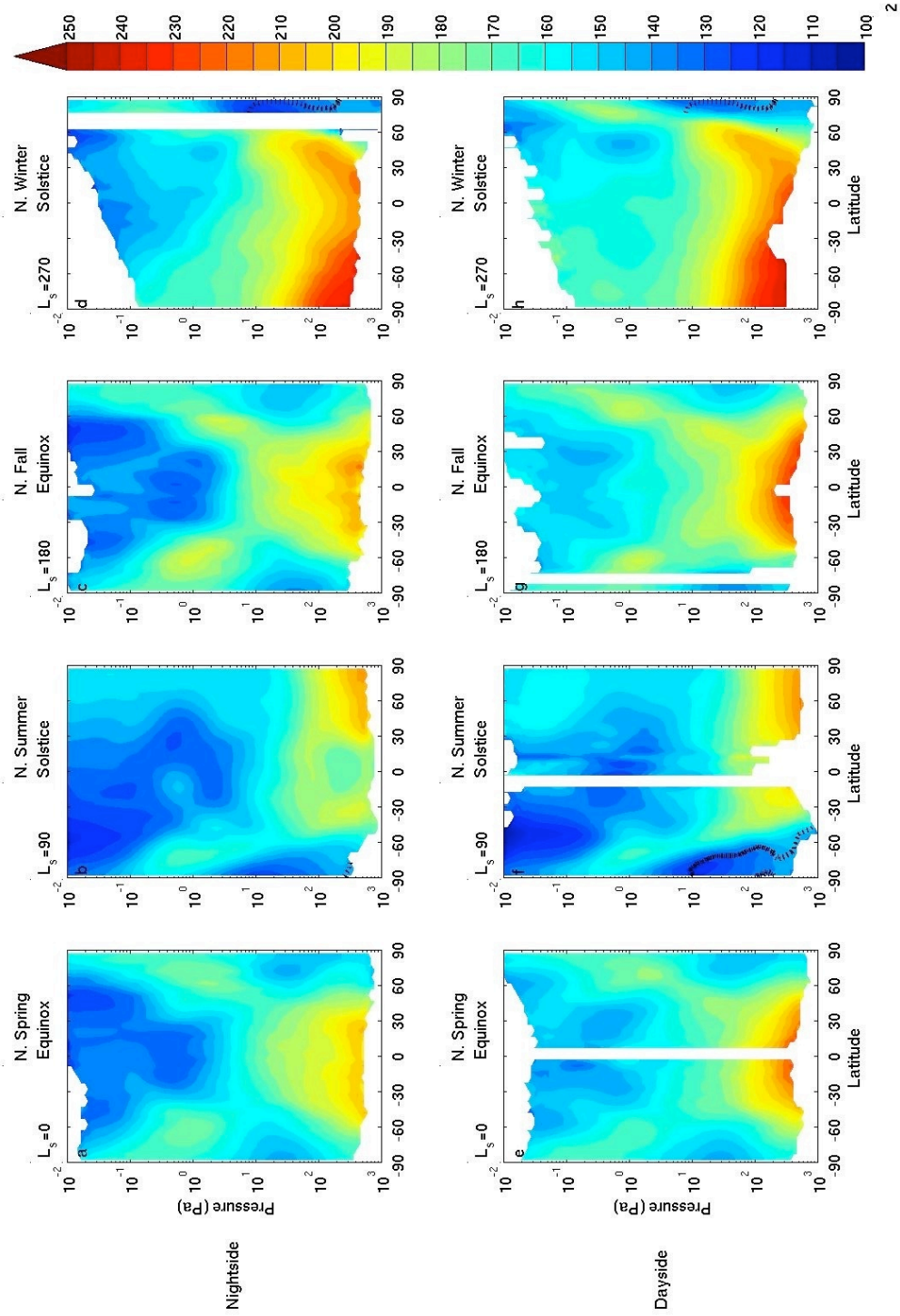
Figure 2.2. Zonal average temperature (K) for the labeled time of day and L_s bins during MY 29. Contours are every 5 K. The black contour indicates the CO_2 frost point.
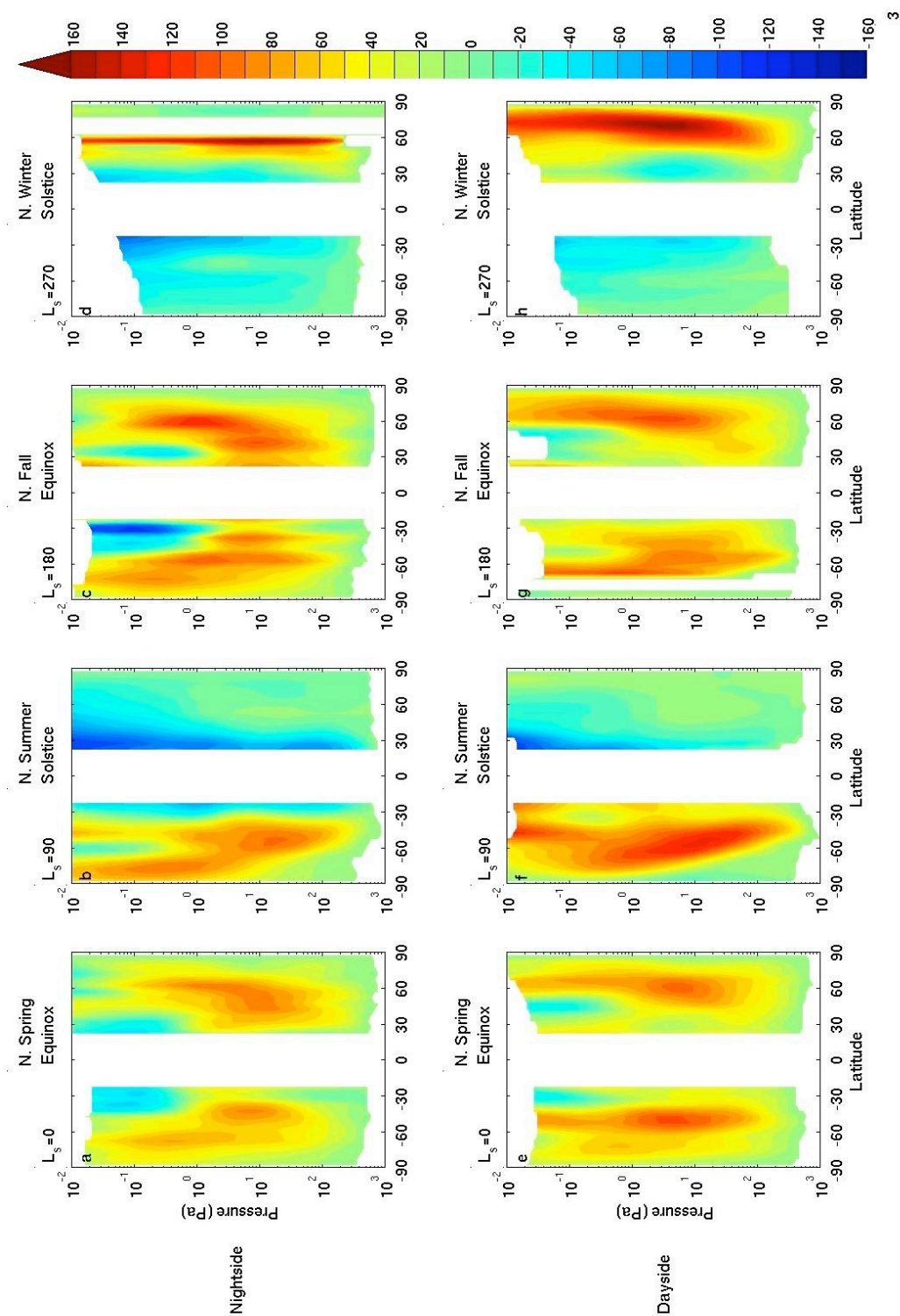
Figure 2.3. Estimated zonal wind velocity (ms^{-1}) for the labeled time of day and L$_s$ bins during MY 29. Contours are every 10 ms^{-1}.
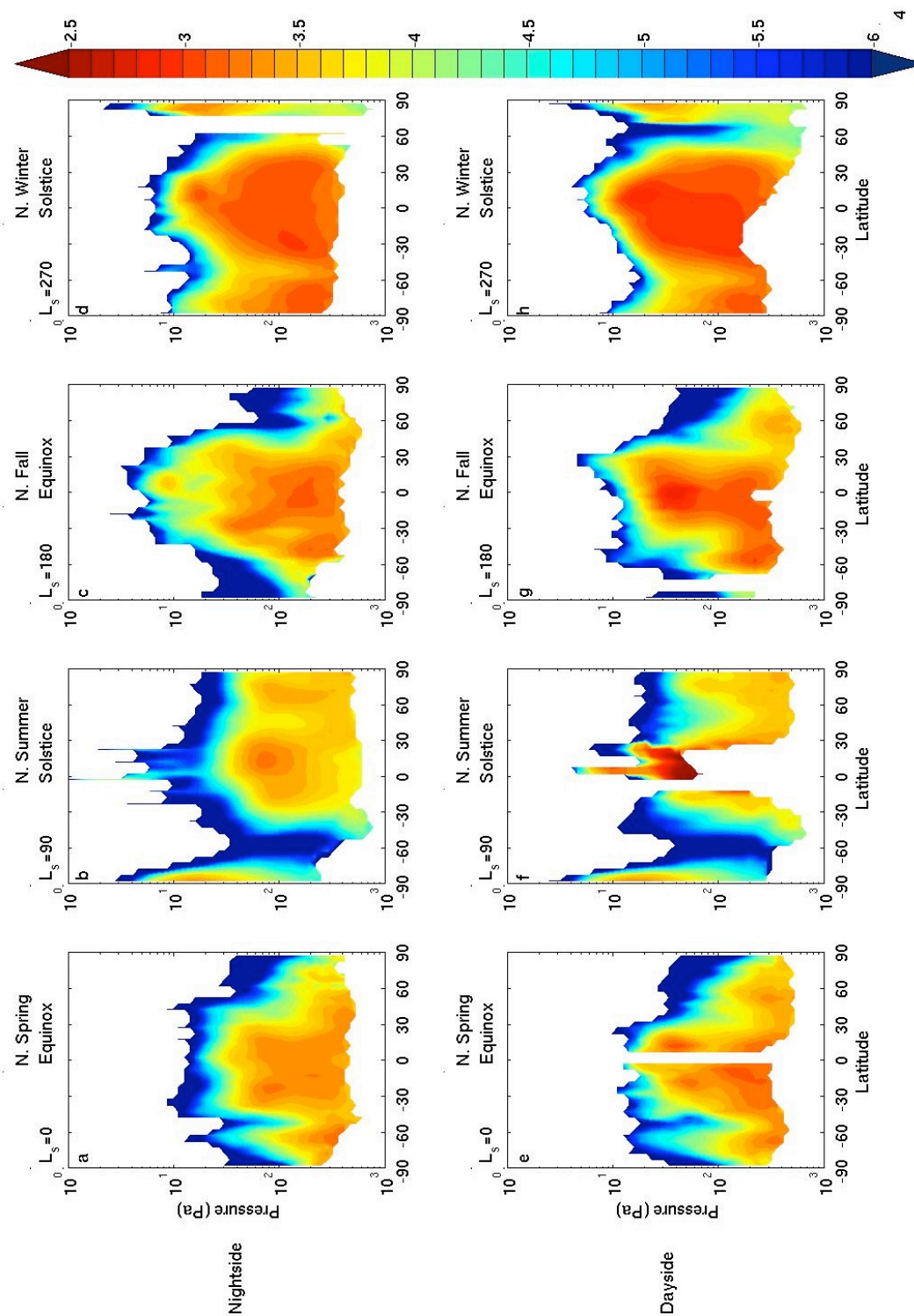
Figure 2.4. Log$_{10}$ of the zonal average dust density scaled opacity (m^2 kg^{-1}) for the labeled time of day and L$_s$ bins during MY 29. Contours are every 0.1 log units.
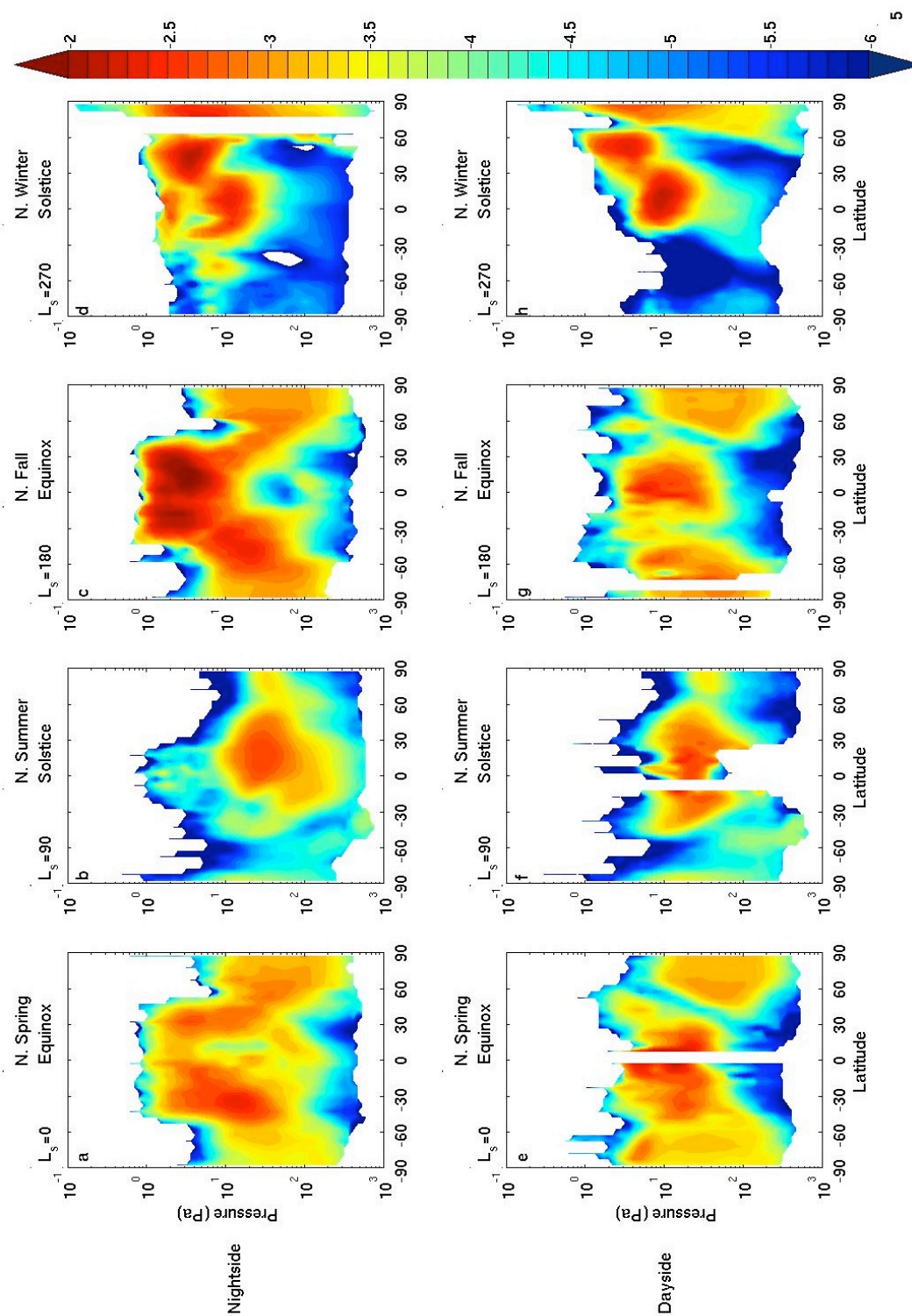
Figure 2.5. Log$_{10}$ of the zonal average water ice density scaled opacity (m^2 kg^{-1}) for the labeled time of day and L$_s$ bins during MY 29. Contours are every 0.1 log units.

MCS limb observations *a priori* makes retrieval success unlikely at high aerosol opacities, systematically biasing the zonal averages toward regions/vertical ranges with low dust/ice opacities.

2.3.2 Qualitative Reconstruction of the Mean Meridional Circulation

The observed thermal structure and aerosol distributions in Figures 2.2—2.5 are the result of multiple, often coupled processes with scales ranging from the global to the microscale. Thus, substantial improvement in our understanding of the mean meridional circulation eventually will rely upon the assimilation of temperature and aerosol concentrations into a general circulation model (GCM) [e.g., *Lewis et al.*, 2007; *Wilson et al.*, 2008] or direct measurements of the wind field.

While eagerly awaiting assimilation-driven modeling of the mean meridional circulation or direct wind measurements over the broad vertical range of the atmosphere observed by MCS, the observations and analysis presented in Figures 2.2—2.5 can be used in combination with insights from theory primarily developed for understanding the atmospheric circulation of the Earth (at the level of *Holton* [2004]) and an ensemble of radiative-convective models of the martian atmosphere [e.g., *Colburn et al.*, 1989; *Joshi et al.*, 1995; *Haberle et al.*, 1997; *Zalucha et al.*, 2010] to develop rough schematics of the mean meridional circulation throughout the lower and middle atmospheres at the equinoxes and solstices.

I first will make direct inferences from the zonal average plots about upwelling, downwelling, and the vigor of meridional and vertical mixing. I then will supplement those direct inferences with insights previously gleaned from theory and modeling to construct qualitative schematics of the mean meridional circulation, indicating where the schematic is ambiguous to motivate future modeling investigations and direct measurements.

Inferring upwelling and downwelling from the thermal structure is primarily an assessment of departure of temperatures from radiative equilibrium. As air is forced to rise (sink) in the atmosphere, it will cool (warm) adiabatically. Therefore, in the absence of diabatic heating by absorption of visible and infrared radiation by aerosols or trace gas species (at least those not included in radiative equilibrium models), temperatures cooler (warmer) than radiative equilibrium directly indicate upwelling (downwelling) driven by dynamical processes.

The vertical distribution of dust in Mars's atmosphere is a measure of the non-surface radiative forcing of atmospheric circulations on all scales and indicative of the meteorological systems that lift dust. (Studies of dust lifting, transport, and radiative forcing are the subject of Chapters 4 and 5; my primary focus here is on the connection between seasonal variability in the dust distribution and seasonal variability in the circulation.) But the global atmospheric circulation also re-distributes lifted dust, so dust can be a useful tracer of the mean meridional overturning circulation, particularly in the lower atmosphere [*Richardson and Wilson*, 2002; *Kahre et al.*, 2006]. Characteristic sedimentation velocities are of the same magnitude as characteristic vertical velocities of

the planetary-scale circulation, $\sim 10^{-2}$ ms^{-1}, so when dust is injected into the atmosphere at presumably higher vertical velocities, it will tend to rise or remain stable in zones of mean upwelling but sink more quickly by its own negative buoyancy in combination with the large-scale flow in zones of mean downwelling. In addition, sedimentation of martian dust is sufficiently slow that dust can be advected thousands of kilometers from where it is lifted [*Murphy et al.*, 1993], making dust a tracer of both horizontal and vertical flows on timescales shorter than its atmospheric residence time. However, this method of inference is complicated by the dependence of the sedimentation velocity on air density and particle size. The sedimentation velocity increases with height, so dust may not be fully distributed through a region of positive vertical velocity. Other complications include the potential removal or obscuration of dust by condensation of water ice or carbon dioxide ice.

The vertical distribution of water ice in the atmosphere constrains the vertical profile of water vapor and radiative forcing by water ice. Water ice thus can be a tracer of moist air at temperatures sufficiently cold for saturation and the path of water vapor from its sources (mainly warming water ice caps at the poles), which is controlled in part by the mean meridional circulation. In the simulations of *Richardson et al.* [2002], a water ice maximum over the northern tropics originates from water vapor coming from the northern (summer) pole near the surface and then strongly upwelling into colder atmosphere at ~ 150 Pa. Following this result, we will infer that an area with high concentrations of water ice spanning a strong vertical temperature gradient is a zone of upwelling. Such an inference can be complicated by variations in available condensation

nuclei and advection, diffusion, and sedimentation of water ice. In addition,

sublimating water ice in the atmosphere can be a source of water vapor. *Hinson and*

Wilson [2004] and *Lee et al.* [2009], however, point out that if the water ice distribution

is tidally controlled, the effects of advection, diffusion, and sedimentation can be mostly

neglected.

2.4 The Mean Meridional Circulation at the Equinoxes

2.4.1 Description of Thermal Structure and Aerosol Distributions

The principal exceptions to the general hemispheric symmetry of the thermal structure at

northern spring equinox (Figures 2.2a and 2.2e) are the temperature minima near poles

(which I call the "polar vortices" though vorticity is not diagnosed here.) The winter

leaving north polar vortex extends from the remnant cold surface to pressures near 10 Pa.

The surface and lower atmosphere are warmer in the south, and so confine the vertical

extent of the southern polar vortex. At northern fall equinox (Figures 2.2c and 2.2g), the

thermal structure is very similar to northern spring equinox, except that the high latitudes

at ~1 Pa and the tropics at ~10 Pa are warmer. The estimated zonal wind distribution at

both equinoxes consists of two zonal jets in the mid-latitudes.

The dust distributions at both equinoxes are relatively symmetric about the equator. Dust density scaled opacity is higher and dust penetrates to higher altitudes near the equator than at the poles (Figures 2.4a, 2.4c, 2.4e, and 2.4h). Dust appears to penetrate to lower pressure levels in the tropics at northern fall equinox than at northern spring equinox.

The water ice distributions at both equinoxes differ between day and night due to the influence of the thermal tides [*Lee et al.*, 2009]. They, however, are broadly similar at the same time of day. The clearest difference appears on the nightside, where the layer of water ice in the tropics between 1 and 10 Pa is up to an order of magnitude higher in density scaled opacity at northern fall equinox than northern spring equinox.

Thus, while there are some second-order differences, the thermal structure and aerosol distributions at both equinoxes are sufficiently similar that their qualitative mean meridional circulations will be effectively interchangeable.

2.4.2 Diagnosis of Upwelling and Downwelling

Figures 2.6a-c re-plot zonal average nightside temperature (Figure 2.2a), dust density scaled opacity (Figure 2.4a), and water ice density scaled opacity (Figure 2.5a) for northern spring equinox with upward and downward (solid for definite, dashed for ambiguous) arrows to indicate zones of upwelling and downwelling inferred from the zonal average fields. At the equinox, the temperature maxima of the polar warmings are ~170 K, and from the ensemble of model we see that it is at least 35 K above radiative equilibrium temperatures. Importantly, significant amounts of ice or dust are absent from
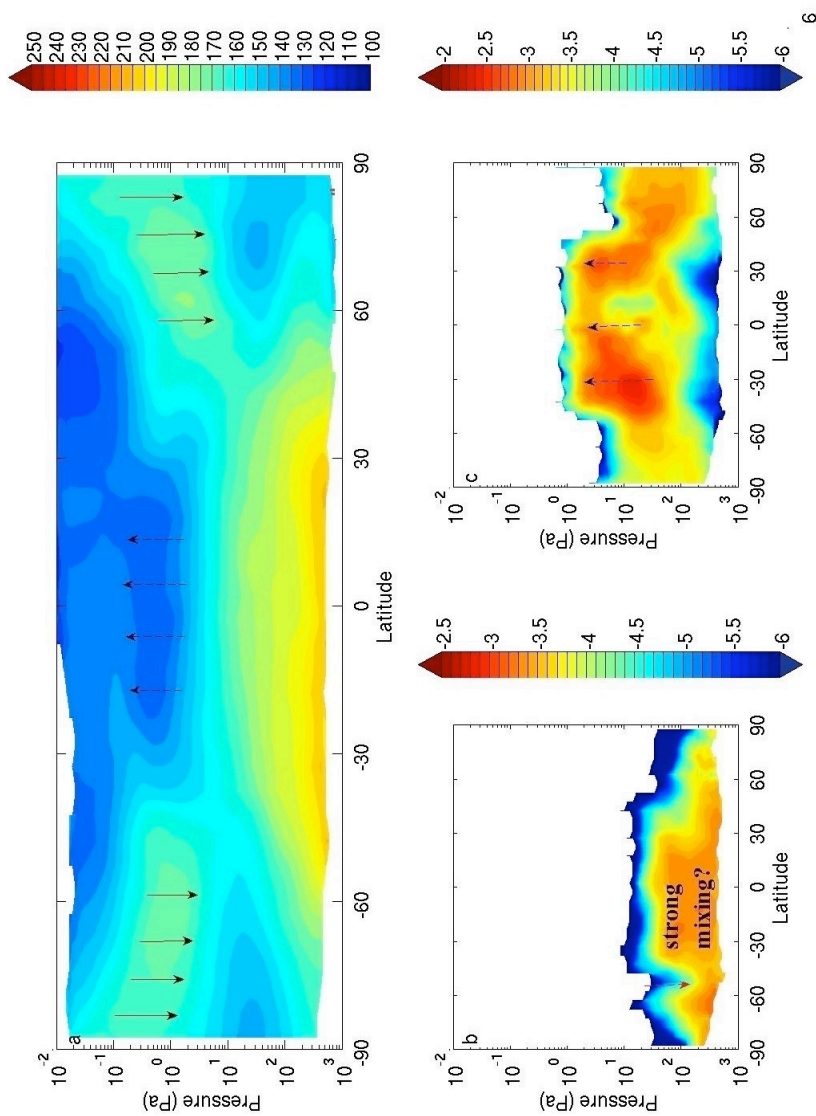
Figure 2.6. Characteristic zonal average fields for an equinoctial case (L$_s$=0°, nightside) with inferred zones of upwelling (upward arrows), downwelling (downward arrows), and vigorous mixing (label) indicated. Definite inferences are marked with solid arrows. More ambiguous inferences are marked with dashed arrows. The color of arrows is for sake of clarity and has no other significance: (a) temperature (K), identical to Figure 2.2a; (b) dust density scaled opacity (m^2 kg^{-1}), identical to Figure 2.4a; (c) water ice density scaled opacity (m^2 kg^{-1}), identical to Figure 2.5a.

the warmings and the magnitudes of the temperature maxima are fairly similar between the dayside and nightside, thus excluding the possibility that diabatic heating of aerosol is driving the strong departure from radiative equilibrium. Instead, dynamically driven downwelling is indicated.

Nightside temperatures at ~1 Pa in the tropics are ~130 K and dayside temperatures are ~150 K, a variation likely driven by the tides [*Lee et al.*, 2009]. The average temperature is thus at least 10 K below radiative equilibrium. Water ice is present at the lower end of this zone of very cold temperatures, but water ice will absorb infrared radiation from below, re-emit it at a lower temperature, and produce a net diabatic heating, which cannot explain why temperatures are cooled below radiative equilibrium.

Dust density scaled opacities at 200 Pa are relatively similar from pole to pole, but the vertical extent of dust at these density scaled opacities is significantly deeper than elsewhere from 40° S to 25° N, indicating strong vertical and meridional mixing in the lower atmosphere at these latitudes. There is a minimum in dust density scaled opacities at ~50° S at 100 Pa. We infer that this minimum is probably not an effect of scavenging by water but due, instead, to downwelling, since ice density scaled opacities at this latitude and level are relatively similar to ice density scaled opacities at this level at higher latitudes, where the vertical extent of dust is deeper.

High ice density scaled opacities are observed over a broad vertical range centered at ~10 Pa at between 45° S and 45° N, which is a region with a vertical temperature gradient. We therefore infer broad upwelling at this level and region.
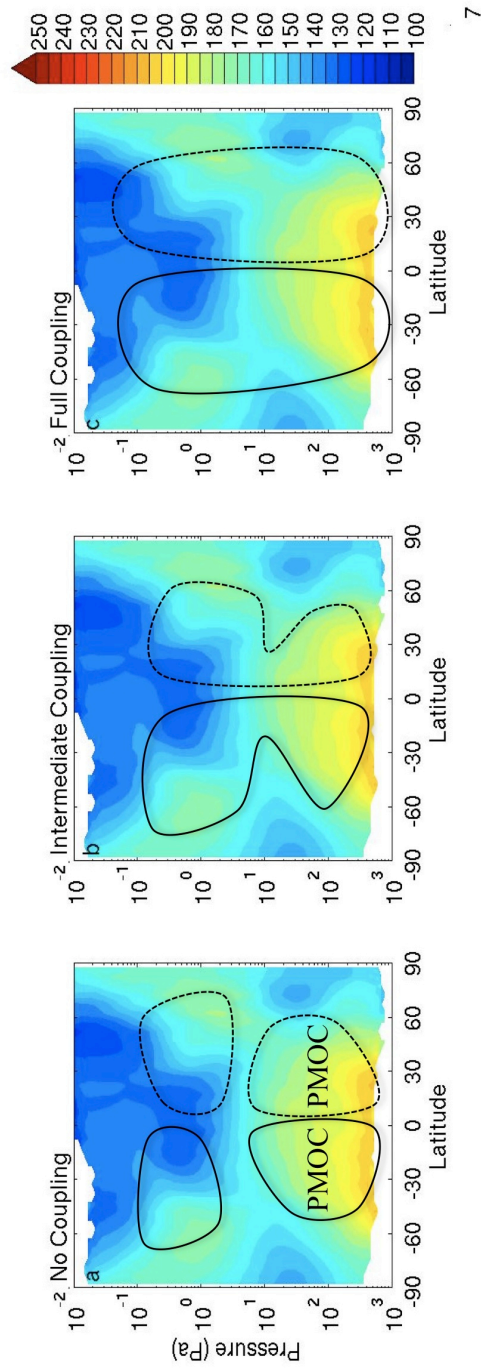
Figure 2.7. Characteristic temperature fields for the equinoctial case: (a, b, and c) as in Figure 2.6 marked with schematic streamlines of the inferred mean meridional circulation for three possible states of coupling as labeled over the boxes in each column. The solid streamlines indicate counter-clockwise flow and the dashed streamlines indicate clockwise flow.

The upwelling and downwelling zones identified here are consistent with meridional cells symmetric about the equator in both the lower and middle atmospheres that rise at the equator and sink at higher latitudes. In the lower atmosphere, the average insolation is strongest at the equator, so the differential heating between the equator and pole creates an unstable flow regime due to incompatibility between radiative equilibrium and angular momentum conservation. To resolve this instability, equatorial air rises from the surface and moves poleward. This air cools at higher latitudes, sinks, and becomes a return flow back to the equator, forming two meridional circulation cells symmetric about the equator: the PMOCs. In the middle atmosphere, theory and modeling suggest that similar cells can be driven by dissipation of waves and tides or aerosol diabatic forcing [e.g., *Holton et al.*, 1995; *Forget et al.*, 1999; *Forbes and Miyahara*, 2006; *Hartogh et al.*, 2007; *Wilson et al.*, 2008].

It is, however, unclear to what extent the lower and middle atmospheric meridional cells are coupled kinematically. Different possible scenarios consistent with the inferred upwelling and downwelling are illustrated on the same temperature plot as Figure 2.6a in Figures 2.7a-c. The lower and middle atmospheric cells in one hemisphere may be fully kinematically coupled in a single cell, in which air rises at the equator into the middle atmosphere, strongly descends within the middle atmospheric polar warming to the surface (Figure 2.7c). Or the lower atmospheric meridional cell may be separated from the middle atmospheric meridional cell by a region of weak vertical motion (opposite to the mutual upwelling or downwelling in the cells) (Figure 2.7a). In the former case, there would be substantial mixing of constituents both meridionally and

vertically. In the latter case, mixing would be primarily meridional, isolating the lower

from the middle atmosphere (and by extension, the upper atmosphere) with implications

for the atmospheric loss of water vapor and other constituents. I note that a Mars GCM

simulation of this season [*Forget et al.*, 1999, Figure 10] suggests the local temperature

maxima of the polar warmings are consistent with an intermediate state of coupling

(Figure 2.7b), in which the PMOC extends deeply into the middle atmosphere in the

tropics, is pulled poleward more strongly in the middle atmosphere than in the lower

atmosphere by whatever is forcing the middle atmospheric meridional cell, and returns to

the deep tropical PMOC in the middle atmosphere. Thus, the PMOC in the model is

kinematically coupled with the mean meridional cell in the middle atmosphere in the

tropics but not at higher latitudes.

2.5 The Mean Meridional Circulation at the Solstices

2.5.1 Description of Thermal Structure and Aerosol Distributions

The thermal structure and aerosol distributions at northern summer and northern winter

solstices differ significantly. Temperatures throughout the atmosphere (except in the

polar vortex) are considerably warmer at northern winter solstice than northern summer

solstice (Figures 2.2b, 2.2d, 2.2f and 2.2h). In the lower atmosphere ($p > 10$ Pa) at

northern winter solstice, temperatures are usually highest in the southern high latitudes,

are lower toward the tropics, and have a secondary maximum in the northern mid-latitudes that tilts poleward at lower pressures. This qualitative thermal structure is only weakly apparent at northern summer solstice. In the middle atmosphere, there is a temperature maximum at ~1 Pa near the winter pole at both solstices, which is slightly warmer at northern winter solstice. The estimated zonal wind structures are qualitatively similar at both solstices and consist of a strong westerly jet (stronger at northern winter solstice) in the mid-high latitudes of the winter hemisphere and weak westerlies or easterlies in the mid-high latitudes of the summer hemisphere (Figures 2.3b, 2.3d, 2.3f and 2.3h).

At both solstices, dust is primarily restricted to the summer hemisphere and winter hemisphere tropics (Figures 2.4b, 2.4d, 2.4f and 2.4h). A region of extremely dust clear air generally separates the dust in the winter tropics from the dust in the winter high latitudes (likely CO_2 ice being retrieved as dust). This region of dust clear air is broader at northern summer solstice. In the winter tropics and summer hemisphere, dust density scaled opacity is higher at northern summer solstice. The summer hemisphere and tropical dust distributions at the northern summer and northern winter solstices also differ in stratification. Dust density scaled opacity is constant or decreases with height at northern winter solstice but tends to increase with height in the tropics below 60 Pa at northern summer solstice.
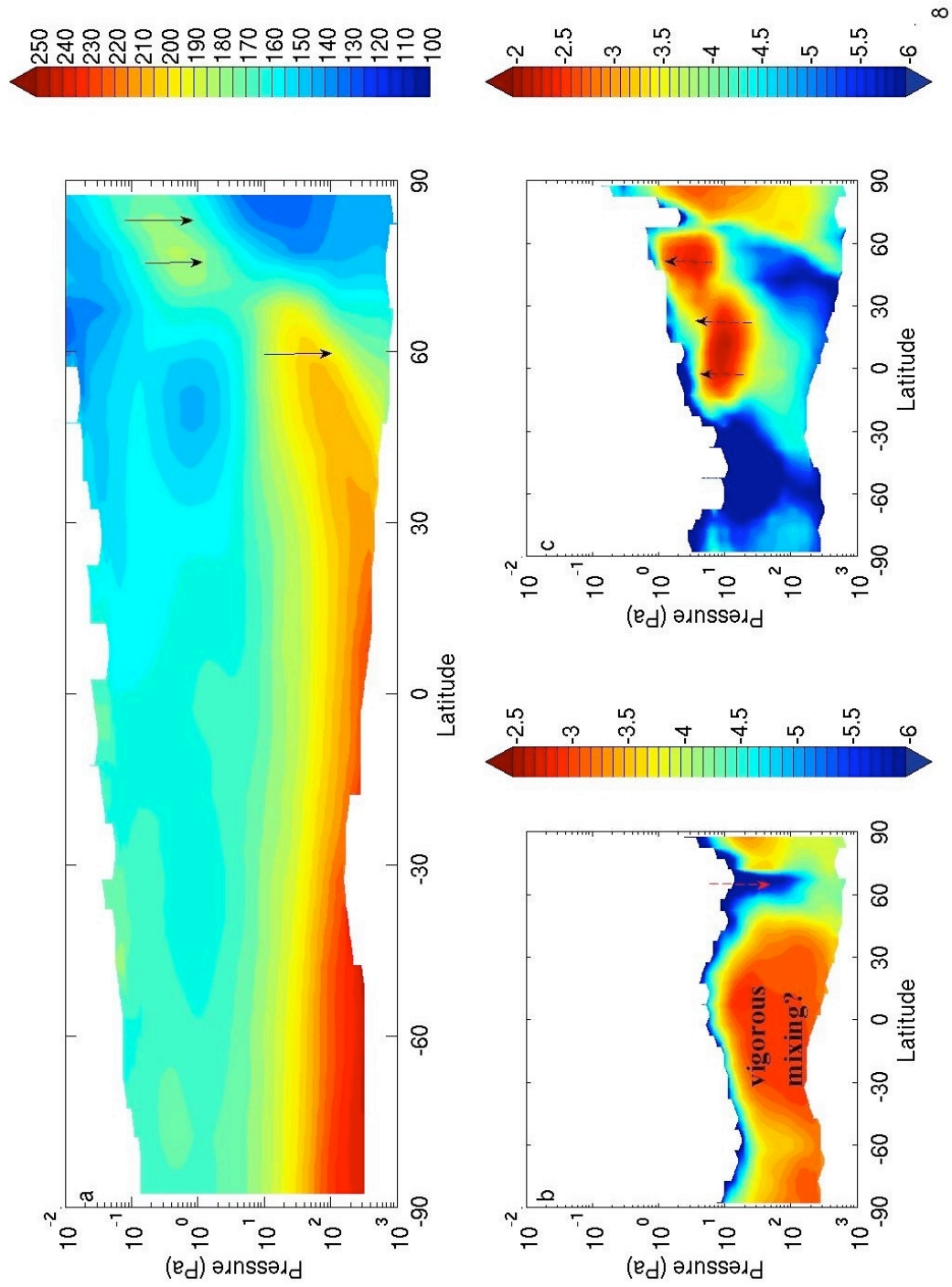
Figure 2.8. As Figure 2.6 but for northern winter solstice (L$_s$=270º, dayside).

The water ice distributions at the solstices differ significantly (Figures 2.5b, 2.5d, 2.5f and 2.5h). The northern summer solstice distribution is dominated by a high density scaled opacity layer of water ice in the northern tropics at ~30 Pa, but smaller amounts of water ice are present at all latitudes at $p > 10$ Pa. At northern winter solstice, the thickest layers of water ice are restricted to the summer hemisphere at $p < 10$ Pa. Note that water ice density scaled opacity is higher in the winter polar vortex at northern winter solstice.

Due to differing topography and summer insolation between the northern and southern hemispheres, the southern summer solstitial circulation (at least the PMOC) is believed to be more vigorous than its northern analog [*Zurek et al.,* 1992; *Richardson and Wilson*, 2002; *Takahashi et al.*, 2003]. Because of this prior knowledge and the significant differences in thermal structure and aerosol distributions between the two solstices in Figures 2.2—2.5, the circulation at each solstice will be considered separately.

2.5.2 Diagnosis of Upwelling and Downwelling

Figures 2.8a-c re-plot zonal average dayside temperature (Figure 2.2g), dust density scaled opacity (Figure 2.3g), and water ice density scaled opacity (Figure 2.4g) for southern summer solstice with arrows indicating upwelling and downwelling as in Figures 2.6a-c. The temperature of the middle atmospheric polar warming near the north pole is ~180 K. Because the temperature of this warming exceeds temperatures at this level at all other latitudes, it can be inferred to be much warmer than radiative

equilibrium even without consulting a model. Comparison with the ensemble of models, (see particularly *Haberle et al.* [1997]) suggests the departure from radiative equilibrium of the observed warming is at least 70 K. The warming is above the level of high ice concentrations and is at latitudes with no or limited solar insolation at this season, so downwelling is inferred. In the lower atmosphere, there is substantial temperature inversion at a level of ~50 Pa at 60° N. Comparison with the model of *Haberle et al.* [1997] suggests the departure from radiative equilibrium of the observed warming is at least 50 K. This region is mostly free of water ice and dust and just on the edge of the noon terminator, which suggests diabatic heating is minimal, so downwelling is inferred.

Dust density scaled opacities are high and roughly constant with pressure at pressures greater than 20 Pa from 40° to 30° N, indicating strong vertical and meridional mixing in the lower atmosphere at these latitudes. There is a minimum in dust concentration at ~60° N at 100 Pa (that continues to the pole if the dust there is CO_2 ice). Water ice concentrations at this latitude and level are higher than at lower latitudes, so this minimum could be as easily due to scavenging as it could be due to downwelling.

Water ice concentrations are high in a tilting region stretching from a level of ~100 Pa at 30° S to a level of ~3 Pa at 50° N. Temperatures decrease with height throughout this latitudinal band. If we interpret this feature as due to gradual drying of vapor-rich air from the summer pole upwelling across the equator, we may infer broad upwelling throughout this latitudinal band.

The upwelling and downwelling zones identified here are consistent with single meridional cells in the lower and the middle atmospheres. The lower atmosphere cell (the PMOC) rises in the southern mid-latitudes and sinks at 60° N. The theory of *Lindzen and Hou* [1988] suggests the latitude of PMOC downwelling corresponds to the latitude of upwelling in the opposite hemisphere, but there is no definite confirmation of this idea from the observations. In the middle atmosphere, the downwelling near the pole indicates a middle atmospheric cell, but it is unclear from the observations whether the upwelling of this cell takes the form of weak upwelling in the middle atmosphere from the summer pole to the winter mid-latitudes or instead manifests as stronger, more localized upwelling in some particular latitudinal band.

The discontinuity between the warming due to downwelling in the lower atmosphere near 60° N and the warming due to downwelling in the middle atmosphere near the north pole suggests that the PMOC in the lower atmosphere is not fully kinematically coupled with the meridional cell in the middle atmosphere. The polar warming in a simulation of the circulation in this season by the Mars GCM used in Chapter 2.4.2 [*Forget et al.*, 1999, Figure 7] is 50 K warmer than the observed polar warming. In this simulation, the meridional mass streamfunction is consistent with nearly complete coupling between the PMOC and the mean meridional cell in the middle atmosphere, since the streamlines of the PMOC in the northern high latitudes remain vertical as low as 15 km above the surface (as opposed to 55 km in the equinoctial case). Because of the similarity between the temperature of the polar warming simulated by *Forget et al.* [1999] and observed dust storm polar warmings, it is possible that dust
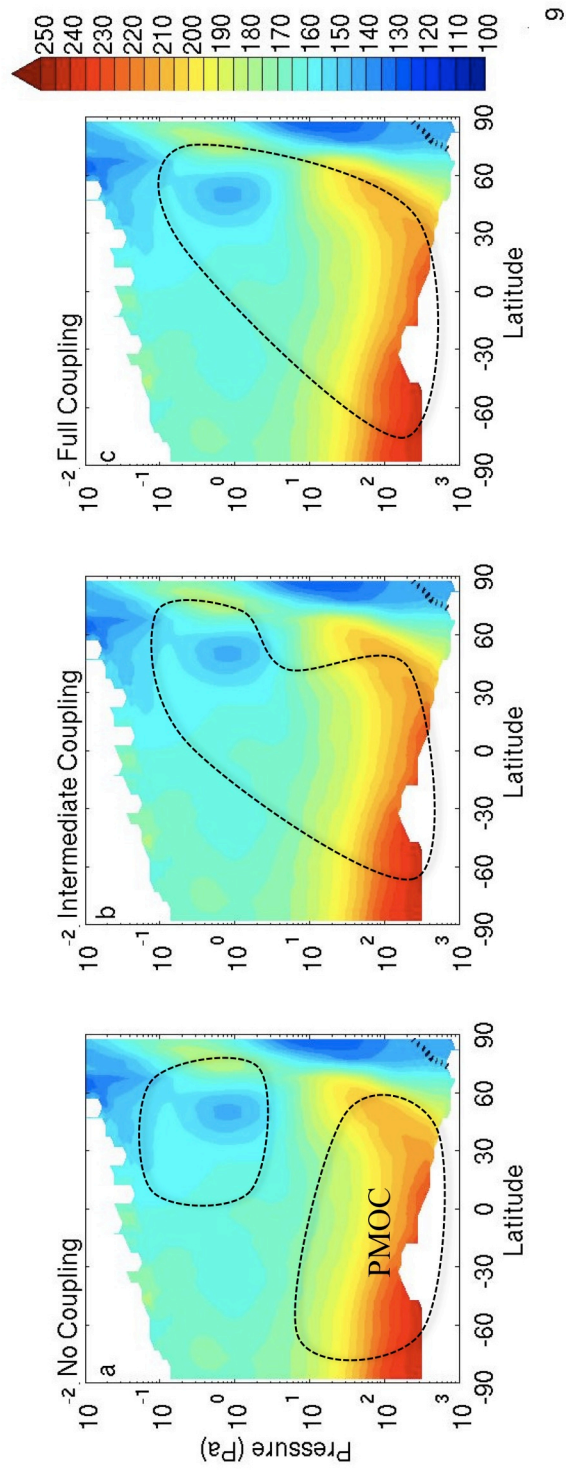
Figure 2.9. As Figure 2.7 but for northern winter solstice.
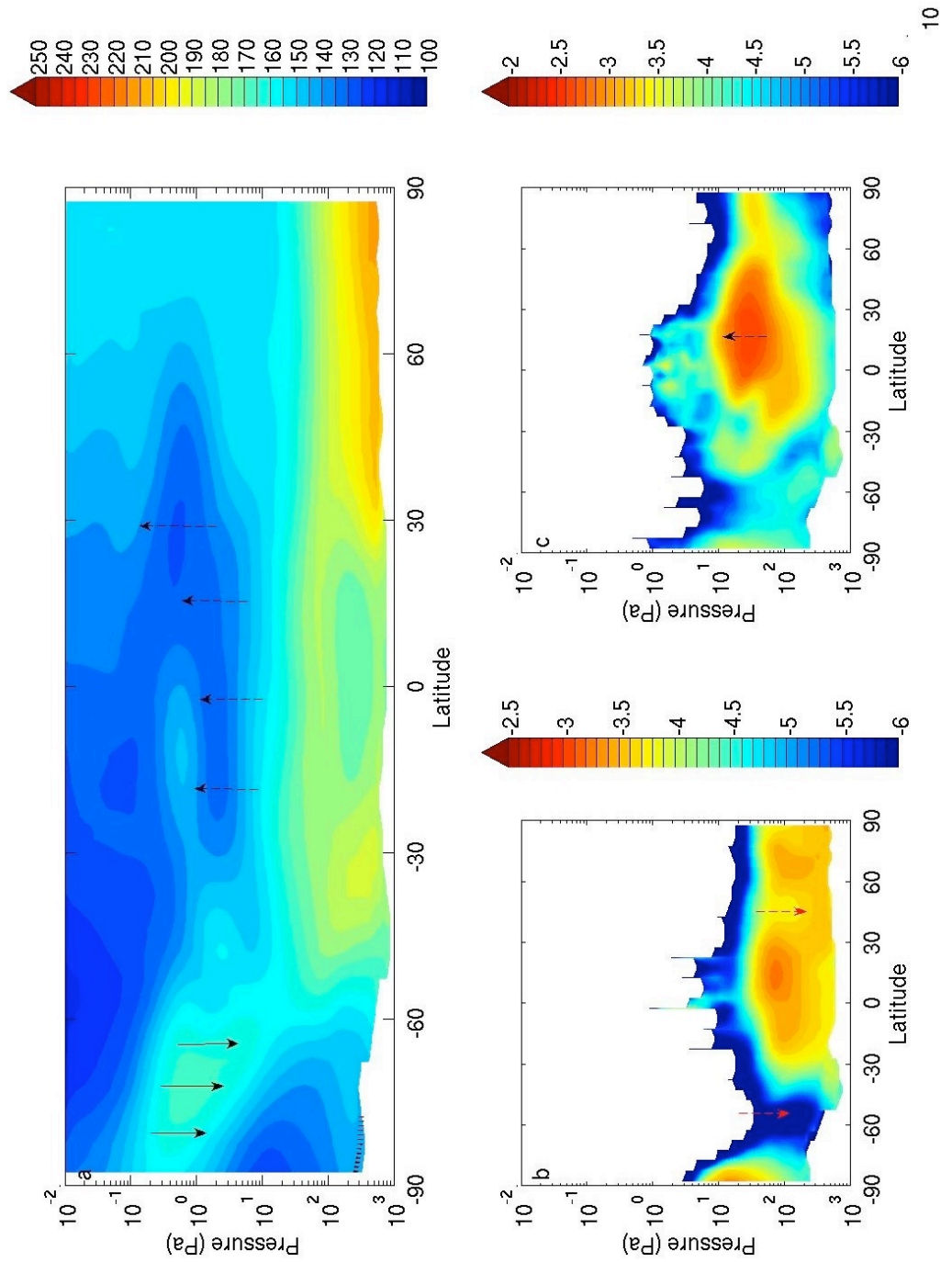
Figure 2.10. As Figure 2.6 but for the northern summer solstice (L$_s$=90°, nightside).

storm polar warmings are the result of a fully kinematically coupled lower and middle atmospheric meridional circulation. The mean meridional circulations in the simulations of *Wilson et al.* [1997] and *Kuroda et al.* [2009] are consistent with this idea.

From the observations alone, little can be inferred about the vertical structure of tropical upwelling. So I cannot determine whether the lower and middle atmospheric meridional cells are in an intermediate state of coupling or fully decoupled. Figures 2.9a-c show possible structures of the mean meridional cells for different states of kinematic coupling.

The dust-clear air in the winter high-latitudes is consistent with the area of the atmosphere heated by downwelling in the lower atmospheric PMOC. On the poleward side of the vortex wall, water ice opacities increase again (Benson et al., submitted to *J. Geophys. Res.*), but density scaled opacities are much lower than in the tropical cloud belt. The southern winter atmosphere is seen to be much clearer than the northern winter atmosphere, consistent with Mars Odyssey Gamma Ray Spectrometer argon observations [*Sprague et al.,* 2007] that suggest that the southern polar vortex is much more dynamically isolated than that of the north.

Figures 2.10a-c re-plot zonal average nightside temperature (Figure 2.2b), dust density scaled opacity (Figure 2.3b), and water ice density scaled opacity (Figure 2.4b) for southern summer solstice with arrows indicating upwelling and downwelling as in Figures 2.6a-c and 2.8a-c. The temperature of the middle atmospheric polar warming near the south pole is ~170 K (Figure 2.10a). Because the temperature of this warming exceeds temperatures at this level at all other latitudes, it can be inferred to be much

warmer than radiative equilibrium even without consulting a model. The full ensemble

of radiative-convective models (particularly *Zalucha et al.* [2010]) suggests temperatures

exceed radiative equilibrium by at least 35 K. The region of warming is free of aerosol,

so downwelling is inferred. Temperatures at ~1 Pa in the tropics average ~135 K. The

average temperature is thus at least 20 K below radiative equilibrium [*Colburn et al.*,

1989], so upwelling is inferred there.

Downwelling is inferred in the vicinity of the region of dust-clear air at 60° S and

~100 Pa (Figure 2.10b), though downwelling also likely occurs significantly equatorward

of this latitude, where there is a maximum in temperature and a minimum in water ice,

possibly indicating a region of adiabatic warming. Dust density scaled opacity has a

notable minimum at ~45° N and ~100 Pa. Since water ice density scaled opacity at this

pressure level is higher in the southern tropics than in this region, enhanced scavenging

by water ice is not a convincing explanation for the minimum, so downwelling is inferred

there. Water ice concentrations are highest at ~30 Pa over the northern tropics (Figure

2.10c). Temperatures are decreasing with altitude at this pressure level. If this feature is

due to condensation of vapor rich air from the summer pole upwelling in the northern

tropics, broad upwelling throughout this latitudinal band may be inferred.

Thus, the inferred circulation in the lower atmosphere consists of two PMOCs

that upwell in the northern tropics: a stronger, broader cell that downwells in the southern

mid-latitudes and a weaker, narrower cell that sinks in the northern mid-latitudes. In the

middle atmosphere, another cell likely upwells through the tropics and downwells near

the winter pole. As at southern summer solstice, observations argue against full kinematic
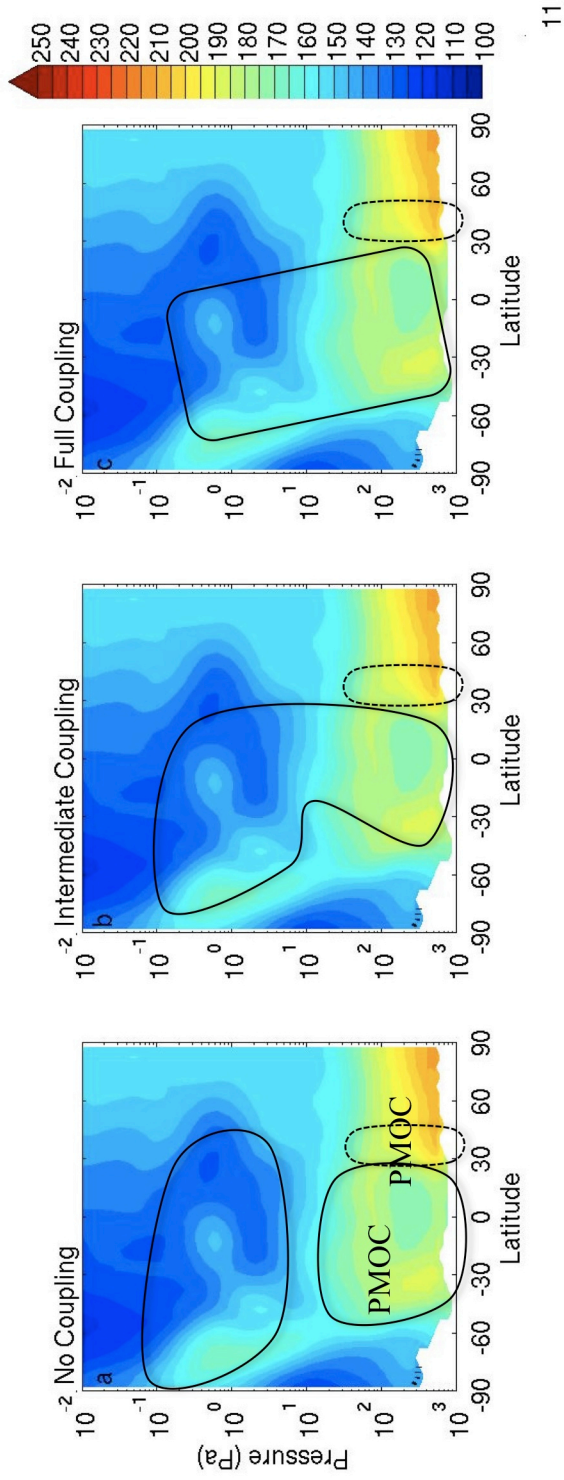
Figure 2.11. As Figure 2.7 but for the northern summer solstice.

coupling, but the exact degree of kinematic coupling cannot be determined. Possible options are plotted in Figures 2.11a-c. Note that a Mars GCM simulation of this season [*Hartogh et al.*, 2007] simulates a similar thermal structure and a circulation in which the PMOC and a middle atmospheric meridional cell are partially coupled.

2.6 An Alternative Approach to the Analysis of Kinematic Coupling

As noted by *Wallace and Hobbs* [1976], planetary atmospheres act like heat engines "in a gross, statistical sense," in which energy is concentrated by solar absorption in the lower atmosphere of the tropics and summer hemisphere and re-distributed by circulations like the PMOC toward cooler air at higher altitudes and latitudes. Thus, the generation of mechanical energy to maintain atmospheric circulations depends on the positive thermodynamic efficiency of the atmospheric heat engine implied by this general effective diffusion of heat

Thus, complete kinematic decoupling of the lower and middle atmospheric mean meridional circulations is unlikely to produce a middle atmosphere in which the equator is substantially cooler than the pole. The middle atmospheric cell in that case would be a thermally indirect circulation equivalent to a heat engine running strongly in reverse. The negative efficiency at northern summer solstice would be ~25%. Such a circulation would need to be sustained entirely by dissipation as heat of waves and tides propagating

into the middle atmosphere from below, since waves and tides are ultimately driven by diabatic heating in the lower atmosphere. The analysis in Chapter 3 suggests that zonal average direct heating by gravity wave dissipation in the middle atmosphere is 1 K or less. Unless dissipation by tides or other types of waves is substantially larger, this gradient must be sustained by effective eddy diffusion of heat from the tropical lower atmosphere.

In that case, the lower and middle atmospheric mean meridional circulations must be at least partially coupled throughout the year. Coupling can be assessed quantitatively by balancing eddy diffusion against the net excess radiation in the middle atmosphere due to the polar warming and the equatorial cooling. For example, high effective eddy diffusivities according in such a scheme likely would occur in dust storm polar warmings and so would indicate nearly full coupling. Such an analysis is beyond the scope of this study.

2.7 Summary

The first simultaneous and systematic observations of the thermal structure and aerosol distributions of lower and middle martian atmospheres to above 80 km have been used to perform a simple, qualitative analysis of the background seasonal variability of the mean meridional circulation. This analysis provides evidence of a vigorous and clearly delineated middle atmospheric circulation at all seasons of the year. Because this circulation maintains a strong positive equator to pole gradient in temperature, it is

thermodynamically implausible without invoking some amount of kinematic coupling between the circulations of the lower and middle atmospheres. However, in all cases during the year analyzed, the coupling is much weaker than indicated by GCM simulations of dust storm polar warmings.

As the retrieval algorithm improves, an increased volume of data from higher aerosol opacity locations and seasons will become available, allowing the meteorology of cloud systems and dust storms and interannual variability to be studied in more detail. Further downstream, MCS information on the spatial distribution of temperature and aerosol radiative heating offers the best opportunity for assimilation of spacecraft data, potentially yielding "reanalysis" data for Mars, as is now standard for Earth science. The quality and detail of the MCS data suggest that a new range of problems within martian meteorology now can be attacked with a combination of data and atmospheric modeling. Much as atmospheric modeling over the last decade has found a need for an extended vertical range, the MCS observations argue strongly that future observations of the atmosphere for the purpose of meteorology and climate should at least match the MCS observational vertical range and resolution for temperature and aerosols.

Bibliography

Angelats i Coll, M., F. Forget, M. A. López-Valverde, and F. González-Galindo (2005), The first Mars thermospheric general circulation model: The Martian atmosphere from the ground to 240 km, *Geophys. Res. Lett.*, *32*, L04201, doi:10.1029/2004GL021368.

Barnes, J.R. (1980), Time spectral analysis of midlatitude disturbances in the Martian atmosphere, *J. Atmos. Sci.*, *37*, 2002-2015.

Barnes, J.R. (1981), Midlatitude disturbances in the Martian atmosphere: a second Mars year, *J. Atmos. Sci.*, *38*, 225-234.

Barnes, J.R. (1991), A simple nearly analytic model of a gravity wave driven middle atmospheric circulation, *J. Atmos. Sci.*, *48*, 225-235.

Clancy, R. T., B. J. Sandor, M. J. Wolff, P. R. Christensen, M. D. Smith, J. C. Pearl, B. J. Conrath, and R. J. Wilson (2000), An intercomparison of ground-based millimeter, MGS TES, and Viking atmospheric temperature measurements: Seasonal and interannual variability of temperatures and dust loading in the global Mars atmosphere, *J. Geophys. Res.*, *105*(E4), 9553–9571.

Colburn, D.S., J.B. Pollack, and R.M. Haberle (1989), Diurnal Variations in Optical Depth at Mars, *Icarus*, *79*, 159-189.

Deming, D., M. J. Mumma, F. Espenak, T. Kostiuk, and D. Zipoy (1986), Polar warming

in the middle atmosphere of Mars, *Icarus*, *66*, 366-379.

Forbes, J.M., and S. Miyahara (2006), Solar Semidiurnal Tide in the Dusty Mars Atmosphere, *J. Atmos. Sci., 63* (7), 1798-1817.

Forget, F., F. Hourdin, R. Fournier, C. Hourdin, O. Talagrand, M. Collins, S.R. Lewis, P.L. Read and J.-P. Huot (1999), Improved general circulation models of the Martian atmosphere from the surface to above 80 km, *J. Geophys. Res 104*, 24155–24175.

Haberle, R.M., C.B. Leovy, and J.M. Pollack (1982), Some effects of global dust storms on the atmospheric circulation of Mars, *Icarus*, *50*, 322-367.

Haberle, R.M., J.B. Pollack, J.R. Barnes, R.W. Zurek, C.B. Leovy, J.R. Murphy, J. Schaeffer, and H. Lee (1993), Mars atmospheric dynamics as simulated by the NASA/Ames general circulation model I. The zonal mean circulation, *J. Geophys. Res., 98*, 3093-3124.

Haberle, R. M., H. Houben, J. R. Barnes, and R. E. Young (1997), A simplified three-dimensional model for Martian climate studies, *J. Geophys. Res., 102*(E4), 9051–9067.

Hartogh, P., A. S. Medvedev, T. Kuroda, R. Saito, G. Villanueva, A. G. Feofilov, A. A. Kutepov, and U. Berger (2005), Description and climatology of a new general circulation model of the Martian atmosphere, *J. Geophys. Res., 110*, E11008, doi:10.1029/2005JE002498.

Hartogh, P., A.S. Medvedev, and C. Jarchow (2007), Middle atmosphere polar warmings on Mars: Simulations and study on the validation with sub-millimeter observations, *Planet. Space. Sci.*, *55* (9), 1103-1112.

Hinson, D. P., and R. J. Wilson (2004), Temperature inversions, thermal tides, and water ice clouds in the Martian tropics, *J. Geophys. Res.*, *109*, E01002, doi:10.1029/2003JE002129.

Holton, J.R. (2004), *An Introduction to Dynamic Meteorology*, 4th ed., 535 pp. Elsevier, Amsterdam.

Holton, J.R. P.H. Haynes, M.E. McIntyre, A.R. Douglass, R.B. Rood, and L. Pfister (1995), Stratosphere-Troposphere Exchange, *Rev. Geophys.*, *33* (4), 404-439.

Jakosky, B.M. and T.Z. Martin (1987), Mars: North-polar atmospheric warming during dust storms, *Icarus 72*, 528–534.

Joshi, M. M., S. R. Lewis, P. L. Read, and D. C. Catling (1995), Western boundary currents in the Martian atmosphere: Numerical simulations and observational evidence, *J. Geophys. Res.*, *100*(E3), 5485–5500.

Kahre, M. A., J. R. Murphy, and R. M. Haberle (2006), Modeling the Martian dust cycle and surface dust reservoirs with the NASA Ames general circulation model, *J. Geophys. Res.*, *111*, E06008, doi:10.1029/2005JE002588.

Kleinböhl , A., J. T. Schofield, D. M. Kass, W. A. Abdou, C. R. Backus, B. Sen, J. H. Shirley, W. G. Lawson, M. I. Richardson, F. W. Taylor, N. A. Teanby, and D. J. McCleese (2009), Mars Climate Sounder limb profile retrieval of atmospheric temperature, pressure, dust, and water ice opacity, *J. Geophys. Res.*, *114*, E10006, doi: 10.1029/2009JE003358.

Kuroda, T., N. Hashimoto, D. Sakai, and M. Takahashi (2005), Simulation of the Martian Atmosphere Using a CCSR/NIES AGCM, *J. Met. Soc. Japan*, *83* (1), 1-19.

Kuroda, T., A.S. Medevedev, P. Hartogh, and M. Takahashi (2009), On Forcing the Winter Polar Warmings in the Martian Middle Atmosphere during Dust Storms, *J. Meteor. Soc. Japan*, *87*(5), 913-921.

Lee, C., W.G. Lawson, M.I. Richardson, N.G. Heavens, A. Kleinböhl, D. Banfield, D.J. McCleese, R. Zurek, D. Kass, J.T. Schofield, C.B. Leovy, F.W. Taylor, A.D. Toigo, (2009), Thermal tides in the Martian middle atmosphere as seen by the Mars Climate Sounder, *J. Geophys. Res.*, *114*, E03005, doi:10.1029/2008JE003285.

Lewis, S.R., P.L. Read, B.J. Conrath, J.C. Pearl, and M.D. Smith (2007), Assimilation of thermal emission spectrometer atmospheric data during the Mars Global Surveyor aerobraking period, *Icarus*, *192*(2), 327-347.

Lindzen, R.S. and A.Y. Hou (1988), Hadley circulations for zonally averaged heating centered off the equator. *J. Atmos. Sci.*, *45*, 2416-2427.

McCleese, D. J., J. T. Schofield, F. W. Taylor, S. B. Calcutt, M. C. Foote, D. M. Kass, C. B. Leovy, D. A. Paige, P. L. Read, and R. W. Zurek (2007), Mars Climate Sounder: An investigation of thermal and water vapor structure, dust and condensate distributions in the atmosphere, and energy balance of the polar regions, *J. Geophys. Res.*, *112*, E05S06, doi:10.1029/2006JE002790.

Moudden, Y., and J. C. McConnell (2005), A new model for multiscale modeling of the Martian atmosphere, GM3, *J. Geophys. Res.*, *110*, E04001, doi:10.1029/2004JE002354.

Murphy, J. R., R. M. Haberle, O. B. Toon, and J. B. Pollack (1993), Martian Global Dust Storms: Zonally Symmetric Numerical Simulations Including Size-Dependent Particle Transport, *J. Geophys. Res.*, *98*(E2), 3197–3220.

Richardson, M.I. and R.J. Wilson (2002), A topographically forced asymmetry in the martian circulation and climate. Nature *416* (6878), 298-301.

Richardson, M. I., R. J. Wilson, and A. V. Rodin (2002), Water ice clouds in the Martian atmosphere: General circulation model experiments with a simple cloud scheme, *J. Geophys. Res.*, *107*(E9), 5064, doi:10.1029/2001JE001804.

Richardson, M. I., A. D. Toigo, and C. E. Newman (2007), PlanetWRF: A general purpose, local to global numerical model for planetary atmospheric and climate dynamics, *J. Geophys. Res.*, *112*, E09001, doi:10.1029/2006JE002825.

Schneider, E.K. (1983), Martian great dust storms: interpretive axially symmetric models, *Icarus*, *55*(2), 302-331.

Smith, M. D., J. C. Pearl, B. J. Conrath, and P. R. Christensen (2001), Thermal Emission Spectrometer results: Mars atmospheric thermal structure and aerosol distribution, *J. Geophys. Res.*, *106*, 23,929–23,945, doi:10.1029/2000JE001321.

Sprague, A. L., W. V. Boynton, K. E. Kerry, D. M. Janes, N. J. Kelly, M. K. Crombie, S. M. Nelli, J. R. Murphy, R. C. Reedy, and A. E. Metzger (2007), Mars' atmospheric argon: Tracer for understanding Martian atmospheric circulation and dynamics, *J. Geophys. Res.*, *112*, E03S02, doi:10.1029/2005JE002597.

Takahashi, Y. O., H. Fujiwara, H. Fukunishi, M. Odaka, Y.-Y. Hayashi, and S. Watanabe (2003), Topographically induced north-south asymmetry of the meridional circulation in the Martian atmosphere, *J. Geophys. Res.*, *108*(E3), 5018, doi:10.1029/2001JE001638.

Wallace, J.M. and P.V. Hobbs (1976), *Atmospheric Science: An Introductory Survey*, 467 pp. Academic Press, New York.

Wilson, R.J. (1997), A general circulation model simulation of the Martian polar warming,. *Geophys. Res. Lett., 24* (2), 123-126.

Wilson, R.J. and K. Hamilton (1996), Comprehensive model simulation of thermal tides in the martian atmosphere, *J. Atmos. Sci.*, *54*, 1290-1326.

Wilson, R. J., D. Banfield, B. J. Conrath, and M. D. Smith (2002), Traveling waves in the Northern Hemisphere of Mars, *Geophys. Res. Lett.*, *29*(14), 1684, doi:10.1029/2002GL014866.

Wilson, R. J., S. R. Lewis, L. Montabone, and M. D. Smith (2008), Influence of water ice clouds on Martian tropical atmospheric temperatures, *Geophys. Res. Lett.*, *35*, L07202, doi:10.1029/2007GL032405.

Zalucha, A. M., R. A. Plumb, and R. J. Wilson (2010), An Analysis of the Effect of Topography on the Martian Hadley Cells, *J. Atmos. Sci.*, in press, doi: 10.1175/2009JAS3130.1.

Zurek, R. W., and S. E. Smrekar (2007), An overview of the Mars Reconnaissance Orbiter (MRO) science mission, *J. Geophys. Res.*, *112*, E05S01, doi:10.1029/2006JE002701.

Zurek, R.W., J.R. Barnes, R.M. Haberle, J.B. Pollack, J.E. Tillman, and C.B. Leovy (1992), Dynamics of the Atmosphere of Mars in H.H. Kieffer, B.M. Jakosky, C.W. Snyder, and M.S. Matthews, *Mars*, 1498 pp., University of Arizona Press, Tucson.

Chapter 3   Convective Instability in the Martian Middle Atmosphere

3.1 Introduction

The Mars Climate Sounder (MCS) on Mars Reconnaissance Orbiter (MRO) [*McCleese et al.*, 2007] has observed Mars's atmosphere and surface for 1.5 martian years. The radiance data collected by MCS can be used to retrieve temperature profiles of moderate resolution (~5 km) from the surface to deep in the middle atmosphere (~85 km). Thus, MCS bridges the gap between temperature sounding nearer the surface provided by past nadir infrared spectroscopy and radio occultation, and measurements in the upper atmosphere from aerobraking experiments, stellar occultation, and other techniques. MCS's ability to map the thermal structure of the middle atmosphere globally also may allow it to detect and map dry convective instabilities within the middle atmosphere: a phenomenon of interest for martian middle atmospheric dynamics and comparative planetology with the Earth.

Since the 1960s [e.g., *Knudsen and Sharp*, 1965; *Hodges*, 1967; *Lindzen*, 1981; *Whiteway and Carswell*, 1994; *Sica and Thorsley*, 1996; *Williams et al.*, 2002], dry convective instabilities have been observed throughout the Earth's stratosphere and mesosphere in association with wave-like perturbations. Recent studies in the terrestrial extratropics have observed convective instabilities in thermal profiles and/or convective roll structures near the mesopause [*Collins and Smith*, 2004; *Liu et al.*, 2004; *Williams et al.*, 2006], which they interpret to result from superposition of internal gravity waves with the thermal tides. The large amplitudes of the thermal tides on Mars [*Zurek*, 1976; *Lee et al.*, 2009] and suspected tidal filtering of gravity waves observed in Mars's upper

atmosphere [*Wang et al.*, 2006] suggest that such tidal-gravity wave interactions may occur on Mars.

The wave dissipation due to such interactions (or the unstable breakdown of tides or gravity waves alone) could be a potent source of turbulent drag and force vigorous meridional circulations within Mars's middle atmosphere, potentially driving the strong temperature inversion observed in the middle atmosphere near the winter pole [e.g., *Deming et al.*, 1986; *McCleese et al.*, 2008]. This idea was first explored in depth by *Jaquin* [1989] and *Barnes* [1990] and expanded upon primarily in modeling work [*Theodoré et al.*, 1993; *Joshi et al.*, 1995; *Collins et al.*, 1997; *Forget et al.*, 1999; *Forbes and Miyahara*, 2006; *Hartogh et al.*, 2007], but observational constraints on tidal and gravity wave drag within Mars's atmosphere remain limited.

Present observational constraints on gravity wave activity come from analyses of Mars Global Surveyor (MGS) Radio Science (RS) lower atmospheric temperature profiles [*Creasey et al.*, 2006], which are restricted to the equator and the summer hemisphere, where weak zonal winds may inhibit the vertical propagation of waves into the middle atmosphere. The accelerometers of aerobraking spacecraft are sensitive to density fluctuations due to both tides and gravity waves in the upper atmosphere. Using data from MGS and Mars Odyssey (ODY) accelerometry, *Fritts et al.* [2006] estimates gravity wave momentum fluxes per unit mass in the upper atmosphere at 95-130 km to be at least an order of magnitude greater than those on the Earth and infer that gravity waves experience dissipation to considerable depth in the atmosphere.

Modeling studies such as *Barnes* [1990] suggest that the wave drag critical for middle atmospheric polar warmings is below the level observed by *Fritts et al.* [2006],

above the level observed by *Creasey et al.* [2006], and within the winter extratropics, where the strong westerly zonal jets should enhance the transmission of gravity waves vertically. Thus, the broad vertical range of MCS retrievals is well situated to look for dry convective instabilities that could result from tidal or gravity wave dissipation in the martian middle atmosphere and provide potentially more dynamically relevant constraints on the forcing of the circulation due to these phenomena.

In this study, we will use MCS temperature retrievals to detect and map regions of convective instability. In Chapter 3.2, we describe the retrieval dataset and its analysis. In Chapter 3.3, we investigate spatiotemporal variability in convective instability in the middle atmosphere. In Chapter 3.4, we consider the driving mechanisms for the observed instabilities and implications of the observed instabilities for atmospheric dynamics. In Chapter 3.5, we summarize our results.

3.2 Data and Analysis

3.2.1. Dataset

MCS is a limb and on-planet scanning filter radiometer [*McCleese et al.*, 2007]. It measures thermal emission in the mid- and far infrared wavelength range. Using the measured radiances, vertical profiles of temperature, pressure, dust and water ice currently are retrieved over an altitude range from ~10 to 85 km at a vertical resolution of ~5 km as described in detail by *Kleinböhl et al.* [2009]. The retrieval product contains an error estimate for each retrieved profile. The temperature error estimate is calculated by finding the radiance difference due to a small temperature perturbation at each altitude

level and scaling it by the root sum of the squares (RSS) of the instrument noise and the residual radiance that cannot be fit by the retrieval algorithm [*Kleinböhl et al.*, 2009].

Due to instrument issues [*Kleinböhl et al*., 2009], the MCS observations during L_s=180°—255° of Mars Year 28 (MY 28, as defined by *Clancy et al.* [2000]) are of lower quality (limb staring). The altitude coverage is limited to below ~50 km in the southern hemisphere and above ~15 km over the north pole. In addition, the calibration is not as good during this time and the uncertainties are larger in regions with low radiances, especially near the top of the MCS coverage. The retrieved temperature profiles during this period do agree well with profiles immediately afterwards [*Kleinböhl et al.,* 2009]. Due to MRO issues, MCS observations are not available after L_s=328° in MY 29.

To assemble a full martian year for study, we primarily use L_s=0° to 328° of MY 29 and L_s=328° to 360° of MY 28. The observations during L_s=110°—168° of MY 28 are used to supplement the observations of MY 29 for northern spring and summer. These seasons are thought to have limited interannual variability [*Richardson*, 1998; *Wilson and Richardson*, 2000; *Cantor et al.*, 2002; *Liu et al.*, 2003]. After accounting for the bias in the altitude coverage, we use the retrieved profiles from limb staring observations and observations during the remainder of MY 28 (through L_s=328°) for interannual comparisons in the southern spring and summer seasons.

The current retrieval algorithm [*Kleinböhl et al.*, 2009] does not attempt to retrieve high haze layers. If given a radiance profile from an atmosphere with a haze layer, it will introduce an artificial temperature minimum and/or maximum. This usually produces a very sharp inversion in the temperature profile resulting in an artificially

unstable lapse rate. The temperature of this inversion is significantly warmer than nearby profiles. While the retrieval processing is designed to avoid retrieval near high hazes, some still may cause problems.

Inspection of radiance profiles suggests that high hazes are very rare in the extratropics during the winter. The tropics are far more affected (see Chapter 3.3.1). The high hazes in this region may be equatorial mesospheric clouds such as those recently described by *Clancy et al.* [2007], *Montmessin et al.* [2007], and *Inada et al.* [2007]. Note that condensation in the cold phase of vertically propagating gravity waves is one possible origin of high hazes, so there may be preferential exclusion of retrievals in regions of intense gravity wave activity.

MCS's vertical resolution of ~5 km should be sufficient to resolve zones of convective instability in the middle atmosphere due to thermal tides and gravity waves. High resolution observations of gravity wave driven instabilities in the Earth's atmosphere suggest the instabilities have a fractal character: longer gravity waves/tides saturate to produce 5—15 km zones of neutral or near-neutral stability that are genuinely unstable at higher resolution due to perturbations by smaller-scale waves [*Williams et al.*, 2006]. On Mars, a hypothetical longer wave could be one phase of the diurnal thermal tide with a vertical wavelength of ~30 km, such that a gravity wave with a wavelength as short as 10 km might produce a resolved instability. We assess horizontal sensitivity by considering an instability arising from superposition of a tide with a gravity wave propagating within a two-dimensional plane.

For medium frequency waves, the vertical wavelength of a gravity wave is ~$2\pi[|(u-c)|/N]$, where u is the mean wind, c is the phase speed, and N is the Brunt-Väisälä

frequency [*Fritts and Alexander*, 2003]. In Mars's middle atmosphere, N is $\sim 10^{-2}$ s, so vertical wavelengths of 10-30 km will correspond to stationary waves ($c=0$) in a mean wind of 15—45 ms^{-1}. So this investigation should be especially sensitive to convective instabilities due to waves under these mean wind conditions, depending on phase speed.

Each MCS retrieval is averaging over an atmospheric slice $\sim$10 km wide by $\sim$300 km long (narrowing to $\sim$100 km near the surface). It can be considered a locally vertical profile when analyzing regions of convective instability in the middle atmosphere, despite the overall lengthwise variability in weighting function peaks between the surface and 80 km [cf. *Kleinböhl et al.*, 2009, Figure 12]. The orientation of the slice depends on the time of day (or latitude) of the observation. Over most of the planet, the long direction is primarily north-south (slightly west of north on the dayside and slightly west of south on the night side). Over the poles, the long direction is oriented westward. MRO's orbital velocity of 3 km/s is sufficiently fast that the MCS observations capture the instantaneous appearance of the atmosphere, especially gravity waves. In the current observation mode, with $\sim$30 s between retrieved profiles, individual profiles overlap by 50% with their nearest neighbors.

For gravity waves with relevant vertical wavelengths, the horizontal wavelength in the direction of propagation will be a significant fraction of the long dimension of the slice observed by MCS. Thus, the convective instability due to the breaking of a gravity wave traveling parallel to the MCS view direction (usually meridional) should be easily detected. Those traveling perpendicular to the MCS viewing direction (usually zonal) will be more difficult to see since the instability will be averaged with the adjacent stable atmosphere. Large groups of parallel zonal gravity waves breaking at the same altitudes

would be readily discernable. Thus, except for very high latitudes, MCS observations and retrievals are expected to be more sensitive to the convective instability due to the breaking of meridionally propagating waves than that due to zonally propagating waves. See *Wu and Waters* [1996] for an analogous analysis of sensitivity.

To avoid biasing of zonal averages by heavier sampling at particular longitudes, the retrievals and quantities derived from them (as described in Chapter 3.2.2) are binned in 36 (5° resolution) latitudinal bins, 64 (5.625° resolution) longitudinal bins, and L_s bins at 5° resolution. This spatial resolution is comparable to Mars general circulation model grids in space and about as fine in time as possible to permit the bins to be filled, given the MCS observation pattern and a completely successful retrieval algorithm. Due to the limited local time sampling, the observations are further separated into dayside (9:00—21:00 LST) and nightside (21:00—9:00 LST) bins, centered at MRO's nominal 3:00/15:00 LST orbit [*Zurek and Smrekar*, 2007].

The variability in the longitudinal sampling of the retrieval dataset is depicted in Figure 3.1. Sampling is controlled by a variety of factors, some of which are intrinsic to the data as collected by the instrument, e.g., periods in which data was not collected because the instrument was stowed (no or little longitudinal sampling at all latitudes) and some of which are related to the present limitations in the retrieval algorithm, e.g., the exclusion of retrievals with large residual errors due to the neglect of scattering in the current retrieval procedure (no or limited longitudinal sampling at particular latitudes).
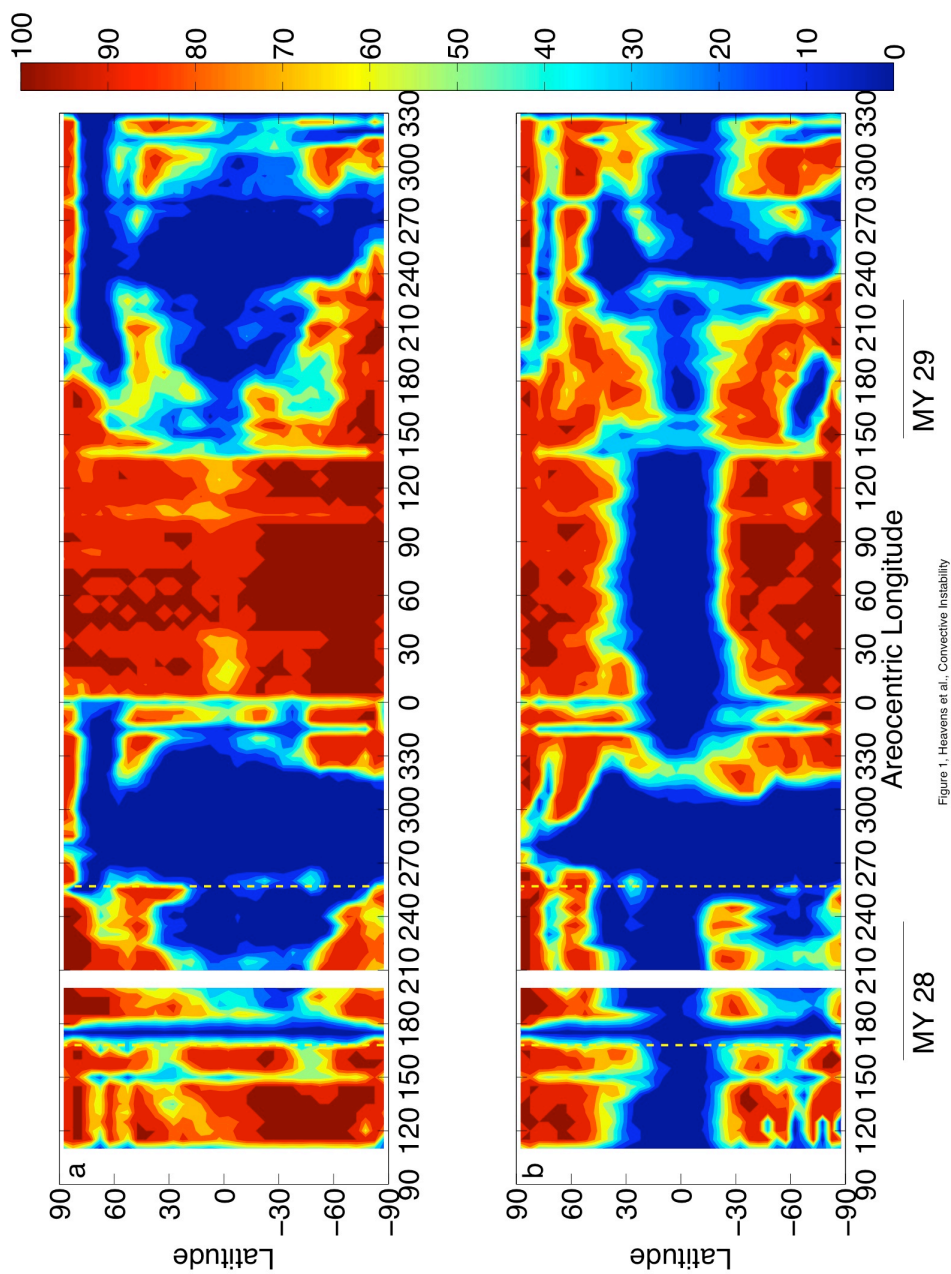
Figure 3.1. Percentage of longitudinal bins with successful MCS retrievals for each L_s/latitudinal bin as described in the text. The dashed yellow lines denote the period of limb staring: (a) nightside; (b) dayside. Contours are every 10%.

3.2.2 Analysis

Convective instability is quantified in two ways: (1) by calculating the difference, $\Gamma(p)$,

between the dry adiabatic lapse rate and the lapse rate at each pressure level in a retrieved

temperature profile using a hydrostatic height coordinate; and (2) by calculating the

maximum Convective Available Potential Energy (CAPE) [*Holton*, 2004] in the middle

atmosphere, $CAPE_{MA}$, at pressures less than 50 Pa in the retrieved temperature profile.

The 50 Pa criterion ensures that convective instabilities in the middle atmosphere are

easily distinguished from the convective boundary layer in the lower atmosphere. *Hinson*

et al. [2008] has shown that the depth of the convective boundary layer is up to 10 km

above high altitude regions such as Tharsis, so a pressure cutoff corresponding to ~25 km

above the datum is reasonable.

In calculating $CAPE_{MA}$, it is assumed that the buoyancy in the temperature profile

arises from the adiabatic cooling of a hypothetical parcel of air at a temperature, T_p,

within the observed superadiabatic environment. Let the base of the superadiabatic region

be at a height, z_b. The parcel cools adiabatically at z_b and begins to rise, since it is more

buoyant than the environment. The parcel continues to rise until some height, z_t, above

the top of the superadiabatic region where the parcel is neutrally buoyant. Thus, in height

coordinates:

$$CAPE_{MA} = \int_{z_b}^{z_t} -g(z) \frac{T_p(z) - T(z)}{T(z)} dz \qquad (3.1)$$

The dry adiabatic lapse rate is $-g/c_p$, where g is the acceleration due to gravity

and c_p is the isobaric heat capacity, but g may vary ~5% within the vertical range of the

profile and c_p may vary by around a factor of 2 over a temperature range of 100—250 K

[*Bücker et al.*, 2003]. We make a first order correction to *g* using altitude information derived from the geometric pointing of the instrument. The isobaric heat capacity is approximated by the zero pressure isobaric heat capacity of CO_2 as modeled by *Bücker et al.* [2003] but with simplified piecewise equations that fit at least 99% of the variance in c_p at temperatures between 100 and 250 K:

$$c_p = 510.5 + 1.122T,$$
$$T > 150,$$
$$c_p = -0.14659T^2 + 42.104T - 2356.2,$$
$$T \leq 150$$

(3.2)

where *T* is in degrees Kelvin and c_p is in J K^{-1} kg^{-1}.

An example of a temperature profile with a convective instability and the lapse rates derived from it are shown in Figures 3.2a-b. The profile has a temperature maximum of 180 K at 30 Pa and may be unstable with respect to moist CO_2 convection near the surface. The large temperature error estimates above ~0.5 Pa are primarily due to the detector signal and noise being of comparable magnitudes when observing an atmosphere at exceptionally low temperature and pressure. Figure 3.2b shows that the lapse rate at ~0.4 Pa is clearly higher than the -4.5 K km^{-1} commonly quoted as the dry adiabatic lapse rate for the lower atmosphere, and it is also higher than the estimated dry adiabatic lapse rate. The difference between this lapse rate and the derived lapse rate is $\Gamma(p)$ and the $CAPE_{MA}$ due to this instability is ~232 J/kg. However, the instability is on the edge of the region where estimated temperature errors are becoming large, so the error in the estimate of $\Gamma(p)$ may be large as well. To estimate the error in $\Gamma(p)$ I generate 1000 random simulated realizations of the temperature profile based on the retrieval uncertainty using a Monte Carlo (MC) method driven by covariance data generated from
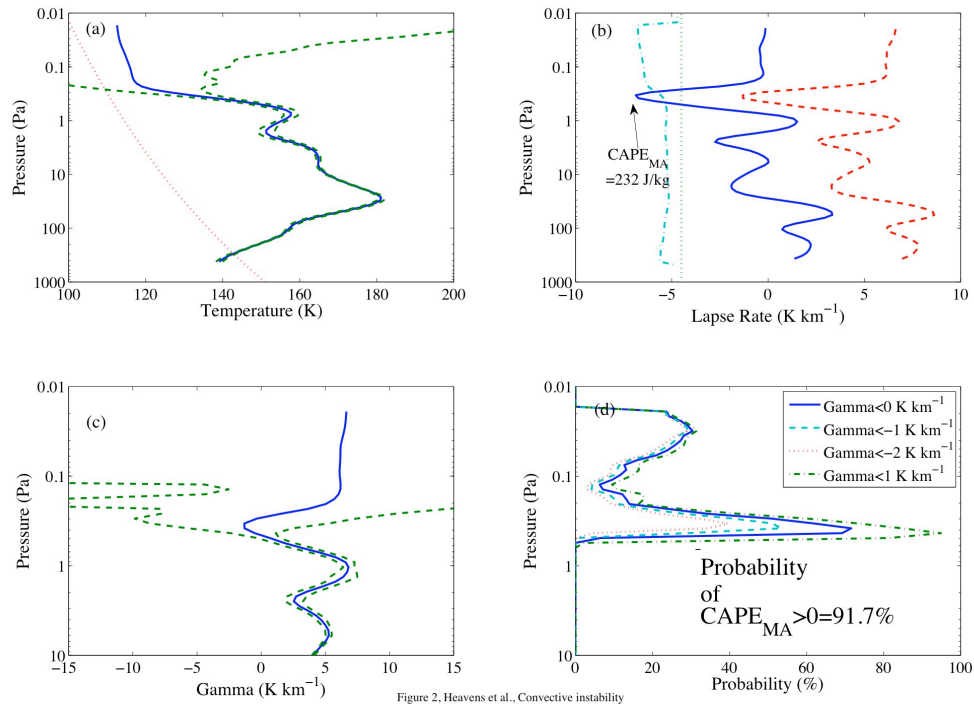
Figure 2, Heavens et al., Convective instability

Figure 3.2. (a) Example retrieved temperature profile with a dry instability (57° S, 89° E, L_s=125.3267, MY 28, 15:45 LST). Solid blue line shows temperature, $T(p)$, in K. Dashed green lines show 1-sigma error estimates for temperature. Dotted red line shows frost point of CO_2 based on algorithm of *Span and Wagner* [1996]; (b) solid blue line shows lapse rate for the retrieval in (a), dotted green line indicates constant lapse rate of -4.5 K km^{-1}, dot-dashed turquoise line shows variability in estimated dry adiabatic lapse rate with pressure, and dashed red line shows the estimated $\Gamma(p)$; (c) solid blue line shows estimated $\Gamma(p)$ from retrieval in (a) compared with 95% confidence intervals from the MC simulations; (d) Probability based on MC simulation of this profile that $\Gamma(p)$ is less than some particular threshold.

a representative sample of 1043 profiles: all of the dayside retrieved temperature profiles from 60° to 70° S, L_s=120°—130° of MY 29. $\Gamma(p)$ was calculated for each of the 1,000 MC realizations. In Figure 3.2c, $\Gamma(p)$ derived from the temperature profile is compared with the 95% confidence interval derived from the MC realizations (using the 26th and 975th lowest MC estimate of $\Gamma(p)$ at each pressure level). Like the temperature error, the divergence in the MC simulated $\Gamma(p)$ begins to grow at ~0.5 Pa. The probability of instability ($\Gamma(p) < 0$ K km^{-1}) exceeds 70% at ~0.5 Pa (Figure 3.2d), where the original profile was unstable. The extreme temperature uncertainties above 0.1 Pa (exceeding 80 K) create a secondary peak with a ~30% probability of instability. In this case, 91.7% of the realizations had a positive CAPE$_{MA}$. Statistically, this profile is only marginally unstable due to the retrieval uncertainties, although the region with the highest probability of instability does not correspond to the region of largest uncertainties.

Figure 3.3 shows the results of performing the Monte Carlo simulations on 2949 retrieved profiles. Instability thresholds of CAPE$_{MA} > 0$ J kg^{-1} and 50 J kg^{-1} were used to analyze both the retrieved and simulated profiles. For both thresholds, the cases where many of the simulated profiles exceed the threshold mostly correspond to retrieved profiles that are also unstable (Figures 3.3a and 3.3b). Fortunately, CAPE$_{MA}$ and the simulated probability of exceeding a particular CAPE$_{MA}$ threshold are linearly related (Figures 3.3c-d) when CAPE$_{MA} > $ ~50 J kg^{-1}. A small number of temperature profiles with derived CAPE$_{MA} > $~300 J kg^{-1} are unstable to 95% confidence (Figure 3.3c). Thus, we will call profiles with CAPE$_{MA} > 300$ J kg^{-1}, "significant instabilities." This linear relationship should hold for MCS temperature profiles in general. Figure 3.4 shows a
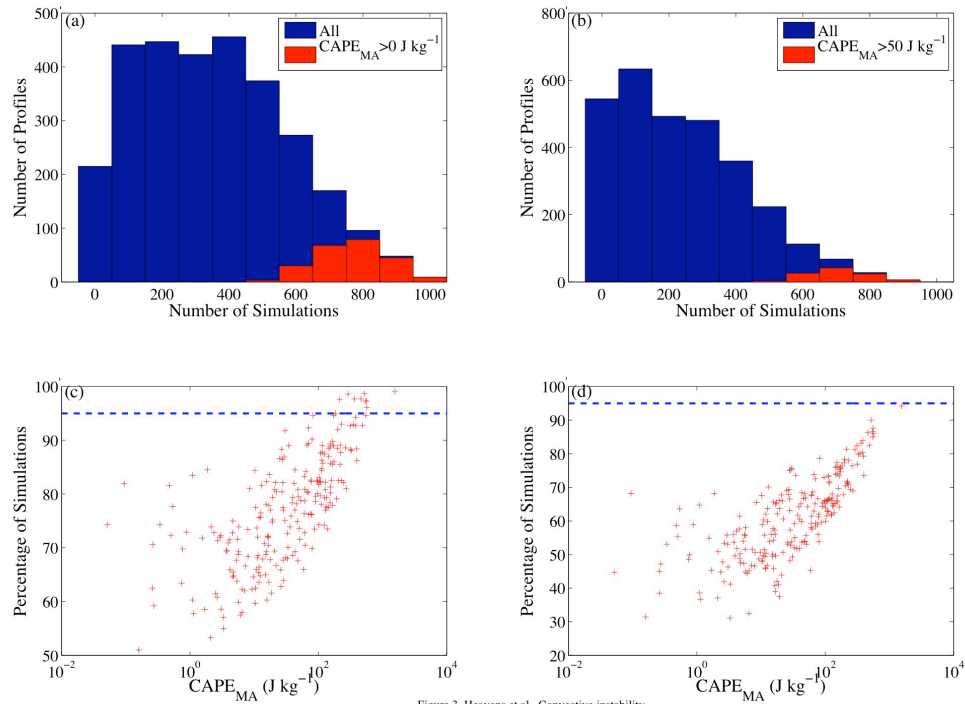
Figure 3, Heavens et al., Convective instability

Figure 3.3. Results of MC simulations of dayside retrievals from 60°-70° S, L_s=90°-120° of MY 29: (a) histogram of MC simulations with $CAPE_{MA}$>0 J kg^{-1} for all retrieved profiles and for all retrieved profiles with $CAPE_{MA} > 0$ J kg^{-1}; (b) histogram of MC simulations with $CAPE_{MA} > 0$ J kg^{-1} for all retrieved profiles and for retrievals with $CAPE_{MA} > 50$ J kg^{-1}; (c) percentage of simulations with $CAPE_{MA} > 0$ J kg^{-1} vs. derived $CAPE_{MA}$. The 95% confidence level is indicated with a blue dashed line; (d) percentage of simulations with $CAPE_{MA}$>50 J kg^{-1} vs. derived $CAPE_{MA}$. The 95% confidence level is indicated with a blue dashed line.

simple test of this idea, in which a temperature profile from near the north pole during

northern winter of MY 28 with CAPE$_{MA}$ of ~1000 J kg^{-1} is perturbed by +/- 2 times the

error estimate. A convective instability is present in both perturbed profiles, so the

instability is significant to at least 95% confidence as expected.

Inspection of this sample also shows that the isothermal condition imposed at the

top of the profile above the top detector weighting function [*Kleinböhl et al.*, 2009]

prevents unstable lapse rates from being derived where the temperature uncertainty

estimate is larger than ~8 K, so there is little justification to set an upper bound for

CAPE$_{MA}$ analysis.

The temperature profile in Figure 3.4 exemplifies the best-resolved convective

instabilities in MCS retrieved profiles. The unstable layer is ~5 km deep, the approximate

resolution of the retrieved profile, although it is embedded in a ~15 km deep region with

an enhanced lapse rate relative to most profiles below 10^{-1} Pa. The broad vertical retrieval

weighting functions smooth the retrieved temperature profile so that it poorly represents

the sharp temperature gradients of the instabilities. Convective instabilities must be

vertically extended and/or very strong to be detected in MCS profiles. Thus, this study

only provides a lower bound on the magnitude and distribution of convective instability

in the middle atmosphere.

3.2.3 Zonal Wind Estimates

For a necessary calculation in Chapter 3.4.2, we estimate the zonal gradient wind, $\tilde{U}(p)$.

This estimate is derived from the zonal average temperature by taking the lowest pressure
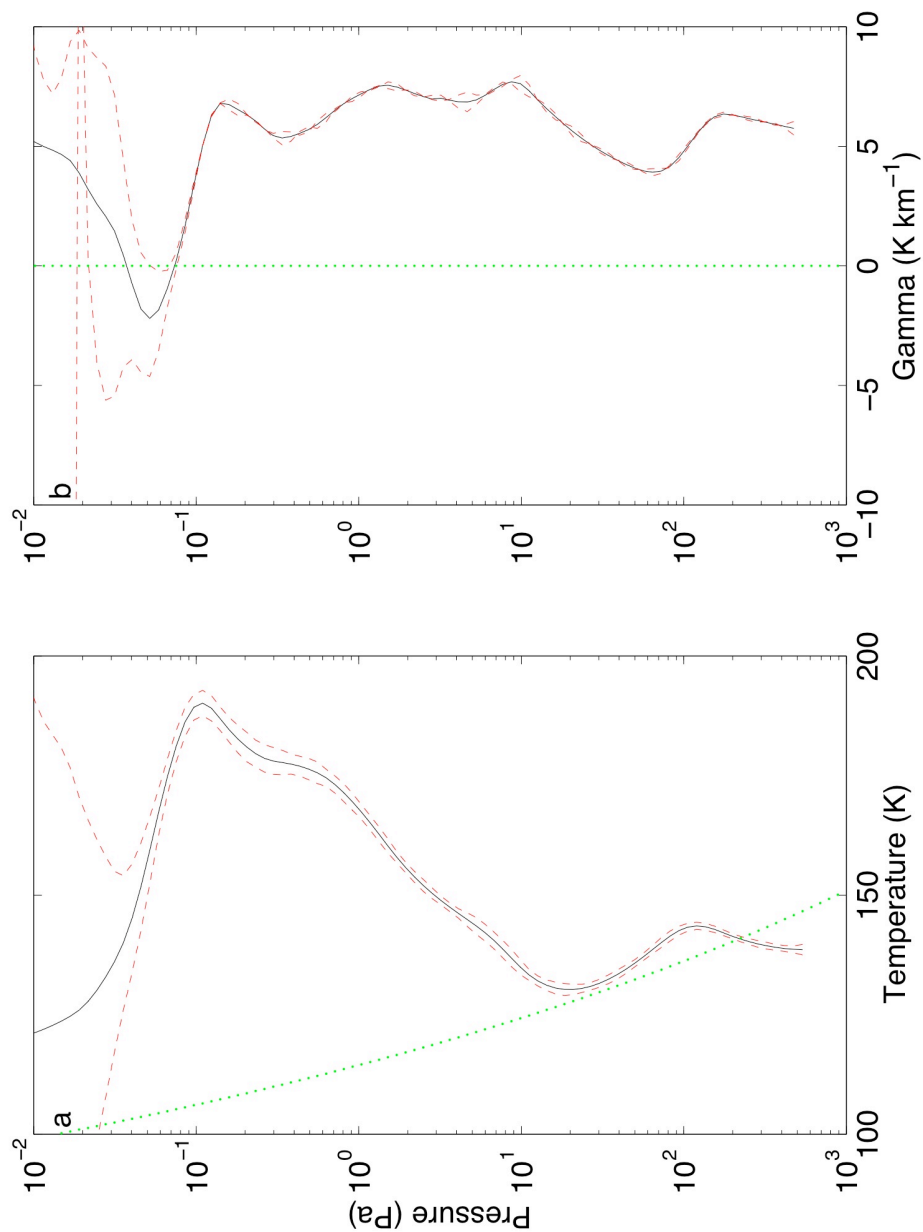
Figure 3.4. (a) Example retrieved temperature (K) profile with a dry instability (86° N, 160° W, L_s=265.1393, MY 28, 6:53 LST) with +/-2σ temperature error estimates (solid and dashed lines respectively). The dotted line indicates the CO_2 frost point; (b) $\Gamma(p)$ for the temperature profiles in (a). The dotted line indicates $\Gamma(p)$=0 K km^{-1}.

level with retrieved temperature data in each latitudinal bin as a level of no motion,

p_{LNM}, and estimating the thermal wind, $\hat{U}(p)$:

$$\hat{U}(p) = \int\limits_{p_{LNM}}^{p} \frac{R_d}{f} \left(\frac{dT}{dy}\right)_p d\ln p' \tag{3.3}$$

where R_d is the specific gas constant, f is the Coriolis parameter for the latitudinal bin,

and $\left(\dfrac{dT}{dy}\right)_p$ is the temperature gradient at constant pressure. To compute the gradient wind

$\tilde{U}(p)$, we iteratively apply Eq. 3.4 to convergence [*Holton*, 2004].

$$\tilde{U}_{n+1}(p) = \frac{\tilde{U}_n}{1 + \dfrac{\sqrt{\tilde{U}_n^2}}{|fR_M|}} \tag{3.4}$$

where R_M is the radius of Mars. Eqs. 3.3 and 3.4 are only appropriate for winds in

approximate geostrophic balance and so cannot be used for diagnosis of zonal winds in

the tropics due to the low magnitude of the Coriolis parameter. Therefore, $\tilde{U}(p)$

calculated in the tropics is not plotted.

3.3 Results

3.3.1 Global Results

Figures 3.5a-b show example nightside and dayside zonal averages of $T(p)$ at northern

summer solstice in which polar middle atmospheric temperature maxima of ~180 K are

observed at a pressure level of ~1-2 Pa (~40-50 km above the local surface) in the high

southern latitudes.
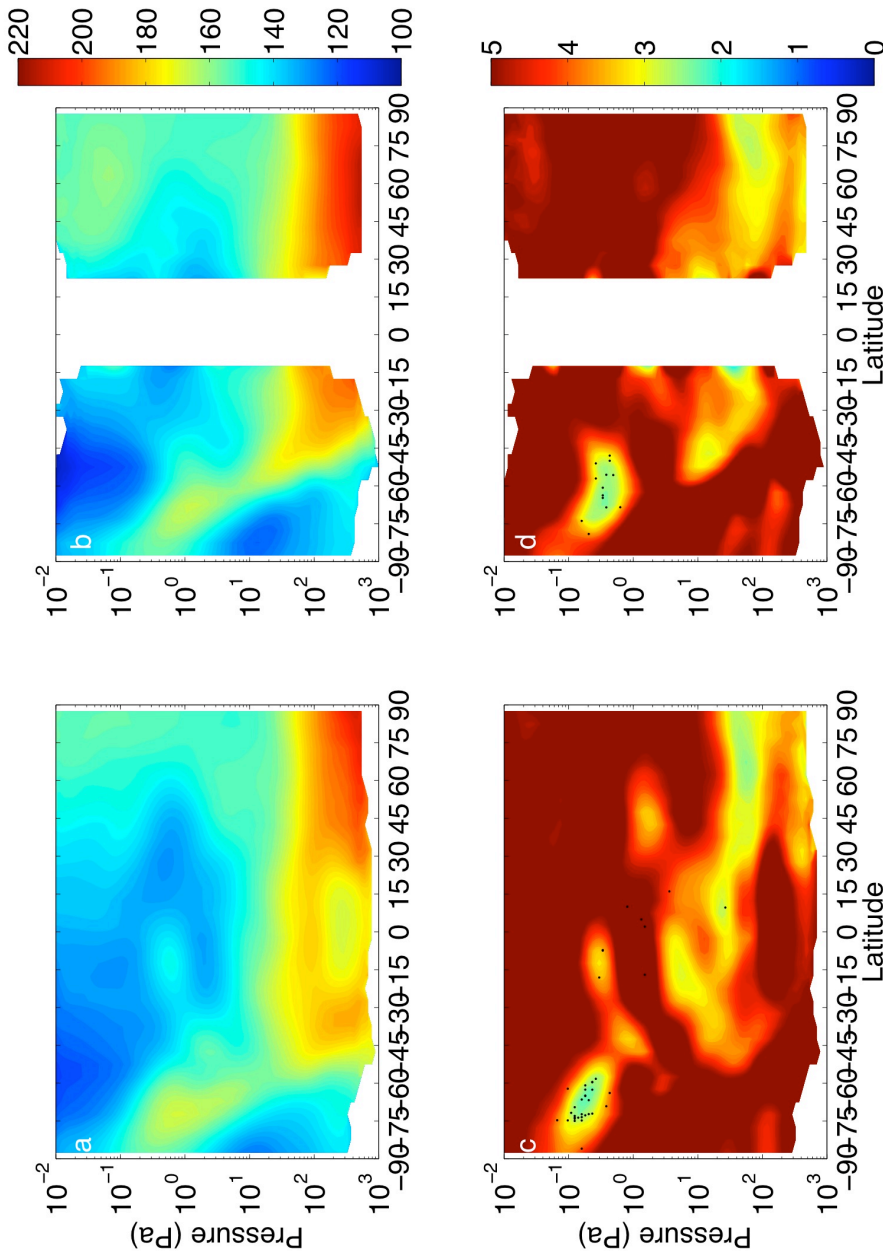
Figure 5, Heavens et al., Convective Instability

Figure 3.5. (a) zonal average of $T(p)$ (K), MY 29, L_s=87.5°-92.5°, nightside; (b) zonal average of $T(p)$ (K), MY 29, L_s=87.5°-92.5°, dayside; (c) zonal average of $\Gamma(p)$ (K km^{-1}), MY 29, L_s=87.5°-92.5°, nightside. (d) Zonal average of $\Gamma(p)$, MY 29, L_s=87.5°-92.5°, dayside. The color scale for $\Gamma(p)$ is saturated at 5 K km^{-1} to de-emphasize positive lapse rates. Missing data is indicated in white. Black dots in (c) and (d) mark the locations of the minimum $\Gamma(p)$ of significant instabilities.

Figures 3.5c-d show zonal average $\Gamma(p)$ during the same L_s range and the pressures at which individual profiles with $CAPE_{MA} > 300$ J kg^{-1} are most unstable (the locations of significant instabilities). The zonal average structure is not unstable anywhere, but very low values of $\Gamma(p)$ and the densest concentration of significant instabilities are at ~0.3 Pa (~60 km above the local surface) from 50° S nearly to the pole. Only lapse rates in the lower atmosphere near the north pole are comparably close to the dry adiabatic lapse rate. The southern zone of low stability lies ~2 scale heights directly above the polar warming described by *McCleese et al.* [2008] (and seen in Figures 3.5a-b). There is a middle atmospheric temperature maximum of ~160 K at very low pressures over the north pole, but lapse rates over this region appear more stable.

In a few cases on the nightside, significant instabilities occur at ~3 Pa over the tropics in a region of the atmosphere that is on the average very stable (Figure 3.5c). Inspection suggests these instabilities are artifacts of retrieval through high hazes. In this particular case, there are sufficient profiles in the same longitudinal bin such that the zonal average lapse rate is far from adiabatic and zonal average $CAPE_{MA}$ is low, but care must be taken at other seasons.

Figures 3.6a-f show how $CAPE_{MA}$ is distributed among individual profiles in single latitudinal bins. In the latitude/L_s bins whose distributions are depicted in Figures 3.6a-d and 3.6f, the fraction of profiles with $CAPE_{MA}$ in a given $CAPE_{MA}$ interval decreases with increasing $CAPE_{MA}$. The distribution and zonal average $CAPE_{MA}$ for each of these bins is consistent and physically plausible. The distribution in Figure 3.6e is different. It is flat, and the average is much higher than expected. One of the high

Figure 3.6. (a) Histogram of CAPE$_{MA}$ (50 J kg^{-1} binning resolution) in individual profiles from six different L$_s$/latitudinal bins. See captions within figure for details.
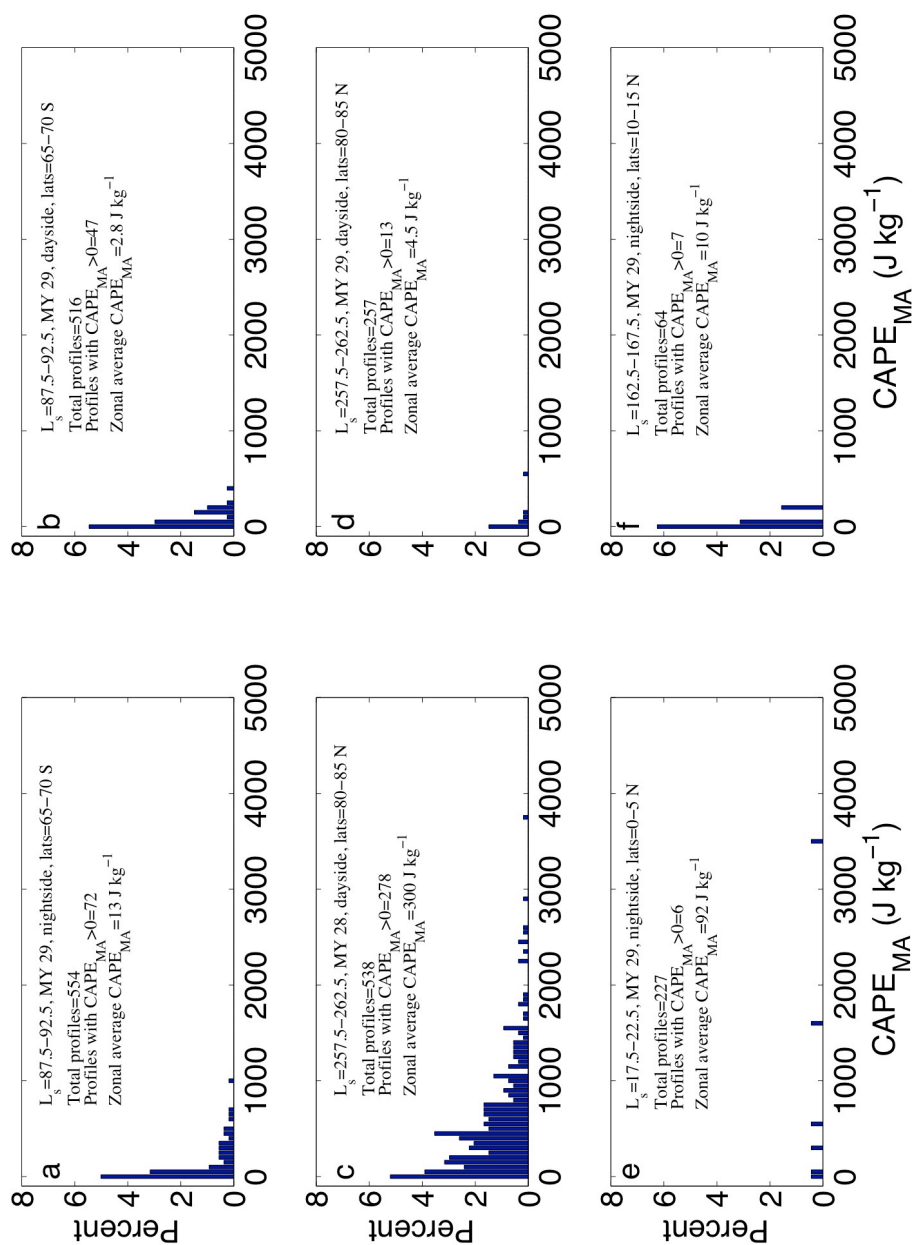
Figure 6, Heavens et al., Convective Instability

CAPE$_{MA}$ profiles is the only one in its longitude bin, heavily weighting the mean. An inspection indicates the presence of a high haze.

In order to eliminate such artifacts, the zonal average CAPE$_{MA}$ is filtered with two binomial one-tailed tests at 95% confidence with the null hypotheses: (1) the fraction of profiles CAPE$_{MA}$ > 0 J kg^{-1} is random, assuming the ordinary probability is the fraction of profiles meeting this criterion in the dataset (2.92%); (2) the fraction of profiles 0 J kg^{-1} < CAPE$_{MA}$ < 50 J kg^{-1} is random, assuming the ordinary probability is the fraction of profiles meeting this criterion in the dataset (1.44%). Latitude/L$_s$ bins with high CAPE$_{MA}$ typically pass (1), but if the distribution is similar to Figure 3.6e, it will not pass (2). These tests should not be considered statistically rigorous but only as an empirical filter to direct attention from occurrences of instability attributable to high hazes.

Figures 3.7, 3.8 and 3.9 show the minimum zonal mean $\Gamma(p < 50$ Pa$)$, the pressure at which it occurs, and the filtered zonal average CAPE$_{MA}$ over the seasons. They provide an overview of middle atmospheric convective instabilities in the MCS retrieved profiles and the zonal average stability structure. During most of the spring and summer, the lowest values of $\Gamma(p)$ in the extratropics are at pressures greater than 50 Pa (Figure 3.7). While nightside average lapse rates in the northern extratropics can be relatively high during northern spring and summer, lapse rates in individual profiles remain sub-adiabatic, and zonal average CAPE$_{MA}$ is below 1 J kg^{-1}.

In the southern extratropics during the same season (its fall and winter), the situation is very different. Zonal average CAPE$_{MA}$ can be up to 100 J kg^{-1} on both the dayside and nightside. The minimum $\Gamma(p < 50$ Pa$)$ is at $p < 1$ Pa and is ~10 km higher on

Figure 3.7. Latitudinal and seasonal variability during MY 28 and 29 in the minimum zonal average $\Gamma(p <$ 50 Pa) (K km^{-1}) using retrieved profiles from limb scanning data only: (a) nightside; (b) dayside; The color scale for those plots is saturated at 0 and 5 K to emphasize marginally unstable lapse rates. White space represents L_s/latitudinal bins without retrieved profiles from limb scanning data.

Figure 3.8. Latitudinal and seasonal variability during MY 28 and 29 in the pressure (Pa) at which the minimum zonal average $\Gamma(p < 50$ Pa) is observed using retrieved profiles from limb scanning data only: (a) nightside; (b) dayside. The dashed black line is the 1 Pa contour. White space represents L_s/latitudinal bins without retrieved profiles from limb scanning data.

Figure 9, Heavens et al., Convective Instability

Figure 3.9. Latitudinal and seasonal variability during MY 28 and 29 in $CAPE_{MA}$ (J kg^{-1}) using retrieved profiles from limb scanning data only and filtered as described in the text: (a) nightside; (b) dayside. The color scale is $\log_{10}$ and saturates below 1 J kg^{-1}. White space represents L_s/latitudinal bins without retrieved profiles from limb scanning data.

the nightside than the dayside (also see Figures 3.5c and 3.5d). The lowest values of Γ

(p) are generally between 1.5 and 2.5 K km^{-1} but are as low as 0.2 K km^{-1} on the dayside

between 60° and 65° S at L$_s$=125° of MY 28 (Figure 3.7). The extremely low zonal

average $\Gamma(p)$ at this latitude and season is most likely an underestimate due to poor

sampling, in which only unstable perturbations of the mean stability structure are

sampled. Only four longitudinal bins include retrievals (one in each bin). After

accounting for the limitation in available data, interannual variability between MY 28 and

MY 29 appears weak during this season.

In the northern extratropics during its fall and winter, zonal average $\Gamma(p)$ has a

minimum at ~0.1 Pa and is in fact unstable at poorly sampled latitudes (12 longitudinal

bins) at L$_s$=260° of MY 28. At better-sampled latitudes (58 longitudinal bins), the lowest

zonal average $\Gamma(p)$ at this time is ~ 1 K km^{-1}, a large number of unstable layers in

individual profiles are within this zone of low mean stability (Figure 3.10a), and zonal

average CAPE$_{MA}$ is up to 500 J kg^{-1}. (Figures 3.10a-f have a similar format to Figures

3.5c-d to illustrate the full mean stability structure of the atmosphere and the location of

the most unstable layers in individual profiles.) Note that both $\Gamma(p)$ and zonal average

CAPE$_{MA}$ in the northern extratropics differ significantly between MY 28 and MY 29. We

will investigate this interannual variability in greater detail in Chapter 3.3.2.

In the tropics, $\Gamma(p)$ usually has a weak minimum (greater than ~3 K km^{-1})

between 1 and 30 Pa. During late northern summer and early northern fall, $\Gamma(p)$ is as low

as ~1 K km^{-1}. Zonal average CAPE$_{MA}$ in the tropics is less than 1 J kg^{-1}, except for one

small nightside region at L$_s$ ~180°. This CAPE$_{MA}$ is mostly contributed by marginally

unstable layers in individual profiles within a zone of low mean stability at ~5 Pa (Figure
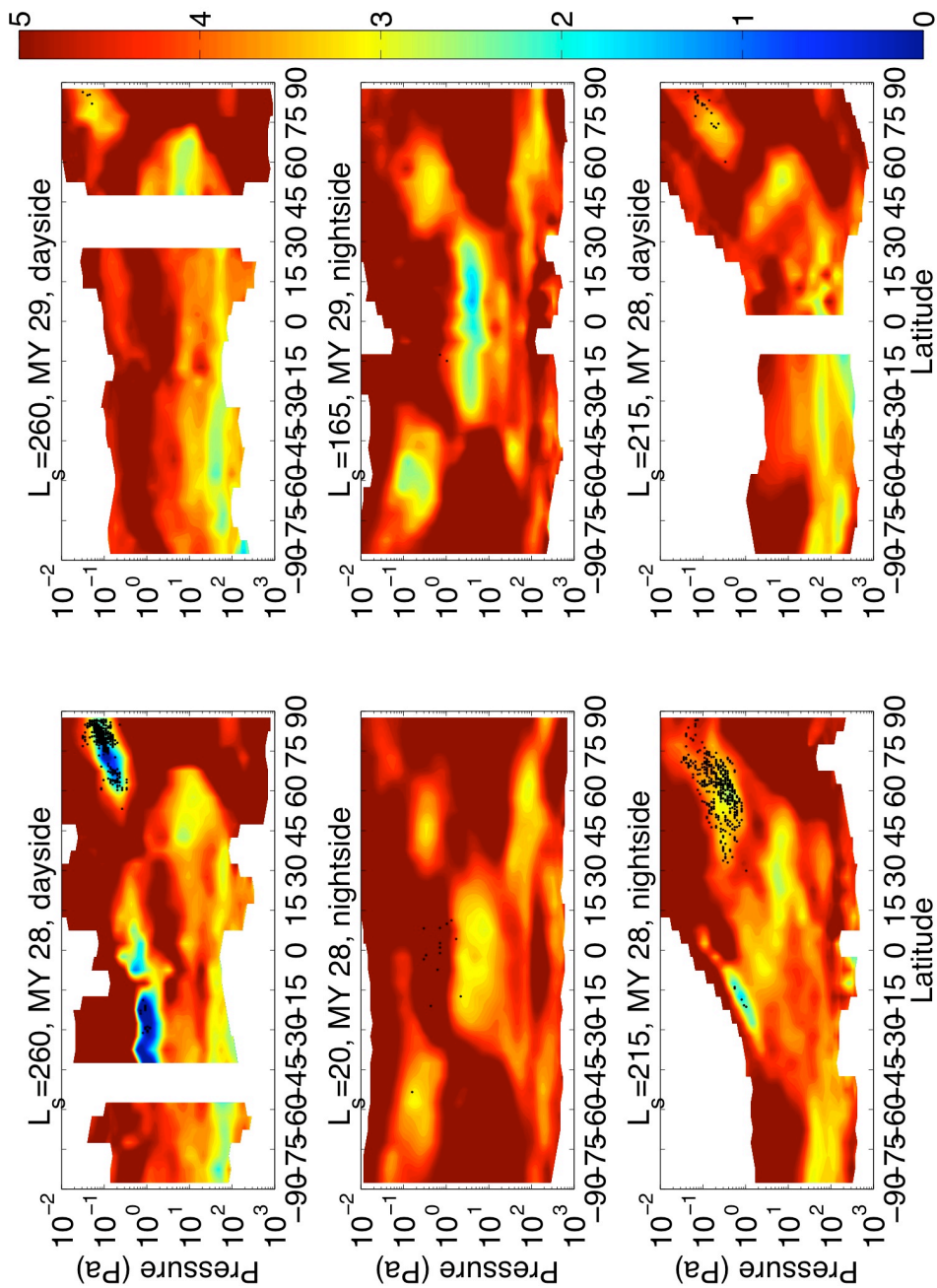
Figure 3.10. Zonal average of $\Gamma(p)$ (K km^{-1}). Black dots mark the locations of the minimum $\Gamma(p)$ of significant instabilities. The color scale for $\Gamma(p)$ is saturated at 5 K km^{-1} to de-emphasize positive lapse rates. Missing data is indicated in white.

3.10d). The biggest impact of our empirical filter is during L_s=0°-30° of MY 29; without it, zonal average $CAPE_{MA}$ is as high as 100 J kg^{-1} on the nightside because of retrievals through high hazes. These appear as significant instabilities in otherwise stable regions in the zonal average (Figure 3.10c).

3.3.2 Convective Instability in the Northern Extratropics

Zonal average $CAPE_{MA}$ was much higher during MY 28 than in MY 29 from L_s=180° to 280°: ~100—500 J kg^{-1} in MY 28 but only 1-10 J kg^{-1} during MY 29 (Figures 3.13a-b). $CAPE_{MA}$ also was higher during this year, season, and latitudinal band than it was in the southern extratropics during southern fall and winter. (Note the inclusion of retrieved temperature profiles from limb staring data.) The distribution of $CAPE_{MA}$ in individual profiles (Figures 3.6c-d) and the mean stability structure between the two years clearly differ as well (Figures 3.10a-b) at L_s=260º, the peak of instability during MY 28.

During MY 28, significant convective instabilities were widespread in the northern extratropics from northern fall equinox but were reduced to levels lower than those in southern hemisphere winter after L_s=266° (Figures 3.11a-b). A global dust storm began around L_s=261.5° of MY 28 (results presented by B.A. Cantor et al., Observations of the Martian Atmosphere by MRO-MARCI: An Overview of 1 Mars Year, Third International Workshop on Mars Modeling and Observations, Lunar and Planetary Institute, Williamsburg, VA, 10-13 November 2008), so the convective instability was suppressed ~7 sols after the beginning of the dust storm. The suppression is roughly synchronous with the initial polar vortex displacement and breakdown due to this storm described by D.M. Kass et al. (MCS Views of the 2007 Global Dust Storm, paper
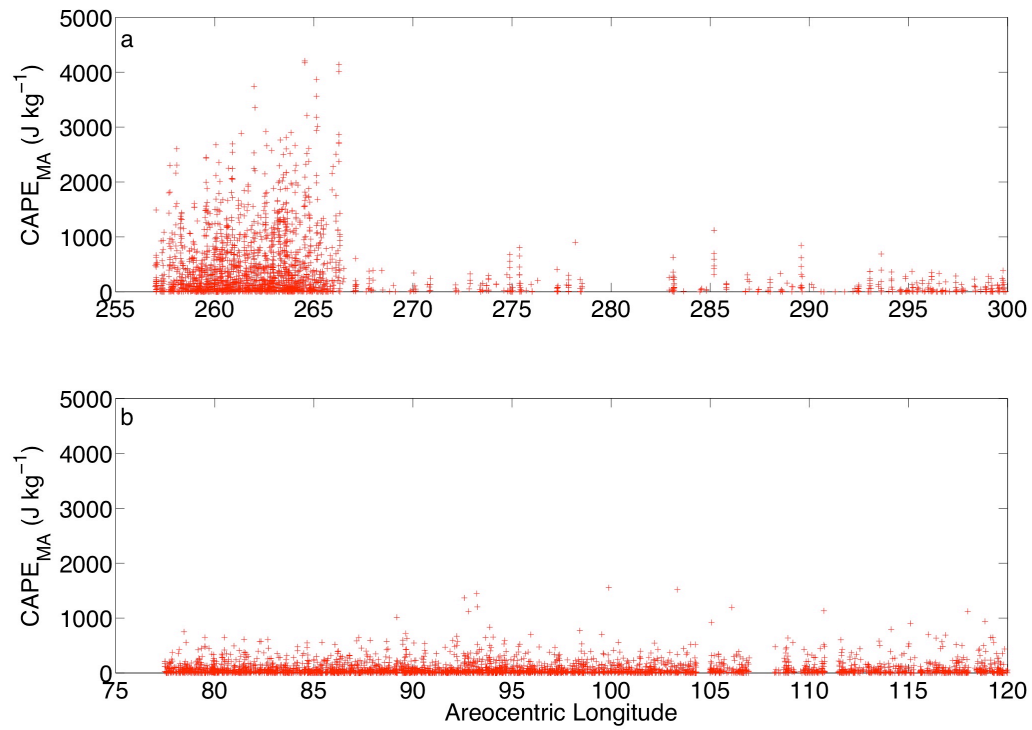
Figure 11, Heavens et al., Convective Instability

Figure 3.11. (a) $CAPE_{MA}$ in individual profiles with latitudes north of 60°N vs. L_s in MY 28, L_s=257°—

300°; (b) $CAPE_{MA}$ in individual profiles with latitudes south of 60°S vs. L_s, MY 29, L_s=77°—120°.
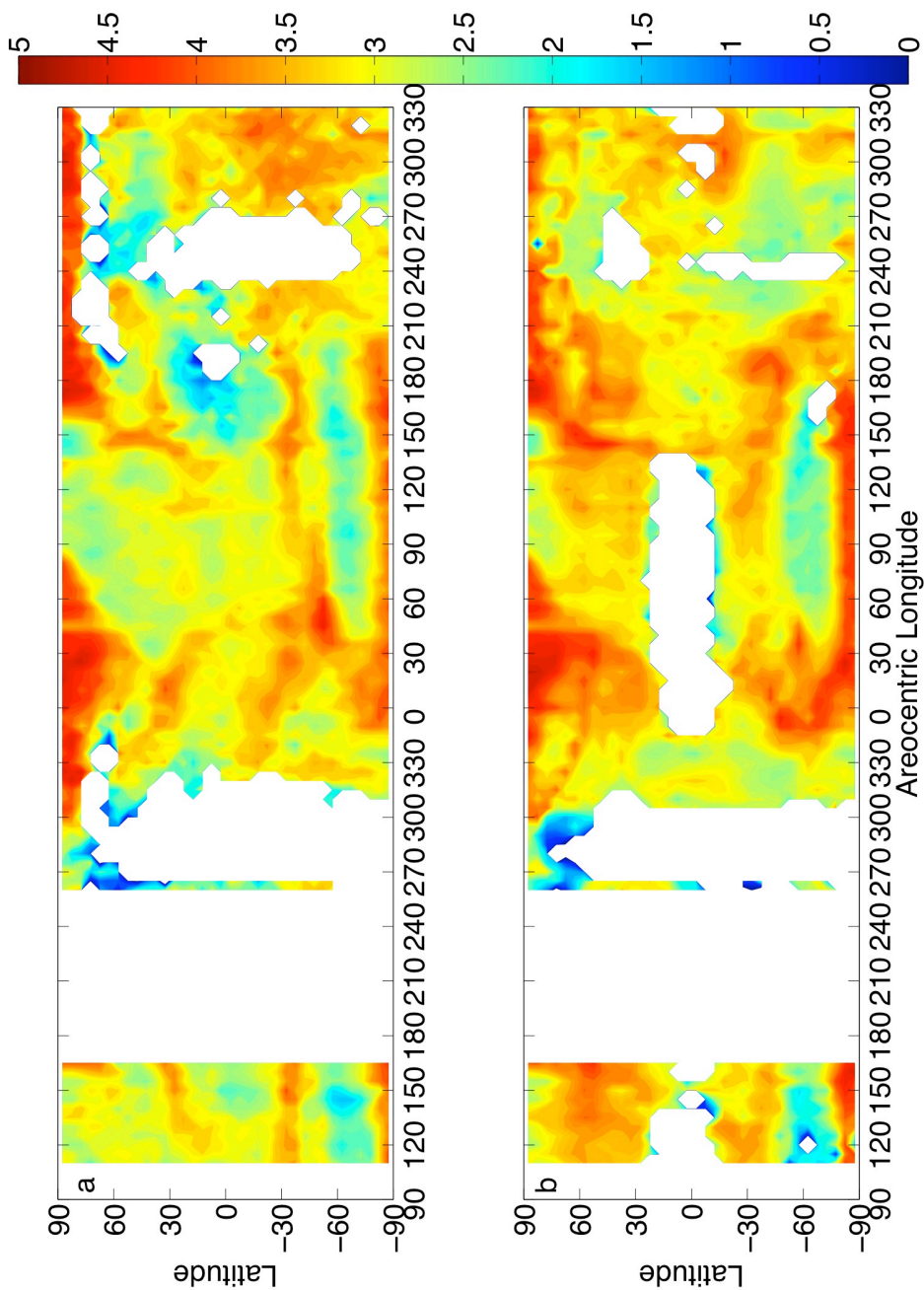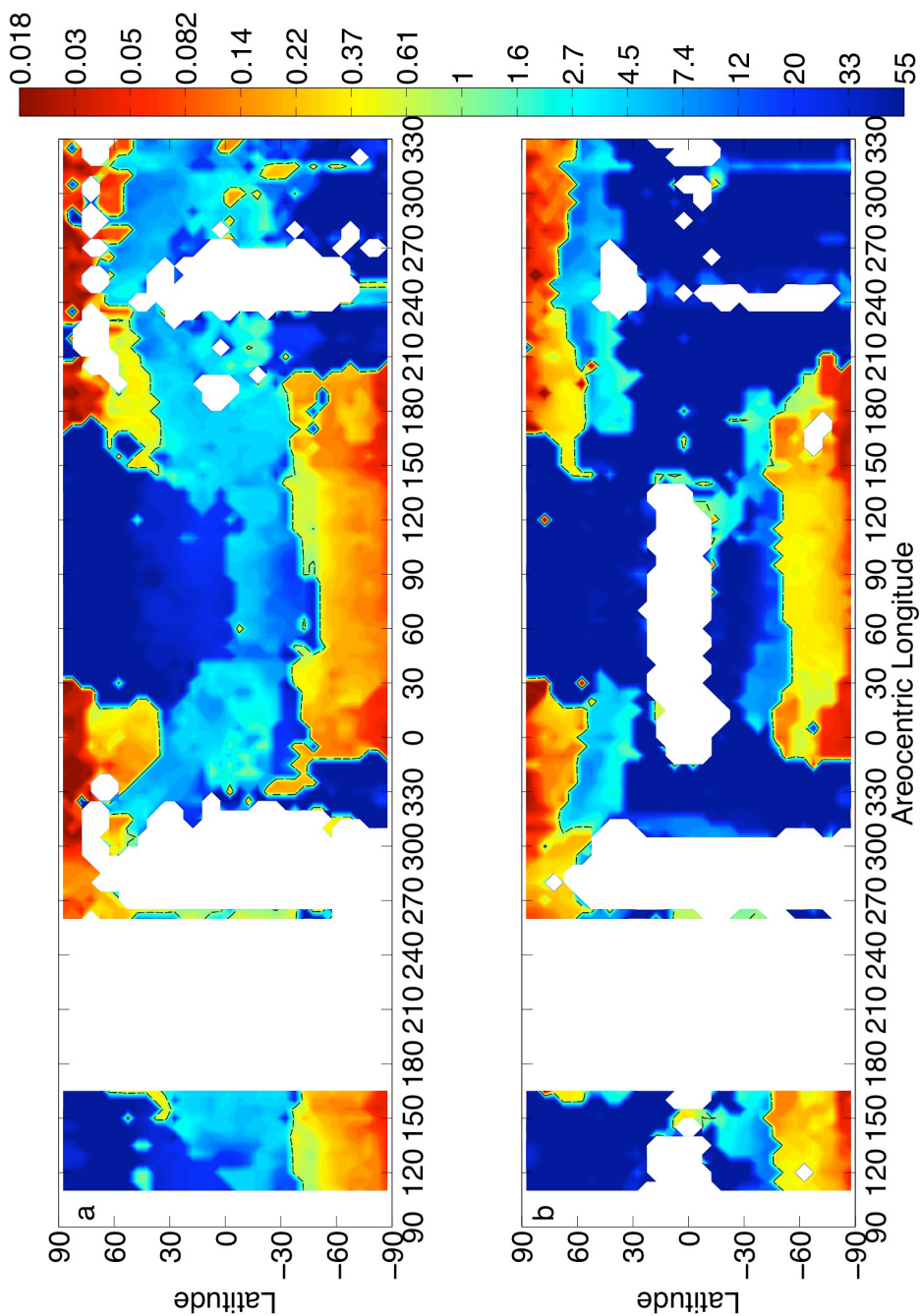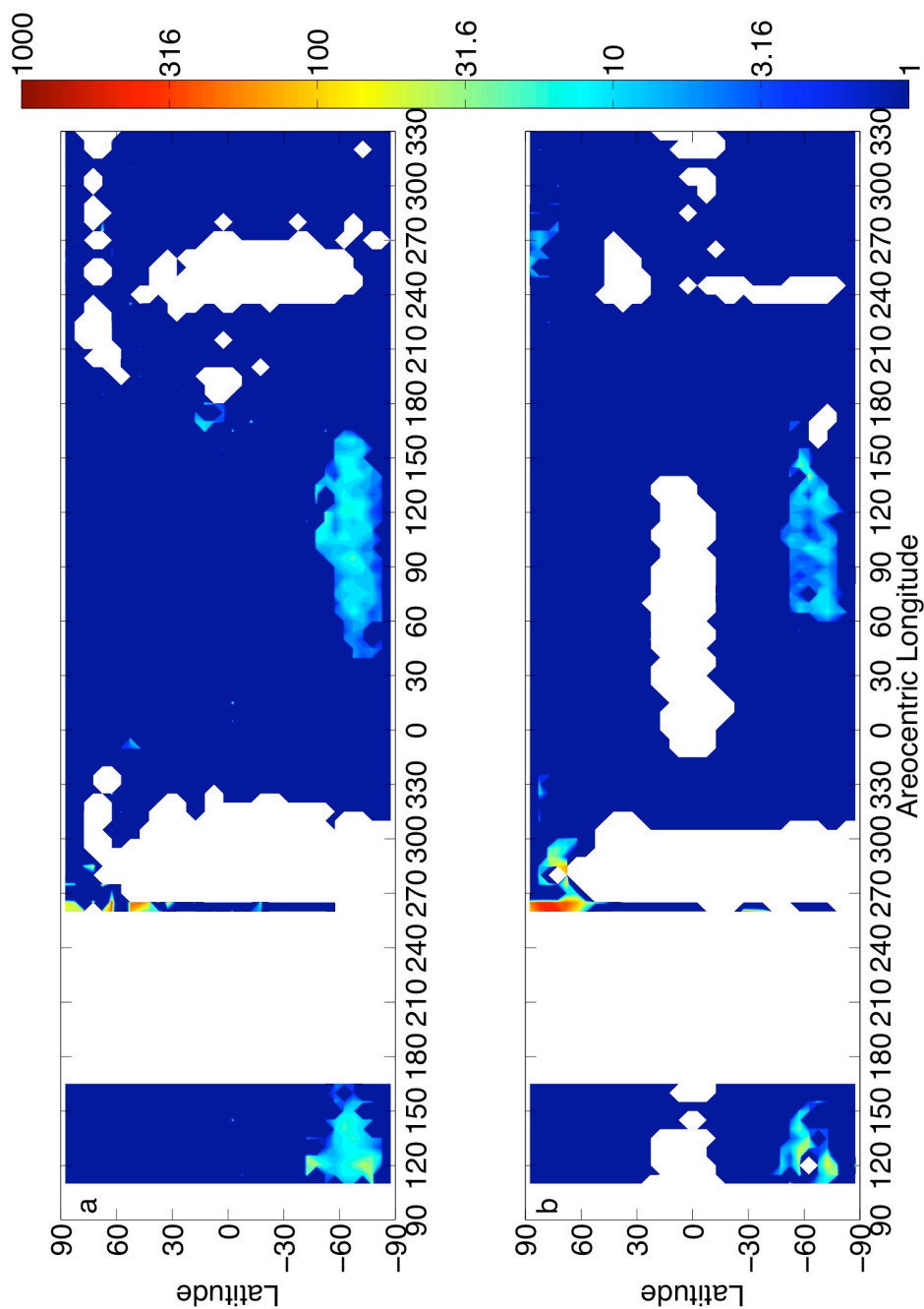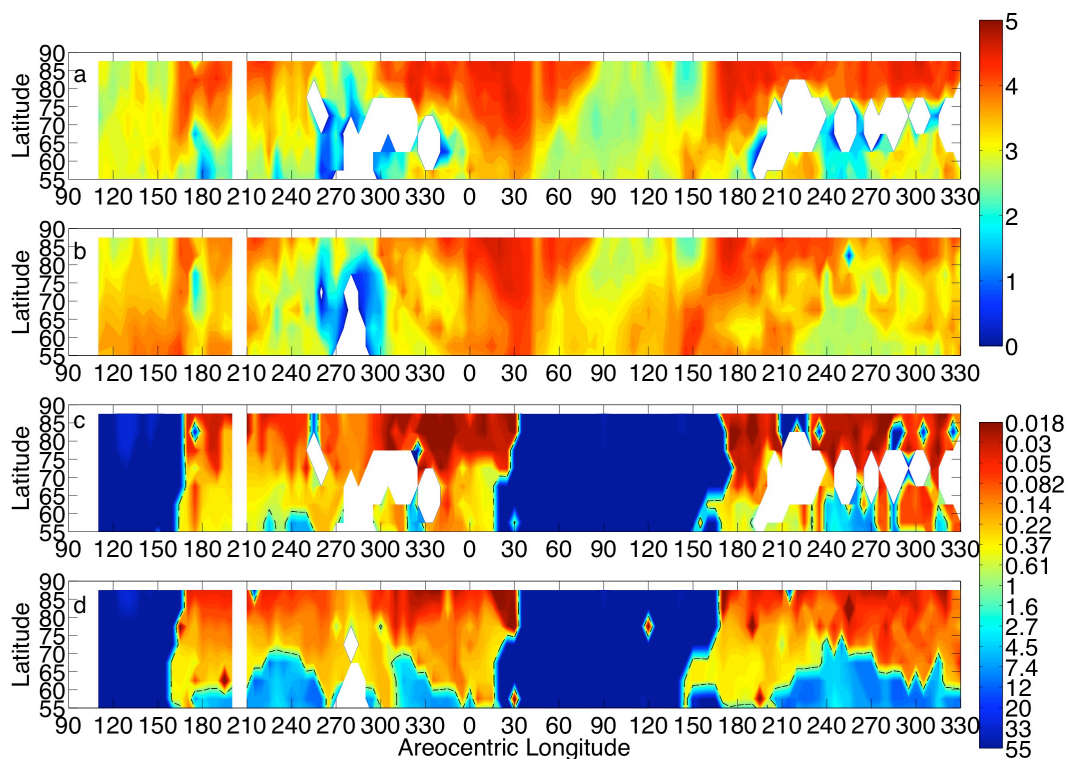
Figure 12, Heavens et al., Convective Instability

Figure 3.12. Latitudinal and seasonal variability during MY 28 and 29 in the minimum zonal average $\Gamma(p < 50$ Pa$)$ (K km^{-1}) and the pressure (Pa) at which it occurs using retrieved profiles from both limb staring and limb scanning data: (a) $\Gamma(p < 50$ Pa$)$, nightside; (b) $\Gamma(p < 50$ Pa$)$, dayside; (c) pressure of occurrence for (a); (d) pressure of occurrence for (b). Only latitudes north of 55° N are shown as discussed in the text.
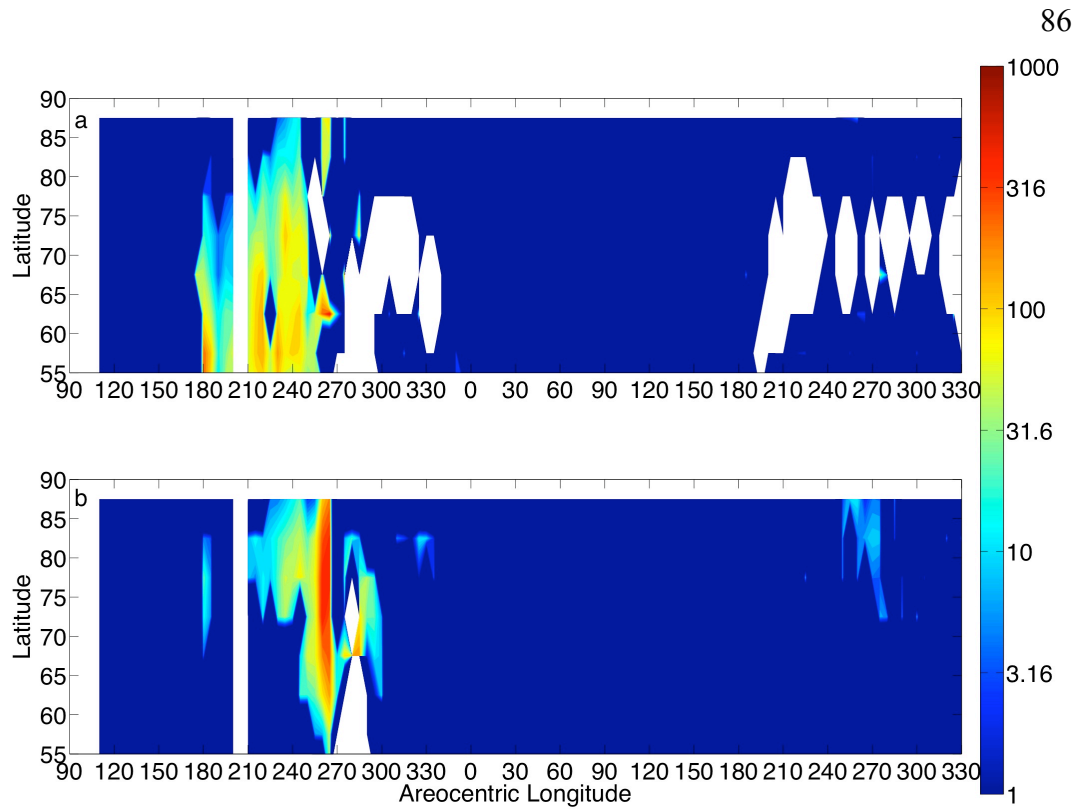
Figure 13, Heavens et al., Convective Instability

Figure 3.13. Latitudinal and seasonal variability during MY 28 and 29 in the zonal average CAPE$_{MA}$ (J kg^{-1}) using retrieved profiles from both limb staring and limb-scanning data: (a) nightside; (b) dayside. Only latitudes north of 55° N are shown as discussed in the text.

presented at the 39th Meeting of the Division for Planetary Sciences of the American

Astronomical Society, Orlando, FL, 7-12 October 2007). There is strong dayside-

nightside variability in $CAPE_{MA}$ between 55º and 70º N during L_s=180°-260° of MY 28

(Figures 3.13a-b). The least stable average lapse rates occur at $p > 1$ Pa at this latitudinal

band and season during both MY 28 and MY 29 (Figures 3.12a-d). Figures 3.10e-f show

this dayside-nightside variability is connected to changes in the width of a zone of low

mean stability at ~0.3 Pa in the northern extratropics. Significant instabilities in

individual profiles are present on the nightside, but not on the dayside during MY 28.

Neither the zone of low mean stability at ~10 Pa in the northern tropics/mid-latitudes, nor

the poleward extension on the dayside contain profiles with significant instabilities. Thus,

whatever phenomenon is generating the instability in this latitudinal band and season

during MY 28 could generate it within a zone of low mean stability at ~0.3 Pa but not

within a zone of low mean stability at ~10 Pa. The existence of a zone of low mean

stability at ~0.3 Pa at this latitudinal band and season during MY 29 without significant

$CAPE_{MA}$ may imply that whatever phenomenon was generating the instability during MY

28 was weaker during MY 29.

3.4 Discussion

3.4.1 Interpretation of Middle Atmospheric Convective Instabilities

We propose that the convective instabilities described in Chapters 3.2 and 3.3 are the

result of gravity wave saturation modulated by the thermal tides. (The diurnal tide is

particularly apparent in MCS observations, but modeling suggests the semi-diurnal tide may be equally or more important during large-scale dust storm activity [*Forbes and Miyahara*, 2006]). Above the tidal anti-nodes, there are regions of lower stability with respect to the mean thermal structure. (In the case of pure tidal breakdown, these regions actually would be convectively unstable.) An internal gravity wave has a warm phase and a cold phase in the vertical. The boundary between the warm and the cold phase is a perturbation toward instability. Thus, if the unstable phase of an internal gravity wave propagates through a region of low stability due to the tide and/or the mean thermal structure, a convective instability may be created. As the tidal anti-nodes move up and down during the course of the day, the level of gravity wave saturation will change. In this way, the tides can modulate where gravity wave saturation occurs without being unstable on their own.

Tidal modulation is evident in Figures 3.5a and 3.5b, which show a strong vertically propagating tidal anti-node centered at 15° S at a level of 0.7 Pa on the nightside that rises to 0.07 Pa on the dayside. In Figure 3.5c, this anti-node is associated with a local minimum in $\Gamma(p)$ near which occur significant instabilities in two individual profiles. The region of low stability at 65° S at ~0.3 Pa on the nightside is lower on the dayside due to the influence of the tide. The tide appears to be defining the sharpness of the top of the middle atmospheric temperature maximum [*McCleese et al.*, 2007; *Lee et al.*, 2009]. There is similar day-night variability in the stability structure in middle of northern fall of MY 28 (Figures 3.10e-f).

The observed variability in stability, however, does not appear consistent with pure tidal breakdown. Away from the poles, MCS observes at approximately the same

local time (and thus same tidal phase). In the case of pure tidal breakdown, we would

expect the zonal average $\Gamma(p)$ for nightside or dayside to be unstable. There indeed are

instances of unstable zonal average $\Gamma(p)$, but these instances are in bins with longitudinal

sampling no greater than 20%. Where longitudinal sampling is complete, the minimum

zonal average $\Gamma(p)$ is always greater than 1.5 K km^{-1}, requiring a significant additional

perturbation to explain the unstable lapse rates in individual profiles.

A plausible case in which gravity waves may have destabilized portions of the

atmosphere already close to neutral stability is illustrated in Figures 3.14a-d. Figures

3.14a-c show longitudinal cross-sections of $\Gamma(p)$ in individual profiles along an orbit.

Figure 3.14d illustrates the zonal average $\Gamma(p)$ on both the dayside and nightside. At this

latitude, the instrument is looking more westward than northward or southward and thus

its observations broadly integrate over a range of local times centered at ~4:30 LST on

the nightside and ~13:00 LST on the dayside. While there is some diurnal variability (not

necessarily tidal in origin), the mean atmosphere on both the dayside and nightside is

highly stable (lapse rates more stable than isothermal) between 50 and 0.2 Pa and near

neutral stability (lapse rates less stable than isothermal) between 0.2 and 0.02 Pa.

Figures 3.14a-c show several examples of smaller-scale perturbations in $\Gamma(p)$ that

are coherent between profiles within the broad layer of near-neutral stability. For

instance, Figure 3.14b shows a nearly isothermal perturbation at ~0.5 Pa, a highly stable

perturbation at ~0.25 Pa, and an unstable perturbation at ~0.06 Pa. If these perturbations

were gravity waves propagating vertically, their vertical and horizontal wavelengths

would be ~10 and ~150 km respectively.
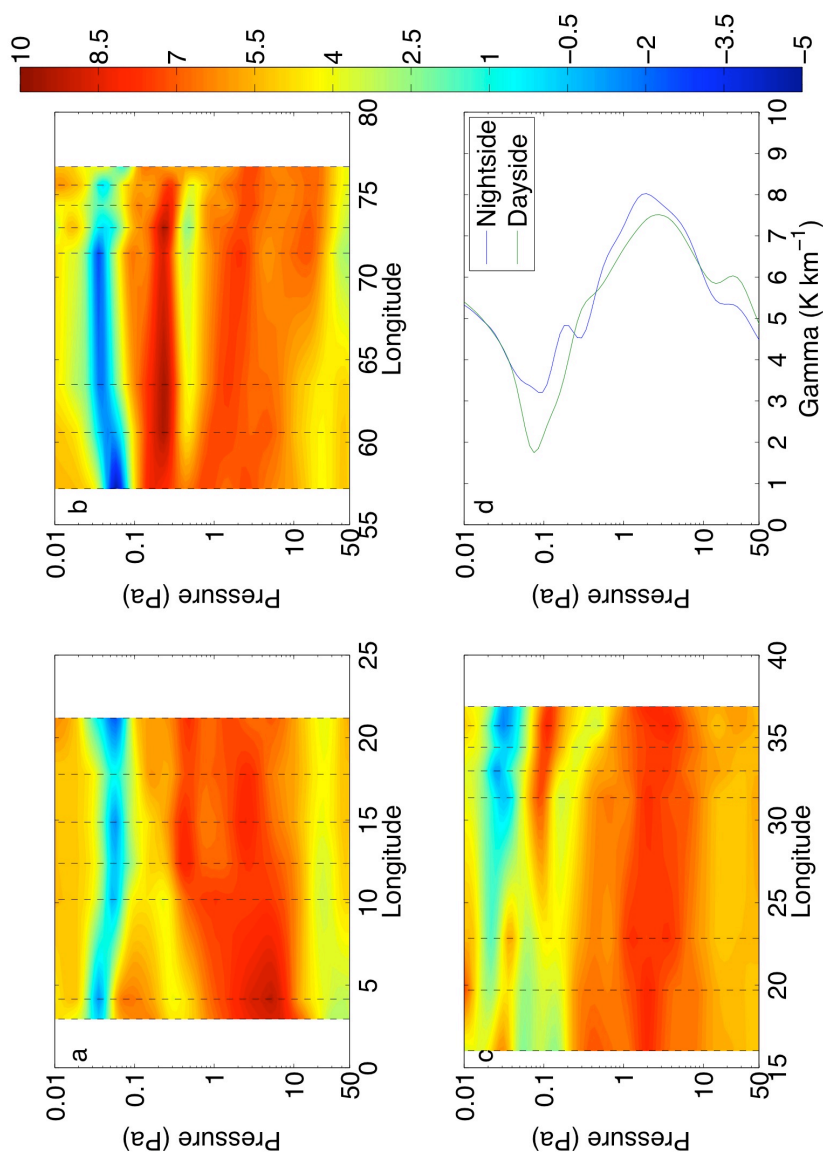
Figure 3.14. Cross-sections of $\Gamma(p)$ constructed from individual profiles retrieved from observations during northern fall of MY 28 near the north pole: (a) orbit number 4177 (17 June 2007), latitudes=80.6369°—84.8568° N, L_s= 259.5701°—257.5707°, 4:12—5:24 LST; (b) orbit number 4140 (15 June 2007), latitudes=80.0047°—84.7466° N, L_s= 257.7412°—257.7419°, 12:27-13:43 LST; (c) orbit number 4181 (18 June 2007), latitudes=80.2689°—84.9621° N, L_s= 259.7657°—259.7664°, 12:17—13:39 LST; (d) zonal average $\Gamma(p)$, MY 28, L_s=257.5°—262.5°. The black dashed lines in the cross-sections indicate the mean longitudes of the profiles. Breaks in spacing likely indicate where retrieval was unsuccessful.

Even in the absence of the perturbations, pure tidal breakdown would be an unlikely explanation for the instabilities at this latitude and season. On the dayside, about half of the profiles have $CAPE_{MA} > 0$ (Figure 3.6c), but the minimum zonal average $\Gamma(p)$ is 1.7 K km^{-1}. Thus, for every perturbation toward instability within the region of near-neutral stability, there should be (and inspection suggests it) a perturbation toward high stability, as would be expected for a region experiencing a high flux of vertically propagating gravity waves with randomly distributed phases. The coherent structures seen in Figures 3.14a-c are not easily identified at other latitudes and seasons, where instabilities are far less common, but we suspect that the convective instabilities observed elsewhere in the middle atmosphere are caused by the same mechanism.

3.4.2 Dynamical Significance

The primary effect gravity waves and tides have on the circulation can be described by the zonal momentum equation as in *Barnes* [1990]:

$$\frac{\partial \overline{U}}{\partial t} - f\overline{V} = F_x + \frac{\partial}{\partial z}\left(D\frac{\partial \overline{U}}{\partial z}\right) \tag{3.5}$$

where $\overline{U}$ and $\overline{V}$ are the mean zonal and meridional winds, F_x is the zonal wave drag, and D is a diffusion constant. Modeling shows that the westerly jets tend to be stabilized in the presence of wave drag by enhancement of the mean meridional flow toward the pole and downwelling, as implied by the second left hand side term of Eq. 3.5. At least to first order, the major difference between wave drag due to gravity waves and tides is their differing phase speeds. Gravity waves have low or stationary phase speeds typical of lower atmospheric winds, while sun-synchronous tides have a phase speed that matches

the planetary rotation speed at the latitude at which they propagate [*Lindzen*, 1981].

Thus, gravity waves and tides usually accelerate the mean flow in different ways.

Because we interpret the convective instabilities (and thus dissipation) to result primarily

from gravity waves, we will focus on the wave drag due to gravity waves alone.

F_x can be defined in terms of the vertical convergence of the momentum flux in

the x-direction:

$$F_x = -\frac{1}{\rho}\frac{\partial}{\partial z}\left(\rho\langle u'w'\rangle\right)$$

(3.6)

where ρ is the density and $\langle u'w'\rangle$ is the zonal momentum flux of the gravity waves. The

key observational constraint for modeling the effect of gravity waves on the martian

circulation then would be an estimate of the zonal momentum flux. Because MCS is

probably most sensitive to meridionally propagating waves, the gravity wave saturation

detected may be primarily a source of meridional rather than zonal momentum to the

circulation. So we will focus on estimating the drag due to the inferred saturating waves

in Figure 3.14, a case in which MCS may be more sensitive to zonally propagating

waves.

To estimate the wave drag, I adopt the drag parameterization of *Barnes* [1990]:

$$F_x = \frac{-\gamma k_h(\overline{U} - c)^3}{N}\left[\frac{1}{2H} - \frac{3\frac{d\overline{U}}{dz}}{2(\overline{U} - c)}\right]$$

(3.7)

where γ is a parameter called the "intermittency factor," k_h is the horizontal wavenumber

of the waves, and H is the scale height. Note that Eq. 3.7 is evaluated at the level of
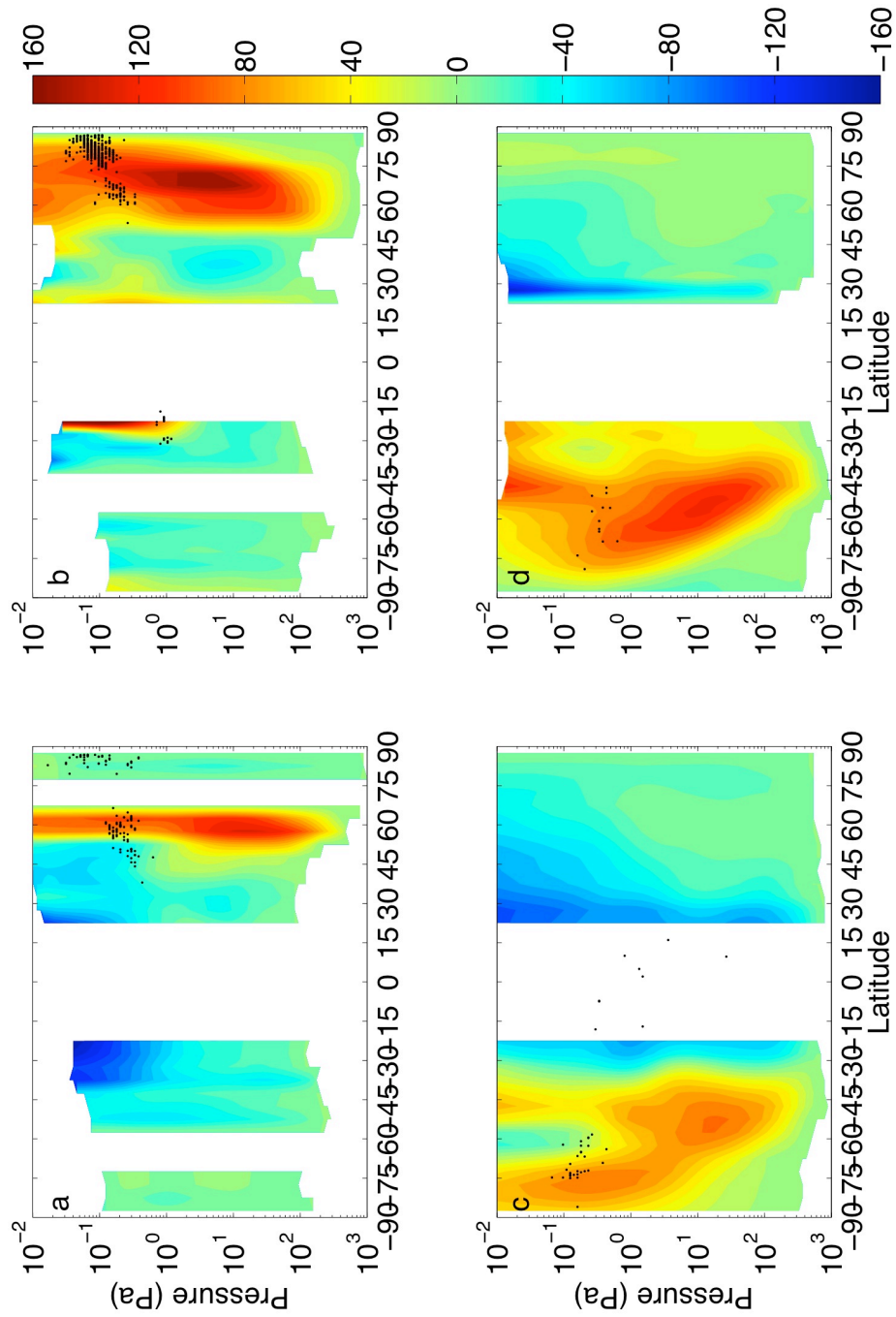
Figure 3.15. Estimated zonal gradient wind, $\tilde{U}(p)$ (ms^{-1}) for: (a) L$_s$=260°, MY 28, nightside; (b) L$_s$=260°, MY 28, dayside; (c) L$_s$=90°, MY 29, nightside; (d) L$_s$=90°, MY 29, dayside.

gravity wave breaking. As a guide to estimate $\overline{U}$ and $\dfrac{d\overline{U}}{dz}$, Figures 3.15a-d show the

estimated zonal gradient wind, $\tilde{U}$, for nightside and dayside of $L_s=260°$ during MY 28

and $L_s=90°$ durinMY 29 along with the locations of the most unstable profiles, just as in

Figures 3.5 and 3.10.

Let us then consider a stationary wave ($c=0$) with $k_h=4\times10^{-5}$ m^{-1} (a horizontal

wavelength of ~150 km) in a mean zonal wind of 75 ms^{-1} (the estimated dayside zonal

wind at 10^{-1} Pa at 80°—85° N in Figure 3.15b) with $N=10^{-2}$ s^{-1}, and $H=8,000$ m. The

vertical wind shear, $\dfrac{d\overline{U}}{dz}$, is ~2×10^{-4} s^{-1} at the same pressure level and latitude/L_s bin.

Fritts and Alexander [2003] says that the intermittency factor, "can be thought of as

describing the fractional coverage of the wave dissipation event within the larger scale

space- and/or time-averaging interval." One simple and perhaps overly generous estimate

of the intermittency factor is the fraction of profiles in the zonal averaging bin that

contain instabilities, which is 0.52 for the dayside of $L_s=260°$ during MY 28 (Figure

3.6c). (In general, we expect the intermittency factor to be directly but not necessarily

linearly proportional to average CAPE$_{MA}$.) In that case, $F_x=-0.05$ ms^{-2} or

-4,500 ms^{-1} sol^{-1}. If waves of similar horizontal wavelength are creating the instabilities

in the southern extratropics, drag there during southern fall and winter may be an order of

magnitude weaker, since zonal average CAPE$_{MA}$ and the proportion of unstable profiles

is around an order of magnitude lower. The zonal winds in the region of breaking are

similar, though they are generally faster in the northern extratropics.

The estimated drag in the northern extratropics before the 2007 global dust storm

is significantly greater than tidal drag in model simulations of middle atmospheric north

polar warmings during planetary dust events [*Wilson*, 1997; *Forbes and Miyahara*, 2006] but is of comparable magnitude to estimates (-1000 ms^{-1}sol^{-1}) by *Barnes* [1990] of the gravity wave drag necessary to produce up to 50 K departures from radiative equilibrium.

Nevertheless, we would like to emphasize that our quantitative estimates of wave drag are tenuous, since: (1) convective instability is only one process by which tides and gravity waves dissipate; (2) the vertical resolution of MCS may underresolve convective instabilities; (3) and the instability analysis presented above provides very limited information about the characteristics of the waves that produce the observed instabilities and the fullness of their distribution with wavelength, phase speed, and intermittency factor. Thus, any dynamical interpretation that connects (or disconnects) the observed instabilities with the occurrence and vigor of polar warmings is entirely tentative, and thus considerable additional observational and modeling work will be required to demonstrate it.

With these caveats in mind, the interannual variability in the occurrence of convective instabilities in the northern extratropics during northern fall creates a natural sensitivity experiment, in which the potential dynamical influence of the wave drag associated with the observed convective instabilities can be investigated. Figures 3.16a-d show variability in the nightside zonal average temperature structure in four different latitudinal bins, all in the northern hemisphere but ranging from near the pole to the edge of the northern tropics. Temperatures closer to the tropics at ~1—10^{-2} Pa are considerably cooler in northern fall of MY 28 (Figures 3.16c-d) than in northern fall of MY 29. Dayside temperatures at ~1—10^{-2} Pa appear cooler in northern fall of MY 28 as well, but
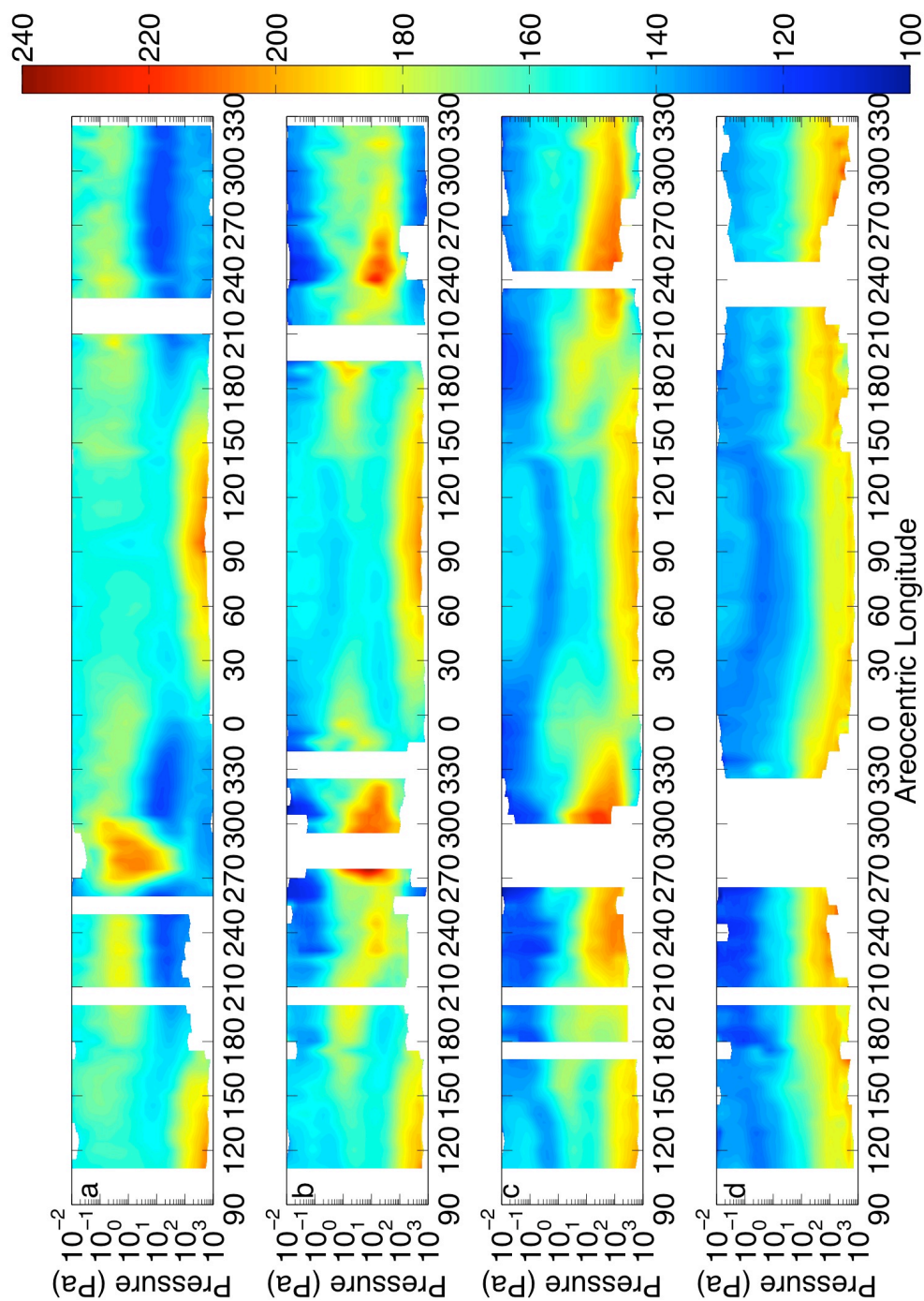
Figure 3.16. Nightside zonal average temperature (K) vs. p and L_s (includes retrievals from limb staring data) for the latitudinal bins: (a) 75°—80° N. (b) 60°—65° N. (c) 45°—50° N. (d) 25°—30° N.

the effects of the tide displace the region of coldest temperatures to lower pressures beyond MCS's vertical range (already limited in limb staring mode). To determine the potential interannual variability in tropical middle atmospheric temperatures more rigorously, we account for the estimated errors in the retrievals.

The random error in an average of independent measurements (applicable since the error at a pressure level is characteristic of an individual retrieval) is found by:

$$\sigma_{avg} = \frac{\sqrt{\sum_i \sigma_i^2}}{n} \qquad (3.8)$$

where in this case, σ_I is the temperature error in the retrieval and n is the number of retrievals in the average. Recall that this formula is applied twice to determine the error in the zonal average: once to determine the error in each longitudinal bin average and once to determine the error in the zonal average itself. In addition, recall that the error in a difference of independent variables is given by the square root of the sum of the square of their individual errors.

Figures 3.17a-c show the difference (and error estimates) between nightside 0.1 Pa temperatures in MY 28 and 29 in two latitudinal bands near the northern tropic and one latitudinal band just south of the equator. The interannual variability in 0.1 Pa temperatures is fairly similar in all three latitudinal bands. Temperatures during MY 28 and MY 29 are relatively similar until around $L_s=180°$, when MY 28 temperatures become 10—25 K cooler than in MY 29. This drop is not coincident with the change in MCS observing mode between limb scanning and limb staring but occurs before it (Figure 3.17c) or ~10 degrees of L_s after it (Figures 3.17a-b). Temperatures are steadily
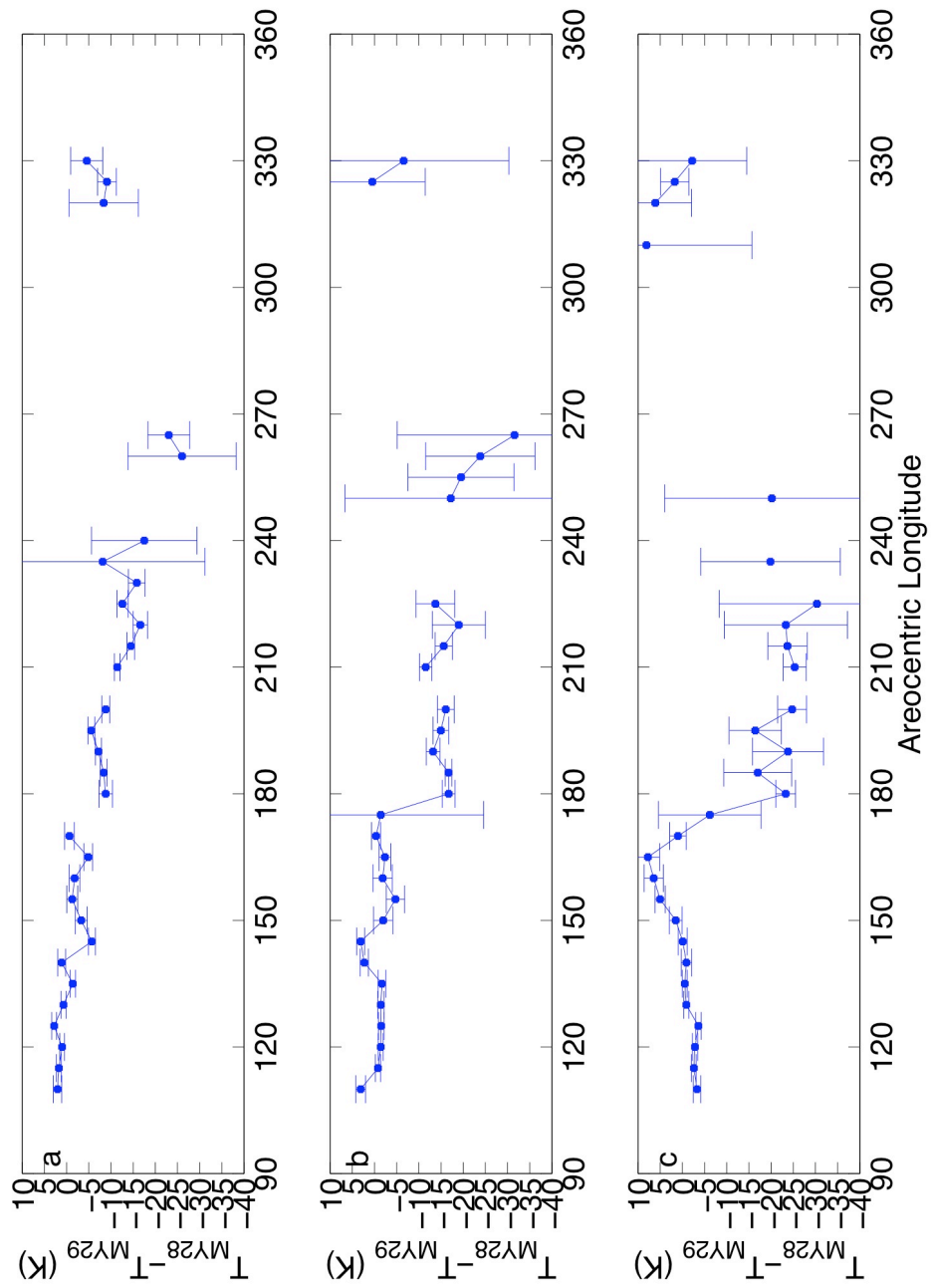
Figure 17, Heavens et al., Convective Instability

Figure 3.17. Nightside zonal average temperature difference (K) between MY 28 and 29 (K) at 0.1 Pa. The error bars show the 2σ estimate of the error in the temperature difference. (a) 35°—40° N; (b) 25°—30° N; (c) 5°—10° S.

cooler up to $L_S=265°$. When interannual comparison is again possible in late southern summer, 0.1 Pa temperatures are similar in both years. Therefore, tropical temperatures at 10^{-1} Pa at ~3:00 LST were ~25 K cooler during northern fall of MY 28 than during northern fall of MY 29.

These cooler temperatures could be connected to the inferred wave drag in the northern extratropics, which would slow the winter westerly jet and force strong upwelling and adiabatic cooling equatorward of the drag and downwelling/ adiabatic warming poleward. *Forbes and Miyahara* [2006] model an analogous circulation driven by the dissipation of the semi-diurnal tide. The temperature of the feature we attribute to the adiabatic warming (the high latitude polar middle atmospheric temperature maximum) (Figure 3.16a) is similar in both years (before the onset of the planetary dust event), which initially appears inconsistent with this hypothesis. However, the fundamental requirement on a meridional circulation driven by wave drag is that it maintain thermal wind balance consistent with the dragged jet. The thermal wind shear is proportional to the meridional temperature gradient (see Eq. 3.3), i.e., the pole to tropical temperature gradient, which is higher at $1—10^{-2}$ Pa during northern fall of MY 28 than in northern fall of MY 29.

Interannual variability in tropical temperatures at $1—10^{-2}$ Pa during northern fall and winter could have consequences for dust storm activity, in particular the development of the 2007 global dust storm in MY 28. *Rafkin* [2009] has attempted to integrate the proposed hurricane analogy for martian dust storms with thermodynamic models of terrestrial hurricanes. *Rafkin*'s [2009] numerical simulations of small dust storms show that their intensity is dependent on the difference between the inflow temperature of

dusty air at the surface and the outflow temperature of the storm's circulation, as would be expected from a simple Carnot heat engine model. In effect, a steeper lapse rate at the top of the circulation results in a stronger dust storm. The dust storms simulated by *Rafkin* [2009] are relatively small and shallow compared with planetary-scale dust storms on Mars, but the basic heat engine framework may be relevant to these larger circulations, which may penetrate into the middle atmosphere [*Jaquin et al.*, 1986; *Newman et al.*, 2002]. Colder temperatures lower in the tropical atmosphere could permit more efficient dust storms if regional dust storm activity that initially develops in the southern mid-latitudes breaks into the tropical middle atmosphere. Thus, strong extratropical wave breaking could prime Mars's atmosphere for planetary-scale dust activity.

3.4.3 Possible Causes for Interannual Variability in Northern Extratropical Instability

Because of its potential significance for global dust storm amplification, it is important to understand why middle atmospheric convective instability in the northern extratropics is so variable between two observed years. Interannual variability may arise most immediately from the lower mean stability in the northern extratropics at a level of ~1—0.1 Pa during MY 28 (Figures 3.10a-b), which could allow even a uniform gravity wave flux to saturate more easily. These differences are not limited to the northern extratropics. There is an unstable region at ~1 Pa in the southern tropics (Figures 3.10a and 3.10e) during northern fall of MY 28 that is not apparent in MY 29 (Figure 3.10b). The zonal average stability structure is related to both the mean meridional circulation

and the thermal tides, both of which can be affected by gravity wave drag on the zonal wind field, raising the possibility of feedback.

In addition, the gravity wave flux itself is probably variable. The lowest zonal average $\Gamma(p < 50 \text{ Pa})$, when longitudinal sampling is complete or nearly so, is rarely less than 2 K km^{-1} in both the northern and southern extratropics. In these cases, zonal average $CAPE_{MA}$ can vary by more than an order of magnitude for the same minimum zonal average $\Gamma(p < 50 \text{ Pa})$ and is generally highest in the northern extratropics during MY 28.

Interannual variability in gravity wave flux and changes in gravity flux before or after a global dust storm could be related to interannual variability in (1) baroclinic wave activity [*Barnes*, 1980, 1981]; or (2) moist carbon dioxide convection in polar night [*Cornwall and Titus*, 2009]. However, a connection between these phenomena and gravity wave generation has not been established for Mars, so a definite explanation for the interannual variability in middle atmospheric convective instability in the northern extratropics will require considerable additional research.

3.5. Summary

I have detected widespread convective instability or near-instability within Mars's middle atmosphere, which I propose is the result of gravity wave saturation modulated by the thermal tides. I am able to characterize much of this instability's spatial and temporal variability. The most notable aspect of this variability is the contrast between the northern and southern extratropics. During both years of observation, middle atmospheric convective instability was moderately frequent in the southern extratropics during

southern fall and winter. In the northern extratropics, middle atmospheric convective instability was at the highest levels observed anywhere on the planet between the beginning of the fall and the onset of the 2007 global dust storm, at which point it fell to relatively low levels and continued at low levels even in northern winter of the next year. At the minimum, this contrast suggests that gravity wave sources and propagation conditions can differ greatly between northern fall and winter and southern fall and winter on Mars and in the same hemisphere during different years.

While the estimates of the wave drag on the atmospheric circulation in this study are highly tentative, the interannual variability in convective instability in the northern extratropics may provide a potential insight into the effect of extratropical wave drag on the circulation. During MY 28, strong wave drag may have strengthened middle atmospheric upwelling at the equator and produced an observed cooling of northern mid-latitude and tropical middle atmospheric temperatures, which could have favored development of a global dust storm in MY 28.

The existence of a possible gravity wave saturation signal such as convective instability in MCS retrieved temperature profiles and its potential dynamical importance should motivate further efforts to observe tidal and gravity wave dissipation in the martian atmosphere. One future area of investigation could be analysis of the brightness temperature variances in limb-sounding and airglow data, which is a standard technique for investigating gravity waves in the Earth's atmosphere and may allow easier distinction of the relative role of gravity waves and the tides, surer connection with gravity wave sources, and easier quantification of the profile of dissipation than possible

in this study [*Wu and Waters*, 1996; *Fritts and Alexander*, 2003]. MCS calibrated

radiance data could be useful in this regard.

Bibliography

Barnes J. R. (1980), Time spectral analysis of midlatitude disturbances in the Martian atmosphere, *J. Atmos. Sci.*, *37*, 2002–2015.

Barnes J. R. (1981), Midlatitude disturbances in the Martian atmosphere: A second Mars year. *J. Atmos. Sci.*, *38*, 225–234.

Barnes, J.R. (1990), Possible effects of breaking gravity waves on the circulation of the middle atmosphere of Mars, *J. Geophys. Res., 95* (B2), 1401-1421.

Bücker, D., R. Span, and W. Wagner (2003), Thermodynamic Property Models for Moist Air and Combustion Gases, *J. Eng. Gas Turbines Power*, *125*(1), 374-384.

Cantor, B., M. Malin, and K.S. Edgett (2002), Multiyear Mars Orbiter Camera (MOC) observations of repeated Martian weather phenomena during the northern summer season, *J. Geophys. Res.*, *107*(E3), 5014, doi:10.1029/2001JE001588.

Clancy, R.T., B.J. Sandor, M.J. Wolff, P.R. Christensen, M.D. Smith, J.C. Pearl, B.J. Conrath, and R.J. Wilson (2000), An intercomparison of ground-based millimeter, MGS TES, and Viking atmospheric temperature measurements: Seasonal and interannual variability of temperatures and dust loading in the global Mars atmosphere, *J. Geophys. Res., 105*, 9553–9571

Clancy, R.T., M.J. Wolff, B.A. Whitney, B.A. Cantor, and M.D. Smith (2007), Mars equatorial mesospheric clouds: Global occurrence and physical properties from Mars

Global Surveyor Thermal Emission Spectrometer and Mars Orbiter Camera limb observations, *J. Geophys. Res.*, *112*, E04004, doi:10.1029/2006JE002805.

Collins, M., S.R. Lewis, and P.L. Read (1997), Gravity wave drag in a global circulation model of the Martian atmosphere: Parametrisation and validation, *Adv. Space. Res.*, *44*, 1395–1409.

Collins, R.L. and R.W. Smith (2004), Evidence of damping and overturning of gravity waves in the arctic mesosphere: Na lidar and OH temperature observations, *J. Atmos. Solar-Terrest. Phys., 66* (10), 867-879.

Cornwall, C. and T.N. Titus (2009), Spatial and temporal distributions of Martian north polar cold spots before, during, and after the global dust storm of 2001, *J. Geophys. Res.*, *114*, E02003, doi:10.1029/2008JE003243.

Creasey, J.E., J.M. Forbes, and D.P. Hinson (2006), Global and seasonal distribution of gravity wave activity in Mars' lower atmosphere derived from MGS radio occultation data, *Geophys. Res. Lett.*, *33*, L01803, doi:10.1029/2005GL024037.

Deming, D., M.J. Mumma, F. Espenak, T. Kostiuk, and D. Zipoy (1986), Polar warming in the atmosphere of Mars, *Icarus*, *66*, 366-379.

Forbes, J.M., and S. Miyahara (2006), Solar Semidiurnal Tide in the Dusty Mars Atmosphere, *J. Atmos. Sci.*, *63* (7), 1798-1817.

Forget, F., F. Hourdin, R. Fournier, C. Hourdin, O. Talagrand, M. Collins, S.R. Lewis, P.L. Read, and J.-P. Huot (1999), Improved general circulation models of the Martian atmosphere from the surface to above 80 km, *J. Geophys. Res.*, *104*, 24,155–24,176.

Fritts, D.C. and M.J. Alexander (2003), Gravity wave dynamics and effects in the middle atmosphere, *Rev. Geophys.*, *41* (1), doi:10.1029/2001RG000106.

Fritts, D.C., L. Wang, and R.H. Tolson (2006), Mean and gravity wave structures and variability in the Mars upper atmosphere inferred from Mars Global Surveyor and Mars Odyssey aerobraking densities, *J. Geophys. Res.*, *111*, A12304, doi:10.1029/2006JA011897.

Hartogh, P., A.S. Medvedev, and C. Jarchow (2007), Middle atmospheric polar warmings on Mars: Simulations and study on the validation with submillimeter observations, *Adv. Space. Res*, *55*, 1103-1112.

Hinson, D.P., M. Pätzold, S. Tellmann, B. Hausler, and G.L. Tyler (2008), The depth of the convective boundary layer on Mars, *Icarus*, *198,* 57-66.

Hodges, R.R., Jr. (1967), Generation of turbulence in the upper atmosphere by internal gravity waves, *J. Geophys. Res.*, *72*, 3455-3458.

Holton, J.R. (2004), *An Introduction to Dynamic Meteorology*, 4th Edition, Elsevier, Amsterdam.

Inada, A., M.I. Richardson, T.H. McConnochie, M.J. Strausberg, H. Wang, and J.F. Bell (2007), High-resolution atmospheric observations by the Mars Odyssey Thermal Emission Imaging System, *Icarus*, *192* (2), 378-395.

Jaquin, R.F. III (1989) The middle Martian atmosphere, Ph.D. Thesis, 122 pp., Cornell University, Ithaca, NY, September.

Jaquin, R.F. III, P. Gierasch, and R. Kahn (1986), The vertical structure of limb hazes in the Martian atmosphere, *Icarus*, *72*, 528-534.

Joshi, M. M., B.N. Lawrence, and S.R. Lewis (1995), Gravity wave drag in three-dimensional atmospheric models of Mars, *J. Geophys. Res.*, *100*, 21,235–21,245.

Kleinböhl, A., J.T. Schofield, D.M. Kass, W.A. Abdou, C.R. Backus, B. Sen, J.H. Shirley, W.G. Lawson, M.I. Richardson, F.W. Taylor, N.A. Teanby, and D.J. McCleese (2009), Mars Climate Sounder limb profile retrieval of atmospheric temperature, pressure, dust and water ice opacity, *J. Geophys. Res., 114*, E10006, doi:10.1029/2009JE003358.

Knudsen, W.C. and G.W. Sharp (1965), Evidence for temperature stratification in the E region, *J. Geophys. Res.*, *70*, 143-160.

Lee, C., W.G. Lawson, M.I. Richardson, N.G. Heavens, A. Kleinböhl, D. Banfield, D.J. McCleese, R. Zurek, D. Kass, J.T. Schofield, C.B. Leovy, F.W. Taylor, A.D. Toigo, (2009), Thermal tides in the Martian middle atmosphere as seen by the Mars Climate Sounder, *J. Geophys. Res.*, *114*, E03005, doi:10.1029/2008JE003285.

Lindzen, R.S. (1981), Turbulence and Stress Owing to Gravity Wave and Tidal Breakdown, *J. Geophys. Res.*, *86*(C10), 9707–9714.

Liu, A. Z., R.G. Roble, J.H. Hecht, M.F. Larsen, and C.S. Gardner (2004), Unstable layers in the mesopause region observed with Na lidar during the Turbulent Oxygen Mixing Experiment (TOMEX) campaign*, J. Geophys. Res., 109*, D02S02, doi:10.1029/2002JD003056.

Liu, J., M.I. Richardson, and R.J. Wilson (2003), An assessment of the global, seasonal, and interannual spacecraft record of Martian climate in the thermal infrared, *J. Geophys. Res., 108*(E8), 5089, doi:10.1029/2002JE001921.

McCleese, D. J., J.T. Schofield, F.W. Taylor, S.B. Calcutt, M.C. Foote, D.M. Kass, C.B. Leovy, D.A. Paige, P.L. Read, and R.W. Zurek (2007), Mars Climate Sounder: An investigation of thermal and water vapor structure, dust and condensate distributions in the atmosphere, and energy balance of the polar regions, *J. Geophys. Res., 112*, E05S06, doi:10.1029/2006JE002790.

McCleese, D.J., J.T. Schofield, F.W. Taylor, W.A. Abdou, O. Aharonson, D. Banfield, S.B. Calcutt, N.G. Heavens, P.G.J. Irwin, D.M. Kass, A. Kleinböhl, W.G. Lawson, C.B. Leovy, S.R. Lewis, D.A. Paige, P.L. Read, M.I. Richardson, N. Teanby, and R.W. Zurek (2008), *Nature Geosci., 1*, 745-749, doi:10.1038/ngeo332.

Montmessin, F., B. Gondet, J.-P. Bibring, Y. Langevin, P. Drossart, F. Forget, and T. Fouchet (2007), Hyperspectral imaging of convective CO_2 ice clouds in the equatorial mesosphere of Mars, *J. Geophys. Res.*, *112*, E11S90, doi:10.1029/2007JE002944.

Newman, C.E., S.R. Lewis, P.L. Read, and F. Forget (2002), Modeling the Martian dust cycle: 2. Multi-annual radiatively active dust transport simulations, *J. Geophys. Res.*, *107* (E12), 5124. doi:10.1029/2002JE001920.

Rafkin, S.C.R. (2009), A Positive Radiative-Dynamic Feedback Mechanism for the Maintenance and Growth of Martian Dust Storms. *J. Geophys. Res.*, *114*, E01009, doi:10.1029/2008JE003217.

Richardson, M.I. (1998), Comparison of Microwave and Infrared Measurements of Martian Atmospheric Temperatures: Implications for Short-Term Climate Variability, *J. Geophys. Res.*, *103*(E3), 5911-5918.

Sica, R. J., and M.D. Thorsley (1996), Measurements of superadiabatic lapse rates in the middle atmosphere, *Geophys. Res. Lett.*, *23*(20), 2797–2800.

Span, R. and W. Wagner (1996), A New Equation of State for Carbon Dioxide Covering the Fluid Region from the Triple-Point Temperature to 1100 K at Pressures up to 800 MPa, *J. Phys. Chem. Ref. Data*, *25*, 1509, doi:10.1063/1.555991.

Theodoré, B., E. Lellouch, E. Chassefiére, and A. Hauchecorne (1993), Solstitial Temperature Inversions in the Martian Middle Atmosphere, *Icarus*, *105*(2), 512-528.

Wang, L., D.C. Fritts, and R.H. Tolson (2006), Nonmigrating tides inferred from the Mars Odyssey and Mars Global Surveyor aerobraking data, *Geophys. Res. Lett.*, *33*, L23201, doi:10.1029/2006GL027753.

Whiteway, J.A., and A.I. Carswell (1994), Rayleigh Lidar Observations of Thermal Structure and Gravity Wave Activity in the High Arctic during a Stratospheric Warming. *J. Atmos. Sci.*, 51, 3122–3136.

Williams, B. P., M.A. White, D.A. Krueger, and C.Y. She (2002), Observation of a large amplitude wave and inversion layer leading to convective instability in the mesopause region over Fort Collins, CO (41°N, 105°W), *Geophys. Res. Lett.*, *29*(17), 1850, doi:10.1029/2001GL014514.

Williams, B.P., D.C. Fritts, C.Y. She, and R.A. Goldberg (2006), Gravity wave propagation through a large semidiurnal tide and instabilities in the mesosphere and lower thermosphere during the winter 2003 MaCWAVE rocket campaign, *Ann. Geophys.*, *24*, 1199-1208.

Wilson, R.J. (1997), A general circulation model of the Martian polar warming, *Geophys. Res. Lett.*, *24*, 123–126.

Wilson, R.J. and M.I. Richardson (2000), The Martian Atmosphere during the Viking Mission, 1, Infrared Measurements of Atmospheric Temperatures Revisited, *Icarus*, *145*, 555-579.

Wu, D.L. and J.W. Waters (1996), Gravity-Wave-Scale Temperature Fluctuations Seen

by the UARS MLS, *Geophys. Res. Lett.*, *23*(23), 3289–3292

Zurek, R.W. (1976), Diurnal tide in the Martian atmosphere, *J. Atmos. Sci.*, *33*, 321-337.

Zurek, R.W. and S.E. Smrekar (2007), An Overview of the Mars Reconnaissance Orbiter (MRO) Science Mission, *J. Geophys. Res. Planets*, 112, E5, doi: 10.1029/2006JE002701.

Chapter 4   The Vertical Distribution of Dust in the Martian Atmosphere during Northern Spring and Summer

4.1 Introduction

Because it is strongly radiatively active and highly temporally and spatially variable in its abundance, suspended dust is the martian atmosphere's most meteorologically important component. On this account, observations of its optical properties and spatial and temporal variability have been a part of almost every major spacecraft mission sent to Mars. However, the information provided by these missions about the vertical distribution of atmospheric dust has been limited. Mariner 9 provided information about the vertical distribution of dust during global dust storm conditions [*Conrath*, 1975; *Anderson and Leovy*, 1978]. *Jaquin et al.* [1986] used Viking Orbiter limb imagery to investigate a reddish "continuous haze," which was interpreted to be more dust-rich than the "detached" water ice hazes observed above it. *Jaquin et al.* [1986] also determined that this continuous haze was seasonally and latitudinally variable in height. Observations of Tharsis by instruments on the Phobos spacecraft during early northern spring suggested that dust was well-mixed vertically below 25 km [*Chassefiére et al.*, 1995]. More recently, limb observations from the Thermal Emission Spectrometer (TES) on Mars Global Surveyor (MGS) have been used to retrieve vertical profiles of dust during global dust storm conditions [e.g., *Clancy et al.*, 2009].

Measurements of the vertical distribution of dust in particular (as opposed to the column opacity) are relevant to two important problems of martian meteorology. First, dust has a significant effect on the general circulation of the martian atmosphere. Solar

radiation absorbed by dust during the daytime is a crucial source of diabatic heating

to the lower atmosphere and thus may be one driver of the planet's vigorous principal

meridional overturning circulation (PMOC) (sometimes called "the Hadley circulation")

and a modifier of Mars's strong thermal tides (see *Zurek et al.* [1992] for discussion). By

absorbing and emitting infrared radiation both day and night, dust, like water vapor on

the Earth, either can limit or enhance the radiative cooling of the atmosphere to space. As

a result, even relatively small amounts of dust in the atmosphere can influence the

circulation by enhancing the static stability [*Haberle et al.*, 1982; *Schneider*, 1983].

The effects of dust on the circulation can be highly non-local. From Mariner 9 and

later observations, it is known that the winter polar middle atmosphere of Mars is much

warmer than would be expected from considerations of radiative equilibrium [*Leovy*,

1982]. Middle atmospheric temperatures over the south pole during northern winter

observed by the Thermal Emission Spectrometer (TES) on Mars Global Surveyor (MGS)

and Mars Climate Sounder (MCS) on Mars Reconnaissance Orbiter (MRO) are 10—30 K

warmer than predicted by most Mars climate models [*Smith et al.*, 2001; *McCleese et al.*,

2008]. Modeling studies attribute middle atmospheric polar warming to adiabatic heating

due to the downwelling of the PMOC and connect the intensity of PMOC downwelling to

the amount of dust in the atmosphere and to the level and intensity of wave breaking in

the middle atmosphere [*Haberle et al.*, 1982; *Schneider*, 1983; *Barnes*, 1990; *Haberle et

al.*, 1993; *Forget et al.*, 1999; *Hartogh et al.*, 2007]. Basic considerations from theory,

simple nearly inviscid axisymmetric circulation models [*Schneider*, 1983] and more

sophisticated terrestrial models [*Rind and Rossow*, 1984; *Wang and Rossow*, 1998]

suggest that the Hadley circulation of a planet is sensitive to the vertical distribution of

atmospheric heating. Thus, knowledge of the vertical distribution of dust in the atmosphere provides a key constraint for Mars General Circulation Models (GCMs), analogous to the constraint cloud observations provide for terrestrial GCMs.

Information about the vertical distribution of dust also can provide insights into the mechanisms by which dust enters and leaves the atmosphere. *Conrath* [1975], for instance, attributed the vertical distribution to the competing effects of sedimentation and vertically uniform vertical eddy diffusion. This simple picture has been complicated by (1) the possibility of additional removal processes such as the enhancement of sedimentation by the condensation of volatiles on dust particles (S.M. Nelli and J.R. Murphy, Interrelationship between the Dust and Water Cycles in the Martian Atmosphere: Numerical Modeling Studies, paper presented at the 200th Meeting of the American Astronomical Society, Albuquerque, NM, June 2002); (2) more detailed modeling of vertical transport above the boundary layer due to dynamical processes such as the thermal tides [*Wilson and Hamilton*, 1996]; (3) more detailed treatment of mixing within the boundary layer [*Taylor et al.*, 2007]; (4) explicit consideration of variability in dust size [*Kahre et al.*, 2008] and (5) consideration of particular dust sources such as mountain slopes [*Lee et al.*, 1982; *Rafkin et al.*, 2002] and dry convective helical vortices ("dust devils") [*Kahre et al.*, 2006; *Cantor et al.*, 2006; *Greeley et al.*, 2006]. However, these processes have been investigated primarily by modeling constrained by both the limited observational information about the vertical distribution of dust and more widespread observations of modification of surface features by aeolian processes.

For the last 1.5 martian years, the Mars Climate Sounder (MCS) on Mars Reconnaissance Orbiter (MRO) has been making global, high signal to noise

observations of infrared radiance from Mars's limb (and some nadir and off-nadir observations as well) in nine broadband channels with varying sensitivity to dust, temperature, and other aerosol (see *McCleese et al.* [2007] for description of the instrument and observing strategy.) Simultaneous retrievals from MCS limb observations of temperature, dust, and water ice at moderate vertical resolution (~5 km) are now available [*Kleinböhl et al.*, 2009]. These retrievals provide an extensive dataset to investigate both the contribution of dust to both the vertical heating structure of the atmosphere and also dust lifting and transport processes.

In this study, I focus on the zonal average vertical dust distribution during martian northern summer, L_s=111º—177º of Mars Year (MY) 28 (2006—2007), and martian northern spring and summer, L_s=0º—180º of MY 29 (2007—2008). (For a discussion of the Mars Year convention used, see *Clancy et al.* [2000]). These periods have dense MCS retrieval coverage and (not coincidentally) mostly exclude the canonical "dust storm season" (L_s=161º—346º) classified by *Martin and Zurek* [1993] and thus might be called, "the clear season." While general weather patterns during the clear season are thought to be highly repeatable, even in the wake of a global dust event [*Richardson,* 1998; *Wilson and Richardson*, 2000; *Cantor et al.*, 2002], recent work by *Smith* [2009] suggests that mid to late summer tropical dust activity may have considerable interannual variability. Therefore, I can test whether this variability is evident in the planetary-scale vertical dust distribution. I also can investigate the contribution of dust to the vertical heating structure during the season in which *McCleese et al.* [2008] infer an unexpectedly intense PMOC.

In Chapter 4.2, I describe the retrieval dataset used and its limitations, which circumscribe this investigation. In Chapter 4.3, I present a new scheme for representing

vertical dust distributions in a compact and quantitative fashion based on MCS

vertical dust profiles. In Chapter 4.4, I use the scheme developed in Chapter 4.3 to

analyze zonal average dust opacity profiles, both as a guide to interpretation of the

representation scheme and also as a way of investigating planetary-scale variability in the

distribution of dust vertically during these seasons and their impact on the radiative

forcing of the atmosphere. In Chapter 4.5, I discuss seasonal and diurnal variability in the

vertical dust distribution and describe the vertical heating profile due to dust. In Chapter

4.6, I summarize the results of this study. In Chapter 5, I consider the implications of the

characteristic vertical dust distribution observed from the middle of northern spring to the

middle of northern summer for dust transport processes.

4.2 Data and Basic Analysis

4.2.1 Retrieval Characteristics

Atmospheric retrievals from MCS observations provide vertical profiles of pressure, p,

(Pa), temperature, T, (K), dust opacity, i.e., fractional extinction due to dust per unit

height, $d_z\tau$, (km^{-1}) at 463 cm^{-1}, and water ice opacity (km^{-1}) at 842 cm^{-1}. All of the

vertical profile quantities except pressure are gridded on pressure coordinates at

approximately a factor of five higher resolution than the ~5 km vertical resolution of the

instrument detector array (and thus the retrievals). The pressure at the surface, p_s, (Pa) is

extrapolated from the pressure retrieval using the hydrostatic equation. *Kleinböhl et al.*

[2009] provides both a history of data and retrieval coverage and also a description of the

retrieval algorithm and an evaluation of its success under different observational

conditions. For $d_z\tau > 10^{-5}\,\mathrm{km^{-1}}$, the estimated uncertainty in $d_z\tau$ is typically ~5%. The

retrievals analyzed here use an advanced version of the retrieval algorithm, which

includes a simple scattering approximation in the radiative transfer.

Retrievals from limb observations have an important limitation key to these

investigations. The lowest detector used for the retrieval of dust must have a line-of-sight

(LOS) opacity less than 2.5 and a contribution of less than 10% from the surface in the

detector field of view (FOV). (Note that the airmass factor in the limb is ~50.) The

practical effect is that retrieved vertical profiles of dust (with rare exceptions) do not

include information from detectors observing limb paths less than ~8 km above the

surface. Thus, they provide limited information about dust within the lowest scale height

of the atmosphere. In some cases, retrieved profiles only use information from detectors

observing at higher levels than ~8 km above the surface, further limiting information

about low-level dust.

A small number of retrievals from late northern summer of MY 28 are generally

omitted from this analysis. Between 9 February 2007 and 14 June 2007 (L_s=180°—257°

of MY 28), MCS operated in a mode known as "limb staring" in which the limb was

observed at a constant angle relative to the spacecraft. This degraded mode of operation

primarily affects the altitude range of the atmosphere observed by the instrument and the

calibration of the data. Therefore, retrievals from data collected from this period provide

less information about high altitudes in the southern hemisphere and low altitudes near

the north pole than retrievals from data collected when the instrument was scanning the

limb. In addition, retrievals from limb staring data have greater uncertainties in areas of

the atmosphere where radiances are low due to the poor calibration of the instrument in

limb staring mode. Agreement between retrievals from limb staring and limb

scanning retrievals (in which the limb is observed at varying angles) are good [*Kleinböhl*

et al., 2009], but the limited vertical range of limb staring retrievals (and hemispheric

differences in the vertical range) makes reconstruction of the dust distribution more

difficult.

4.2.2 Zonal Averaging and Derived Quantities

To avoid biasing of zonal averages by heavier sampling at particular longitudes, the

retrievals are separated into "dayside" (9:00—21:00 LST) and "nightside" (21:00—9:00

LST) bins and further binned in 36 (5° resolution) mean latitudinal bins, 64 (5.625°

resolution) mean longitudinal bins, and L_s bins at 5° resolution: a resolution comparable

to Mars general circulation model grids. Mean latitude and longitude refer to the

coordinates at the tangent point observed by the center of the MCS detector array at ~40

km above the surface. Since MCS retrievals have relatively broad horizontal weighting

functions biased in the direction of the detector array, this latitude and longitude is

usually a better indicator of the location of even dust retrieved near the surface than the

latitude and longitude at which the limb intersects the surface.

Caution must be exercised when averaging aerosol opacity retrievals. Aerosol

opacity is not reported at all in some retrievals for a variety of reasons, such as that there

is a high likelihood of misattribution of opacity to one aerosol vs. another, as happens

with carbon dioxide ice and dust at the winter pole. See *Kleinböhl et al.* [2009] for further

discussion. Retrievals without any reported aerosol opacity are not included in the

averages reported here. In all other cases, aerosol opacity is reported at some continuous

subset of pressure levels, for example, each pressure level in a range from 200 to 20

Pa. At pressures higher than 200 Pa, there is not enough information to retrieve aerosol

opacity accurately. At pressures lower than 20 Pa, the radiance contributed by the aerosol

opacity is comparable to the noise of the radiance measurements. In the averaging

process, the unreported aerosol opacity at high pressures is not included, that is, the

average of the retrieved aerosol opacity at 200 Pa is the average of all aerosol opacities

reported at 200 Pa. But since the unreported opacity on the lower pressure end is

unreported because it is so low, the retrieval is altered so that these unreported values

have a value of 0 instead. This averaging routine minimizes the effects of a small number

of retrievals with measurable aerosol opacity at high altitudes.

The variability in the longitudinal sampling of the zonal averages is depicted in

Figures 4.1a and 4.1b. Longitudinal sampling is controlled by a variety of factors, some

of which are intrinsic to the data as collected by the instrument, e.g., periods in which

data was not collected because the instrument was stowed, and some of which are related

to the limitations of the retrieval algorithm, e.g., the exclusion of retrievals with a bad

pressure retrieval due to high LOS optical depth in the channels used for pressure

retrieval. The absolute breaks in coverage in an L_s bin are indicated in white. The break at

$L_s=210°$ during MY 28 is a period during which the instrument was stowed.

Figures 4.1a and 4.1b suggest longitudinal sampling by dayside profiles is much

poorer than from nightside profiles. In fact, dayside coverage over the equator is

practically non-existent. This discrepancy is not well understood but may be due to

incorrect representation in the retrieval algorithm of the scattering by tropical water ice

clouds of upwelling radiation from the surface.
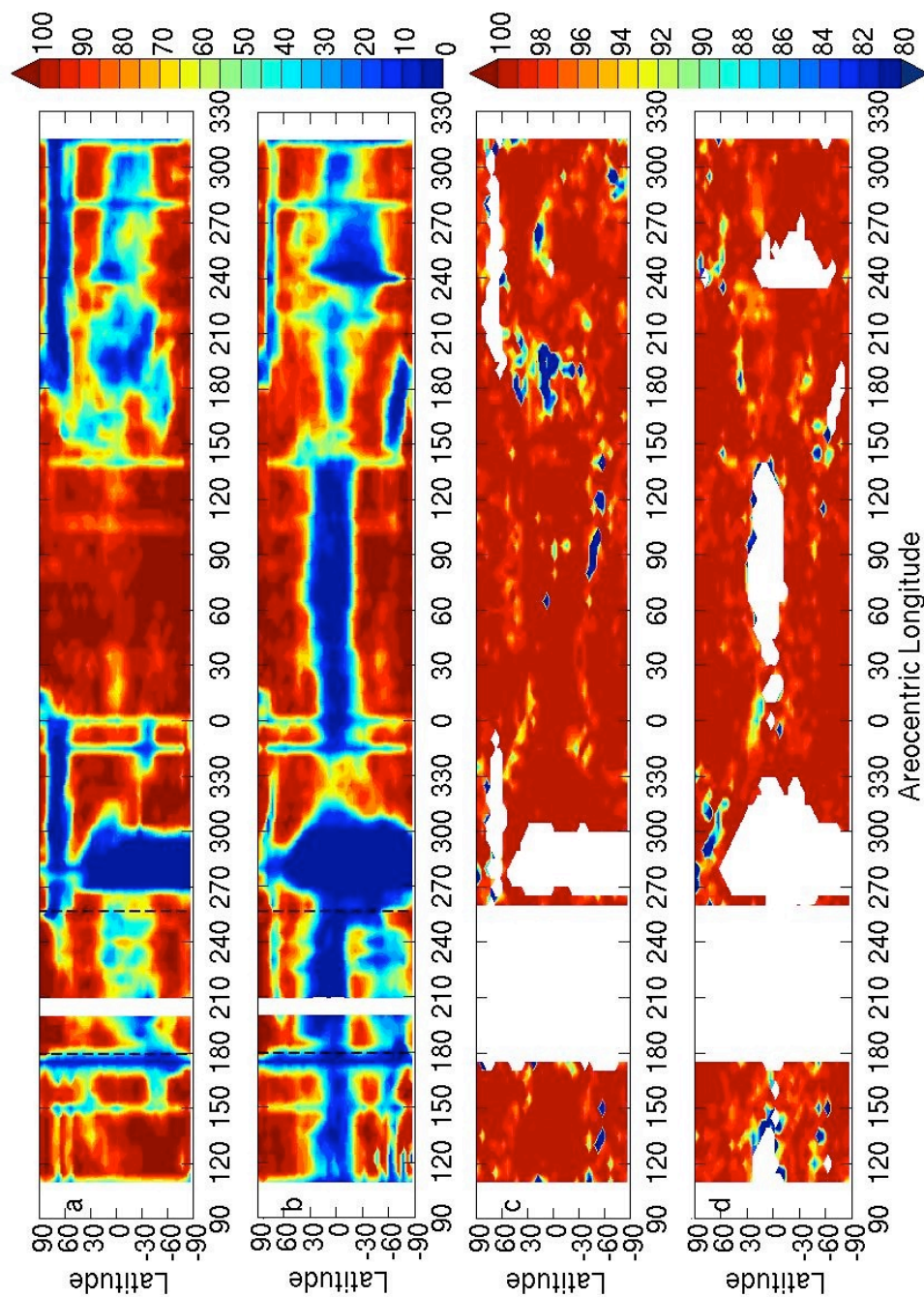
Figure 4.1. (a) Percentage of longitudes in the binning scheme described in Chapter 4.2.2 sampled by nightside retrievals vs. latitude and L_s; (b) percentage of longitudes in the binning scheme described in Chapter 4.2.2 sampled by dayside retrievals as a function of latitude and L_s; (c) $100*R^2$ for the empirical fitting scheme described in Chapter 4.3.2 for nightside retrievals as a function of latitude and L_s; (d) $100*R^2$ for the empirical fitting scheme described in Chapter 4.3.2 for dayside retrievals as a function of latitude and L_s.

120

4.2.3 A5 Channel Opacity and the Utility of Density

Scaled Opacity

For a variety of scientific and engineering applications (including some discussed in this Chapter), opacity in the A5 channel is not a particularly convenient or intuitive quantity to use. However, it is the retrieved quantity related to dust that most immediately follows from MCS observations of radiance. The conversion factor between A5 channel opacity and visible opacity at 600—700 nm is ~7.3. This factor differs from what is reported in *Kleinböhl et al.* [2009], because it accounts for the higher visible/infrared opacity ratio of the smaller dust particles assumed in the new retrieval algorithm [*Clancy et al.*, 2003].

Given some model of the size, shape, and composition of the dust particles, opacity can be converted to three other quantities: volumetric number density, N_v; mass number density, N_m; and mass mixing ratio, q. For consistency's sake, I make the same assumption as used in the retrieval algorithm: that the dust is compositionally uniform and made of spherically symmetric particles with a modified gamma size distribution of the form:

$$n(r) \propto r^a \exp(-br^c) \tag{4.1}$$

The parameters used for the dust distribution in the version of the retrieval dataset used here are not the same as in *Kleinböhl et al.* [2009] but have been tuned to minimize misfitting error in the retrieval algorithm.

Following *Taylor et al.* [2007], the opacity as a function of the volumetric number density is:

$$d_z\tau = \int_0^\infty Q_{ext}\pi r^2 N_v n(r)dr \tag{4.2}$$

The variables, π, N_v and Q_{ext} can be extracted from the integral, since the latter is only a function of the dust distribution, not of radius, such that:

$$N_v = \frac{d_z\tau}{Q_{ext}\pi \int\limits_0^\infty r^2 n(r)dr} \tag{4.3}$$

The value of Q_{ext} used by the retrieval algorithm is 0.35. $\pi \int\limits_0^\infty r^2 n(r)dr$ in Eq. 4.3 is the average geometric cross-section of the distribution, G. So Eq. 4.3 becomes:

$$N_v = \frac{d_z\tau}{Q_{ext}G} \tag{4.4}$$

where G is assumed to be 1.26 $(\mu m)^2$ in the retrieval algorithm. So N_v $(m^{-3})=2.3\times10^9$ $d_z\tau$ (km^{-1}). The mass number density, N_m, then can be obtained by dividing N_v by the atmospheric density, ρ.

The mass mixing ratio is obtained similarly. Scaling Eq. 4.3 by ρ, we obtain the density-scaled opacity:

$$\frac{d_z\tau}{\rho} = \frac{N_v Q_{ext}\pi}{\rho}\int\limits_0^\infty r^2 n(r)dr \tag{4.5}$$

We can form an expression for the mass mixing ratio by calculating the ratio between the mass of dust particles in a given volume and the mass of air in the same volume:

$$q = \frac{\rho_D N_v \int\limits_0^\infty \frac{4}{3}\pi r^3 n(r)dr}{\rho} \tag{4.6}$$

Eqs. 4.5 and 4.6 can be combined so that:

$$q = \frac{4}{3} \frac{\rho_D}{Q_{ext}} \frac{d_z\tau}{\rho} \frac{\int_0^\infty r^3 n(r) dr}{\int_0^\infty r^2 n(r) dr} \qquad (4.7)$$

The integral ratio above is equal to "the effective radius," r_{eff}, which is 1.06 μm for the distribution used by the retrieval algorithm. So:

$$q = \frac{4}{3} \frac{\rho_D}{Q_{ext}} \frac{d_z\tau}{\rho} r_{eff} \qquad (4.8)$$

Assuming ρ_D=3000 kg m^{-3}, q (ppm) =1.2×10^4 $d_z\tau/\rho$ (m^2 kg^{-1}).

Since these derivations are model dependent, we only will report $d_z\tau$ and $d_z\tau/\rho$, which can be derived from the retrievals directly. For dust with definite, spatially and temporally invariant distributions of size, shape, and composition, the number density is linearly proportional to $d_z\tau$, and the mass mixing ratio is linearly proportional to $d_z\tau/\rho$.

If Eq. 4.8 is re-arranged, $d_z\tau/\rho$ is proportional to the product of Q_{ext}/r_{eff} and q. The parameter Q_{ext} is dependent on the size distribution, so that if there is significant particle size segregation in the atmosphere, variability with size in Q_{ext}/r_{eff} could result in inferring an apparent enhancement of mass mixing ratio above the surface when no enhancement is actually present. For example, if small dust particles lie over large ones and Q_{ext}/r_{eff} is significantly larger for small particles, a given mass mixing ratio of small particles will have greater opacity than the same mass mixing ratio of large particles. Table 4.1 shows the results of Mie scattering simulations of Q_{ext} for dust size distributions with different r_{eff} but the same variance as the size distribution used in the retrievals. The variability in the ratio over a reasonable size range for dust is no more

Table 4.1. Results of Mie scattering simulations to test the sensitivity of Q_{ext}/r_{eff} in the MCS A5 channel to particle size

r_{eff} (μm)	Q_{ext}/r_{eff} (μm^{-1})	Q_{ext}/r_{eff} normalized by the value at 1.06 μm
0.75001	0.3095	0.970
1.06070	0.3305	1
1.50000	0.3619	1.10
2.12160	0.3956	1.20
2.99930	0.4137	1.25
4.2432	0.3998	1.21
5.99960	0.3524	1.07

than 30%. In addition, the segregation of sub-micron particles over greater than micron-sized particles will produce an apparent depletion of mass mixing ratio in a truly uniformly mixed profile. This analysis, however, does not consider the effect on the retrieval procedure of assuming different particle size distributions.

The rough interchangeability of mass mixing ratio and density scaled opacity is useful for understanding the radiative and dynamical significance of particular vertical profiles of dust. In an optically thin atmosphere (even for non-uniform dust), the quantity $d_z\tau/\rho$ also is proportional to the unit heating rate per unit mass due to dust at fixed wavelength, J. Thus, the dust mass mixing ratio (outside of dust storm conditions) is a good proxy for the diabatic heating rate and vice versa.

4.3 A New Scheme for Representing Martian Vertical Dust Distributions

4.3.1 Motivation

Conrath [1975] created an idealized profile for representing vertical dust distributions in the martian atmosphere by considering the competing effects of sedimentation and mixing during a decaying global dust storm and modeling the mass mixing ratio of dust in the atmosphere as:

$$q = q_0 \exp\left[\nu(1 - \sigma^{-1})\right] \tag{4.9}$$

where q_0 is the mass mixing ratio at the surface, ν is the ratio between the characteristic dust diffusion time and the characteristic dust sedimentation time at the surface (the Conrath parameter), and σ is exp(-z/H), where z is the height and H is the atmospheric

scale height. In the isothermal approximation of the atmospheric pressure and density profiles generally used by *Conrath* [1975] and in a coordinates system with a small pressure at the top of the domain (p_{top}), this definition of σ is approximately equal to the definition of σ used in GCMs for the coordinates of the vertical computational grid:

$$\sigma = \frac{p - p_{top}}{p_s - p_{top}} \tag{4.10}$$

When used in a GCM, e.g., *Forget et al.* [1999], a pseudo-σ, $\tilde{\sigma}=p/p_0$, is often substituted for σ in Eq. 4.9, where p_0 is a reference pressure, e.g., 700 Pa in *Forget et al.* [1999], below which q is taken to be q_0.

Forget et al. [1999] modified this scheme of *Conrath* [1975] using analyses of Mariner and Viking data by *Anderson and Leovy* [1978] and *Jaquin et al.* [1986] to account for the seasonal variability in the height of observable dust in the atmosphere:

$$q = q_0 \exp\left[\nu(1 - \tilde{\sigma}^{-l})\right] \tag{4.11}$$

where l is equal to the ratio between a reference height, Z_0 and the maximum height of observed dust, z_{max}, which is treated as a function of latitude and areocentric longitude (L_s).

The column opacity, τ, is the integral of Eqs. 4.9 or 4.11 with height from the top of the atmosphere to the level of interest, provided they are multiplied by $\rho_0\sigma$ or $\tilde{\rho}_0\tilde{\sigma}$ to recover $d_z\tau$, and then multiplied by $dz=Hd\sigma/\sigma$ or $Hd\tilde{\sigma}/\tilde{\sigma}$ to permit integration on the σ coordinates to obtain optical depth. But as first described by *Conrath* [1975], the resulting optical depths involve exponential integrals, which are computationally expensive. Thus, the GCM described by *Forget et al.* [1999] actually computes optical depth as:

$$\tau = \tau_0 \tilde{\sigma} \exp\left[\nu\left(1 - \tilde{\sigma}^{-l}\right)\right] \qquad (4.12)$$

which is obtained using a similar procedure to the exact integration by assuming that the exponential function in Eq. 4.12 is a constant (a suitable approximation for $\nu=0.007 \ll 1$) and incorporating H, ρ_0, and q_0 into a reference optical depth, τ_0.

The vertical dust distribution reconstructed from MCS dust profiles suggest there is a need for an alternative scheme to those of *Conrath* [1975] and *Forget et al.* [1999] to quantify vertical variation in the mass mixing ratio of dust, Figure 4.2 shows a zonal average of nightside retrievals from $L_s=87.5°$ to $92.5°$ (hereafter called $L_s=90°$ for shorthand) of two quantities: (1) the density scaled opacity (filled color contours) calculated from the retrieved temperature, pressure, and dust opacity; (2) the numerically evaluated height derivative of Eq. 4.12, i.e., the dust opacity (red contours), calculated from the observed pressure and temperature scaled as for (1). The values of τ_0 used to calculate (2) are those used in the Mars Year 24 scenario of the Mars Climate Database [*Lewis et al.*, 1999; *Montmessin et al.*, 2004] scaled by a factor of 3.6 to account for the assumed visible/infrared MCS dust opacity ratio and the visible/9 μm opacity ratio used in *Forget et al.* [1999]. The key feature of this figure is the contrast between the nearly constant density-scaled opacity bubble between 60—400 Pa produced by the modified Conrath scheme of *Forget et al.* [1999] and the greater and more vertically narrow maximum in density-scaled opacity at ~60 Pa observed in the MCS retrievals near the equator and both poles. (The slight enhancement in the Mars Year 24 scenario distribution at ~60 Pa is an artifact of a spurious thermal inversion often retrieved in the tropical lower atmosphere in this season and represents an 8% enhancement above the near-surface dust density scaled opacity.) Note that the mean density scaled opacity at the
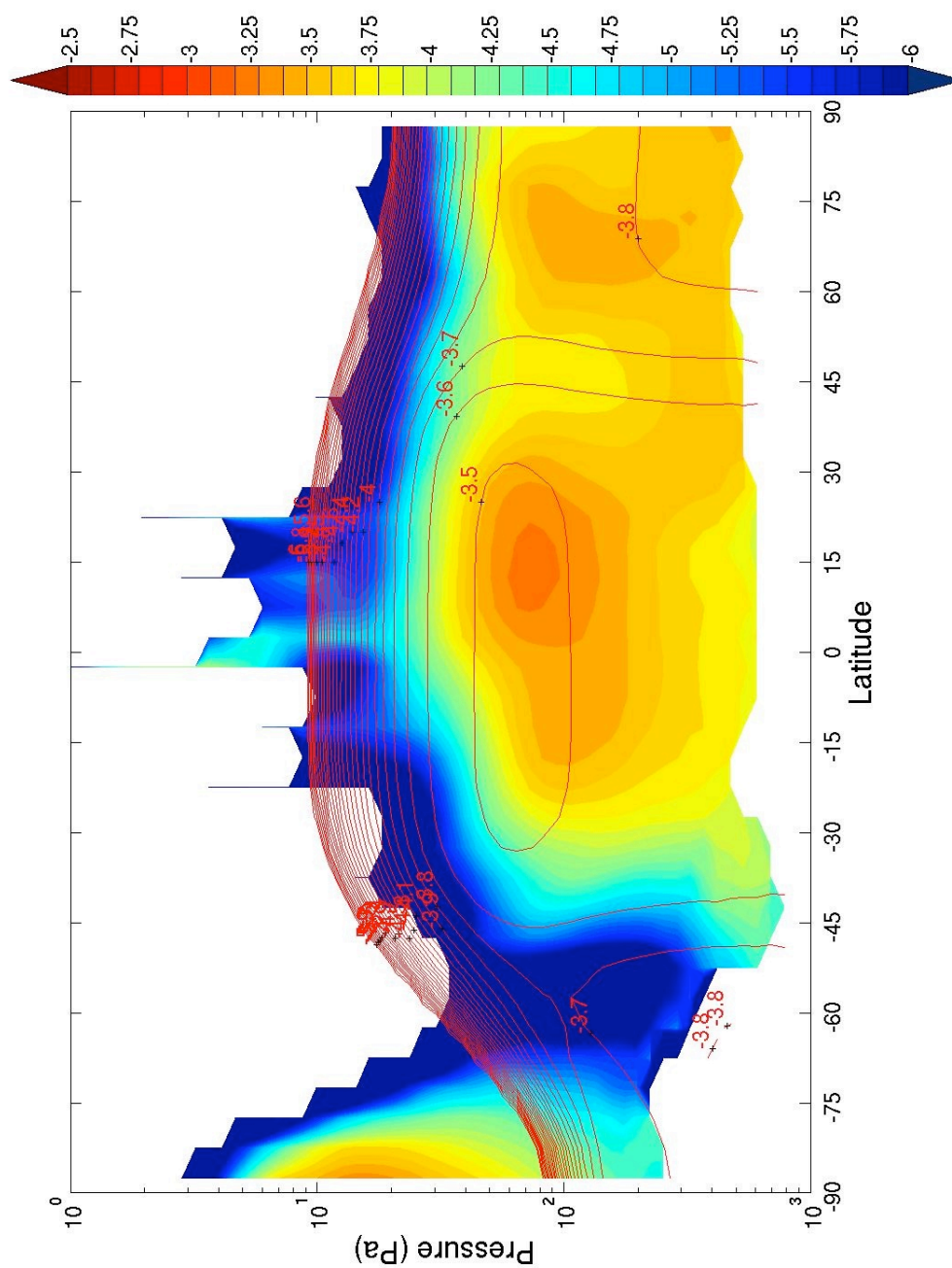
Figure 4.2. Log$_{10}$ of zonal average dust density scaled opacity (m^2 kg^{-1}) interpolated onto pressure coordinates for nightside retrievals, L$_s$=90°, MY 28: (colors) from MCS retrievals; (labeled red contours) based on the Mars Year 24 MGS dust scenario in the Mars Climate Database with MCS retrieval pressure and temperature information. Contours are every 0.1 log units. White space below the colors indicates no data. White space above the colors and the darkest blue indicates density scaled opacity below 10^{-6} m^2 kg^{-1}.
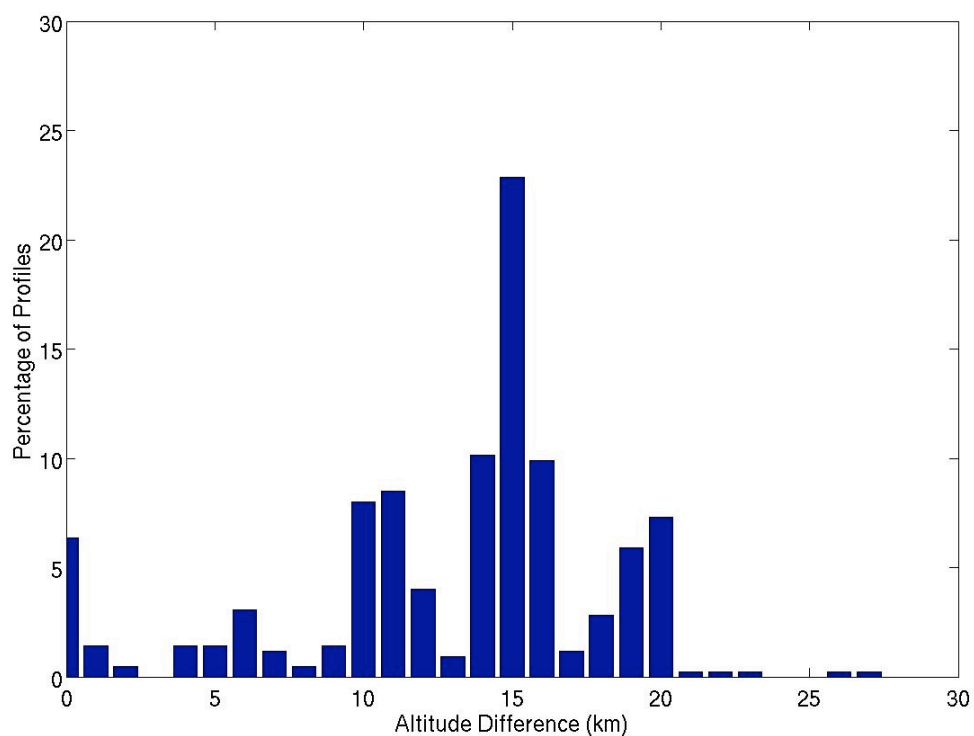
Figure 4.3. Histogram of the difference between the lowest altitude (relative to the Mars Orbiter Laser Altimeter areoid) at which dust opacity was reported and the altitude at which the highest dust density scaled opacity was calculated in each individual retrieval (424 total) from 20° to 25° N, L_s=90° of MY 29, nightside.

highest pressure levels with reported opacity is a factor of four smaller than the

density scaled opacity maximum. A region of dust-clear air near 60° S is also apparent.

The appearance of the "high altitude tropical dust maximum" in the zonal average

of dust density scaled opacity is indicative of the large number of individual retrieved

profiles with maxima in dust density scaled opacity well above the lower end of the

retrieved profile. Figure 4.3 shows the distribution of the difference in altitude (calculated

from the pointing of the instrument) between the lowest level of the profile at which dust

is reported and the level at which the maximum dust density scaled opacity occurs for all

individual retrievals from 20°to 25° N, MY 29 on the nightside (within the high altitude

tropical dust maximum in Figure 4.2). Around 90% of retrieved profiles have a maximum

in dust density scaled opacity at least 5 km above the lower end of the retrieved profile.

The typical difference is ~15 km. Thus, the high altitude tropical maximum is a

maximum in dust density scaled opacity normally within the vertical range of individual

MCS retrieved profiles.

A Conrath profile will not fit the high altitude tropical dust maximum or a similar

feature. Let us consider one of the zonally averaged density scaled opacity profiles

depicted in Figure 4.2 (Figure 4.4a) and re-write Eq. 4.9 to obtain a σ-varying Conrath

parameter:

$$\nu(\sigma) = \frac{\ln\dfrac{q}{q_0}}{1 - \sigma^{-1}} \tag{4.13}$$

Figure 4.4b shows the result of inverting the profile in Figure 4.4a with Eq. 4.13

by assuming a value of q_0 extrapolated from the highest σ level with density scaled

opacity information, that is, the value of q nearest the surface and thus the one that might
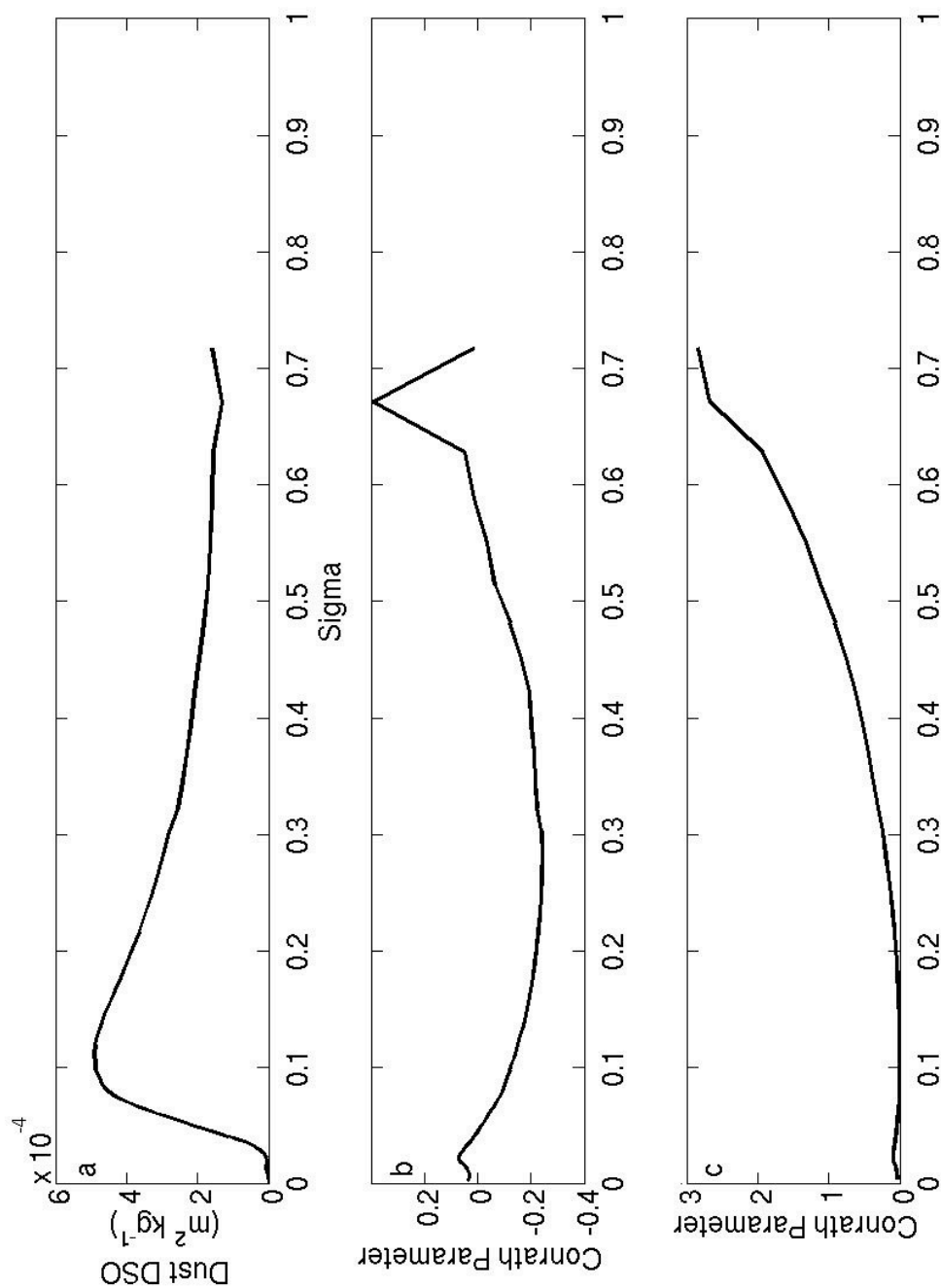
Figure 4.4. (a) Zonal average of the density scaled opacity (m^2 kg^{-1}) interpolated onto σ coordinates for nightside retrievals, L_s=90, MY 28, 10º—15º N; (b) inferred Conrath parameter, ν(σ) for the profile in (a), assuming q_0=1.61×10^{-4} m^2 kg^{-1}; (c) inferred Conrath parameter, ν(σ) for the profile in (a), assuming q_0=4.92×10^{-4} m^2 kg^{-1}.

be characteristic of q in a relict well-mixed convective boundary layer. This inversion results in negative values of the Conrath parameter over a broad range of σ. Most fundamentally, the Conrath parameter is the ratio between the rates of sedimentation and vertical atmospheric diffusion. The model of *Conrath* [1975] accounts for the decrease of the rate of sedimentation with height due to lower atmospheric density, so variability in the Conrath parameter with respect to a vertical coordinate should be interpreted as variability in the vertical atmospheric diffusivity with that vertical coordinate. Therefore, the negative Conrath parameter region in Figure 4.4b is presumably one with negative vertical atmospheric diffusivity, where dust diffuses (in a purely mathematical sense) from regions of lower concentration to those of higher concentration.

Figure 4.4c shows the result of inverting the profile in Figure 4.4a with Eq. 4.13 by assuming a value of q_0 equivalent to the density scaled opacity maximum in the profile. In this case, the Conrath parameter increases toward higher σ (or lower altitude), which could be interpreted to mean that vertical diffusion weakens closer to the surface of Mars, precisely the region of the atmosphere in which vertical diffusion should be most vigorous due to turbulent interactions between the atmosphere and the surface. Thus, the presence of a maximum in mass mixing ratio except at the surface is inconsistent with the assumptions underlying the Conrath profile and motivates an alternative representation scheme for the vertical variation of dust mass mixing ratio in Mars's atmosphere.

4.3.2 Design of the Scheme

This new scheme models opacity retrievals from Mars Climate Sounder as a function of σ in order to represent two principal features observed by inspection of the zonal average density scaled opacity profiles: (1) the decay in density scaled opacity with height and (2) the high altitude maxima in dust density scaled opacity observed significantly above the surface of the tropics and sometimes near the poles. The scheme is empirical and not based on any particular physical model of vertical dust transport. The choice of σ as a vertical coordinate allows easier use of the scheme in GCMs, is quickly adaptable to pressure-gridded MCS retrieved profiles (which also have a retrieved surface pressure), and also was based on the hypothesis that since the ultimate source of dust is the surface, the vertical distribution of dust should be a function of height above the surface. For simplicity, I, like *Conrath* [1975], make use of the isothermal approximation of the variation of the atmospheric density with height.

Opacity was assumed *a priori* to be of the form

$$d_z\tau(\sigma) = d_z\tau_1\sigma f(\sigma) \tag{4.14}$$

where $d_z\tau_1$ is a kind of extrapolated surface opacity, not the opacity in the lowest truly retrieved layer. Eq. 4.14 permits the shape of the density scaled opacity profile (the approximate mass mixing ratio) to be modeled as $f(\sigma)$ and also permits fairly direct integration of $f(\sigma)$ to obtain optical depth under a simplification described below.

To derive a suitable form of $f(\sigma)$, zonally averaged profiles of opacity in 5° L_s bins at from nightside and dayside profiles were interpolated onto a logarithmic σ-grid (105 evenly spaced points from 10^{-3} to 1) and then scaled by σ. The shapes of these
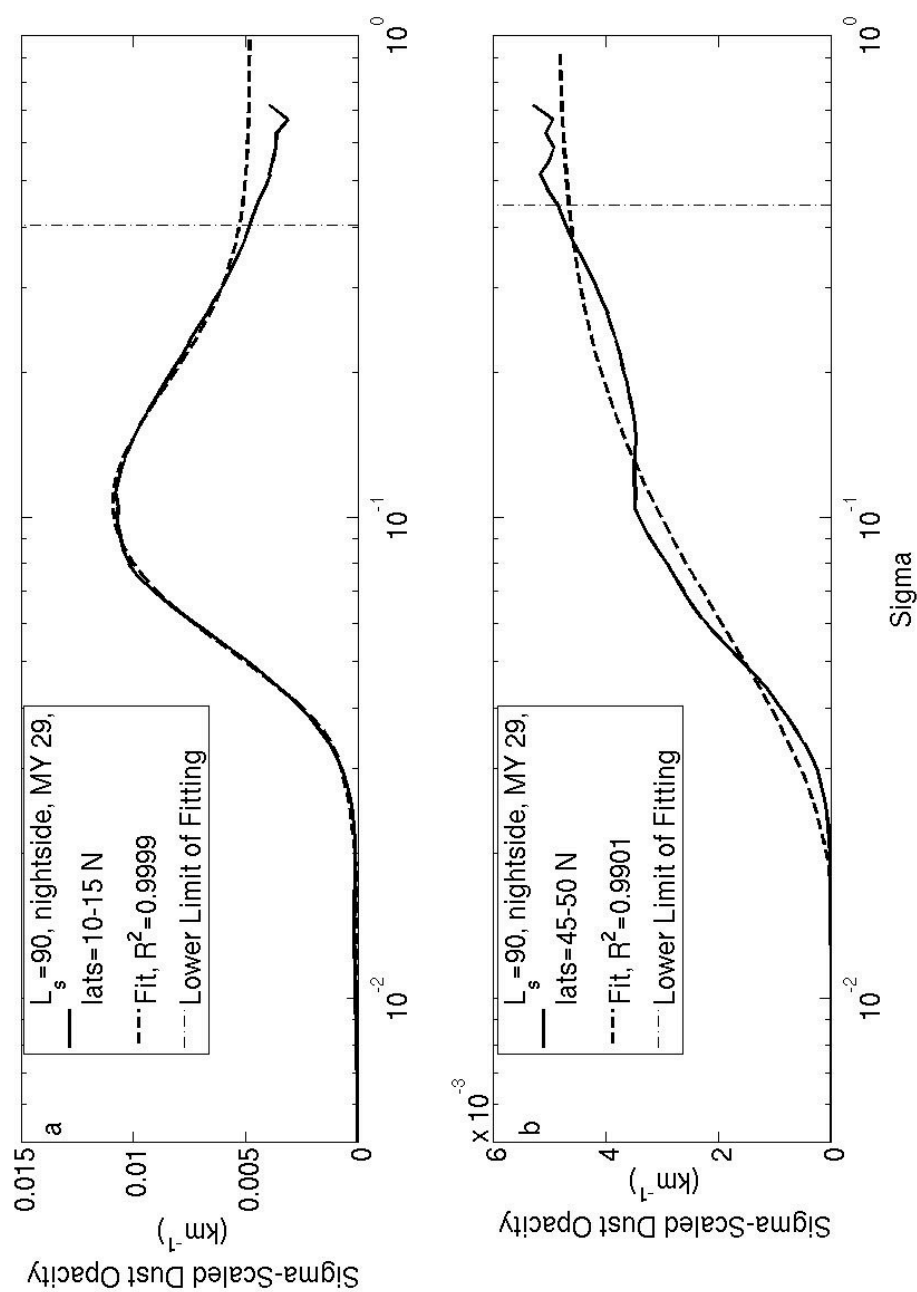
Figure 4.5. Demonstration examples for the fitting scheme which show the zonal average of opacity interpolated onto σ coordinates and scaled by σ (solid line) and the resultant fits (dashed line). (a) Tropical profile used in Figure 4.4 that has a global maximum "pulse" ($d_z\tau_1$=4.8×10⁻³ km⁻¹, B=1.2855, σ_0=0.0312, σ_1=0.1030, m_0=0.6343, m_1=0.8452); (b) northern mid-latitude profile with a weak local maximum that the implemented scheme does not consider significant enough to fit ($d_z\tau_1$=4.9×10⁻³ km⁻¹, σ_0=0.016, m_0=1.8803). The dot-dashed lines show the lower limits of where the zonal average profiles are fit.

scaled profiles fall into two qualitative categories: "perturbed" (Figure 4.5a) and

"unperturbed" (Figure 4.5b) profiles (solid lines). Unperturbed profiles have an

approximately monotonic fall off from a roughly uniform profile at a value assumed to be

approximately equal to $d_z \tau_1$ (probably indicative of a relict or true well-mixed

convective boundary layer) to near zero scaled opacity at the top of the grid. Perturbed

profiles have a significant global (or sometimes local) maximum in scaled opacity at

some $\sigma < 1$. Even the example "unperturbed" profile in Figure 4.5b appears to be slightly

perturbed at $\sigma = 0.1$. Inspection suggested that a good f(σ) for unperturbed profiles was:

$$f(\sigma) = \Xi(\sigma - \sigma_0)\left\{1 - \exp\left[\frac{-(\sigma - \sigma_0)^2}{m^2}\right]\right\} \qquad (4.15)$$

where Ξ is the Heaviside function (the notation prevents confusion with the scale height,

H) and σ_0 is a parameter that effectively sets the top of significant dust in the profile

whereas *m* is a measure of the rapidity of its decay.

Eq. 4.15 produces a poor fit (not shown) to the solid curve in Figure 4.5a due to

the perturbation in the scaled opacity centered at $\sigma \approx 0.08$. This perturbation can be fit by

an additional Gaussian unmultiplied by the Heaviside function, yielding:

$$f(\sigma) = \Xi(\sigma - \sigma_0)\left\{1 - \exp\left[\frac{-(\sigma - \sigma_0)^2}{m_0^2}\right]\right\} + B\exp\left[\frac{-(\sigma - \sigma_1)^2}{m_1^2}\right] \qquad (4.16)$$

where *B* is the amplitude of the perturbation, m_1 is a parameter that governs its width, and

m_0 is the same as *m* in Eq. 4.16.

Some zonal average profiles and some individual retrieved dust profiles have

multiple perturbations. In that case, fitting with multiple Gaussians could be appropriate.

Ideally, there would be some discrete boundary between unperturbed and perturbed

profiles (and thus for an unperturbed profile, fitting using Eq. 4.16 would result in

B=0), but, of course, this situation rarely occurs in practice due to the contributions to

zonal averages from mixtures of unperturbed and perturbed profiles with perturbations at

multiple levels. In addition, overinterpolation and overfitting of the profiles often allows

Gaussians to be fit to minor perturbations that may not be statistically significant. An ad

hoc solution to this problem will be discussed in Chapter 4.3.3.

If we substitute Eq. 4.16 into Eq. 4.14 and integrate in the same way as the

Conrath schemes, we can obtain an optical depth function:

$$\tau(\sigma) = Hd_z\tau_1\left\{\Xi(\sigma-\sigma_0)\left[\sigma - \frac{m_0}{2}\sqrt{\pi}\,\text{erf}\left(\frac{\sigma_0-\sigma}{m_0}\right)\right] + \frac{Bm_1\sqrt{\pi}}{2}\left[\text{erf}\left(\frac{\sigma_1}{m_1}\right) - \text{erf}\left(\frac{\sigma_1-\sigma}{m_1}\right)\right]\right\} \quad (4.17)$$

where erf signifies the error function. While this form is not necessarily practical for

GCM use, it is useful for reconciling total optical depths from nadir observations with

idealized or true vertical profile information more easily obtained from off-nadir

measurements.

Eq. 4.16, however, is inappropriate for fitting MCS data. Consider the logarithmic

σ scale used to plot the profiles in Figures 4.5a-b. On this scale, the perturbation appears

to be a standard symmetric Gaussian. On a linear σ scale, however, the peak is skewed

toward higher values of σ. The result is that the fitting routine tries to fit the peak by

effectively introducing opacity at very high altitudes, which will introduce a radiative-

dynamically important artifact if used in future to develop a prescribed dust scheme. The

problem is actually quite intuitive. The vertical weighting functions of MCS retrievals

should be roughly symmetric in height (and thus in ln σ), so features in them should be

symmetric and best fit by symmetric functions in the same types of coordinates system. Thus, we revise Eq. 4.16:

$$f(\sigma) = \Xi(\ln\sigma - \ln\sigma_0)\left\{1 - \exp\left[\frac{-(\ln\sigma - \ln\sigma_0)^2}{m_0^2}\right]\right\} + B\exp\left[\frac{-(\ln\sigma - \ln\sigma_1)^2}{m_1^2}\right] \qquad (4.18)$$

where the fit is of parameters $\ln(\sigma_0)$ etc., not of σ_0 directly, and m_0 and m_1 are setting Gaussian widths in a different coordinates system than in Eq. 4.16.

Eq. 4.18, however, is not as readily analytically integrable as Eq. 4.16. One very approximate approach would be to fit a profile with Eq. 4.18 and to use Eq. 4.16 in applications (such as prescribed dust schemes) by converting $\ln\sigma_0$ to σ_0. However, m_0 and m_1 cannot be transformed between coordinate systems in the same way. The conversion factor can be derived by denoting m-parameters in Eq. 4.16 by hats and equating one of the analogous Gaussians in Eqs. 4.16 and 4.18 as follows:

$$\exp\left[\frac{-(\ln\sigma - \ln\sigma_0)^2}{m_0^2}\right] = \exp\left[\frac{-(\sigma - \sigma_0)^2}{\hat{m}_0^2}\right] \qquad (4.19)$$

This reduces to:

$$m_0\frac{\sigma - \sigma_0}{\ln\sigma - \ln\sigma_0} = \hat{m}_0 \qquad (4.20)$$

which implies that the transformation is itself a function of σ. But we will not require that the scaling be exact everywhere and will decide to seek the scaling where it is most important, that is, at $\sigma=\sigma_0$. We then convert Eq. 4.20 to a limit:

$$m_0\left(\lim_{\sigma \to \sigma_0}\frac{\sigma - \sigma_0}{\ln\sigma - \ln\sigma_0}\right) = \hat{m}_0 \qquad (4.21)$$

The limit can be evaluated using L'Hôpital's rule such that:

$$m_0 \sigma_0 = \hat{m} \qquad (4.22)$$

providing the desired transformation between *m*-parameters in the different coordinates

systems.

4.3.3 Fitting Profiles Using the Scheme

In some cases, Eq. 4.18 may overfit the data. The nominal resolution of the MCS limb

retrievals is somewhat greater than the resolution of measurements with which they were

made. The procedure that uses Eq. 4.18 begins with an individual opacity retrieval,

which: (1) is interpolated onto a logarithmically spaced σ grid (an operation that results

in additional oversampling of the data); (2) is averaged with similarly interpolated

retrievals in the same latitude-longitude bin on a 5° (latitude) by 5.625° (longitude) bin;

(3) is zonally averaged with all bins with data; (4) is scaled by the logarithmically-spaced

σ grid; (5) which is finally fit on the logarithmically-spaced σ grid. The averaging

process (as in the profile in Figure 4.4a) can introduce a variety of small noisy features

that could be fit with individual Gaussians nearly *ad infinitum*.

This potential oversampling/overfitting catastrophe may be avoided in two ways.

First, interpretations that are dependent on differences much smaller than the "detector

width" of ~5 km should be rejected. Thus, using the fact that the scale height, *H*, of the

martian atmosphere is ~10 km and the difference between two σ levels, σ_x and σ_y, in

height is $\sim H \ln(\sigma_x/\sigma_y)$, differences much less than ~65% between a σ-level parameter are

probably not statistically significant. Second, the major overfitting risk in the scheme is

to use Eq. 4.18 and so fit some statistically insignificant feature in the scaled opacity

profile, when Eq. 4.15 (if transformed to ln σ coordinates) is more suitable. Fitting the

zonal average profiles just with Eq. 4.18 produced likely fitting artifacts such as small

B with $m{\approx}100$. We were able to reduce the occurrence of these artifacts by fitting a

profile separately with Eq. 4.18 and the logarithmic version of Eq. 4.15 and then

performed an F-ratio test using the residual sum of squares from each fit ($RSS_{15,18}$),

where F is defined as:

$$F = \frac{\dfrac{RSS_{15} - RSS_{18}}{RSS_{15}}}{\dfrac{p_{18} - p_{15}}{n - p_{18}}} \tag{4.23}$$

and where p_{15} and p_{18} are the number of free parameters in Eqs. 4.15 and 4.18, $p_{18}{=}5$ and

$p_{15}{=}2$ respectively, and n is the number of degrees of freedom in the data. Ideally, this

ratio tests the null hypothesis that Eq. 4.15 is a better fit to the data than Eq. 4.18 by

comparison with an F distribution with parameters $p_{18}{-}p_{15}$ and $n{-}p_{18}$. Practically, such a

test can be implemented by assuming that RSS will scale linearly with increasing n_{fit}, so

that an F-ratio test is possible for these overinterpolated profiles using an estimate of the

intrinsic n of the data. Ignoring the averaging and interpolation, n should be

approximately equal to 5 for an individual dust opacity retrieval, since ~5 detectors in the

A5 channel of MCS are used to retrieve dust. However, A5 radiances are dependent on

the temperature profile as well, so the ~8 detectors in channels A1, A2, and A3 observe

the same part of the limb as the A5 detectors to retrieve temperature, thereby providing

some implicit constraint on dust. For the fits presented in this Chapter, n is conservatively

assumed to be 10. The critical value of the F-ratio for the 95% confidence interval for

$n{=}10$ is 5.4095, which was used to determine whether a profile should use Eq. 4.15 or

Eq. 4.18. The use of this test explains why the small local maximum in Figure 4.5b is not fit.

The diagnosis of $d_z\tau_l$ presented an additional problem. In Figure 4.5a, it appears that the σ-scaled opacity decreases toward the surface at the lower altitude end of the data. In other zonal average profiles, the opposite trend is seen. If a zonally and vertically averaged H is derived from the available temperature data between 100 and 1000 Pa (or the lowest available pressure level failing any data at pressures greater than 100 Pa), many of these features appear to occur at heights of significantly less than 8 km above the surface. Thus, these features may originate from uncertainties in the extrapolated surface pressure or instances with extremely low LOS opacity near the surface. Thus, we diagnose $d_z\tau_l$ by determining the σ-scaled opacity that would correspond to the σ level corresponding to 8 km above the surface, or failing that, at a σ level 35% less than that. If there is no data at even this σ level, the fitting scheme is not used. These flexible criteria allow the fitting scheme to be used in almost all areas with available retrievals in northern spring and summer, particularly in late northern summer near the north pole, where low level water ice clouds normally limit the vertical range of retrievals to 12-13 km. Outside of this region, $d_z\tau_l$ is almost always a diagnosis of the 8 km σ-scaled opacity. Due to this method of diagnosis, the perturbation features either can be accentuated or diminished relative to the lower region of assumed uniform mixing. In addition, the fitting is only done on the domain between the σ level of diagnosis and the top of the domain at $\sigma=10^{-3}$.

The fitting scheme was implemented using standard Matlab non-linear fitting algorithms. These algorithms seek to minimize the unfit variance of the fit. If these algorithms are used without guessing initial parameters, the fitting routine often either

finds a local minimum in unfit variance that is a qualitatively and quantitatively poor

fit or fails to converge on a solution entirely. To minimize these problems, the fitting

scheme guessed initial parameters by mimicking the strategy I would have used to fit the

curve by trial and error. For example, σ_0 should mark where σ-scaled opacity is "cut off"

by the Heaviside function and is clearly ~0.02 in the example profile in Figure 4.5b, so an

initial guess of σ_0 is based on locating where the mass mixing ratio falls below a certain

ratio to the extrapolated mass mixing ratio at the surface. As another example, B and σ_1

are guessed from the amplitude and location of the highest amplitude local maximum in

σ-scaled opacity. We cannot prove definitely that the global minimum in unfit variance is

found in all cases, only that the fitting scheme in most cases produces solutions that agree

well with the solution obtained by trial and error in the hundreds of cases considered

during the process of designing the fitting scheme.

The fitting scheme was implemented on all zonal average bins with available

retrievals, both nightside and dayside. Figures 4.5a-b show example fits that represent the

profiles well but illustrate that R^2 is somewhat inflated, since a large part of the domain

fit in logarithmic σ space often has limited dust opacity. Only the results for bins in

northern spring and summer with available limb-scanning retrievals will be shown. The

R^2 for the fits is normally very good (>0.9) in northern spring and summer (Figures 4.1c

and 4.1d).

The exceptions are generally pathological. The poor fit indicated in Figure 4.1c at

around L_s=65° of MY 29, for instance, is due to the zonal average profile containing two

local maxima in dust density scaled opacity of similar magnitude that are widely
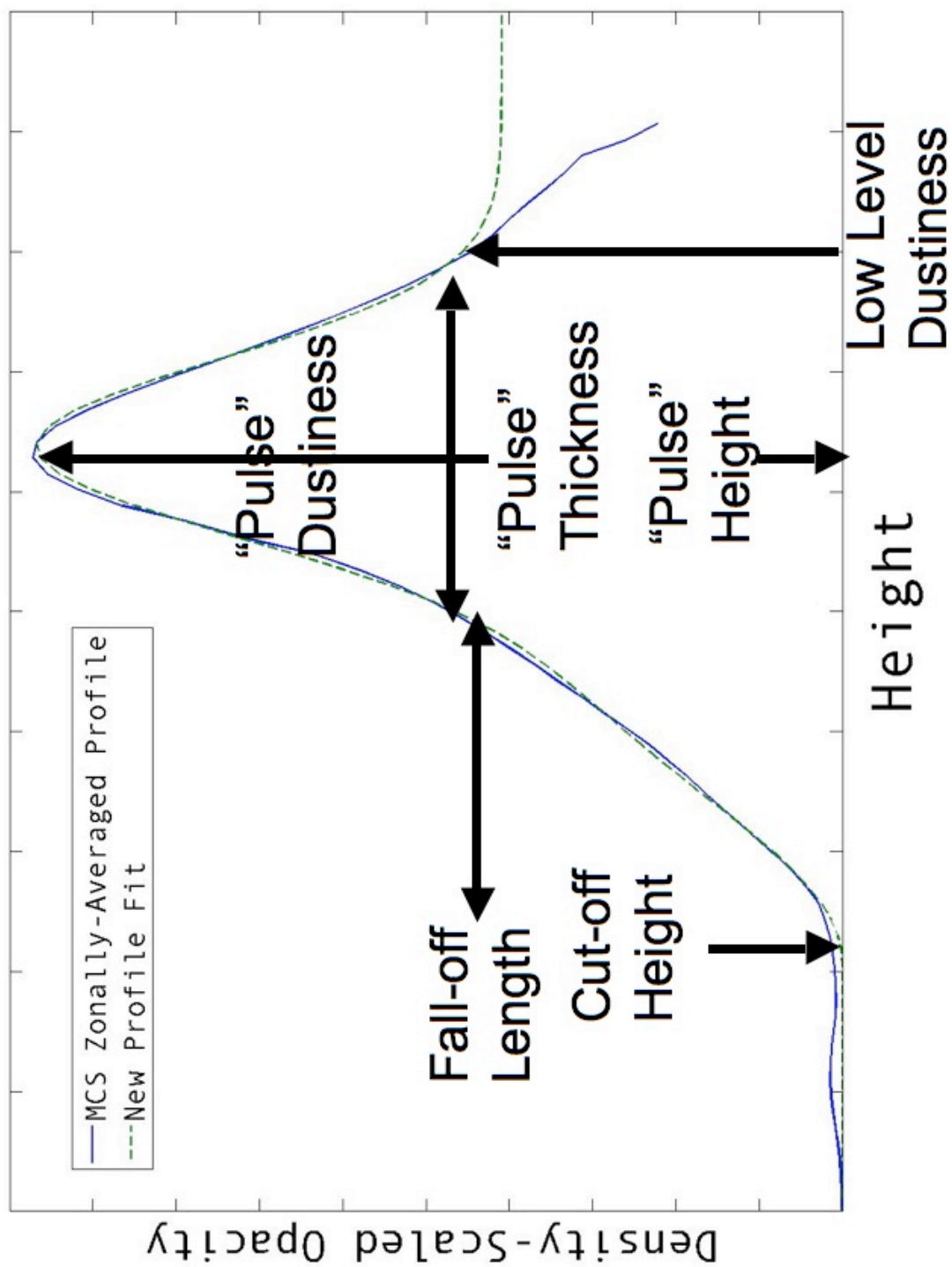
Figure 4.6. Schematic of how fitting scheme can be used to derive six parameters that can represent how the vertical distribution of dust changes within Mars's atmosphere.

separated in altitude. The local maximum at high altitude (~50 km) is a relatively rare feature of the zonal average profiles at this latitude and season.

4.3.4 Deriving More Intuitive Parameters from the Fitting Scheme

While the parameters of Eq. 4.18 are structured conveniently for curve fitting, the connection between their variability and variability in the distribution of mass mixing ratio with height is not always intuitive. For example, in the dust clear region, B is often very high, possibly because dust is not being lifted at the surface but intrudes from lower latitudes at relatively high altitude. While B is proportional to the magnitude of the maximum in dust mass mixing ratio sufficiently above ~8 km from the surface, we cannot use B to track the latitudinal and seasonal variability in this high altitude dust maxima seen in Figure 4.2 in the tropics and near the south pole. Yet the parameters in Eq. 4.18 may be combined with one another, H, and ρ_0 (the estimated atmospheric density at the surface) to derive six parameters whose seasonal and latitudinal variability does indicate important changes in the vertical distribution of dust. (The atmospheric density at the surface is estimated in each individual retrieval from p_s and a temperature derived from extrapolation of constant potential temperature from the highest pressure level at which temperature is reported to the surface). A schematic representation of these parameters is given in Figure 4.6.

First, a "low level dustiness" (LLD), the characteristic density scaled opacity/mass mixing ratio in the vertical range of MCS observations nearest to the

surface, can be defined, which may be in some cases be representative of the mass

mixing ratio of dust in the boundary layer [*Hinson et al.*, 2008]:

$$LLD = \frac{d_z \tau_1}{\rho_0} \qquad (4.24)$$

Second, Eq. 4.24 is weighted by *B* to obtain a characteristic density scaled opacity

corresponding to the dust mass mixing ratio in the principal local maximum or global

maximum in the profile, the "perturbation" or "pulse dustiness," PD:

$$PD = B\frac{d_z \tau_1}{\rho_0} \qquad (4.25)$$

Note that since the fall off from constant mass mixing ratio generally occurs

above this maximum, the true local or global maximum in mass mixing ratio usually is

proportional to LLD+PD.

Third, the altitudes above the surface at which the peak of the "pulse" occurs or

above which the dust mass mixing ratio cuts off to effectively zero, "the pulse height",

PH, and the cut off height, CH can be estimated as:

$$CH = -H\ln\sigma_0$$
$$PH = -H\ln\sigma_1 \qquad (4.26a\text{-}b)$$

Finally, the characteristic length scale of decay of density scaled opacity from LLD to 0

or the characteristic length scale of the "pulse," the "pulse thickness" (PT) and the "cutoff

length" (CL) can be estimated:

$$CL = m_0 H$$
$$PT = m_1 H \qquad (4.27a\text{-}b)$$
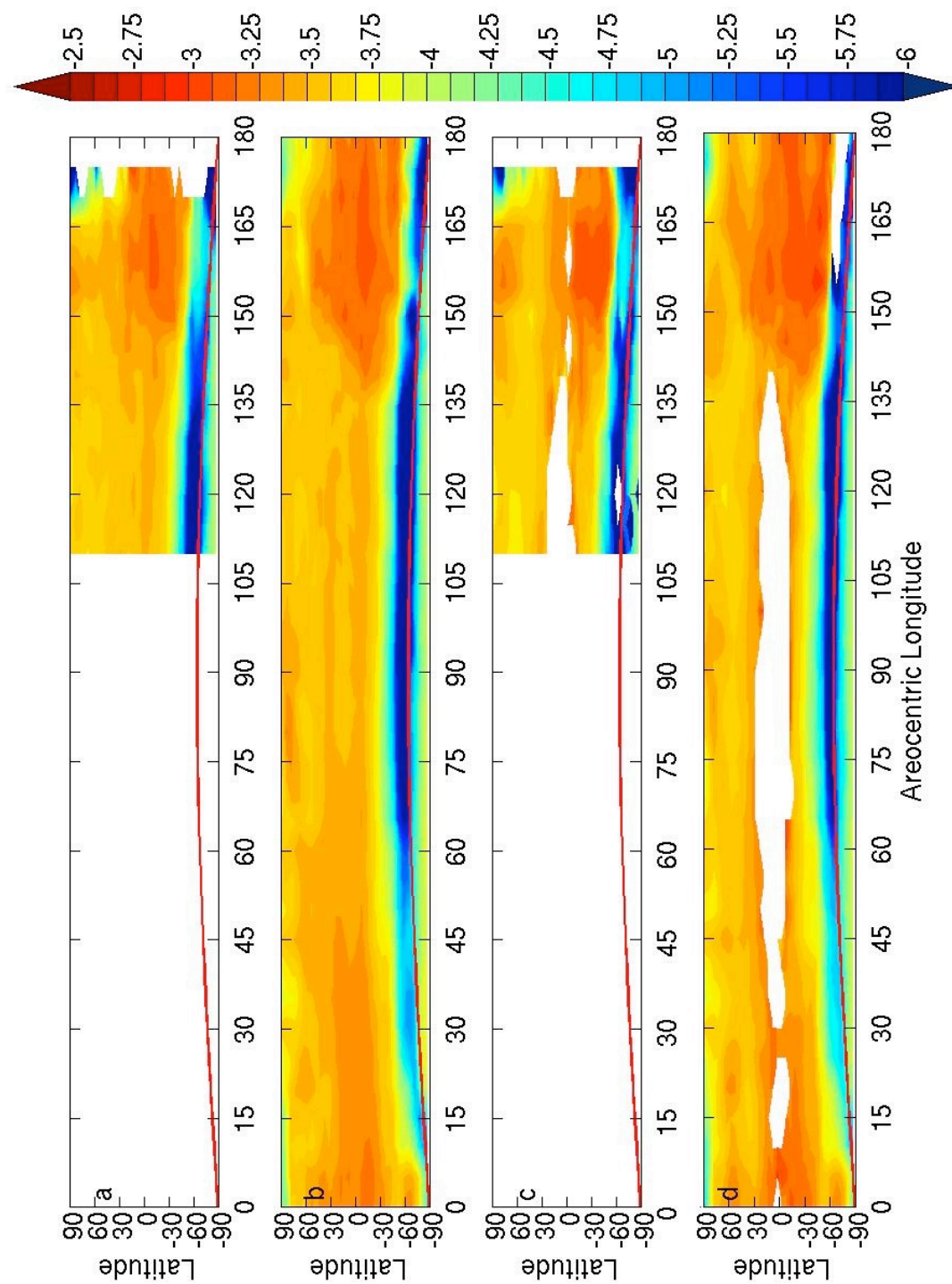
Figure 4.7. Latitudinal and seasonal variability in $\log_{10}(\text{LLD})$, $(\text{m}^2\,\text{kg}^{-1})$ during northern spring and summer. The red line marks the northern edge of southern polar night: (a) MY 28, nightside; (b) MY 29, nightside; (c) MY 28, dayside; (d) MY 29, dayside. White space is missing data. The deepest blue represents $\text{LLD} < 10^{-6}\,\text{m}^2\,\text{kg}^{-1}$ or effectively dust free areas.
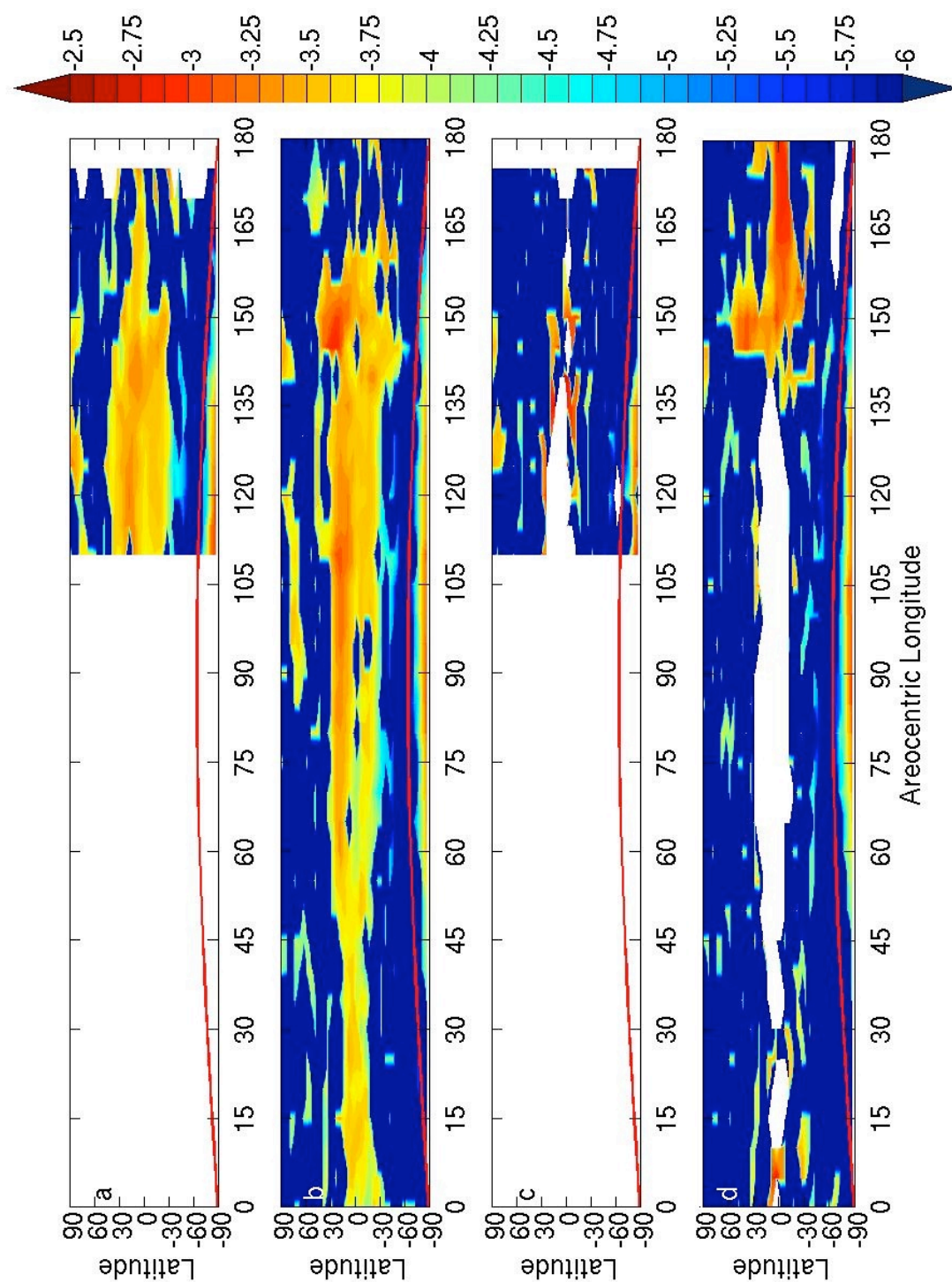
Figure 4.8. Latitudinal and seasonal variability in $\log_{10}(PD)$, (m^2 kg^{-1}) during northern spring and summer. The red line marks the northern edge of southern polar night. (a) MY 28, nightside; (b) MY 29, nightside; (c) MY 28, dayside; (d) MY 29, dayside. White space is missing data. The deepest blue represents $PD < 10^{-6}$ m^2 kg^{-1}.
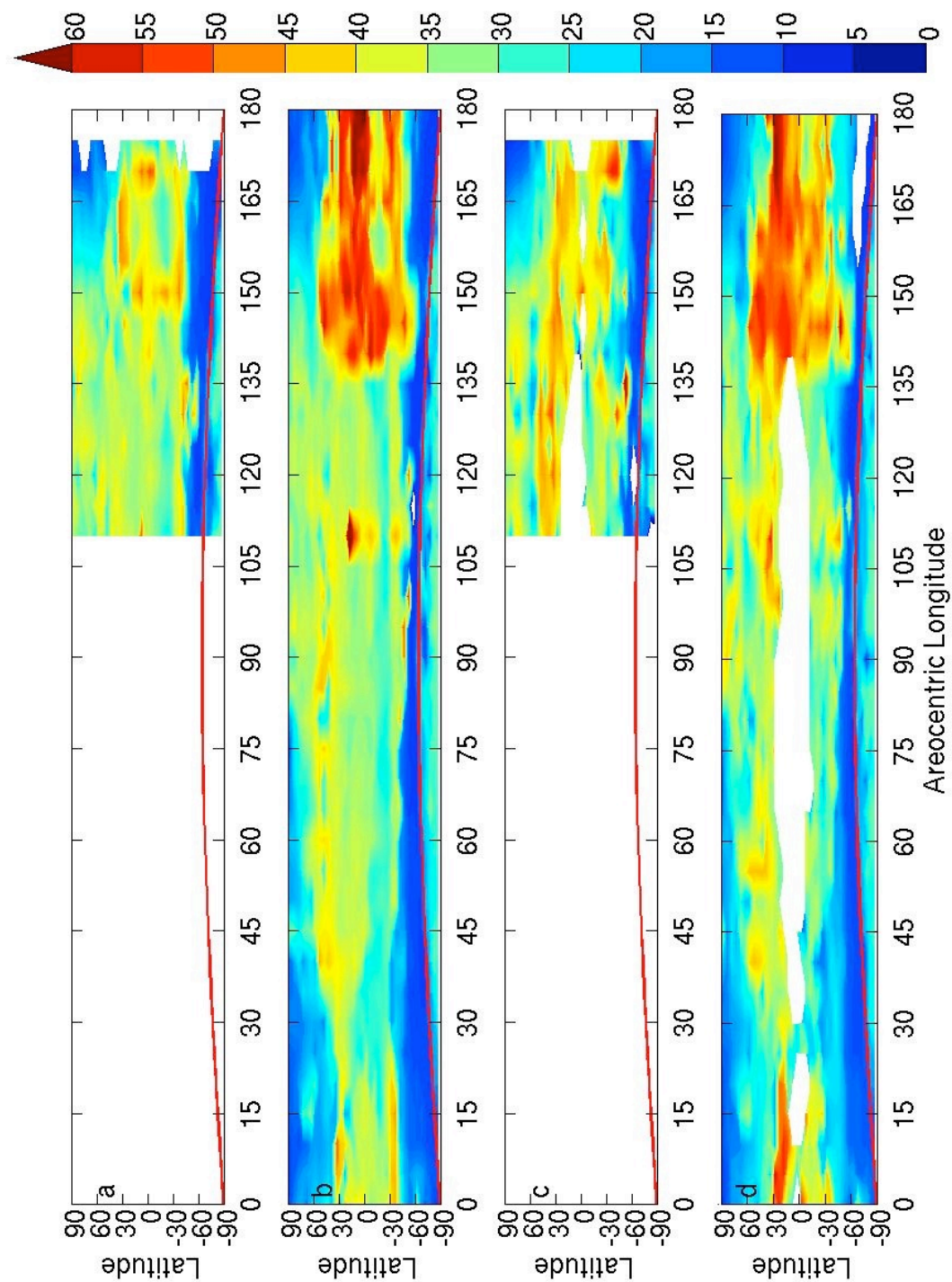
Figure 4.9. Latitudinal and seasonal variability in CH (m) during northern spring and summer. (a) MY 28, nightside; (b) MY 29, nightside; (c) MY 28, dayside; (d) MY 29, dayside. The red line marks the northern edge of southern polar night.

4.4 Results

Figures 4.7a-d show the seasonal and latitudinal variability in LLD. LLD is ~ $O(10^{-4} \text{ m}^2$

$\text{kg}^{-1})$ throughout the tropics and the northern hemisphere. LLD is significantly lower near

the north pole at the beginning of spring and the end of summer in MY 29. LLD is

effectively zero ~15° north of the northern edge of southern polar night, a limit which

bounds an effective "dust clear" region. Within polar night, LLD increases in the

direction of the south pole to values intermediate between the "dust clear region" and the

dustier regions to the north of it. Seasonally, northern extratropical LLD is relatively

constant, while tropical LLD is higher in early spring and even higher in late summer

than in the intervening season as the "dust clear" region shrinks and much higher values

of LLD are observed in the southern extratropics. LLD is higher in the northern tropics

and mid-latitudes during late summer in MY 29 than in MY 28.

Figures 4.8a-d show the seasonal and latitudinal variability in PD. The contrast

between LLD and PD is considerable. In most cases, high values of PD are restricted to

the tropics, though PD is also high near the southern pole and at some times in early

summer near the northern pole. Significant PD is restricted to very near the equator until

$L_s=35°$ and then is of greater magnitude in the northern tropics than the southern tropics

until late summer. PD in the tropics during late summer is generally higher in MY 29

than in MY 28.

Figures 4.9a-d show seasonal and latitudinal variability in CH. CH is less than 10

km throughout the dust-clear region. It is also very low near the north pole in early

northern spring and late northern spring, indeed for a longer period than LLD is relatively

low in that region at similar times of year. Through most of northern spring and summer
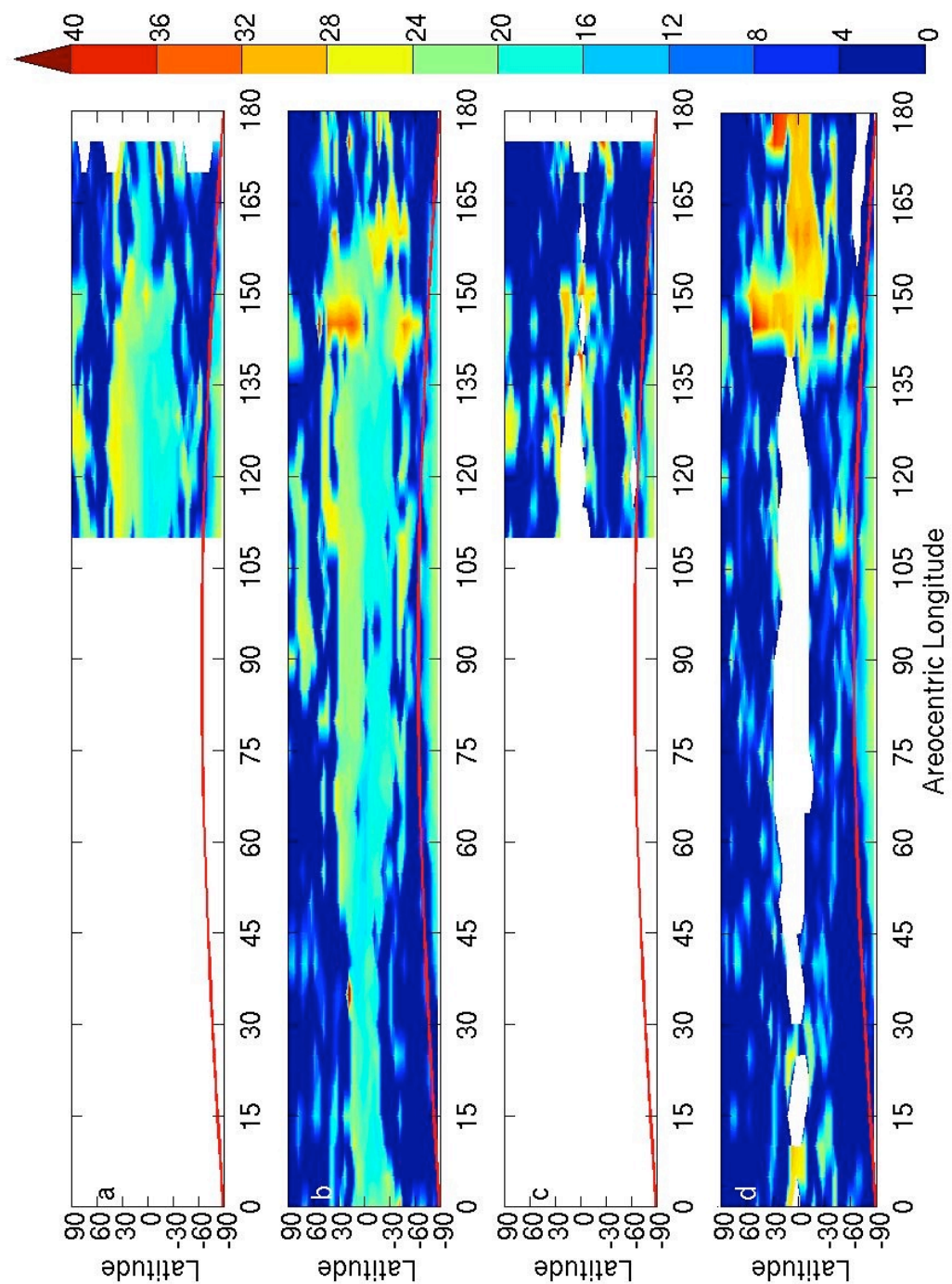
Figure 4.10. Latitudinal and seasonal variability in PH (m) during northern spring and summer. (a) MY 28, nightside; (b) MY 29, nightside; (c) MY 28, dayside; (d) MY 29, dayside. The red line marks the northern edge of southern polar night.

150
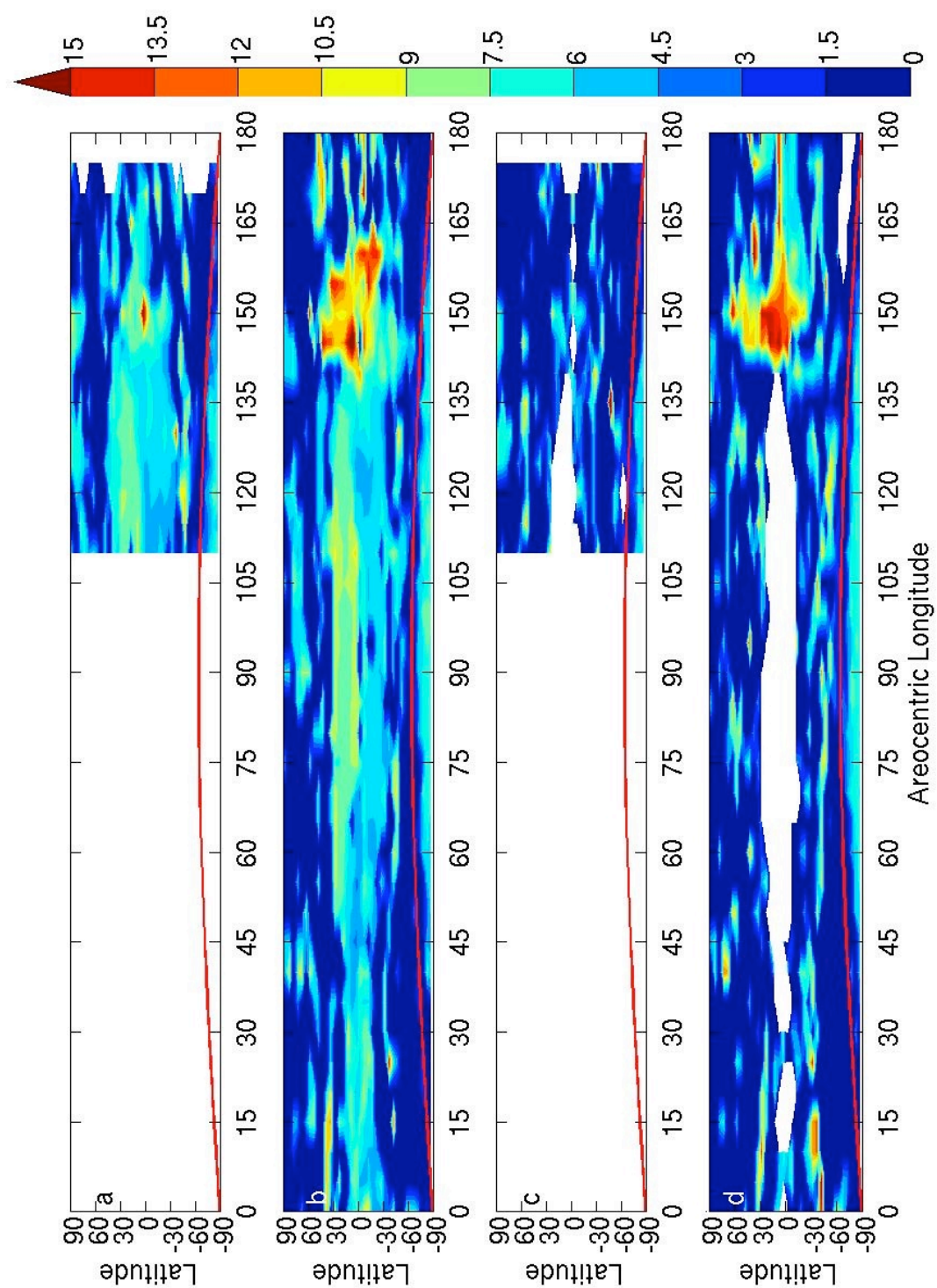
Figure 4.11. Latitudinal and seasonal variability in PT (m) during northern spring and summer. (a) MY 28, nightside; (b) MY 29, nightside; (c) MY 28, dayside; (d) MY 29, dayside. The red line marks the northern edge of southern polar night.

over the rest of the planet, CH is ~ 20—30 km. At about L_s=150° in MY 28, CH in

the tropics increases briefly to 40—45 km. A little earlier in MY 29 (L_s=140°), CH also

increases to values as high as 60 km. This increase is far more latitudinally broad than in

MY 28 and is much longer in duration, lasting at least the end of northern summer.

Figures 4.10a-d show seasonal and latitudinal variability in PH. The principal feature of

interest is that PH is higher in the northern tropics and slightly further north (~20—25

km) than in the southern extratropics (~15 km). PH of the north and south polar pulses is

~20—25 km as well. In the late summer, however, PH differs significantly between MY

28 and MY 29, decreasing from values earlier in the summer in MY 28 but increasing to

~30—35 km in dayside profiles in MY 29 after L_s=140°. Since a pulse at ~10 km is a

feature effectively irresolvable from low level dustiness, tropical values of PH indicate

that the pulse is practically non-existent in the southern tropics during late summer of

MY 28. However, the pulse is quite resolvable from low level dustiness through most of

the spring and summer, especially in the northern tropics.

Figures 4.11a-d show seasonal and latitudinal variability in PT. The apparent

correlation between PH and PT is striking. Higher pulses appear to be thicker pulses. The

quantitative thickness could be interpreted in terms of the full width at half maximum of

the pulse, which should be ~1.66 PT. From this calculation, the high altitude dust

maximum in the northern tropics is normally 12—15 km (2—3 MCS detectors) thick and

is about half of that thickness in the southern tropics. The north polar and south polar

maxima also are at least a detector thick by this measure. PT in the tropics increases

during late summer of MY 29 to 12—15 km. A similar increase is not seen during MY

28.

Figure 4.12. Latitudinal and seasonal variability in CL (m) during northern spring and summer. (a) MY 28, nightside; (b) MY 29, nightside; (c) MY 28, dayside; (d) MY 29, dayside. The red line marks the northern edge of southern polar night.
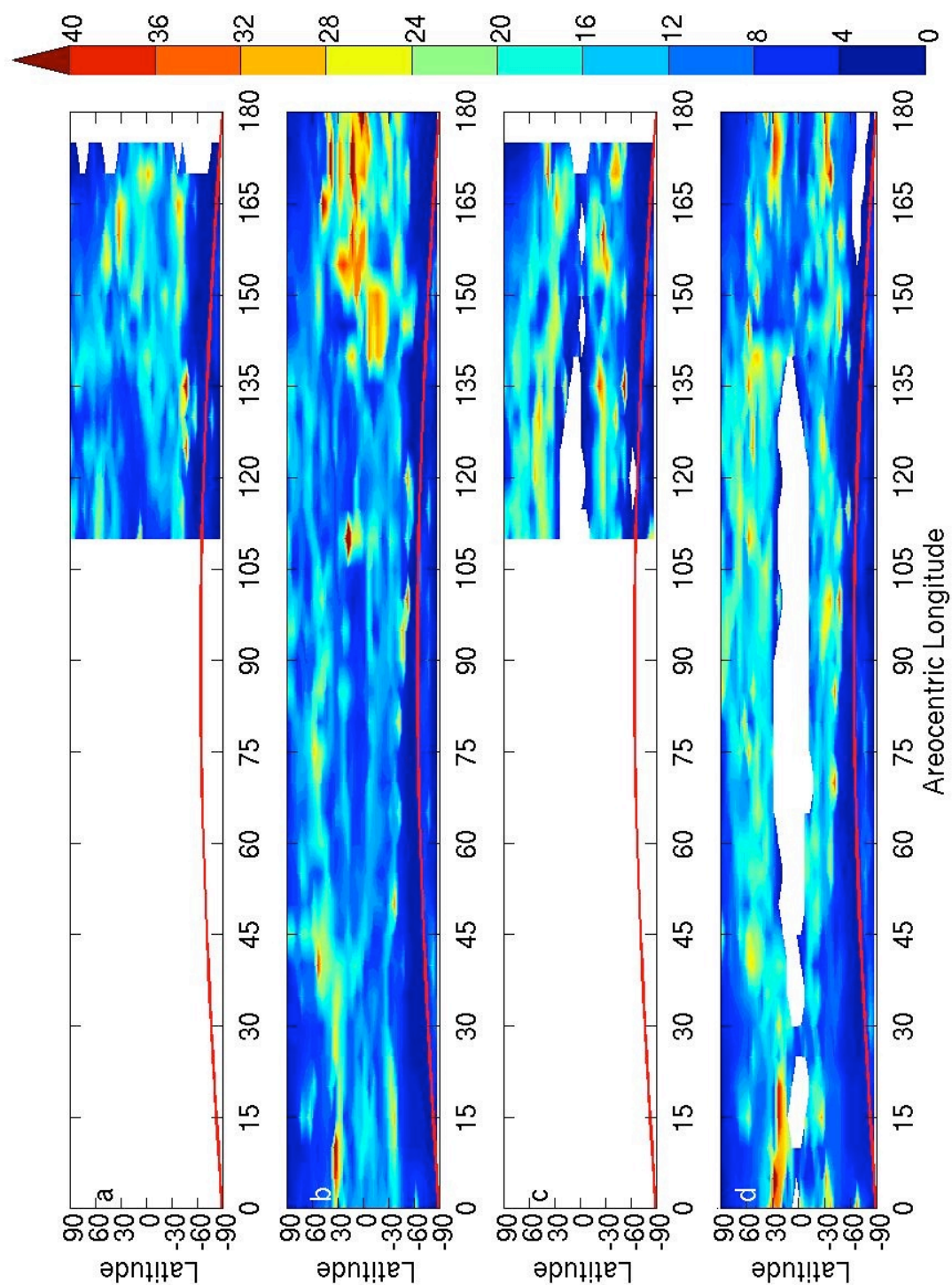
Figures 4.12a-d show seasonal and latitudinal variability in CL. This

parameter appears to be somewhat noisier than the others with less clear coherent

behavior in various latitudinal bands or seasons. The most notable feature is the relatively

low tropical values of CL between L_s=40° and 140° in MY 29 and L_s=110° and 155° in

MY 28, which indicate that tropical dust falls to zero very quickly above the high altitude

dust maximum before changes in the tropical vertical dust distribution during late

northern summer. CL also generally appears to be higher on the dayside than the

nightside.

4.5 Discussion

4.5.1 The Tropical Dust Distribution

From L_s=110° to 160° of MY 28 and from L_s=45° to 140° of MY 29, the tropical dust

distribution has a well-defined character. The lower end of MCS's vertical range is

clearer of dust than any other time of year (Figures 4.7a-b). At about 25 km above the

surface of the northern tropics, dust concentrations are enriched by a factor of two to four

relative to the lower end of MCS's range. A generally weaker enrichment is seen in the

southern tropics at ~15 km above the surface. (Figures 4.8a-b and 4.10a-b). Therefore,

the high altitude tropical dust maximum seen in Figure 4.2 and its greater northern

magnitude and intensity are persistent features of the planetary vertical dust distribution

for roughly a quarter of the martian year. Also notable is that the dust generally

penetrates to no higher than 10 km above the high altitude tropical dust maximum

(Figures 4.9a-b). This sharp cutoff above the maximum is particularly evident around the

northern summer solstice at the equator (Figure 4.12b), where CL falls below 5000 m. One possible explanation for this sharp cutoff could be the scavenging of the top of the dust haze by water ice condensation. The diurnal variability in CL then may be due to changes in altitude of water ice condensation, which are suspected to be tidally modulated [*Lee et al.*, 2009].

The relative stability of the tropical dust distribution during mid to late spring and early summer makes the changes in the dust distribution at these latitudes at the end of the period all the more striking. In MY 28, the alteration in the dust distribution is relatively gradual: the primary change that can be seen before the period of limb staring is an erosion of the high altitude tropical dust maximum in the southern tropics and mid-latitudes as LLD decreases and a significant pulse no longer can be fit (Figures 4.7a and 4.8a). In addition, PH lowers and the northern extent of the high altitude tropical maximum shrinks (Figure 4.10a), but LLD primarily increases south of the equator. CH increases somewhat at L_s=150° but only by ~10 km (Figure 4.9a). In MY 29, the change is both greater in magnitude and considerably more abrupt. LLD and PD increase suddenly throughout the tropics and into the northern and southern mid-latitudes (Figures 4.7b and 4.7d; Figures 4.8b and 4.8d). In many cases, LLD is greater than PD.

These differences in the seasonal evolution and character in late summer of the dust distribution between MY 28 and MY 29 are likely due to greater "early season" tropical dust storm activity [*Malin et al.*, 2008; *Smith,* 2009] observed by MARCI and THEMIS, which may most strikingly manifest itself in an aspect of the distribution not as easily observed by these instruments: the depth of penetration of dust. Dustier conditions near the surface also could explain the earlier and greater degradation in longitudinal

sampling and higher values of LLD in the northern tropics and mid-latitudes during this season (Figures 4.1a-b; Figures 4.8a-d) in MY 29. (Note that in late summer of MY 28, MCS was experiencing some technical issues, which resulted in data collection gaps, so the sampling contrast due to retrieval success between MY 29 and MY 28 is not as readily captured by Figures 4.1a-b as it could be).

The results in Chapter 4.4 do not show whether the high altitude tropical dust maximum is present on the dayside as well as the nightside. Retrievals on the dayside near the equator around northern summer solstice are difficult due to the high LOS opacity due to water ice in some MCS channels. Successful retrievals that meet quality control standards in this region and season generally do not report retrieved dust lower than ~20 km above the surface, so the fitting scheme is inapplicable to them.

For comparison of the nightside and dayside tropical vertical dust distributions, Figures 4.13a-b show the zonal average dust density scaled opacity at 20°—25° N for all retrievals during MY 28 and MY 29 (including those from limb-staring observations) for the nightside and the dayside. (Note the decay in dust concentrations after the 2007 global dust storm during late southern summer of MY 28.) Figures 4.13c-d show the sampled longitudinal bins (colored red) to create the zonal averages. Outside of northern spring and summer, agreement between nightside and dayside zonal averages is generally good. For instance, just before southern summer solstice of MY 29, the vertical dust distribution on both the dayside and nightside resembles a profile of uniform mass mixing ratio up to 20 Pa with a density scaled opacity of 8×10^{-4} m^2 kg^{-1}. During the increase in dust concentration and depth of penetration during late northern summer of MY 29, nightside-dayside agreement is similarly good.
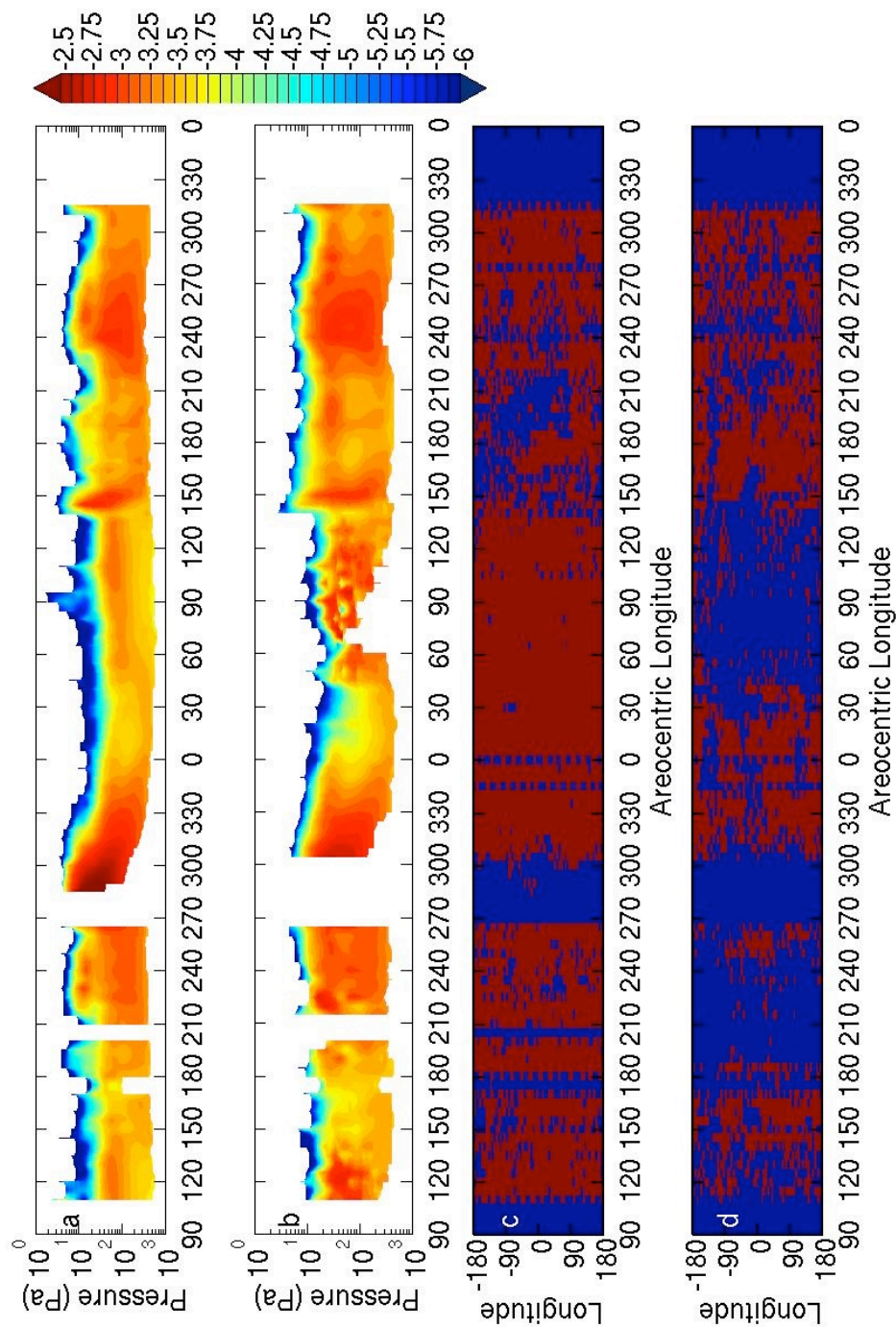
Figure 4.13. (a) Nightside $\log_{10}$ zonal average dust density scaled opacity ($m^2\,kg^{-1}$) at 20°-25° N during MY 28 and 29; (b) Dayside $\log_{10}$ zonal average dust density scaled opacity ($m^2\,kg^{-1}$) at 20°-25° N during MY 28 and 29; (c) Longitudinal sampling for (a): red indicates there is at least one successful retrieval in the longitudinal bin, blue indicates there are no retrievals in the longitudinal bin; (d) Longitudinal sampling for (b): red indicates there is at least one successful retrieval in the longitudinal bin, blue indicates there are no retrievals in the longitudinal bin.

In contrast to the rest of the year, the vertical dust distribution on the nightside around northern summer solstice of MY 29 has a maximum in density scaled opacity of 6×10^{-4} m^2 kg^{-1} at 60 Pa (a factor of three to four greater than nearer than the surface), while dust appears to be more uniformly mixed on the dayside. Longitudinal sampling (Figures 4.13c-d) is better on the nightside, and dust is not being retrieved to as low altitudes on the dayside as on the nightside, so the discrepancy could be attributed to profiles with high altitude dust maxima being preferentially unsuccessfully retrieved. For example, 424 retrievals are included in the nightside zonal average in this latitudinal band at L_s=90° of MY 29, but there are only 11 retrievals contributing to the zonal average on the dayside.

Characteristic retrieval spacing at this latitude is ~1.8°, there are thirteen orbits per day, and there are 11 days in the L_s bin, so we would expect ~400 retrievals in the zonal average if all retrievals were successful. From Figure 4.3, ~90% of individual profiles on the nightside in this bin contain a resolved maximum in dust density scaled opacity. Therefore, it is plausible that all retrievals with such a feature on the dayside were unsuccessful. Thus, in light of the good agreement in the vertical dust distribution between dayside and nightside retrievals during the rest of the year, there is likely a high altitude tropical dust maximum on the dayside.

4.5.2 Winter Polar "Dust"

The decomposition of the vertical dust distribution presented in Chapter 4.4 also illuminates the high altitude (~25 km) dust maximum within ~15° of the south pole between L_s=45° and 150°. The source of this dust is quite mysterious. On one hand,

advection and diffusion from elsewhere is unlikely, given the presence of the wide

dust-clear region to its north. On the other hand, a local source is equally unlikely, since

any dust deposited during the summer is frozen into carbon dioxide ice and inhibited

from lifting.

A recent climatology of polar dust and water ice column opacities retrieved from

TES nadir observations by *Horne and Smith* [2009] might resolve this conundrum. *Horne*

and Smith [2009] shows that dust column opacities over both poles peak during the

winter, that is, there is no apparent southern polar clearing region during northern spring

and summer. Indeed, polar dust column opacities in the 9 micron band (1075 cm^{-1}) are

>0.5 within ~30° of the south pole at the southern winter solstice. *Horne and Smith*

[2009] attributes these high dust opacities to intense polar cap edge dust storm activity.

Since present MCS retrievals usually do not report dust opacity below 8 km, the apparent

dust-clear region in the southern extratropics could be the site of extremely intense and

shallow dust storm activity, which then advects toward the pole. Retrievals from data

early in the MCS mission that include nadir observations in the southern extratropics

show the dust-clear region is in fact clear to the surface (N. Teanby et al., Vertical

Profiles of Temperature and Dust from Mars Climate Sounder, paper presented at the 39th

Meeting of the Division for Planetary Sciences of the American Astronomical Society,

Orlando, FL, October 2007). Moreover, invoking shallow dust storms near the southern

pole would not explain the peak in density scaled opacity at ~25 km. However, a source

of opacity not considered by *Horne and Smith* [2009] also could play a role.

The south polar high altitude dust maximum differs from the analogous equatorial

and north polar pulses in relative magnitude. *B,* the parameter that measures the relative

magnitude of the pulse and dust density scaled opacity at ~8 km) for these latter

pulses ranges from 0.5 to 3, whereas B of 8—10 is typical in early summer for the south

polar pulse. If summer equatorial water ice profiles were analyzed in the same way as we

have analyzed dust, B of 10—20 might be expected. In other words, the dust maximum

over the southern pole has a vertical distribution close to that of a detached condensate

cloud. *Kleinböhl et al.* [2009] notices that MCS temperature retrievals near the southern

pole in winter are very near the carbon dioxide frost point and in some cases cold enough

to deposit carbon dioxide ice. Similarly supersaturated temperature profiles are present in

both the TES and MGS Radio Science (RS) observations, which are thought to permit the

formation of deep convective clouds [*Colaprete et al.*, 2008]. *Kleinböhl et al.* [2009]

suggests that "small values of dust" retrieved near the winter pole by MCS may be due to

carbon dioxide ice, which is highly scattering in much of the visible and infrared [*Forget

and Pierrehumbert*, 1997], and avoids reporting opacity in profiles with temperatures

below 150 K at the pressure level nearest the surface to minimize contamination of

aerosol profiles by unretrieved carbon dioxide ice.

However, this filter may be imperfect, perhaps filtering out clouds near the

surface through the lower atmosphere temperature criterion but passing through

convective outflow clouds and similar detached cloudiness at higher altitudes. Thus,

carbon dioxide clouds may be responsible for the south polar high altitude dust

maximum. To test this hypothesis, the Convective Available Potential Energy with

respect to carbon dioxide convection ($CAPE_{CO_2}$) was calculated in each temperature

retrieval:

160
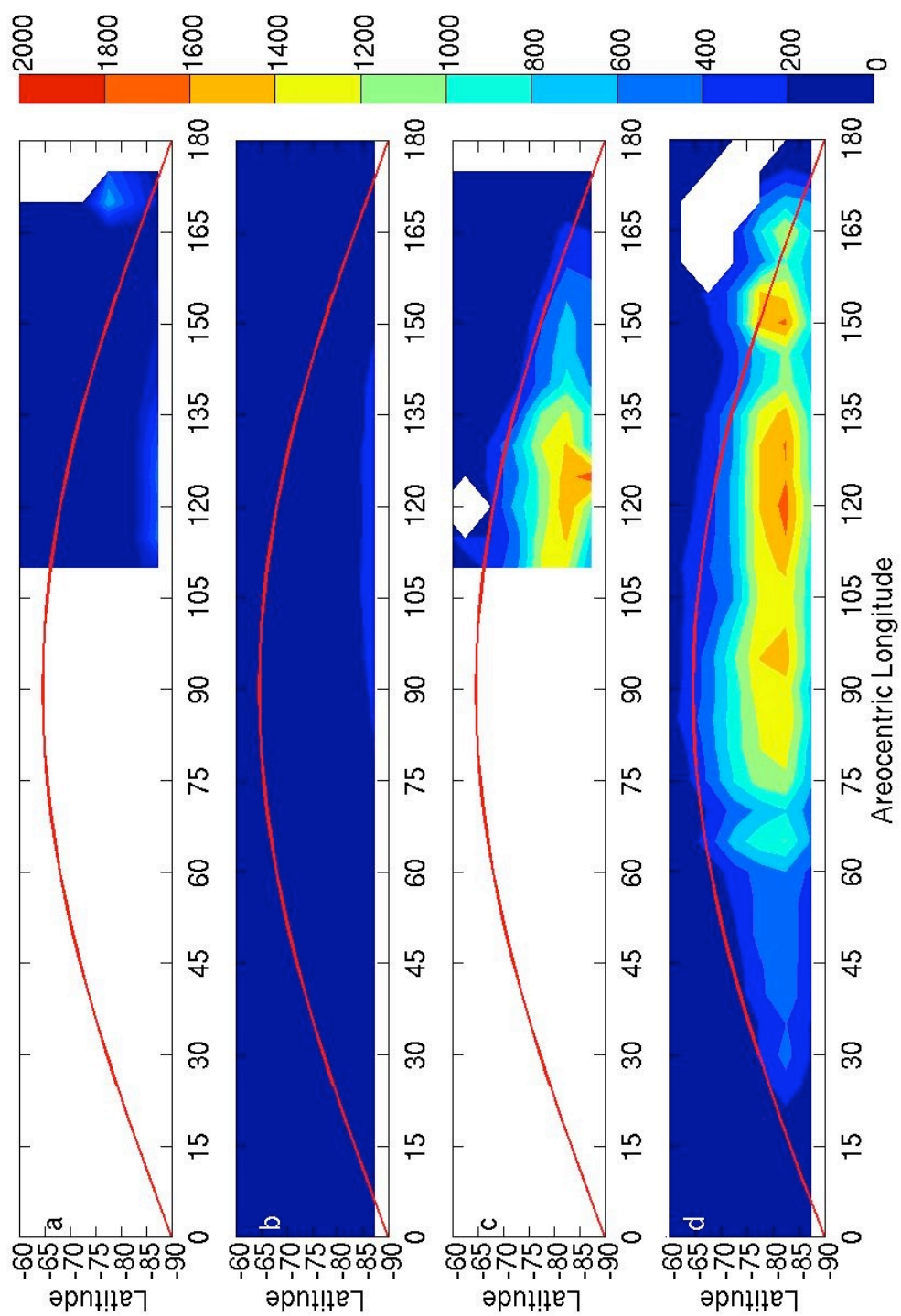
Figure 4.14. Latitudinal and seasonal variability in $CAPE_{CO_2}$ (J kg^{-1}) during northern spring and summer. (a) MY 28, nightside; (b) MY 29, nightside; (c) MY 28, dayside; (d) MY 29, dayside. The red line marks the northern edge of southern polar night.

$$CAPE_{CO_2} = \int_{Z_{LFC}}^{Z_{EQ}} g \frac{T_{sat} - T}{T} dz \qquad (4.28)$$

where dz is the hydrostatic height coordinate, Z_{LFC} is the level of free convection (the lowest level at which the retrieval is supersaturated with respect to CO_2), Z_{EQ} is the highest level at which the retrieval is supersaturated with respect to CO_2, and T_{sat} is the CO_2 frost point.

Figures 4.14a-b show seasonal variability in zonally-averaged $CAPE_{CO_2}$ near the south pole. $CAPE_{CO_2}$ is much lower in nightside retrievals than dayside retrievals: an effect related to the viewing geometry and the strong horizontal temperature gradients near the pole in which the region nearest the pole contributes the greatest proportion of radiance to observations in which the pole is nearer than the tangent point of the limb than in which the pole is more distant than the tangent point of the limb. Thus, the pole appears colder when the instrument looks past it. One consequence of this effect is that near the north pole during northern winter, $CAPE_{CO_2}$ is higher in nightside retrievals.

Dayside $CAPE_{CO2}$ is ~1000 J/kg near the south pole during much of northern spring and summer, roughly correlating with the climatology of the southern polar high altitude dust maximum. Investigation of carbon dioxide cloudiness with MCS Level 1B data is an ongoing topic of research, but even at this point, I find it reasonable to attribute dust opacity retrieved from MCS observations to the south of the clearing region in the southern extratropics to the scattering effects of carbon dioxide ice rather than absorption of dust. Thus, much of the southern hemisphere of Mars is probably clear of dust during the winter.

4.5.3 Radiative-Dynamical Significance of the High

Altitude Tropical Dust Maximum

The high altitude tropical dust maximum is of great dynamical interest, because the radiative heating profile it produces could differ significantly from what models presently assume. Recall that the diabatic heating and cooling rates due to an aerosol are proportional to its density scaled opacity or mass mixing ratio. The high altitude tropical dust maximum makes the vertical dust distribution of the atmosphere "top-heavy," producing the strongest dust heating/cooling well above the surface. Since the mass mixing ratio at 20 km contributes much less to the column opacity than the mass mixing ratio near the surface, a "top-heavy" mass mixing ratio profile creates a higher rate of diabatic heating/cooling somewhere in Mars's atmosphere than uniformly mixed dust, even for relatively low column opacities. Since GCMs and other models generally assume uniformly mixed dust to some height or decreasing mass mixing ratio with height profiles ("bottom-heavy" profiles), incorporating an equatorial dust pulse should produce a much different dust forcing in GCMs. In fact, this dust forcing has some analogy to the heating profile in the Earth's tropics due to the release of latent heating by moist convection, which tends to peak 5-10 km above the surface [*Tao et al.*, 2001]. A few brief calculations underscore this point.

The visible heating rate, J, can be estimated as:

$$J = 7.3\varepsilon \frac{d_z \tau}{\rho} F_{in} \tag{4.29}$$

where 7.3 is the ratio between visible opacity and MCS A5 opacity, ε is the efficiency of absorption of solar radiation in the visible, and F_{in} is the incident solar radiation. Typical

tropical LLD is 2.5×10^{-4} m^2 kg^{-1}, F_{in} at noon at the sub-solar point on Mars is

~500 W m^2, and ε is minimally the additive inverse of the single scattering albedo,

0.05—0.1 and possibly somewhat higher. Thus, the heating rate then is ~ 4.5×10^{-2}—

9.0×10^{-2} W kg^{-1} or 5.3—10.6 K sol^{-1}. Typical tropical PD is a factor of 0.5—3 higher,

producing zonally averaged heating rates within the pulse as large as ~30 K sol^{-1} if skies

above the dust haze are clear. (The effective heating rate in the equatorial pulse is

proportional to LLD+PD due to the relatively deep mixing of dust at these latitudes).

The dust also will have an infrared heating and cooling effect, depending on the

thermal structure of the atmosphere. During the day, lapse rates are strongly negative

over the tropics, so that dust will tend to re-emit infrared radiation absorbed from the

strongly heated surface at a somewhat lower temperature than the surface, producing net

heating. In a more top-heavy dust distribution, there are higher concentrations of dust

higher on the atmosphere (and therefore at a cooler temperature) relative to a uniformly

mixed profile, so infrared heating, too, will be greater. At night, there is an inversion

within 2 km of the surface [*Gierasch and Goody*, 1968], so the surface emits at fairly

cool temperatures and any aerosol above the inversion (up to ~10 Pa) may re-emit at a

higher temperature than the surface resulting in infrared cooling. (This pattern can be

more complex, see *Schofield et al.*, 1997). To a first approximation in the optically thin

case, the heating rate, *dT/dt*, due to this effect is:

$$\frac{dT}{dt} = \beta \frac{d_z \tau_{dust}}{\rho} \frac{\sigma \left(T_s^4 - T_r^4 \right)}{c_p} \qquad (4.30)$$

where β is a constant of proportionality of order unity (with respect to A5 channel density

scaled opacity) related to the broadband infrared absorption convolved with the emission

temperature of the surface, T_s, σ is the Stefan-Boltzmann constant, and T_r is the re-emission temperature of the dust. In the daytime, T_s is ~260 K and T_r is ~200 K in the high altitude tropical dust maximum, so the infrared heating at noon is ~10 K sol^{-1}, assuming a high altitude tropical maximum with a density scaled opacity of 5×10^{-4} m^2 kg^{-1}. Thus, the visible and infrared heating are of similar magnitudes. At night, the cooling in the high altitude tropical dust maximum will be around -2 K sol^{-1}.

So depending on the efficiency of dust absorption, a zonally and diurnally averaged heating rate of greater than 10 K sol^{-1} due to dust at 20 km above the surface is quite plausible in Mars's tropics. On the Earth, average latent heating rates at ~5—10 km altitude of 5—10 K day^{-1} are observed in the convectively active tropical eastern and central Pacific [*Tao et al.*, 2001].

In northern spring and summer, Mars may have a tropical diabatic heating profile of magnitude and morphology quite similar to that of the Earth, differing only in its deeper penetration into the atmosphere. The high altitude tropical dust maximum at 15—25 km will contribute diabatic heating to circulations less frictionally damped by the surface. And therefore at least qualitatively, the incorporation of the high altitude tropical dust maximum into models may produce a more vigorous lower atmospheric meridional circulation that presently simulated. Modeling by D. Tyler et al. (Dust Effects on Winds and Mixed Layered Depths, paper presented at the Mars Engineering Dust Workshop, Jet Propulsion Laboratory/NASA, Pasadena, CA, 18—19 March 2010) shows that incorporation of the high altitude tropical dust maximum into a modeled dust distribution enhances mixing within the convective boundary layer. A "top-heavy" dust distribution also may raise the condensation level of water ice simulated in models, enhancing

infrared heating due to water ice at higher altitudes in the atmosphere and may drive a

more vigorous atmospheric circulation due to such forcing as simulated in part by *Wilson*

et al. [2008]. Thus, to determine the extent to which the heating profile implied by MCS

data drives a stronger circulation, GCM simulations with both prescribed dust and

prescribed water ice distributions based on vertical information from MCS aerosol

profiles likely will be necessary.

4.6 Summary

I have used MCS retrievals of temperature, dust opacity, and pressure to reconstruct the

latitudinal-vertical distribution of dust during northern spring and summer and have

developed a new framework for analyzing and representing the vertical distribution of

dust in the atmosphere of Mars to describe its seasonal variability. Due to differences

between day and night in the operation of the present retrieval algorithm, information

about diurnal and interannual variability remains limited.

Yet the MCS dataset in northern spring and summer is sufficiently dense to show

that:

1. Over much of the planet, the vertical dust distribution is not consistent with a
   physically plausible single parameter Conrath distribution.

2. Throughout most of northern spring and summer, the dust mass mixing ratio in
   the tropics tends to have a maximum at 15—25 km above the local surface. This
   maximum generally has a greater intensity and altitude in the northern
   hemisphere.

3. Similar maxima in mass mixing ratio sometimes occur near the north pole around the northern summer solstice.

4. Therefore, diabatic atmospheric heating due to dust in the tropical atmosphere of Mars may have a maximum at 15—25 km above the local surface. Heating rates (per mass) due to dust at this altitude are quite similar to heating rates in the tropical atmosphere of the Earth, where heating is mostly due to latent heat release from condensing water in moist convection.

5. Contrary to recent analysis of retrievals from TES data by *Horne and Smith* [2009], the south polar regions of Mars are effectively clear of dust during northern summer, while the north polar regions are nearly as dusty as the tropics. This dust-clear zone near the pole closely tracks the terminator and extends approximately twenty degrees in latitude equatorward of it.

6. The dust aerosol retrieved by MCS near the south pole throughout much of northern spring and summer has a vertical distribution similar to a condensate cloud and is very likely an artifact introduced by scattering from carbon dioxide clouds.

7. There was a significant increase in the depth of dust mixing throughout the tropics and mid-latitudes in MY 29 that greatly exceeded the depth of dust mixing observed in the same season during MY 28. This increase was coincident with "early season" tropical dust storm activity observed by THEMIS and MARCI in mid to late summer of MY 29. MY 28 is thought to have been a year without this type of dust storm activity.

These results introduce important new constraints on the radiative forcing in simulations by atmospheric models.

In Chapter 5, I will consider the implications of the high altitude tropical dust maximum for dust lifting and transport on Mars.

Bibliography

Anderson, E. and C. Leovy (1978), Mariner 9 television limb observations of dust and ice hazes on Mars, *J. Atmos. Sci.*, *35*, 723-734.

Barnes, J.R. (1990), Possible effects of breaking gravity waves on the circulation of the middle atmosphere of Mars, *J. Geophys. Res.*, *95* (B2), 1401-1421.

Cantor, B., M. Malin, and K. S. Edgett (2002), Multiyear Mars Orbiter Camera (MOC) observations of repeated Martian weather phenomena during the northern summer season, *J. Geophys. Res.*, *107*(E3), 5014, doi:10.1029/2001JE001588.

Cantor, B. A., K. M. Kanak, and K. S. Edgett (2006), Mars Orbiter Camera observations of Martian dust devils and their tracks (September 1997 to January 2006) and evaluation of theoretical vortex models, *J. Geophys. Res.*, *111*, E12002, doi:10.1029/2006JE002700.

Chassefiére, E., P. Drossart, and O. Korablev (1995), Post-Phobos model for the altitude and size distribution of dust in the low Martian atmosphere, *J. Geophys. Res.*, *100*(E3), 5525-5539.

Clancy, R. T., B. J. Sandor, M. J. Wolff, P. R. Christensen, M. D. Smith, J. C. Pearl, B. J. Conrath, and R. J. Wilson (2000), An intercomparison of ground-based millimeter, MGS TES, and Viking atmospheric temperature measurements: Seasonal and interannual variability of temperatures and dust loading in the global Mars atmosphere, *J. Geophys. Res.*, *105*(E4), 9553–9571.

Clancy, R. T., M. J. Wolff, and P. R. Christensen (2003), Mars aerosol studies with the MGS TES emission phase function observations: Optical depths, particle sizes, and ice cloud types versus latitude and solar longitude, *J. Geophys. Res.*, *108*(E9), 5098, doi:10.1029/2003JE002058.

Clancy, R.T., M.J. Wolff, B.A. Whitney, B.A. Cantor, M.D. Smith, and T.H. McConnochie (2009), Extension of atmospheric dust loading to high altitudes during the 2001 Mars dust storm: MGS TES limb observations, *Icarus*, *207*, 98-109, doi: 10.1016/j.icarus.2009.10.011.

Colaprete, A., J.R. Barnes, R.M. Haberle, and F. Montmessin (2008), CO_2 clouds, CAPE and convection on Mars: Observations and general circulation modeling, *Planet. Space. Sci.*, *56*(2), 150-180, doi:10.1016/j.pss.2007.08.010.

Conrath, B.J. (1975), Thermal structure of the Martian atmosphere during the dissipation of the dust storm of 1971, *Icarus*, *24*, 36-46.

Forget, F. and R.T. Pierrehumbert (1997), Warming Early Mars with carbon dioxide clouds that scatter infrared radiation, *Science*, *278*, 1273-1276.

Forget, F., F. Hourdin, R. Fournier, C. Hourdin, O. Talagrand, M. Collins, S.R. Lewis, P.L. Read and J.-P. Huot (1999), Improved general circulation models of the Martian atmosphere from the surface to above 80 km, *J. Geophys. Res 104*, 24155–24175.

Gierasch, P., and R. M. Goody (1968), A study of the thermal and dynamical structure of the Martian lower atmosphere, *Planet. Space Sci., 16*, 615-636.

Greeley, R., P.L. Whelley, R.E. Arvidson, N.A. Cabrol, D.J. Foley, B.J. Franklin, P.G. Geissler, M.P. Golombek, R.O. Kuzmin, G.A. Landis, M.T. Lemmon, L.D.V. Neakrase, S.W. Squyres, and S.D. Thompson (2006), Active dust devils in Gusev crater, Mars: Observations from the Mars Exploration Rover Spirit, *J. Geophys. Res.*, *111*, E12S09, doi:10.1029/2006JE002743.

Haberle, R.M., C.B. Leovy, and J.M. Pollack (1982), Some effects of global dust storms on the atmospheric circulation of Mars, *Icarus*, *50*, 322-367.

Haberle, R.M., J.B. Pollack, J.R. Barnes, R.W. Zurek, C.B. Leovy, J.R. Murphy, J. Schaeffer, and H. Lee (1993), Mars atmospheric dynamics as simulated by the NASA/Ames general circulation model I. The zonal mean circulation, *J. Geophys. Res.,* *98*, 3093-3124.

Hartogh, P., A.S. Medvedev, and C. Jarchow (2007), Middle atmosphere polar warmings on Mars: Simulations and study on the validation with sub-millimeter observations, *Planet. Space. Sci.*, *55* (9), 1103-1112.

Hinson, D.P., M. Pätzold, S. Tellmann, B. Häusler, and G.L. Tyler (2008), The depth of the convective boundary layer on Mars, *Icarus*, in press, doi:10.1016/j.icarus/2008.07.003.

Horne, D. and M.D. Smith (2009), Mars Global Surveyor Thermal Emission Spectrometer (TES) observations of variations in atmospheric dust optical depth over cold surfaces, *Icarus*, *200*(1), 118-128.

Jaquin, F., P. Gierasch, and R. Kahn (1986), The vertical structure of limb hazes in the Martian atmosphere, *Icarus*, *72*, 528-534.

Kahre, M. A., J. R. Murphy, and R. M. Haberle (2006), Modeling the Martian dust cycle and surface dust reservoirs with the NASA Ames general circulation model, *J. Geophys. Res.*, *111*, E06008, doi:10.1029/2005JE002588.

Kahre, M.A, J.L. Hollingsworth, R.M. Haberle, and J.R. Murphy (2008), Investigations of dust particle sizes in the martian atmosphere using the NASA Ames General Circulation Model, *Icarus*, *195*, 576-597.

Kleinböhl, A., J. T. Schofield, D. M. Kass, W. A. Abdou, C. R. Backus, B. Sen, J. H. Shirley, W. G. Lawson, M. I. Richardson, F. W. Taylor, N. A. Teanby, and D. J. McCleese (2009), Mars Climate Sounder limb profile retrieval of atmospheric temperature, pressure, dust, and water ice opacity, *J. Geophys. Res.*, *114*, E10006, doi: 10.1029/2009JE003358.

Lee, C., W.G. Lawson, M.I. Richardson, N.G. Heavens, A. Kleinböhl, D. Banfield, D.J. McCleese, R. Zurek, D. Kass, J.T. Schofield, C.B. Leovy, F.W. Taylor, A.D. Toigo, (2009), Thermal tides in the Martian middle atmosphere as seen by the Mars Climate Sounder, *J. Geophys. Res.*, *114*, E03005, doi:10.1029/2008JE003285.

Lee, S.W., P.C. Thomas, and J. Veverka (1982), Wind streaks in Tharsis and Elysium—Implications for sediment transport by slope winds, *J. Geophys. Res.*, *87*, 10025-10041.

Leovy, C. (1982), Martian meteorological variability, *Adv. Space. Res.*, *2*, 19-44.

Lewis, S. R., M. Collins, P. L. Read, F. Forget, F. Hourdin, R. Fournier, C. Hourdin, O. Talagrand, and J.-P. Huot (1999), A climate database for Mars, *J. Geophys. Res.*, *104* (E10), 24,177–24,194.

Malin, M. C., B. A. Cantor, T.N. Harrison, D.E. Shean and M.R. Kennedy. (2008), MARCI Weather Report for 10 November 2008-16 November 2008, MSSS Captioned Image Release #59.

Martin, L. J., and R. W. Zurek (1993), An analysis of the history of dust activity on Mars. *J.Geophys. Res., 98*, 3221-3246.

McCleese, D. J., J. T. Schofield, F. W. Taylor, S. B. Calcutt, M. C. Foote, D. M. Kass, C. B. Leovy, D. A. Paige, P. L. Read, and R. W. Zurek (2007), Mars Climate Sounder: An investigation of thermal and water vapor structure, dust and condensate distributions in the atmosphere, and energy balance of the polar regions, *J. Geophys. Res., 112*, E05S06, doi:10.1029/2006JE002790.

McCleese, D.J., J.T. Schofield, F.W. Taylor, W.A. Abdou, O. Aharonson, D. Banfield, S.B. Calcutt, N.G. Heavens, P.G.J. Irwin, D.M. Kass, A. Kleinböhl, W.G. Lawson, C.B. Leovy, S.R. Lewis, D.A. Paige, P.L. Read, M.I. Richardson, N. Teanby, and R.W. Zurek (2008), *Nature Geosci.*, *1*, 745-749, doi:10.1038/ngeo332.

Montmessin, F., F. Forget, P. Rannou, M. Cabane, and R. M. Haberle (2004), Origin and role of water ice clouds in the Martian water cycle as inferred from a general circulation model, *J. Geophys. Res.*, *109*, E10004, doi:10.1029/2004JE002284.

Rafkin, S.C.R., M.R.V. Sta. Maria, and T.I. Michaels (2002), Simulation of the atmospheric thermal circulation of a martian volcano using a mesoscale numerical model, *Nature*, *419*, 697-699.

Richardson, M. I. (1998), Comparison of microwave and infrared measurements of Martian atmospheric temperatures: Implications for short-term climate variability, *J. Geophys. Res.*, *103*(E3), 5911–5918.

Rind, D. and W.B. Rossow (1984), The Effects of Physical Processes on the Hadley Circulation, *J. Atmos. Sci.*, *41* (4), 479-507.

Schneider, E.K. (1983), Martian Great Dust Storms: Interpretive Axially Symmetric Models, *Icarus*, *35*, 302-331.

Schofield, J.T., J.R. Barnes, D. Crisp, R.M. Haberle, S. Larsen, J.A. Magalhaes, J.R. Murphy, A. Seiff, and G. Wilson (1997), *Science*, *278* (5334), 1752-1758.

Smith, M.D. (2009), THEMIS Observations of Mars aerosol optical depth from 2002—2008, *Icarus*, *202*(2), 444-452, doi:10.1016/j.icarus.2009.03.027.

Smith, M.D., J.C. Pearl, B.J. Conrath, and P.R. Christensen (2001), Thermal Emission Spectrometer results: Mars atmospheric thermal structure and aerosol distribution, *J. Geophys. Res.*, *106*, 23929-23945.

Tao, W.-K., S. Lang, W. S. Olson, R. Meneghini, S. Yang, J. Simpson, C. Kummerow, E. Smith and J. Halverson (2001), Retrieved vertical profiles of latent heat release using TRMM rainfall products for February 1998, *J. Appl. Meteor.*, *40*, 957-982.

Taylor, P.A., P.-Y. Li, D.V. Michelangeli, J. Pathak, and W. Weng (2007), Modelling dust distributions in the atmospheric boundary layer on Mars, *Bound. Lay. Met., 125* (2),305-328.

Wang, J., and W.B. Rossow (1998), Effects of cloud vertical structure on atmospheric circulation in the GISS GCM, *J. Climate*, *11*, 3010-3029.

Wilson, R.J. and K. Hamilton (1996), Comprehensive model simulation of thermal tides in the martian atmosphere, *J. Atmos. Sci.*, *54*, 1290-1326.

Wilson, R. J., and M. I. Richardson (2000), The Martian atmosphere during the Viking mission, part I, Infrared measurements of atmospheric temperatures revisited, *Icarus*, *145*, 555–589, doi:10.1006/icar.2000.6378.

Wilson, R. J., S. R. Lewis, L. Montabone, and M. D. Smith (2008), Influence of water ice clouds on Martian tropical atmospheric temperatures, *Geophys. Res. Lett.*, *35*, L07202, doi:10.1029/2007GL032405.

Zurek, R.W., J.R. Barnes, R.M. Haberle, J.B. Pollack, J.E. Tillman, and C.B. Leovy (1992), Dynamics of the Atmosphere of Mars in H.H. Kieffer, B.M. Jakosky, C.W. Snyder, and M.S. Matthews, *Mars*, 1498 pp., University of Arizona Press, Tucson.

Chapter 5   The High Altitude Tropical Dust Maximum

5.1 Introduction

Because it is strongly radiatively active and highly temporally and spatially variable in its abundance, suspended dust is the martian atmosphere's most meteorologically important component. Indeed, the role of dust in Mars's surface/atmosphere system is analogous to the role of water in Earth's surface/atmosphere system.

First, the more dynamic weather systems of Mars are chiefly associated with dust clouds: dust devils [*Thomas and Gierasch*, 1985; *Balme and Greeley*, 2006; *Cantor et al.*, 2006], dust "cells" [*Cantor et al.*, 2002], and dust storms at various scales [*Kahn et al.*, 1992]. Mars has carbon dioxide and water ice clouds (and the Earth has dust storms). But these types of martian clouds generally are not associated with turbulent weather at the surface, with the possible exception of carbon dioxide snow squall activity in polar night [*Colaprete et al.*, 2008].

Second, meteorological systems re-circulate dust on seasonal timescales, lifting dust from some surfaces, precipitating them upon others, and usually re-charging the original sources from the sinks [*Szwast et al.*, 2006], producing a true "dust cycle." Surface dust is both more reflective and more swiftly heated and cooled than the dark basaltic rock that makes up much of the planet's surface, providing thermal contrast between dusty "continents" and basaltic "seas" [*Zurek et al.*, 1992].

Third, the presence of a small background dust concentration in the atmosphere, which is heated strongly during the day in the visible and weakly cools in the infrared at night, enhances the static stability of the atmosphere in ways not dissimilar to water

vapor in Earth's denser and more humid atmosphere [*Haberle et al.*, 1982; *Schneider*, 1983]. Mars even may have a form of dust related convection analogous to moist convection due to water on the Earth. *Fuerstenau* [2006] proposed that dust devil plumes (and potentially larger dust structures) might be so strongly heated by the sun during the day that parcels within them might be strongly positively buoyant. Such parcels might have vertical velocities of 10 ms^{-1} and reach heights of 8 km or more. This mechanism might explain the great heights reached by larger martian dust devils compared to their terrestrial analogs [*Fisher et al.*, 2005]. The production of positive buoyancy by the solar heating of dust also could explain the "puffy" dust clouds observed in intense dust storm activity that have been compared to deep moist convective "hot towers" on the Earth [*Strausberg et al.*, 2005]. Note that this effect is distinct from the positive feedback effect on winds within lower aspect ratio circulations due to dust heating [*Haberle et al.*, 1993], which does not require positive buoyancy or result in large vertical velocities.

Fourth, the contribution of dust to the lower atmospheric heat budget also has a water-related terrestrial analog. In Chapter 4, I calculated that the tropical zonal average atmospheric mass heating rates on Mars due to dust under relatively clear conditions are similar to or greater than tropical mass heating rates due to moist convective latent heat release on the Earth. Thus, if Earth is a planet defined by its hydrometeorology ("water weather"), Mars is defined by its coniometeorology ("dust weather"), the latter word being derived from the Greek word for dust, *konios*.

Accurate simulation of Mars's modern circulation, past climate, and future weather therefore is dependent on understanding the connection between the synoptic and mesoscale systems that lift and transport dust and the resulting distributions of airborne

and surface dust. Modelers of the martian atmosphere have explored this connection in considerable detail, simulating dust lifting and transport with more or less parameterized routines in planetary and mesoscale models [e.g., *Murphy et al.*, 1990; *Newman et al.*, 2002a, 2002b; *Richardson and Wilson*, 2002; *Rafkin et al.*, 2002; *Basu et al.*, 2004, 2006; *Kahre et al.*, 2005, 2006, 2008].

Several datasets have been used to tune or verify these simulations. These datasets fall into two broad types: (1) nadir column opacity measurements from the surface or orbiters and (2) temperature measurements from orbit, particularly the brightness temperature near the center of the 15 micron CO_2 band, T_{15} [e.g., *Newman et al.*, 2002a; *Basu et al.*, 2004]. The first type of measurement is more sensitive to dust near the surface than dust high in the atmosphere, even though the dust high in the atmosphere still can produce significant radiative heating and cooling. The second type of measurement is more sensitive to finer aspects of the vertical structure of the dust distribution but also can be influenced by dynamical processes indirectly driven by or independent of dust heating phenomena such as water ice clouds, especially if atmospheric dust concentrations are relatively low. The logical alternative to these verification measurements is more direct observation of the vertical dust distribution through infrared or visible limb sounding.

Vertical profiles of temperature, pressure, dust, and other aerosol retrieved from observations by the Mars Climate Sounder (MCS) on Mars Reconaissance Orbiter (MRO) now provide an expansive dataset [*McCleese et al.*, 2007, 2008; *Kleinböhl et al.*, 2009] for observing the vertical structure of Mars's coniometeorological systems,

evaluating present simulations of dust lifting and transport, and indicating avenues for improvement of the parameterizations used to drive these simulations.

This study is very much a first step in using the abundance of retrieved vertical profiles of dust from MCS observations to improve understanding of Mars's coniometeorology. Chapter 4 showed that the vertical and latitudinal dust distribution of Mars in northern spring and summer was very different from that generally assumed, especially by general circulation models forced by prescribed dust concentrations. The most discrepant feature is an apparent maximum in dust mass mixing ratio over the tropics during most of northern spring and summer, "the high altitude tropical dust maximum" (HATDM).

In this study, the HATDM is investigated in greater detail than Chapter 4 in order to determine its cause. In Chapter 5.2, the observed MCS dust distributions at northern summer and southern summer solstices are compared with planetary-scale simulations of active lifting and transport. In Chapter 5.3, the longitudinal structure of the HATDM and its temporal variability is investigated. In Chapter 5.4, the potential roles of dust storm activity, orographic dust lifting, pseudo-moist dust convection, and the scavenging of dust particles by water ice clouds in producing the HATDM are evaluated, and I outline what further observations and modeling work are necessary to constrain the contributions of these processes. In Chapter 5.5, I summarize the results of the study.

5.2 Comparison of MCS Vertical Dust Profiles with Simulations of Active Lifting and Transport

A number of Mars GCMs now have the capability to simulate the lifting, sedimentation, and horizontal transport of dust in Mars's atmosphere. Most modeling studies, however, have focused on the simulation of global dust storms and therefore do not describe the simulated latitudinal and vertical distribution of dust during the clear season. Two exceptions are *Richardson and Wilson* [2002], which uses the Mars GFDL model, and *Kahre et al.* [2006], which uses the Ames Mars GCM.

Figures 5.1a and 5.1b plot the nightside zonal average density-scaled opacity from nightside MCS retrievals for L_s=87.5°—92.5° and 267.5º—272.5º (hereafter L_s=90º and 270º) of MY 29 on a linear scale (cf. *Richardson and Wilson* [2002], Figures 1c-d). (See Chapter 4 for description of the retrievals, zonal averaging, and the significance of density scaled opacity.) The dust distribution observed by MCS is broadly similar to that simulated by *Richardson and Wilson* [2002] at the solstices; high concentrations of dust penetrate deeply (more deeply at southern summer solstice) into the atmosphere in the tropics and the summer hemisphere while the winter extratropics remain fairly clear. The observations at both solstices and the model simulation show regions of lower, less deeply penetrating dust in the summer mid-latitudes or near the pole, which may be attributable (in these particular simulations) to enhancement of the sedimentation of dust in the downwelling of a secondary principal meridional overturning circulation (PMOC) restricted to the summer hemisphere. The latitudes at which these features are located, however, differ between the observations and the simulation.
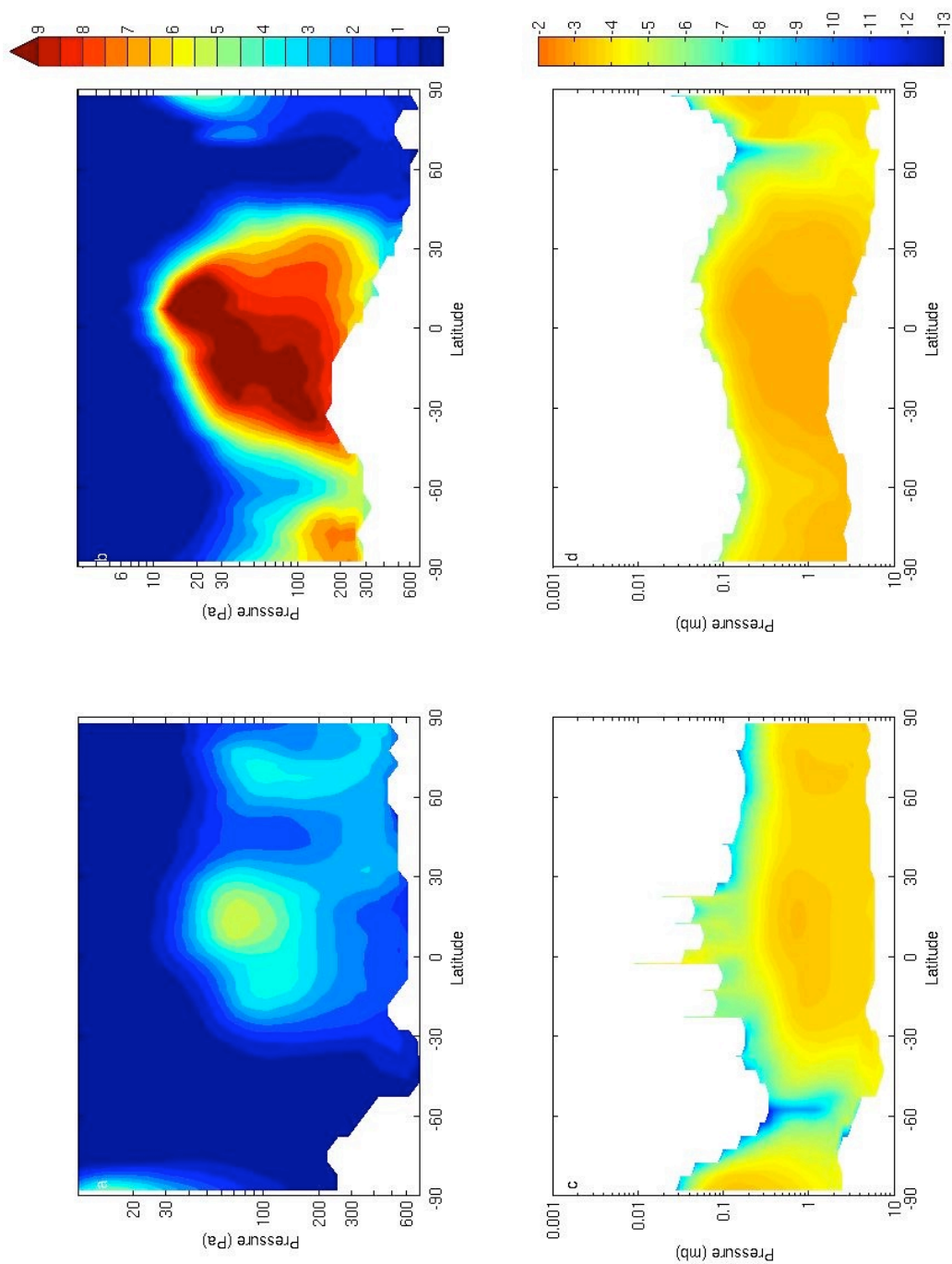
Figure 5.1. (a) Zonal average nightside dust density scaled opacity at $L_s=90°$, MY 29 $\times 10^4$ m^2 kg^{-1}; (b) Zonal average nightside dust density scaled opacity at $L_s=270°$, MY 29 $\times 10^4$ m^2 kg^{-1}; (c) $\log_{10}$ of zonal average nightside dust density scaled opacity at $L_s=90°$, MY 29 (m^2 kg^{-1}); (d) $\log_{10}$ of zonal average nightside dust density scaled opacity at $L_s=270°$, MY 29 (m^2 kg^{-1}).

At northern summer solstice, the observations and the GFDL model simulation disagree about the vertical dust distribution in the tropics. The simulation predicts that dust is roughly uniformly mixed to 80 Pa (perhaps at higher mass mixing ratios in the northern tropics than the southern tropics) and mass mixing ratio decays at lower pressures. MCS retrievals show that the northern and southern tropics are roughly uniformly dusty at ~300 Pa, but there is a maximum in dust mass mixing ratio at ~60 Pa over the tropics that is a little dustier in the northern than the southern tropics. This maximum is enriched by a factor of two to four over zonal average dust density scaled opacity at ~300 Pa. In other words, the model does not simulate the HATDM in the observations.

At southern summer solstice, dust density scaled opacity peaks at ~80 Pa over the equator. This maximum is broader and less enriched relative to ~300 Pa than at northern summer solstice. More poleward (between 40° S and 35° N), this maximum occurs at higher pressure levels. As at northern summer solstice (see Chapter 4), the maximum in dust density scaled opacity at the equator is vertically resolved.

Figures 5.1c-d shows the same data plotted in Figures 5.1a-b on a logarithmic scale and different pressure axes (cf. *Kahre et al.* [2006], Figures 4b and 4d). Even accounting for the broad logarithmic scale, the latitudinal-vertical structure of dust in the simulation of *Kahre et al.* [2006] differs somewhat from the simulation of *Richardson and Wilson* [2002]. But the simulation of *Kahre et al.* [2006] clearly differs from the MCS retrievals as well. *Kahre et al.* [2006] does not simulate a HATDM at northern summer solstice and appears to underestimate the clearing in the winter extratropics. Mixing ratios of ~0.1 ppm poleward of 50° S at 100 Pa are predicted by *Kahre et al.*

[2006]. However, this mass mixing ratio would correspond to a density scaled opacity of $\sim 10^{-5}$ m^2 kg^{-1} (see Chapter 4 for discussion of the conversion method), which is at least an order of magnitude above what is observed in the MCS retrievals. Admittedly, the MCS retrievals have limited sensitivity at very low values of dust, but this sensitivity is on the order of 10^{-6} to 10^{-5} km^{-1}. At 100 Pa, this sensitivity corresponds to density scaled opacities on the order of 10^{-7} to 10^{-6} m^2 kg^{-1}.

In the dust distribution simulated by *Kahre et al.* [2006] at southern summer solstice, dust is uniformly mixed to 10 Pa at $\sim$45° S and there is more dust at higher altitudes than nearer the surface over the tropics. This distribution resembles Figure 5.1b (the logarithmic scale of Figure 5.1d is insufficient to resolve it). This dust distribution may be due to cross-equatorial transport of dust from dust storm activity in the southern mid-latitudes by the PMOC, but *Kahre et al.* [2006] does not discuss this point explicitly.

In summary, the latitudinal distributions of dust simulated by *Wilson and Richardson* [2002] and *Kahre et al.* [2006] are in broad agreement with MCS observations; the tropics and the summer mid-latitudes are dustier than elsewhere on the planet. At northern summer solstice, however, both simulations fail to reproduce the zonal average vertical structure of dust in the tropics. Yet at southern summer solstice, *Kahre et al.* [2006] does simulate a vertical dust distribution fairly consistent with observations. Therefore, these two simulations incorrectly model the processes that control vertical transport of dust in the atmosphere globally in late northern spring and early northern summer but not necessarily at other seasons. The remainder of this Chapter will focus on identifying what processes may be incorrectly modeled.

5.3 The Longitudinal Structure of the HATDM

5.3.1 Approach

The catalog of processes that are capable of producing the HATDM outlined in Chapter 5.4 may not be exhaustive. Therefore, in Chapter 5.3, I will describe the longitudinal structure of the HATDM before, during, and after northern summer solstice and consider its significance with respect to simple models of sedimentation, advection, and vertical eddy diffusion. This more objective analysis will provide general observational information to evaluate explanations for the HATDM.

5.3.2 Spatial Distribution of Dust around Northern Summer Solstice

Figures 5.2a-f show nightside dust density scaled opacity around northern summer solstice of MY 29 averaged over 30º of L_s on six different σ levels, which correspond to 1, 1.5, 2, 2.5, 3, and 3.5 "scale heights" above the surface. Nearest the surface (Figure 5.2a), the northern mid-latitudes are generally less dusty than the region near the pole. In the tropics, there is some longitudinal variability in dust density scaled opacity, which resembles the thermal inertia pattern [*Putzig et al.*, 2005], though the correspondence is not exact. Note the low dust density scaled opacity over Amazonis Planitia (0°—30° N, 180°—135° W) and western Arabia Terra (0°—30° N, 0°—45° E). At this σ level (and all other levels), the region south of 30° S is generally clear of dust. The exceptions are
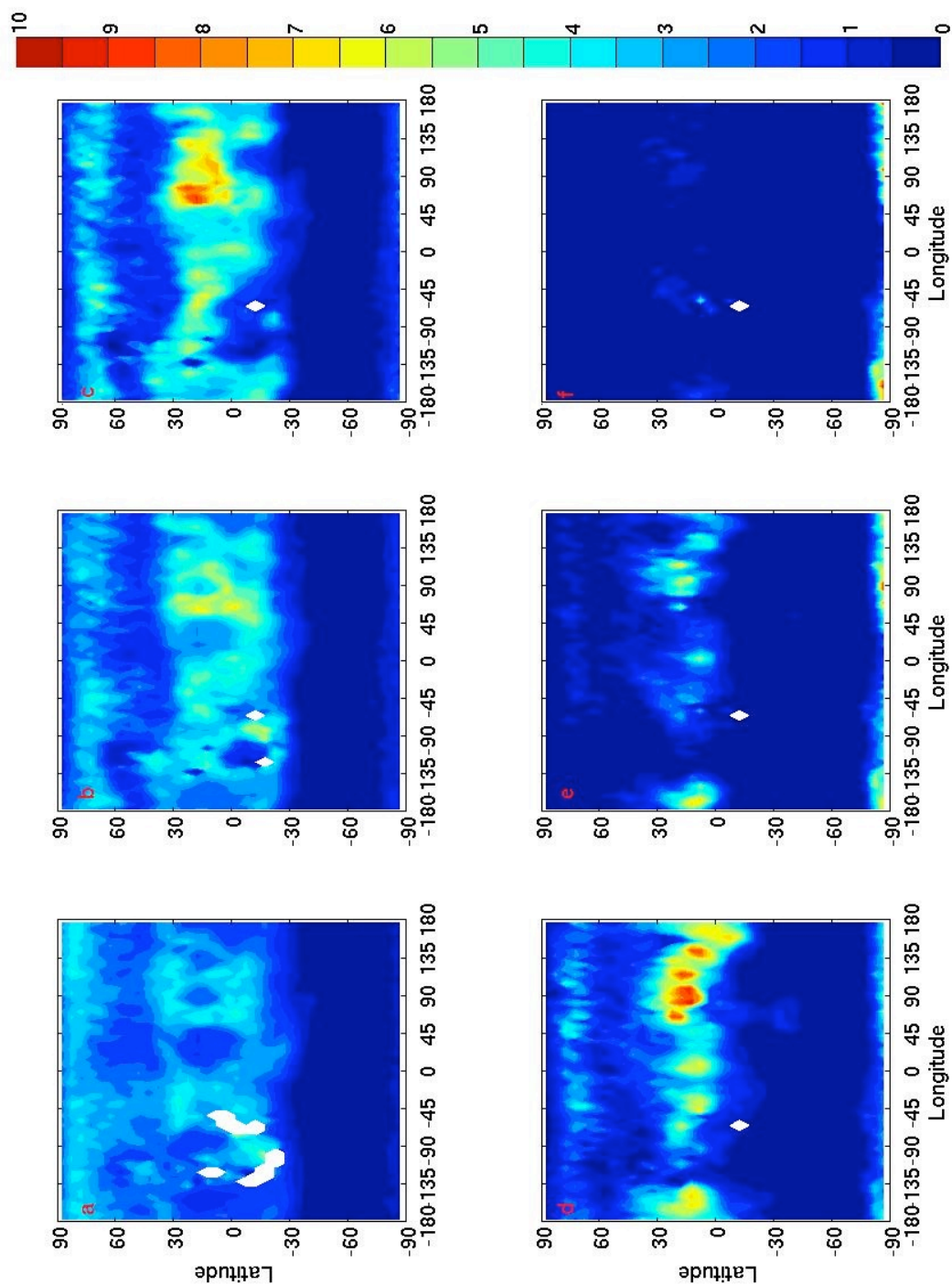
Figure 5.2. Average nightside dust density scaled opacity (L_s=75°-105°) on σ levels equivalent to: (a) 1; (b) 1.5; (c) 2; (d) 2.5; (e) 3; (f) 3.5 "scale heights" above the surface.

near the south pole (CO_2 ice) and over Hellas (40° S, 45°—90° E) in Figure 5.2d.

Dust density scaled opacity in the tropics generally increases with altitude above the

surface in Figures 5.2b-c, except near Arsia Mons and Syria Planum (0°—15° S, 135°—

45° W), where the atmosphere grows clearer. The tropics clear with higher altitude above

the surface (Figures 5.2d-f). The highest average dust density scaled opacities are found

at 2.5—3 scale heights above the surface in the northern tropics near 60°—135° E, a

broad region that spans Syrtis Major, Isidis Planitia, and western Elysium Planitia.

5.3.3 Temporal Variability in the Dust Distribution near the Northern Tropic

The pattern of longitudinal variability derived from the relatively long-term average in

Figure 5.2 also can be extracted from averaging over shorter periods. Retrieval coverage

is sufficiently good that longitudinal cross-sections can be constructed from interpolation

of all retrievals in a narrow latitudinal and L_s range (2° in both cases) with a resolution of

~10° of longitude. Figures 5.3—5.6 show such cross-sections for a narrow latitudinal

band around the northern tropic, which intersects the Elysium Montes at ~150° E; comes

close to the sites of the Mars Pathfinder and Viking Lander 1 sites at ~45° W; intersects

Lycus Sulci at ~135° W; and roughly corresponds to the dustiest part of the HATDM. In

some cases, two nearly simultaneous retrievals are spaced by less than the thickness of

the latitudinal band and so appear close together. The dust distributions in these closely

spaced retrievals are generally similar.
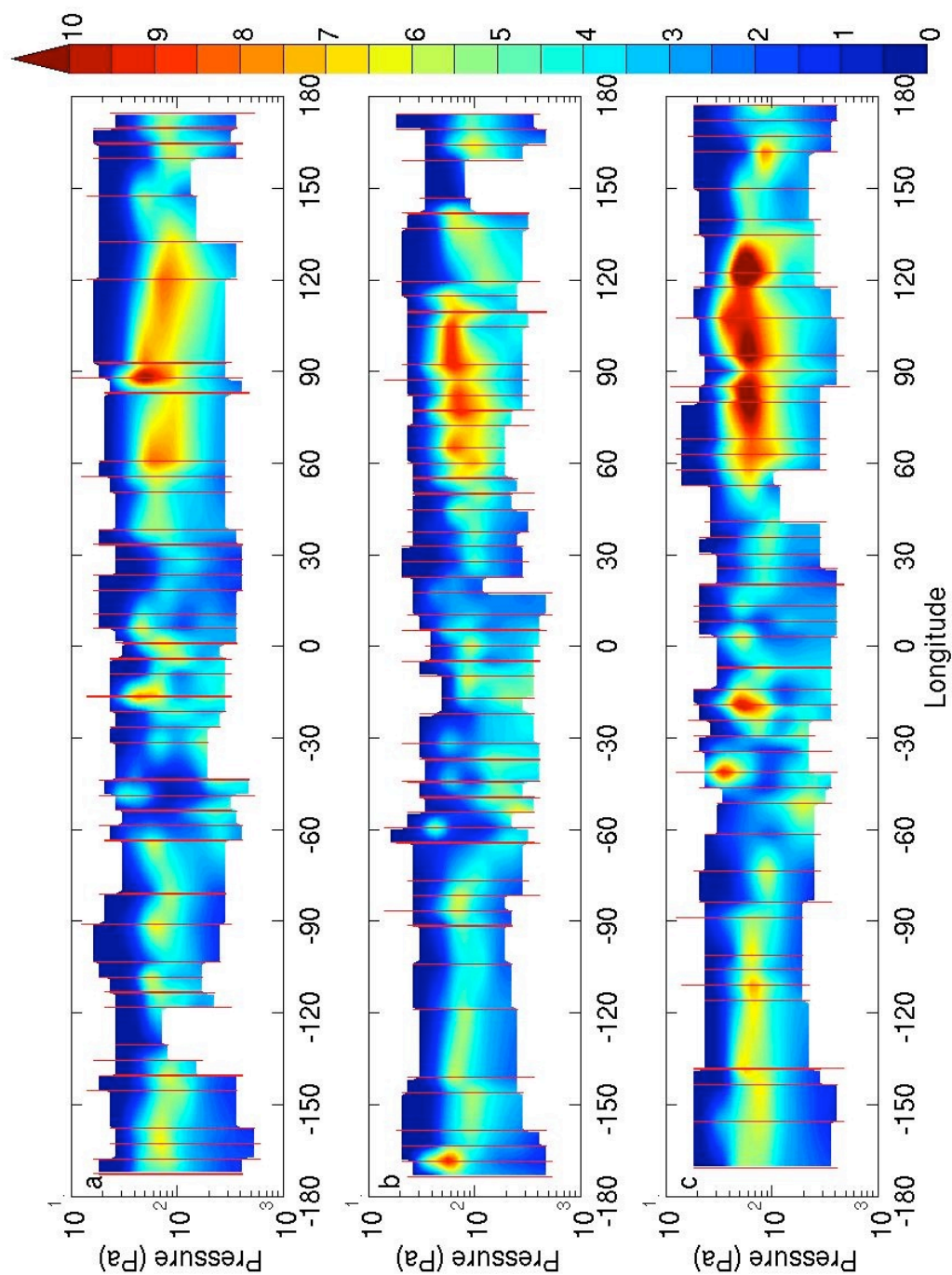
Figure 5.3. Interpolated cross-section of dust density scaled opacity$*10^4$ m^2 kg^{-1} for all nightside retrievals between 24.3°and 26.3° N over : (a) L$_s$=88°—90°, MY 29; (b) 78°—80°, MY 29; (c) 98°—100°. The mean longitude of each retrieval and the vertical range on which dust was retrieved is marked with a red line.
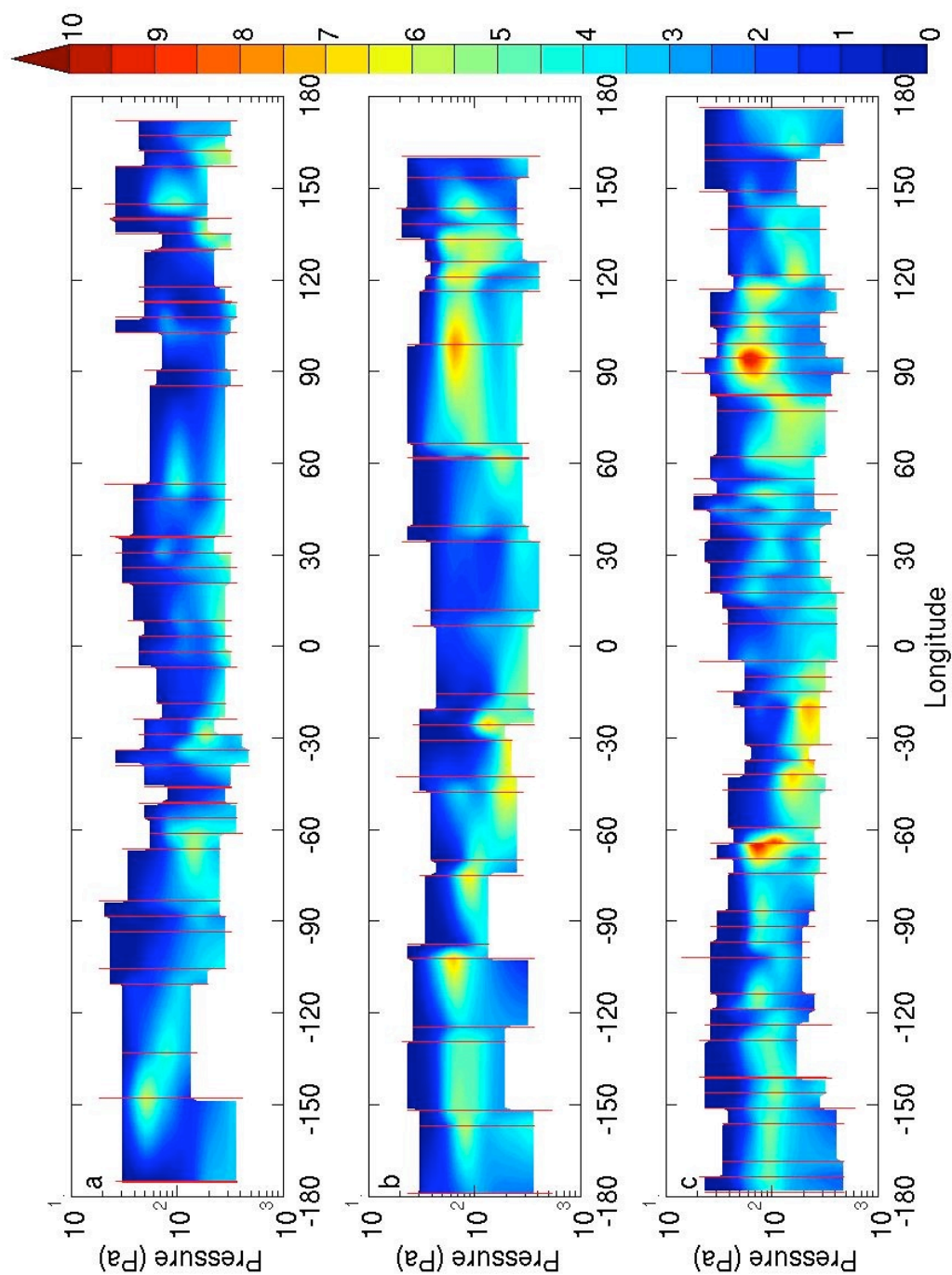
Figure 5.4. Interpolated cross-section of dust density scaled opacity*10^4 m^2 kg^{-1} for all nightside retrievals between 24.3°and 26.3° N over: (a) L$_s$=36°—38°, MY 29; (b) 44°—46°, MY 29; (c) 50°—52°, MY 29. The mean longitude of each retrieval and the vertical range on which dust was retrieved is marked with a red line.

Figure 5.5. Interpolated cross-section of dust density scaled opacity*10^4 m^2 kg^{-1} for all nightside retrievals between 24.3° and 26.3° N over : (a) L_s=132°––134°, MY 29; (b) 134°––136°, MY 29; (c) 138°––140°. The mean longitude of each retrieval and the vertical range on which dust was retrieved is marked with a red line.
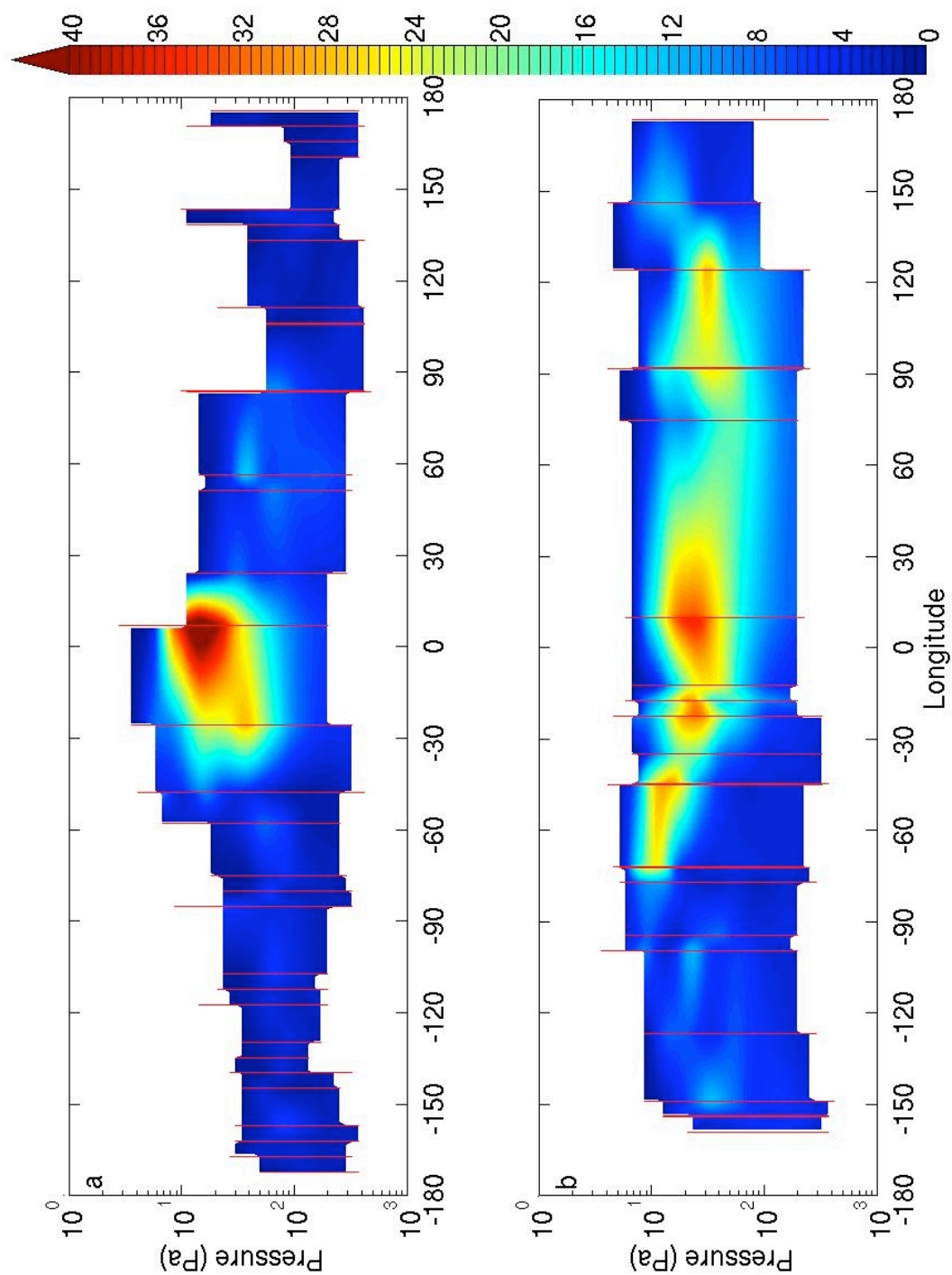
Figure 5.6. Interpolated cross-section of dust density scaled opacity (10^{-4} m^2 kg^{-1}) for all nightside re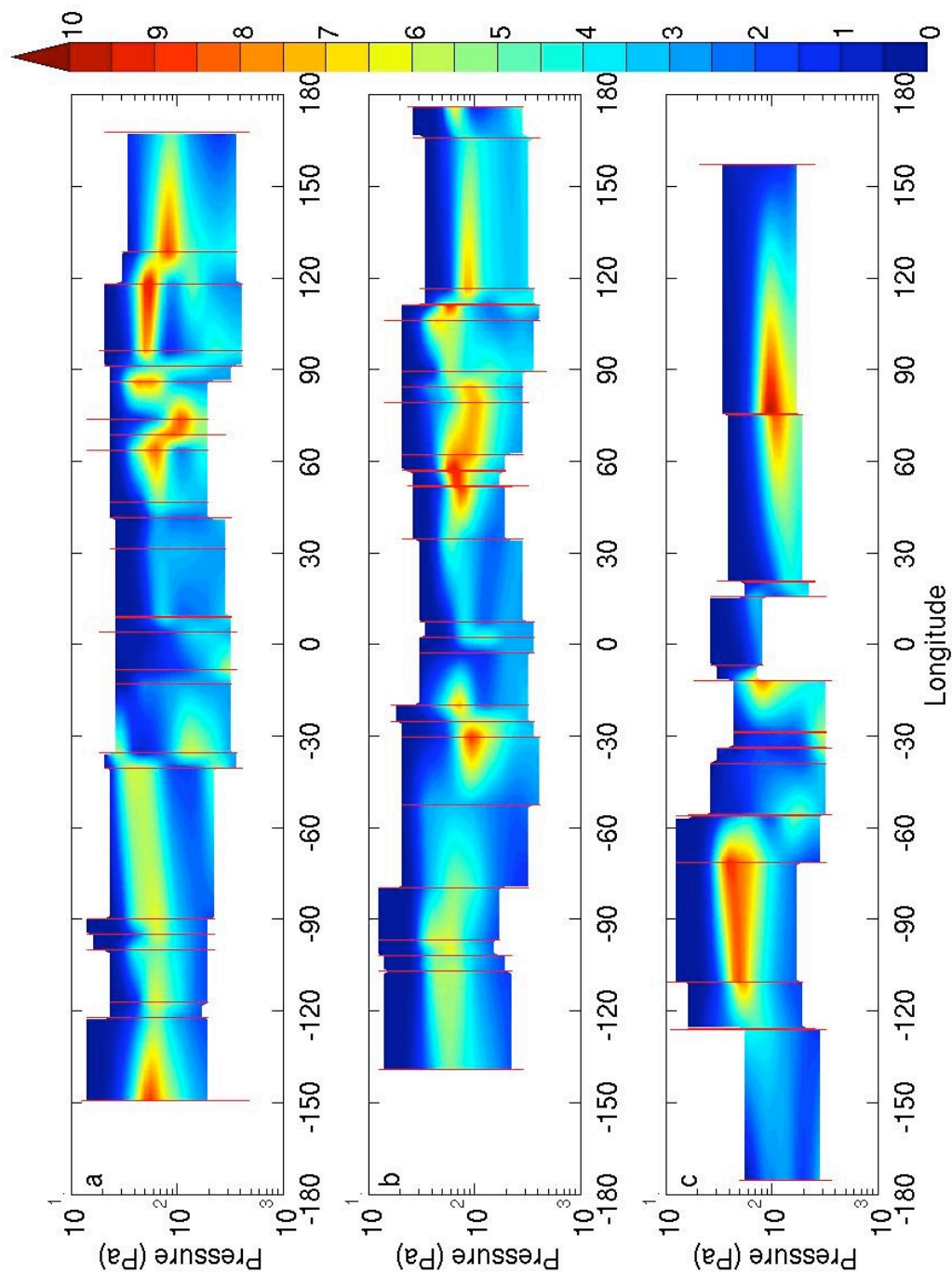trievals between 24.3° and 26.3° N over : (a) L_s=142°—144°, MY 29; (b) 146°—148°, MY 29. The mean longitude of each retrieval and the vertical range on which dust was retrieved is marked with a red line.

Figures 5.3a-c show the longitudinal dust distribution at northern summer solstice and 10° of L_s before and after. The striking feature is how similar the distributions over this period. There is an enriched layer of dust that spans 30° E to 50° W at ~80 Pa. This layer has especially high dust density scaled opacity between 60° and 135° E. The area without the enriched layer generally has more dust at higher pressure levels than the rest of the longitudinal band but can have enriched layers of dust discontinuous with the broader enriched layer.

Figures 5.4a-c shows that a qualitatively similar longitudinal dust distribution first emerges around L_s=40° during MY 29. The distribution may be losing this character at around L_s=135° (Figures 5.5a-c). A longitudinally broad enriched layer emerges at this latitudinal band again at around L_s=140°, but this layer is much higher in dust density scaled opacity and reaches lower pressure levels (as low as 10 Pa). Thus, the characteristic longitudinal pattern of dust at northern summer solstice persists during the exact same period during which the HATDM persists (see Chapter 4). Note that the change between Figures 5.5c, 5.6a, and 5.6b occur over the course of 6° of L_s, a much briefer period than that which separates Figures 5.3b and 5.3c. Therefore, the dust distribution around northern summer solstice is remarkably static in comparison with the distribution later in the summer.

5.3.4 Discussion

Not only is the longitudinal dust distribution within the HATDM relatively static, it is statically inhomogeneous, both longitudinally and as an enriched layer in the vertical. Presumably, on some characteristic timescale, the longitudinal distribution would be

homogenized by advection, while the vertical distribution would be homogenized

(made more uniform) by sedimentation and vertical eddy diffusion. Yet it is not.

In the case of zonal advection, horizontal inhomogeneities should be smoothed on

a timescale equivalent to ratio of the circumference of the latitude circle ($\sim 2 \times 10^7$ m) to

the characteristic zonal wind speed at the level of the enriched layer (10—20 ms^{-1}

easterly [*Forget et al.*, 1999]). This is equivalent to 1—2×10^6 s. The sedimentation

velocity under martian conditions is approximately:

$$v_s = \frac{kr}{\rho} \qquad\qquad (5.1)$$

where k is a constant of proportionality (~ 15 kg s^{-1} m^{-3}), r is the particle radius, and ρ is

the air density [*Murphy et al.*, 1990]. For 1 μm sized particles, Eq. 5.1 would predict

sedimentation velocities of ~ 0.01 ms^{-1} at 20 km above the surface, which would decrease

at lower altitudes. An enriched layer at 20 km would fall to 10 km and thereby become

diluted within ~ 1—3×10^6 s. *Korablev et al.* [1993] estimate the vertical eddy diffusivity

of the atmosphere in the tropics during early northern spring to be $\sim 10^6$ cm^2 s^{-1}, which

corresponds to a vertical mixing time of $\sim 4 \times 10^6$ s for the lower 20 km of the atmosphere.

The timescale on which the dust distribution is static is at least $\sim 3.9 \times 10^6$ s (the difference

between the periods used for Figures 5.3b and 5.3c) and perhaps as great as 1.6×10^7 s (the

difference between the periods used for Figures 5.4c and 5.5a). This timescale is thus

either similar or greater than the timescales of advection, sedimentation, and vertical eddy

diffusion, implying that this dust distribution is sustained by dust lifting, transport, and

removal processes that effectively oppose advection, sedimentation, and eddy diffusion

throughout late northern spring and early northern summer.

As noted in Chapter 4, the transition in the dust distribution at around L_s=140°

is contemporaneous with a regional dust storm in the tropics observed by the Thermal

Emission Imaging System (THEMIS) on Mars Odyssey and the Mars Color Imager

(MARCI) on MRO. Longitudinal sampling is much poorer after this period, so cross-

sections of similar quality to those in Figures 5.3—5.6 cannot be constructed in this

latitudinal band until at least L_s=160°. I shall discuss in the next Section whether the

enriched layer in Figures 5.6a-b is a signature of the dust storm activity observed by

THEMIS and MARCI

5.4 Possible Causes of the HATDM

5.4.1 Approach

In this part of the Chapter, some processes that could produce the HATDM during

northern spring and summer are discussed. In each case, the theoretical and observational

basis for each process are reviewed and past work is supplemented with additional

modeling where necessary. Where possible, I attempt to isolate the signature of the

process within the MCS observations on the basis of previous or contemporaneous

observational records. Finally, I evaluate whether the process is likely to be responsible

the HATDM based on the available evidence. In most cases, the observational record and

past modeling work are insufficient to determine if a process makes a significant

contribution to the HATDM. In those cases, I identify what further modeling experiments

or observations are needed.

5.4.2 Dust Storms

The potential for regional to planetary-scale dust activity to produce equatorial maxima in dust mass mixing ratio by entraining dust into a vigorous cross-equatorial Hadley cell is a well-known phenomenon in GCM and simpler three-dimensional simulations [e.g., *Haberle et al.*, 1982; *Newman et al.*, 2002b; *Kahre et al.*, 2008]. *Newman et al.* [2002b] simulates the evolution of a dust storm in Hellas that produces a zonal average dust mass mixing ratio profile with a maximum stretching from ~60° N to 60° S at 25—35 km of 10—15 ppm. The simulated maximum appears somewhat bifurcated, possibly due to the influence of a weak meridional cell in the southern high latitudes. But the high optical depth region of lifting is mainly restricted to Hellas and is extremely shallow, leaving a gap in mass mixing ratio between the lifting area at the surface and the maximum at 25—35 km.

Dust storms also could enhance the appearance of a maximum in dust mass mixing ratio above the surface in an average such as a zonal average. The retrieval algorithm does not attempt retrieve dust at altitudes at which the line-of-sight opacity is above 2.5 (equivalent to ~0.05 km^{-1} in the retrieved profile) [*Kleinböhl et al.*, 2009]. Assuming the air density at the surface is ~1.5×10^{-2} m^2 kg^{-1}, the limit on dust density scaled opacity near the surface is relatively high (~3.3×10^{-3} m^2 kg^{-1}), but scattering and potentially higher dust grain size near the surface may limit retrieval success or retrieval vertical range in the vicinity of dust storms. Retrievals of outflow from dust storms, which might contain enriched layers of dust at altitude (lower limb opacity), thus may be more successfully retrieved. The preferential inclusion of the retrievals of outflow in an average could create a local maximum in dust mass mixing ratio above the surface. Such
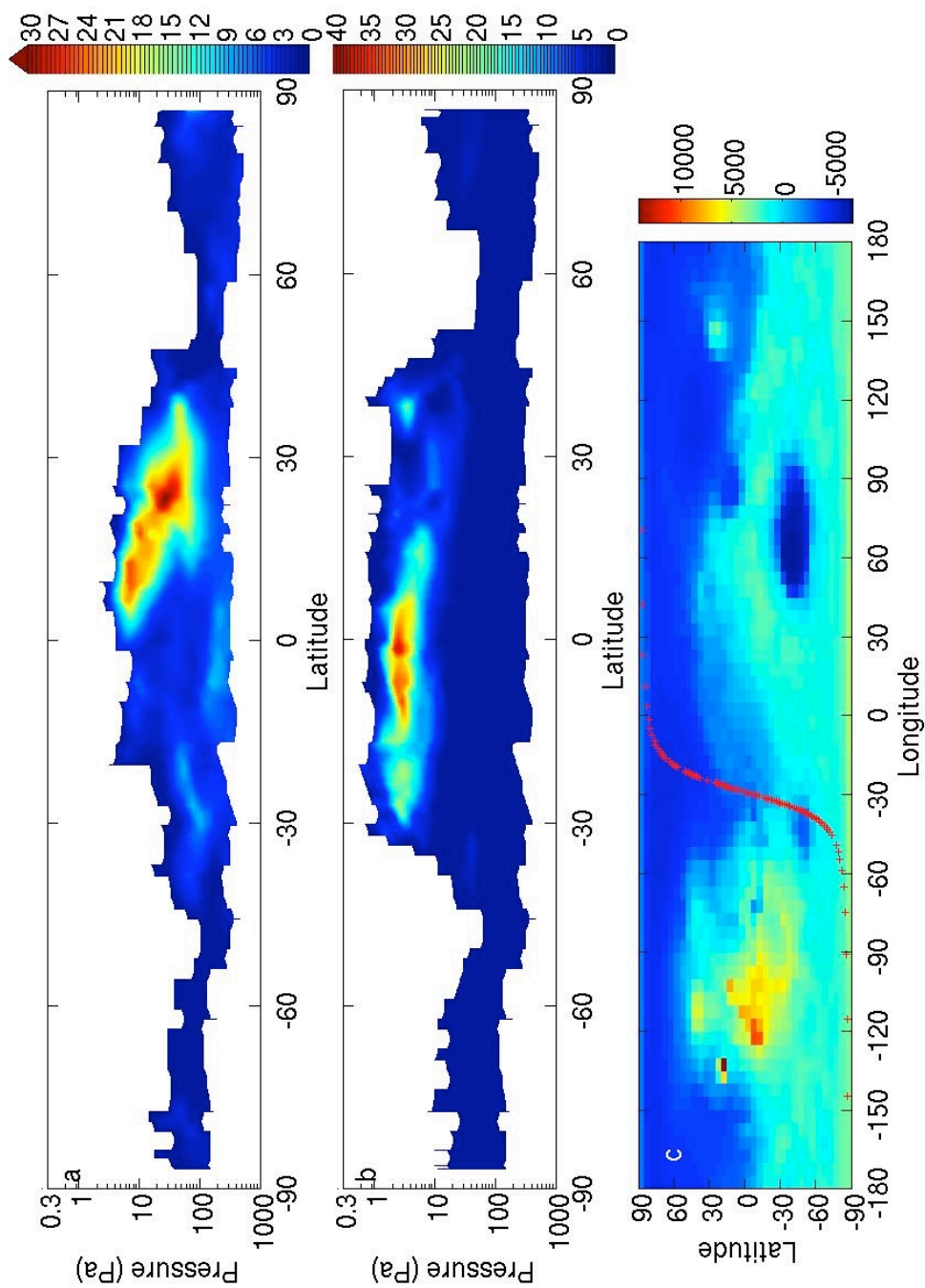
Figure 5.7. (a) and (b) Cross-sections of dust density scaled opacity (10^{-4} m^2 kg^{-1}) and water ice density scaled opacity (10^{-3} m^2 kg^{-1} from all available retrievals in a single nightside MRO pass on 16—17 October 2008 from 23:50 to 00:47 UTC (L$_s$=142.9412°—142.9612°, MY 29). (c) Mean latitude and longitude of each retrieval used in (a) and (b) (red crosses) on a topography (m) map (colors) based on MOLA data.

a maximum would be enhanced relative to a local maximum arising only from the averaging of retrievals of uniformly mixed dust profiles over regions of active lifting with retrievals of detached dust hazes in the outflow of the dust storm.

Enriched layers of dust attributable to dust storm outflow can be observed in MCS retrievals. Figures 5.7a-b show latitudinal cross-sections of dust and water ice density scaled opacity constructed from all nightside retrievals in a single orbit. This particular cross-section contains one of the retrievals used in Figure 5.6a and so effectively intersects it. The mean latitudes and longitudes of these retrievals are marked on a topography map in Figure 5.7c. In Figure 5.7a, there appears to be a haze of dust with density scaled opacity of up to 3×10^{-3} m^2 kg^{-1} over the northern tropics. Water ice clouds with density scaled opacity of up to 4×10^{-2} m^2 kg^{-1} are present south of this haze at pressure level similar to the lowest pressure level (~5 Pa) the dust haze penetrates. Based on the methods described in Chapters 4 and 6, the estimated dust mass mixing ratio is ~40 ppm, while the estimated water ice mass mixing ratio is up to 85 ppm, which is approximately a factor of 5 greater than the estimated zonal average water ice mass mixing ratio at this time of year (Chapter 6). The water ice mass mixing ratio of the cloud also is equivalent to a column-uniform water vapor mixing ratio of ~15 precipitable microns, the approximate zonal average column water vapor mixing ratio observed by the Compact Reconnaissance Imaging Spectrometer (CRISM) on MRO at this latitude and season [*Smith et al.*, 2009].

The observations in Figure 5.7 were made on 16—17 October 2008. *Malin et al.* [2008a] report that during the week of 13—19 October 2008 "water ice clouds and diffuse dust from last week's regional dust storm lingered over the MER-B landing site"

at Meridiani Planum. While the observations in Figure 5.7 were made significantly

westward of Meridiani Planum, even higher dust concentrations were present along the

northern tropic further east (Figure 5.6a). (The retrieval at ~10° E in Figure 5.6a does not

have any successful retrievals near it in the same orbit that could confirm directly that

this haze was present over Meridiani Planum.) *Malin et al.* [2008a] also report dust storm

activity in Chryse Planitia during this week. Since dust concentrations are relatively low

at the longitude of Chryse Planitia (~60° W) in Figure 5.6a, we propose that the dense

dust hazes in Figures 5.6a and 5.7a are the result of advection of dust from "last week's

regional dust storm" reported by *Malin et al.* [2008a], which moved from Solis Planum to

Noachis Terra during the previous week [*Malin et al.*, 2008b].

The high density scaled opacities of the water ice clouds that trail the haze are

consistent with this idea. The estimated water vapor equivalent of these clouds is close to

the measured column mixing ratio of water vapor, suggesting that water vapor was very

deeply mixed in the atmosphere, which is a potential result of water vapor being

transported to high altitudes within the advected dust plume.

If the dust haze was advected across the equator, the direction of transport was

opposite to the sense of the modeled mean meridional circulation in northern summer

[e.g., *Richardson and Wilson*, 2002], in which meridional transport above the surface is

north to south. Therefore, it is possible that the dust was advected in a longitudinally

restricted circulation with flow opposite to the mean meridional circulation. Such a

circulation could be explained by invoking a strong diabatic heat source in the southern

tropics, such as the storm that was the source of the enriched dust layer. In summary,

Figure 5.7 seems to show a spectacular example of outflow from a dust storm

producing an apparent maximum in dust mass mixing ratio at high altitude above the

surface.

Dust storm outflow, however, is not a good explanation for the HATDM in late

northern spring and early northern summer, because dust storm activity is relatively rare

in the tropics during this period. *Cantor et al.* [2001] presents a detailed climatology of

local dust storm activity in 1999. This study lacks coverage in northern spring and early

northern summer, during which the tropical maximum in mass mixing ratio is most

pronounced. But *Cantor et al.* [2001] does present results from earlier studies using

Viking Orbiter data that are consistent with the presence of very few dust storms in or

near the tropics around the summer solstice. Some local dust storm activity is observed at

around L_s=110° just northwest of Elysium Mons, but activity at other longitudes on the

edge of the northern tropics is relatively rare until northern fall. *Cantor et al.* [2006]

presents a less detailed but interannual climatology of dust storm activity over most of the

period of Mars Orbiter Camera (MOC) observations and shows that local dust storm

activity around northern summer solstice is generally confined to the polar cap edges,

especially in the northern hemisphere. Therefore, if local dust storms are responsible for

the tropical maximum in mass mixing ratio, only a small number of dust storms could be

involved.

The THEMIS optical depth measurements [*Smith*, 2009] provide further support

for the absence of dust storms in the tropics. Cap edge dust storm activity in the northern

hemisphere generally has zonal average 1065 cm^{-1} optical depths of 0.1—0.3. The

tropical dust storm activity in mid to late northern summer of MY 29 is associated with

zonal average optical depths of 0.3—0.5 or greater. Zonal average optical depth at 30°-40° N and throughout the tropics is generally 0.05—0.10 through northern spring and summer, which appears to be too low to indicate dust storm activity.

I also have considered the possibility that outflow from north cap edge dust storm activity might be advected into the tropics. Such a plume probably would have to cross the transport barrier due formed by the southerly flow and downwelling due to a secondary PMOC [*Richardson and Wilson*, 2002]. This barrier may be manifested by a region of lower dust density scaled opacity at ~45° N in Figure 5.1a and a mostly longitudinally uniform band of lower dust concentrations at a similar latitude in Figure 5.2. Moreover, the average dust density scaled opacities around the northern cap edge are somewhat lower than those observed in the tropics (Figure 5.2), so it seems unlikely that the northern cap edge activity could be a source of dust for the HATDM.

5.4.3 Orographic Circulations

There are many reasons why high altitude locations on Mars might or might not be unusually active sites for dust lifting. The main argument against dust lifting at high altitudes is that the threshold wind velocity for dust lifting is inversely proportional to the square root of density. This effect may be compensated in part by the higher winds that generally occur at higher altitudes. In addition, pressures at the high altitudes of Mars are on the rapidly increasing portion of the Päschen curve of CO_2, which may permit stronger electric fields than at lower altitudes and enhanced dust lifting by electrostatic effects [*Kok and Renno*, 2006]. Yet concerns about the difficulty of lifting dust from mountain tops may be irrelevant to the role of orography in the dust cycle, since mountains on Mars

might act as a means for dust to be lifted at lower altitudes but injected into the atmosphere at higher altitudes.

The proposed dynamics of orographic injection of dust are fairly simple. During the daytime, the air on the top of the mountain heats more quickly than the air at the bottom of the mountain due to the lower density of the air at the top of the mountain. In addition, the air in contact with the surface of the mountain (either summit or slope) is warmed more quickly than the air at the same altitude away from the mountain. The heated mountain therefore becomes a local center of low pressure, producing a convergent anabatic wind that lifts dust from the slopes and makes the air at the top of the mountain very dusty and even hotter. Simulations by *Rafkin et al.* [2002] of a cloud and hypothetically connected orographic thermal circulation on Arsia Mons showed that the vertical velocities of the anabatic wind were up to 25 ms^{-1} and needed to be balanced by extremely strong (> 40 ms^{-1}) divergent winds at the top of the orographic circulation. The end result is advection of dust at levels on the order of a few ppm at ~20 km altitude at a distance up to 2000 km from the mountain. Such a process would be one plausible source for a HATDM.

The cloud type simulated by *Rafkin et al.* [2002] is called a "mesoscale spiral cloud." This type may be identical to or genetically related to the "aster clouds" observed by *Wang and Ingersoll* [2002]. Aster clouds form in late northern summer or early northern fall, are 200—500 km long, 20—50 km wide, and are found at altitudes of 15 km or more above the surface. Both types of clouds are thought to be generated by strong upslope winds. As of yet, there is no sufficiently detailed climatology of mesoscale spiral clouds or aster clouds to permit direct comparison with MCS retrievals.

Moreover, the present MCS retrieval dataset is not ideal for isolation of orographic cloud dynamics for three key reasons. First, the dearth of dayside equatorial profiles in the tropics throughout much of northern spring and summer limits information about the aerosol distribution over the volcanoes at the time of day and season when the upslope winds are thought to be most active. Second, both observations and modeling [*Benson et al.*, 2006; *Michaels et al.*, 2006] suggest that orographic water ice clouds are strongly entrained into the global wind field once they escape their local mesoscale circulations. Orographic dust clouds likely would be subject to the same effect and would tend to advect zonally. In that case, roughly synchronous (within a few minutes) observations over the volcano and at adjacent longitudes in the same latitudinal band could verify their orographic origins. Such observations would be one possible use of cross-track observations for an instrument on a polar-orbiting spacecraft. Third, if dust advected from the volcano is blown off at relatively shallow depths above the high elevation surface, the current retrievals do not reach close enough to the surface to "see" this dust.

As an example of what is currently possible, Figures 5.8a-e show the seasonal variability in the vertical dust distribution over Mars's five tallest volcanoes in order of increasing latitude (Arsia Mons, Pavonis Mons, Ascraeus Mons, Olympus Mons, and Elysium Mons) during MY 29. The extrapolated surface pressures of each retrieval are shown in order to indicate where retrievals are available and show that the profiles are over relatively high terrain (at least 9 km above the Mars Orbiter Laser Altimeter (MOLA) datum in all cases). An MCS retrieval, however, is an integration of information
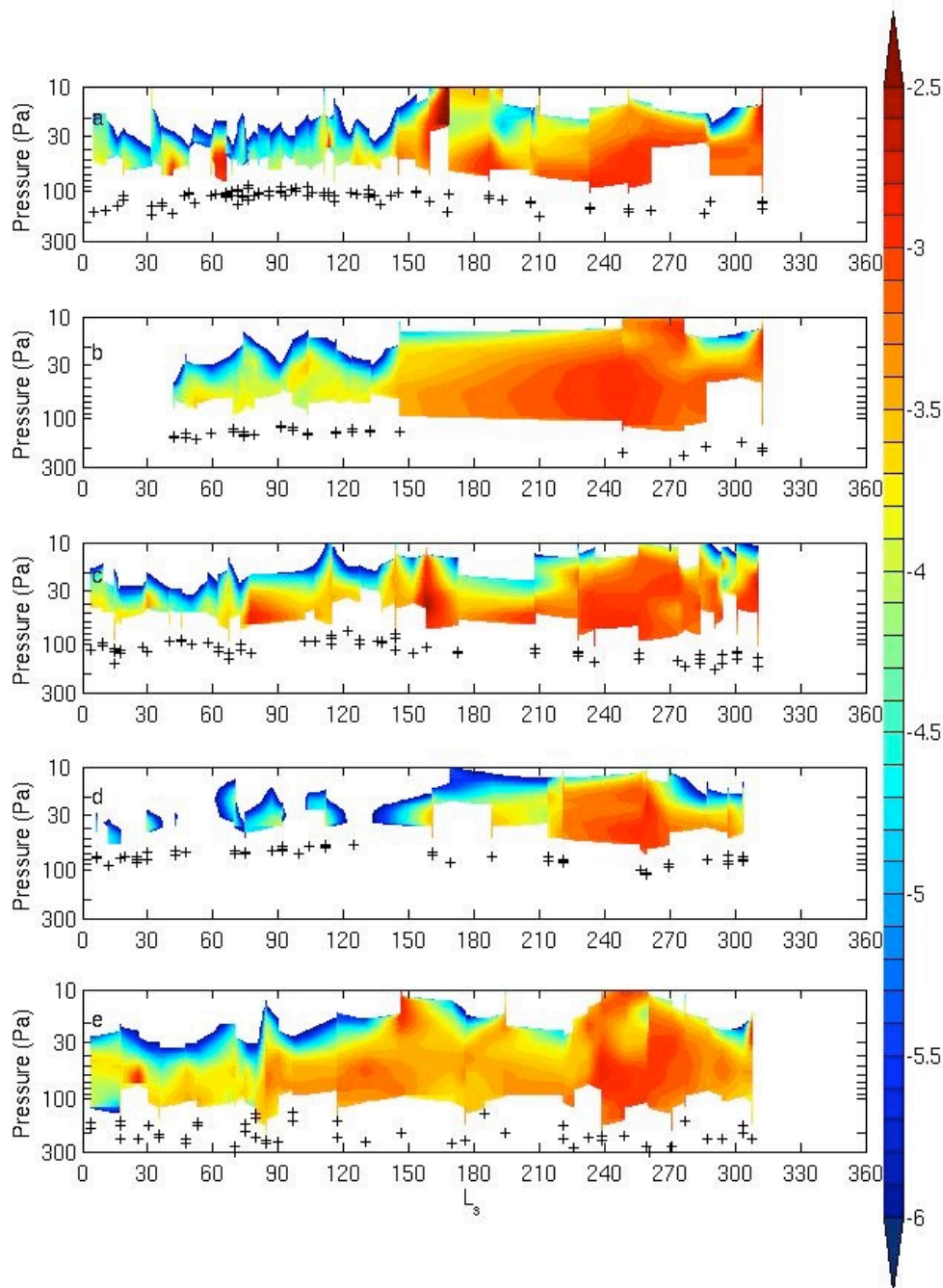
Figure 5.8. Log_{10} of dust density scaled opacity (m^2 kg^{-1}) from both dayside and nightside retrievals. The black crosses indicate the L_s and extrapolated surface pressure for each retrieval: (a) near Arsia Mons (7.5°—11.5° S, 115.5°—125.5° W, estimated scene altitude of the profile > 15 km above the MOLA datum); (b) near Pavonis Mons (1.2° S—2.8° N, 108.4°—118.4° W, estimated scene altitude of the profile > 13 km above the MOLA datum); (c) near Ascraeus Mons (9.8°—13.8° N, 99.5°—109.5° W, estimated scene altitude of the profile > 15 km above the MOLA datum); (d) near Olympus Mons (16.4°—20.4° N, 129°—139° W, estimated scene altitude of the profile > 20 km above the MOLA datum); (e) near Elysium Mons (22.8°—26.8° N, 141.9°—151.9° E, estimated scene altitude of the profile > 9 km above the MOLA datum).

over a relatively broad volume, so Figures 5.8a-e should not be interpreted as equivalent to a record of narrow soundings above the volcano's summit by a balloon or a lidar.

The atmosphere above the volcanoes is dustier in southern spring and summer than in northern spring and summer, just like elsewhere in the tropics (Figure 5.1). In northern spring and summer, the dust distribution over each volcano resembles the dust distribution at the latitude of the volcano if it were cut off at higher pressures, followingthe general pattern of the HATDM, which is dustier and present at lower pressures in the northern tropics than the northern tropics. This contrast can be seen at ~60 Pa during northern spring and much of northern summer. Elysium Mons is much dustier than Pavonis Mons (Figures 5.8e and 5.8b). Olympus Mons (Figure 5.8d) has a very high surface, so retrievals do not reach pressures higher than ~40 Pa. In the zonal average (Figure 5.1), Mars is relatively free of dust at that pressure at this latitude and season, so Olympus Mons is relatively free of dust. In a few exceptional cases, high dust density scaled opacities are observed over the volcanoes at ~60 Pa, the approximate pressure of the HATDM.

Based on the available evidence, orographic injection is not a likely contributor to the HATDM. If aster clouds are the primary means of dust injection, their climatology (as presently known) differs from the HATDM. Like tropical dust storm activity, aster clouds occur too late in northern summer. Moreover, if orographic injection were primarily responsible for the HATDM, longitudinal inhomogeneities in the dust distribution likely should take the form of higher dust density scaled opacities downwind and nearer the volcano than upwind and further away. In Figure 5.3, the cross-sections may sample the

modeled and observed path along which water ice clouds over Olympus Mons advect

[*Benson et al.*, 2006; *Michaels et al.*, 2006], which is north and west of Olympus Mons

(134° W). The cross-section likewise intersects Elysium Mons at ~147° E. Yet the

enriched dust layer is of similar density scaled opacity on both sides of Olympus Mons

and indeed density scaled opacity is usually at least half as high around Elysium Mons

than at 60°—120° E. Orographic injection also does not explain the enriched layers of

dust in individuals retrievals at 20°—40° W in Figure 5.2c, a location distant from

significant topography.

Despite poor evidence for the mechanism causing the HATDM, the parsimony of

orographic injection, however, remains attractive. The simplest way of explaining a layer

of dust at 20 km above the mean altitude of the surface is that it comes from a surface 20

km above the mean. As long as the observational record of dust clouds over volcanoes is

sparse and the daytime dust distribution over or near volcanoes remains poorly known, an

orographic source for the HATDM cannot be fully disproven. Past modeling experiments

have focused on the dust transport out of mesoscale circulations around volcanoes. Future

experiments should simulate the contributions of these circulations to the global dust

distribution in greater detail.

5.4.4 Dust Pseudo-Moist Convection

Dust devils are an attractive possible source for the HATDM, since they are thought to be

the dominant mechanism for lifting dust under relatively clear conditions. *Fuerstenau*

[2006] has proposed that solar heating of the dust load within a dust devil plume could

result in a type of pseudo-moist convection, in which solar heating of the dust load

exceeds adiabatic cooling of the parcel. Dust devil plumes therefore might be capable

of breaking through the top of the boundary layer and detraining significant amounts of

dust at altitude.

To supplement simple calculations of *Fuerstenau* [2006], which neglect the

important process of entrainment of environmental air into dusty parcels, the single

column cloud model of *Gregory* [2000] was modified to simulate the ascent of dust

parcels. The model of *Gregory* [2000] has been successful in representing both shallow

and deep cumulus convection on the Earth. In our model, a parcel with a given initial dust

concentration, q_0, is in thermal equilibrium with the environment and has some initial

vertical velocity, w_0 at the surface ($z=0$). Kinetic energy is defined as:

$$K = \frac{1}{2} w^2 \tag{5.2}$$

and the temperature of the parcel is allowed to evolve discretely in the height domain:

$$T(z + \Delta z) = T(z) - \left(\frac{g}{c_p} \Delta z \right) + \left[\frac{\Delta z}{w(z)} \varepsilon F_0 \cos\xi \exp(-\tau(z)/\cos\xi) \left(\frac{q(z)}{c_p} \varsigma \right) \right] \tag{5.3}$$

where g is the acceleration due to gravity, c_p is the heat capacity, Δz is the resolution of

the height grid, ξ is the solar zenith angle, is the efficiency of absorption of solar

radiation by dust (including scattering), F_0 is the top of the atmosphere flux, τ is the

environmental optical depth in the solar band, and ς is the conversion factor between

mass mixing ratio and density scaled opacity in the solar band.

The buoyancy is then defined as:

$$B = g \frac{T_p - T_{env}}{T_{env}} \tag{5.4}$$

and the entrainment rate, E, is parameterized as:

$$E(z + \Delta z) = \frac{k_e}{w(z)^2} B(z + \Delta z)$$

(5.5)

where k_e is a constant. *Gregory* [2000] estimate the value of this constant to be ~0.045 for deep cumulus convection and ~0.09 for shallow cumulus convection.

The cooling of the temperature of the parcel and dilution of the dust mass mixing ratio by entrainment of environmental air is then represented as:

$$T_p^* = \frac{\left(E\Delta z T_{env} + T_p\right)}{1 + E\Delta z},$$

$$q_p^* = \frac{\left(E\Delta z q_{env} + q_p\right)}{1 + E\Delta z}$$

(5.6a-b)

 if $E > 0$, where the starred quantities denote the transformed quantities after entrainment.

Finally, K is allowed to evolve:

$$K(z + \Delta z) = \left[K(z) + aB(z + \Delta z) - (2bDK(z)) - (2E(z)K(z))\right]\Delta z$$

(5.7)

where a and b are constants derived from large eddy simulations of terrestrial convection, and are estimated to be 1/6 and 0.5 respectively. D is the detrainment rate, which we assume to be zero when $E > 0$ and equal to $-E$ when $E < 0$. This may be an underestimate.

The total Convective Available Potential Energy (CAPE) is then estimated as:

$$CAPE = \int_0^{z_{LNB}} B dz$$

(5.8)

where z_{LNB} is the level of neutral buoyancy.
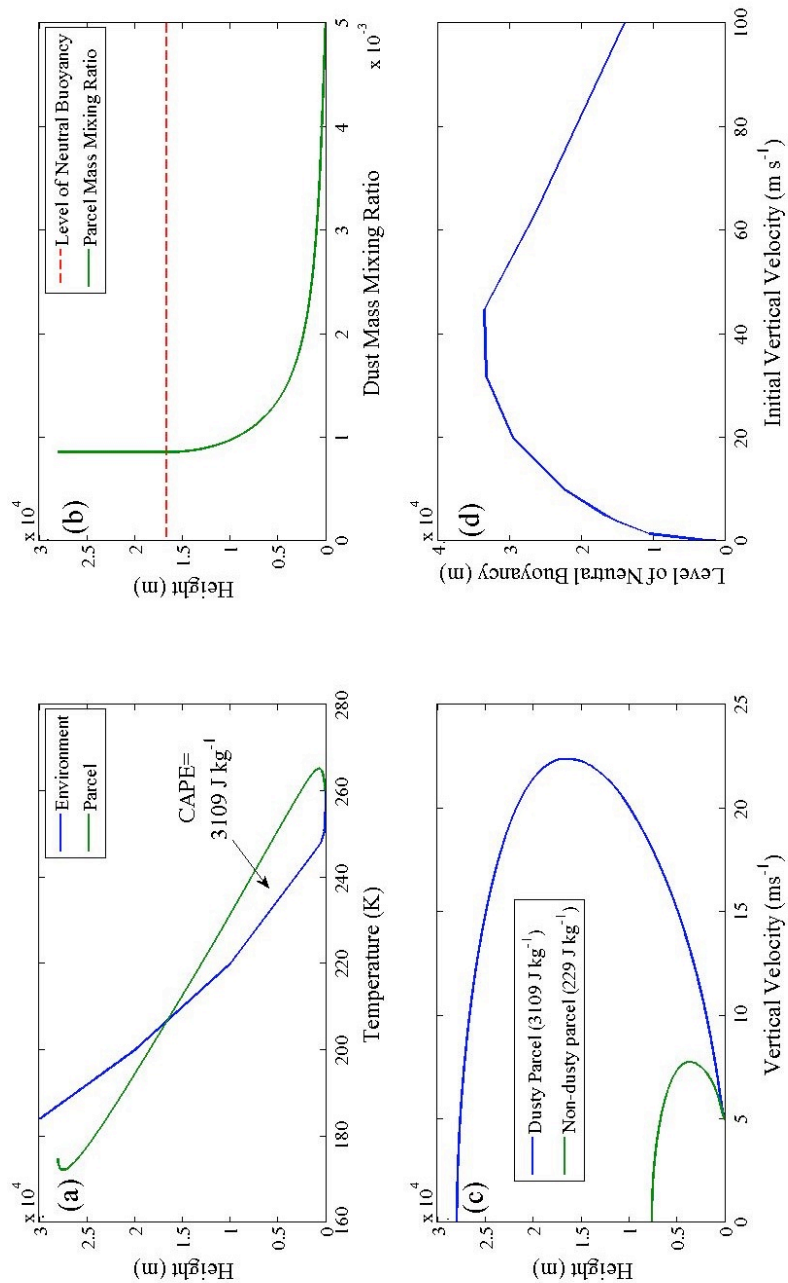
Figure 5.9. Results of simulations of dusty parcels at the Mars Pathfinder site: (a) parcel temperature profile vs. environmental temperature profile; (b) dust mass mixing ratio vs. height; (c) vertical velocity profile of a dusty parcel vs. a dustless parcel; (d) sensitivity of the level of neutral buoyancy to the assumed initial vertical velocity.

Table 5.1. Environmental temperature profile used for the single column model simulations of dust-heated convection

Height (m)	Temperature (K)
0	260
100	251
500	248
1,500	245
10,000	220
20,000	200
30,000	184
40,000	174
50,000	165

Table 5.2. Parameters for the single column model simulations of dust-heated convection

Parameter	Value	Citation (if any)
G	3.73 ms^{-2}	N/A
c_p	756 J kg^{-1}	N/A
ς	482 m^2 kg^{-1}	N/A
Δz	10 m	N/A
p_s	670 Pa	*Schofield et al.* [1997]
q_0	5*10^{-3}	*Metzger et al.* [1999]
w_0	5 ms^{-1}	N/A
τ_0	0.2	N/A
ν	0.1	N/A
k_e	0.09	*Gregory* [2000]
F_0	499 Wm^{-2}	N/A
ε	0.11	*Tomasko et al.* [1999]
ξ	11.8°	N/A

Figures 5.9a-d show the results of a single column simulation using Eqs. 5.2—5.8 of hypothetical dust parcels associated with dust devils observed near the Mars Pathfinder site ~12:40 LST (9:30 UTC) on 15 July 1997 (L_s=148.15°) [*Metzger et al.*, 1999; *Fuerstenau*, 2006]. The environmental temperature profile (Table 5.1) is based on Mars Pathfinder observations, temperature retrievals from the Miniature Thermal Emission Spectrometer, and L_s=145°—150° zonal average temperatures at the approximate latitude of Mars Pathfinder during MY 29 from MCS retrievals. The other parameters of the simulation are given in Table 5.2.

Figure 5.9a shows environmental and parcel temperature profiles of the simulation: a plot analogous to a SKEW—T diagram used in terrestrial weather forecasting. Note that the Convective Available Potential Energy (CAPE) of this parcel is comparable to strong terrestrial thunderstorm activity. The parcel is most strongly heated within the first couple of kilometers of ascent. Within the same height range, environmental temperatures decrease quickly in the superadiabatic layer near the strongly heated surface. At ~1,500 m, the approximate top of the boundary layer in this scenario, the dusty parcel is almost 20 K warmer than the external environment. The heating effect from the more dilute dust loading above ~2,500 m is not strong enough to keep the parcel from cooling more strongly than the environment. This strong gain in buoyancy near the surface relative to the rest of the path of ascent arises from the assumption that entrainment is inversely proportional to the square of velocity, so the parcel's dust concentration is strongly diluted by entrainment of environmental air when it is moving more slowly. On one hand, the low vertical velocity of the parcel enhances radiative

heating relative to adiabatic cooling. On the other hand, it bleeds off dust through

entrainment.

The effect of entrainment on the dust mass mixing ratio is significant. By ~5 km,

the parcel has a mass mixing ratio of ~25% of its initial value (Figure 5.9b). Accounting

for the fall off in density, the opacity of the parcel has fallen by a factor of six. By the

level of neutral buoyancy, the mass mixing ratio has stabilized at ~20% of its initial

value, but the relative opacity is ~5% of its initial value. One objection to the idea that

dust devils are capable of dust injection at these heights is that dust devil heights from

orbital surveys are no higher than ~8 km [*Fisher et al.*, 2005]. These height estimates,

however, are based on the length of the dust devil shadow. To the best of my knowledge,

the opacity limit for shadow detection is unknown, as is the effect of conservative mixing

or entrainment with height on dust devil shadows.

In addition, any dust load of significant depth is subject to a self-shielding effect.

The dust opacity near the surface in the simulated case is ~0.032 m^{-1}. So if the sun is at

high elevation in the sky, only the top 30 m or so of the dust column are strongly heated

and may detach somewhat from a primary plume of greater depth. If this detachment is

primarily vertical, heating of the lower portion of the column will be limited, especially

in the critical region of ascent through the superadiabatic layer. Comparison of the

vertical velocity profile of a dusty parcel and a parcel without dust (equivalent to a fully

shielded parcel) shows that such a shielded parcel would reach neutral buoyancy at

~3—4 km and cease ascent at ~7 km (Figure 5.9c), entirely consistent with observed dust

devil heights. In the case of the shielded parcel, buoyancy is entirely derived from ascent

through the superadiabatic layer, so weakening of this layer later in the day will limit the

ascent of shielded parcels as well. These results suggest that the entire circulation of a dust devil probably does not penetrate the boundary layer. Instead, a number of small thermals detached by solar heating from the main dust devil plume ascend and then bring exceptionally dusty air (800—900 ppm in the simulated case) to 15—25 km altitude.

Figure 5.9d shows the sensitivity of the simulation results to the initial vertical velocity used and suggests that initial vertical velocities as low as ~2 ms^{-1} allow parcels to rise ~10 km. However, if the parcel rises too quickly, solar heating will not be able to compensate for adiabatic cooling, explaining the decay of the level of neutral buoyancy at high (and highly unrealistic) initial vertical velocity. In Figure 5.10, the conditions of the simulation were changed to consider the sensitivity of the results to initial dust mass mixing ratio of the parcel and initial vertical velocity. The colored contours conservatively plot the level of neutral buoyancy for each set of assumed conditions. The white contour marks 4 km, a typical tropical boundary layer height [*Hinson et al.*, 2008], and envelops a v-shaped phase space, in which the range of initial vertical velocities that can support boundary-layer breaking convection broadens with increasing initial mass mixing ratio. At the initial dust mass mixing ratio assumed in the simulation (~5,000 ppm), boundary-layer breaking convection can occur for initial vertical velocities less than 1 ms^{-1}. Thus, even dust plumes with relatively weak vertical velocities, which might arise from processes other than dust devils such as local circulations in craters etc., could be highly unstable with respect to pseudo-moist dust convection.
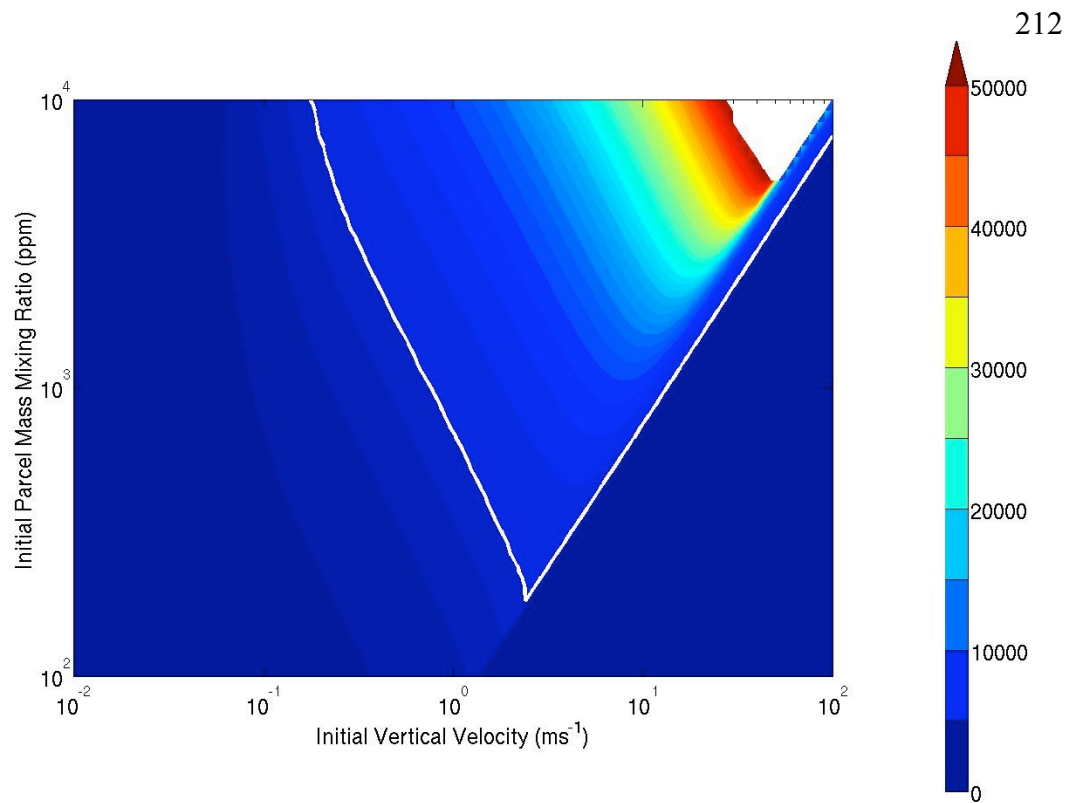
Figure 5.10. Sensitivity of level of neutral buoyancy (m) to initial parcel dust concentration (ppm) and initial parcel vertical velocity (ms^{-1}) The white line indicates the 4,000 m contour, the approximate boundary layer height of the simulation. The white area is indicative of simulations in which the parcel leaves the simulation domain.

Using the results from the simulation, the necessary vertical dust mass flux

($\hat{M}_{dust}$) to produce the HATDM can be estimated as:

$$\hat{M}_{dust} = \frac{\Delta p}{g} \frac{q_{excess}}{t_{sed}}$$ (5.9)

where Δp is the pressure thickness of the enriched layer, q_{excess} is the excess dust mass

mixing ratio of the layer, and t_{sed} is the characteristic time of sedimentation/advection

from the enrichment layer. Assuming Δp=85 Pa, g=3.73 ms^{-2}, q_{excess}=5×10^{-6}, and t$_{sed}$ of

~10^6 s, the necessary dust mass flux is: 1.1×10^{-10} kg m^{-2} s^{-1}. From this result and the

results of the simulation, the fractional area occupied by these thermals ($f_{thermals}$) can be

estimated to be:

$$f_{thermals} = \frac{\hat{M}_{dust}}{\frac{t_{thermals}}{t_{sol}} \rho w q_{thermal}}$$ (5.10)

Assuming that the thermals occur only ~10% of the day and w, $q_{thermal}$, and ρ

correspond to their values at the level of neutral buoyancy of the simulated parcel

(20 ms^{-1}, 9×10^{-4}, and 4×10^{-3} kg m^{-3} respectively), the fractional area occupied by thermals

needs only be 1.6×10^{-5}. Estimates of the fractional area occupied by dust devils range

from 2×10^{-4}-6×10^{-4} [*Ferri et al.*, 2003; *Fisher et al.,* 2005], so the areal footprint of the

thermals can be around an order of magnitude smaller than the areal footprint of dust

devils.

This idea, however, is not observationally falsifiable with the MCS retrieval dataset.

The purported boundary layer breaking dust plumes occur at scales much finer than the

resolution of the observations. Moreover, comparison of dust devil climatologies with

retrieved profiles of dust will not be a sufficiently unambiguous test for two reasons.

First, the two most complete surveys of dust devil activity on Mars disagree about fundamental aspects of the climatology. *Cantor et al.* [2006] analyze orbital imagery of dust devils and find that dust devils are far more common in the north than in the south. *Whelley and Greeley* [2008] analyzes orbital imagery of dust devil tracks and makes the opposite conclusion. Second, the sensitivity of pseudo-moist dust convection to parameters intrinsic to individual plumes such as initial vertical velocity and dust concentration (Figure 5.10) both raises the possibility that dust sources other than dust devils may drive pseudo-moist convection and also may introduce difficult to control intensity related biases in any correlation of dust devil climatologies and the vertical structure of dust.

Instead, the ease at which this effect can be demonstrated by our model and in the analysis of *Fuerstenau* [2006] suggests that this mechanism will become apparent in a mesoscale or large eddy simulation with rapidly updating radiative transfer. If this hypothesis is verified, parameterization within a GCM should be possible by upscaling from the smaller scale simulations. Observational validation likely will require lidar observations in the tropics in tandem with barometry, thermometry, and anemometry from a surface weather station.

5.5.5 Scavenging by Water Ice

Following Eq. 5.1, particles settle at a velocity in proportion to their radius. Eq. 5.1 is a simplification of an approximation of the Cunningham-corrected Stokes velocity at high Knudsen number ($Kn \approx 60$ for a 1 μm particle at the surface of Mars). The full approximation is:

$$v_s \approx \frac{4}{9} \frac{\rho_p r g \delta}{\rho v_t}$$
(5.11)

where δ is a slip-flow correction parameter and v_t is the thermal velocity of the gas [*Murphy et al.*, 1990]. Condensation of water ice on a dust particle will enhance its sedimentation velocity by increasing its radius. The new particle, however, will have a lower density. So if a 1 μm radius dust particle (ρ_p=3000 kg m^{-3}) grows into a 4 μm radius ice particle (the approximate r_{eff} in the aphelion cloud belt [*Clancy et al.*, 2003]), ρ_p of the new particle will be effectively the density of ice (~900 kg m^{-3}). Thus, the sedimentation velocity will increase by ~20%. If the ice particle is 2 μm in radius with a 1 μm radius core of dust, the sedimentation velocity is reduced by ~5%. Thus, if the ice particle sizes are close to the average water ice particle size observed from orbit, condensation of ice on dust does not significantly enhance sedimentation.

Using the Phoenix lidar, *Whiteway et al.* [2009] observed precipitating ice particles at ~ 4 km above the surface at night. Based on their sedimentation velocity, *Whiteway et al.* [2009] calculates that they could be ellipsoidal particles with a volume equivalent to a 35 μm radius sphere (or larger if columnar). Ice particles of this size may nucleate around multiple dust particles and will have sedimentation velocities about an order of magnitude greater than the sedimentation velocities of 1μm dust particles. If water ice clouds with particles of similar size to those observed by *Whiteway et al.* occur in the tropical atmosphere of Mars below the level of the HATDM, the scavenging of water ice by dust could create the appearance of a HATDM, subject to the condition that the vertical dust distribution before interaction with clouds is uniformly mixed to the altitude of the HATDM and the mass mixing ratio of this distribution is at least as great

as the mass mixing ratio of the HATDM. In other words, dust is mixed to the height

of the HATDM during the day and quickly scavenged during the night. In an isothermal

atmosphere, the column opacity (τ) due to such a profile will be:

$$\tau = \int_{0}^{z_{HATDM}} DSO_{HATDM}\,\rho_s\,\exp(-z/H)dz \qquad (5.12)$$

where z_{HATDM} is the characteristic altitude of the HATDM, DSO_{HATDM} is the

characteristic dust density scaled opacity of the HATDM, and ρ_s is the air density at the

surface. Eq. 5.12 integrates to:

$$\tau = DSO_{HATDM}\,\rho_s H\left(1 - \exp\left[\frac{-z_{HATDM}}{H}\right]\right), \qquad (5.13)$$

assuming $DSO_{HATDM}=5.5\times10^{-4}$ m^2 kg^{-1}, $H=10^4$ m, and $z_{HATDM}=2\times10^4$ m, $\tau=0.071$. The

visible column opacity corresponding to that column opacity in the A5 channel would be

0.52. Assuming the ratio between opacity in the 1075 cm^{-1} channel used for dust column

opacity retrieval by THEMIS or TES and visible opacity is ~0.5, the implied column

opacity of the pre-scavenged haze somewhat exceeds retrieved dayside column opacities

at this latitude and season [*Smith*, 2004; *Smith*, 2009]. Yet without exact knowledge of

the dust size distribution, converting an opacity in the MCS A5 channel to opacity in any

other region of the spectrum is sufficiently uncertain that the observed dayside column

opacities by TES and THEMIS could be consistent with a hypothetical pre-scavenged

haze.

Another challenge to the possibility of scavenging is that the height of the

HATDM exceeds the observed height of the convective boundary layer [*Hinson et al.*,

2008] by at least a factor of two. Thus, either the convective boundary layer is deeper

than observed, the deep uniform mixing of the pre-scavenged profile is due to some process other than convective boundary layer overturning, or the pre-scavenged profile is not uniformly mixed. The first explanation is possible. *Hinson et al.* [2008] observes the boundary layer height in the northern tropics before the high altitude tropical maximum has reached its greatest altitude. *Hinson et al.* [2008] also observes in late afternoon, possibly after the boundary layer has reached its greatest depth. The second explanation is more unlikely. Some alternate form of mixing such as the solar heating of dust would need to be invoked. Yet such a process likely deepens the planetary boundary layer. The third explanation would either require a pre-existing vertical dust distribution with a local maximum in mass mixing ratio high above the surface or result in an unrealistically high column opacity.

Thus, within the present observational constraints, exceptionally deep dry boundary layer convection that entrains dust from systems such as dust devils and uniformly mixes this dust to high altitudes could generate the necessary pre-scavenged profile. The rarity of high quality dayside MCS retrievals in the tropics during northern spring and summer does not allow a systematic search for such uniformly mixed profiles. Yet this idea soon may be testable using column opacity retrievals from nadir and off-nadir views by MCS. The dayside dust column opacity could be used to simulate (based on considerations of uniform mixing) a pre-scavenged density scaled opacity limb profile. If scavenging is a significant process, nightside limb profiles in the vicinity of dayside dust column opacity measurements will be depleted in dust with respect to the simulated daytime limb profiles below the altitude of the HATDM.

5.5 Summary

The HATDM is a surprising feature of at least the nighttime vertical dust distribution of Mars for a quarter of its year. While enriched layers of dust at high altitudes above the surface during the rest of the year may be attributable to dust storms, the HATDM does not seem to be driven by dust storm activity. Instead, the existence of the HATDM may be evidence for the significant influence of processes related to topography, boundary layer circulations, and the water cycle on the global dust distribution during the "clear season." Since these processes are physically plausible at other seasons/latitudes, they may influence the dust distribution during the rest of the year.

Bibliography

Balme, M., and R. Greeley (2006), Dust devils on Earth and Mars, *Rev. Geophys.*, *44*, RG3003, doi:10.1029/2005RG000188.

Basu, S., M.I. Richardson, and R.J. Wilson (2004), Simulation of the Martian dust cycle with the GFDL Mars GCM, *J. Geophys. Res.*, *109*, E11006, doi:10.1029/2004JE002243.

Basu, S., J. Wilson, M. Richardson, and A. Ingersoll (2006), Simulation of spontaneous and variable global dust storms with the GFDL Mars GCM, *J. Geophys. Res.*, *111*, E09004, doi:10.1029/2005JE002660.

Benson, J. L., P.B. James, B.A. Cantor, and R. Remigo (2006), Interannual variability of water ice clouds over major Martian volcanoes observed by MOC, *Icarus*, *184*, 365–371, doi:10.1016/j.icarus.2006.03.014.

Cantor, B., M. Malin, and K. S. Edgett (2002), Multiyear Mars Orbiter Camera (MOC) observations of repeated Martian weather phenomena during the northern summer season, *J. Geophys. Res.*, *107*(E3), 5014, doi:10.1029/2001JE001588.

Cantor, B.A., P.B. James, M. Caplinger, and M.J. Wolff (2001), Martian dust storms: 1999 Mars Orbiter Camera observations, *J. Geophys. Res.*, *106*(E10), 23,653–23,687.

Cantor, B. A., K. M. Kanak, and K. S. Edgett (2006), Mars Orbiter Camera observations of Martian dust devils and their tracks (September 1997 to January 2006) and evaluation of theoretical vortex models, *J. Geophys. Res.*, *111*, E12002, doi:10.1029/2006JE002700.

Clancy, R. T., M. J. Wolff, and P. R. Christensen (2003), Mars aerosol studies with the MGS TES emission phase function observations: Optical depths, particle sizes, and ice cloud types versus latitude and solar longitude, *J. Geophys. Res., 108*(E9), 5098, doi:10.1029/2003JE002058.

Colaprete, A., J. R. Barnes, R. M. Haberle, and F. Montmessin (2008), CO2 clouds, CAPE and convection on Mars: Observations and general circulation modeling, *Planet. Space Sci., 56*(2), 150– 180.

Ferri, F., P. H. Smith, M. Lemmon, and N. O. Rennó (2003), Dust devils as observed by Mars Pathfinder, *J. Geophys. Res., 108*(E12), 5133, doi:10.1029/2000JE001421.

Fisher, J. A., M. I. Richardson, C. E. Newman, M. A. Szwast, C. Graf, S. Basu, S. P. Ewald, A. D. Toigo, and R. J. Wilson (2005), A survey of Martian dust devil activity using Mars Global Surveyor Mars Orbiter Camera images, *J. Geophys. Res., 110*, E03004, doi:10.1029/2003JE002165.

Forget, F., F. Hourdin, R. Fournier, C. Hourdin, O. Talagrand, M. Collins, S.R. Lewis, P.L. Read and J.-P. Huot (1999), Improved general circulation models of the Martian atmosphere from the surface to above 80 km, *J. Geophys. Res 104*, 24155–24175.

Fuerstenau, S. D. (2006), Solar heating of suspended particles and the dynamics of Martian dust devils, *Geophys. Res. Lett., 33*, L19S03, doi:10.1029/2006GL026798.

Gregory, D. (2000), Estimation of entrainment rate in simple models of convective clouds, *Q.J.R. Meteorol. Soc, 127*(571), 53-72.

Haberle, R.M., C.B. Leovy, and J.M. Pollack (1982), Some effects of global dust storms on the atmospheric circulation of Mars, *Icarus*, *50*, 322-367.

Haberle, R.M., J.B. Pollack, J.R. Barnes, R.W. Zurek, C.B. Leovy, J.R. Murphy, J. Schaeffer, and H. Lee (1993), Mars atmospheric dynamics as simulated by the NASA/Ames general circulation model I. The zonal mean circulation, *J. Geophys. Res., 98*, 3093-3124.

Hinson, D.P., M. Pätzold, S. Tellmann, B. Häusler, and G.L. Tyler (2008), Depth of the convective boundary layer on Mars, *198*(1), 57-66.

Kahn, R.A., T.Z. Martin, R.W. Zurek, and S.W. Lee (1992), The Martian Dust Cycle in H.H. Kieffer, B.M. Jakosky, C.W. Snyder, and M.S. Matthews, *Mars*, 1498 pp., University of Arizona Press, Tucson.

Kahre, M. A., J. R. Murphy, R. M. Haberle, F. Montmessin, and J. Schaeffer (2005), Simulating the Martian dust cycle with a finite surface dust reservoir, *Geophys. Res. Lett.*, *32*, L20204, doi:10.1029/2005GL023495.

Kahre, M. A., J. R. Murphy, and R. M. Haberle (2006), Modeling the Martian dust cycle and surface dust reservoirs with the NASA Ames general circulation model, *J. Geophys. Res.*, *111*, E06008, doi:10.1029/2005JE002588.

Kahre, M.A., J.L. Hollingsworth, R.M. Haberle, and J.R. Murphy (2008), Investigations of the variability of dust particle sizes in the martian atmosphere using the NASA Ames General Circulation Model, *Icarus*, *195*(2), 576-597.

Kleinböhl , A., J. T. Schofield, D. M. Kass, W. A. Abdou, C. R. Backus, B. Sen, J. H. Shirley, W. G. Lawson, M. I. Richardson, F. W. Taylor, N. A. Teanby, and D. J. McCleese (2009), Mars Climate Sounder limb profile retrieval of atmospheric temperature, pressure, dust, and water ice opacity, *J. Geophys. Res.*, *114*, E10006, doi: 10.1029/2009JE003358.

Kok, J. F., and N. O. Renno (2006), Enhancement of the emission of mineral dust aerosols by electric forces, *Geophys. Res. Lett.*, 33, L19S10.

Korablev, O. I., V. A. Krasopolsky, A. V. Rodin, and E. Chassefiere (1993), Vertical structure of the Martian dust measured by the solar infrared occultations from the Phobos spacecraft, *Icarus*, *102*, 76–87.

Malin, M. C., B. A. Cantor, T.N. Harrison, D.E. Shean and M.R. Kennedy (2008a), MRO MARCI Weather Report for the week of 13 October 2008 – 19 October 2008, Malin Space Science Systems Captioned Image Release, MSSS-55, http://www.msss.com/msss_images/2008/10/22/.

Malin, M. C., B. A. Cantor, T.N. Harrison, D.E. Shean and M.R. Kennedy (2008b), MRO MARCI Weather Report for the week of 6 October 2008 – 12 October 2008, Malin Space Science Systems Captioned Image Release, MSSS-54, http://www.msss.com/msss_images/2008/10/15/.

McCleese, D. J., J. T. Schofield, F. W. Taylor, S. B. Calcutt, M. C. Foote, D. M. Kass, C. B. Leovy, D. A. Paige, P. L. Read, and R. W. Zurek (2007), Mars Climate Sounder: An

investigation of thermal and water vapor structure, dust and condensate distributions in the atmosphere, and energy balance of the polar regions, *J. Geophys. Res.*, *112*, E05S06, doi:10.1029/2006JE002790.

McCleese, D.J., J.T. Schofield, F.W. Taylor, W.A. Abdou, O. Aharonson, D. Banfield, S.B. Calcutt, N.G. Heavens, P.G.J. Irwin, D.M. Kass, A. Kleinböhl, W.G. Lawson, C.B. Leovy, S.R. Lewis, D.A. Paige, P.L. Read, M.I. Richardson, N. Teanby, and R.W. Zurek (2008), *Nature Geosci.*, *1*, 745-749, doi:10.1038/ngeo332.

Metzger, S. M., J. R. Carr, J. R. Johnson, T. J. Parker, and M. T. Lemmon (1999), Dust devil vortices seen by the Mars Pathfinder Camera, *Geophys. Res. Lett.*, *26*(18), 2781–2784.

Michaels, T.I., A. Colaprete, and S. C. R. Rafkin (2006), Significant vertical water transport by mountain‑induced circulations on Mars, *Geophys. Res. Lett.*, *33*, L16201, doi:10.1029/2006GL026562.

Murphy, J. R., O. B. Toon, R. M. Haberle, and J. B. Pollack (1990), Numerical Simulations of the Decay of Martian Global Dust Storms, *J. Geophys. Res.*, *95*(B9), 14,629–14,648.

Newman, C. E., S. R. Lewis, P. L. Read, and F. Forget (2002a), Modeling the Martian dust cycle, 1. Representations of dust transport processes, *J. Geophys. Res.*, *107*(E12), 5123, doi:10.1029/2002JE001910.

Newman, C. E., S. R. Lewis, P. L. Read, and F. Forget (2002b), Modeling the Martian dust cycle 2. Multiannual radiatively active dust transport simulations, *J. Geophys. Res.*, *107*(E12), 5124, doi:10.1029/2002JE001920.

Putzig, N. E., M. T. Mellon, K. A. Kretke, and R. E. Arvidson (2005), Global thermal inertia and surface properties of Mars from the MGS mapping mission, *Icarus* 173, 325-341.

Rafkin, S. C. R., M. R. V. Sta. Maria, and T. I. Michaels (2002), Simulation of the atmospheric thermal circulation of a martian volcano using a mesoscale numerical model. *Nature*, *419*, 697-699.

Richardson, M.I. and R.J. Wilson (2002), A topographically forced asymmetry in the martian circulation and climate. Nature *416* (6878), 298-301.

Schneider, E.K. (1983), Martian Great Dust Storms: Interpretive Axially Symmetric Models, *Icarus*, *35*, 302-331.

Schofield, J. T., J. R. Barnes, D. Crisp, R. M. Haberle, S. Larsen, J. A. Magalhães, J. R. Murphy, A. Seiff, and G. Wilson (1997), The Mars Pathfinder Atmospheric Structure Investigation/Meteorology (ASI/MET) Experiment, *Science*, *278*, 1752–1758.

Smith, M. D. (2004), Interannual variability in TES atmospheric observations of Mars during 1999– 2003, *Icarus*, *108*, 148– 165.

Smith, M.D. (2009), THEMIS Observations of Mars aerosol optical depth from 2002—2008, *Icarus*, *202* (2), 444-452, doi:10.1016/j.icarus.2009.03.027.

Smith, M. D., M. J. Wolff, R. T. Clancy, and S. L. Murchie (2009), Compact Reconnaissance Imaging Spectrometer observations of water vapor and carbon monoxide, *J. Geophys. Res.*, *114*, E00D03, doi:10.1029/2008JE003288.

Strausberg, M. J., H. Wang, M. I. Richardson, S. P. Ewald, and A. D. Toigo (2005), Observations of the initiation and evolution of the 2001 Mars global dust storm, *J. Geophys. Res.*, *110*, E02006, doi:10.1029/2004JE002361.

Szwast, M. A., M. I. Richardson, and A. R. Vasavada (2006), Surface dust redistribution on Mars as observed by the Mars Global Surveyor and Viking orbiters, *J. Geophys. Res.*, *111*, E11008, doi:10.1029/2005JE002485.

Thomas, P. and P.J. Gierasch (1985), Dust Devils on Mars, *Science*, *230* (4722), 175-177.

Tomasko, M. G., L. R. Doose, M. Lemmon, P. H. Smith, and E. Wegryn (1999), Properties of dust in the Martian atmosphere from the Imager on Mars Pathfinder, *J. Geophys. Res.*, *104*(E4), 8987–9007.

Wang, H., and A. P. Ingersoll (2002), Martian clouds observed by Mars Global Surveyor Mars Orbiter Camera, *J. Geophys. Res.*, *107*(E10), 5078, doi:10.1029/2001JE001815.

Whelley, P. L., and R. Greeley (2008), The distribution of dust devil activity on Mars, *J. Geophys. Res.*, *113*, E07002, doi:10.1029/2007JE002966.

Whiteway, J. A., Komguem, L., Dickinson, C., Cook, C., Illnicki, M., Seabrook, J., Popovici, V., Duck, T. J., Davy, R., Taylor, P. A., Pathak, J., Fisher, D., Carswell, A. I., Daly, M., Hipkin, V., Zent, A. P., Hecht, M. H., Wood, S. E., Tamppari, L. K., Renno, N., Moores, J. E., Lemmon, M. T., Daerden, F., Smith, P. H. (2009) Mars Water-Ice Clouds and Precipitation, *Science*, *325* (5936), 68-70. doi: 10.1126/science.1172344.

Zurek, R.W., J.R. Barnes, R.M. Haberle, J.B. Pollack, J.E. Tillman, and C.B. Leovy (1992), Dynamics of the Atmosphere of Mars in H.H. Kieffer, B.M. Jakosky, C.W. Snyder, and M.S. Matthews, *Mars*, 1498 pp., University of Arizona Press, Tucson.

Chapter 6   Water Ice Clouds over the Martian Tropics during Northern Summer

6.1 Introduction

On Mars, water ice clouds both reflect incoming solar radiation and also absorb and re-emit thermal infrared radiation upwelling from the surface in a thin, infrared-transparent atmosphere. Thus, they likely affect the energy budget of both the atmosphere and the surface significantly [*Hinson and Wilson*, 2004; *Wilson et al.*, 2007] and therefore may have a substantial effect on the thermal structure.

Wilson et al. [2008] find significant discrepancies between temperatures in early northern summer simulated by a control run of the UK Mars general circulation model (MGCM) and by a model run assimilating retrievals of temperature and dust column opacity from the Thermal Emission Spectrometer (TES) on Mars Global Surveyor (MGS). *Wilson et al.* [2008] attribute this discrepancy to the radiative effects of water ice clouds, which were not included in the UK MGCM simulations, and find that simulating clouds in the GFDL MGCM results in 5-10 K warmer temperatures in the tropics (in the vicinity of the clouds with the highest water ice mass mixing ratio) and up to 20 K warmer temperatures at 10 Pa at 60° S. Thus, water ice clouds may have both a direct effect on the atmospheric thermal structure through radiative heating/cooling and an indirect effect through dynamical processes.

Observations show that water ice clouds are a common feature in the martian atmosphere. The most optically thick of these clouds are observed on the edge of the winter polar caps and over high volcanoes throughout much of the year and in the tropics

during northern spring and summer [e.g., *Wang and Ingersoll*, 2002; *Smith*, 2004]. While column opacity measurements are useful for constraining the effect of water ice clouds on the surface energy budget, vertical profiling is necessary to constrain their radiative heating/cooling, since the same column opacity could be due to either a shallow ground fog or a vertically extended haze, but the radiative heating rate profiles and dynamical effects in these two cases may be very different.

Retrievals from limb observations by the Mars Climate Sounder (MCS) on Mars Reconnaissance Orbiter (MRO) now provide a rich dataset for exploring the vertical distribution of water ice clouds [*McCleese et al.*, 2007; *Kleinböhl et al.*, 2009]. They already have been used to study south polar hood clouds (Benson et al., 2009, submitted to *J. Geophys. Res.*) and the effects of the thermal tides on clouds [*Lee et al.*, 2009]. Here we use MCS retrievals to investigate the spatial distribution of water ice clouds during northern summer and early northern fall, a period of transition in visible imagery from widespread tropical cloudiness (during the period simulated by *Wilson et al.* [2008]) to the tropics being relatively clear of water ice clouds [*Wang and Ingersoll*, 2002].

6.2 Data and Methods

Atmospheric retrievals from MCS observations provide vertical profiles of pressure, p, (Pa), temperature, T, (K), water ice opacity, i.e., fractional extinction due to water ice per unit height, $d_z\tau$, (km^{-1}) at 842 cm^{-1}, and dust opacity (km^{-1}) at 463 cm^{-1}. *Kleinböhl et al.* [2009] describes the retrieval algorithm and evaluates its success under different observational conditions. For $d_z\tau > 10^{-5}$ km^{-1}, the estimated uncertainty in $d_z\tau$ is typically

~5%. The retrievals analyzed here use an advanced version of the retrieval algorithm

that includes a simple scattering approximation in the radiative transfer.

If the effective radius (r_{eff}) and extinction coefficient (Q_{ext}) of the particle size

distribution and the density of water ice (ρ_{ice}) are known, the mass mixing ratio of water

ice (q_{ice}) can be derived from any individual retrieval (spherical particles are assumed in

this case): $q_{ice} = \dfrac{4}{3} \dfrac{\rho_{ice}}{Q_{ext}} \dfrac{d_z\tau}{\rho} r_{eff}$ (6.1)

where ρ is the atmospheric density. I assume ρ_{ice} =900 kg m^{-3} and use the same

assumptions for r_{eff} (1.41 µm) and Q_{ext} (0.773) as in the retrieval algorithm. While such a

construction is useful for comparison with model output and so will be adopted for the

data analysis, it depends on a variety of unwieldy assumptions. For instance, if the grain

size of water ice particles is much larger than assumed, r_{eff}/Q_{ext} (and q_{ice}) could increase

by a factor of 2. If water ice particles nucleate around dust particles, ρ_{ice} will depend on

the thickness of the water ice layer coating the dust particle.

Somewhat more directly, the infrared heating rate due to water ice in the optically

thin case is for emission of the surface at temperature T_s and re-emission by the cloud at

T_e:

$\dfrac{dT}{dt} = \beta \dfrac{\sigma(T_s^4 - T_e^4)}{c_p} \dfrac{d_z\tau}{\rho}$ (6.2)

where β is a parameter that incorporates variations in the spectral properties of emission,

absorption, and scattering of both the surface and the cloud with temperature and

wavelength; σ is the Stefan-Boltzmann constant, and c_p is the heat capacity of the

atmosphere. Thus, the heating rate is proportional to the density-scaled opacity, $\frac{d_z\tau}{\rho}$,

which can be directly calculated from the retrievals, is proportional to q_{ice} as we calculate

it, and is affected by the uncertainty in the properties of water ice (and dust) only to the

extent that uncertainty affects relative attribution of opacity to dust and water ice in the

retrieval algorithm.

For zonal averaging, the retrievals are separated into "dayside" (9:00—21:00

LST) and "nightside" (21:00—9:00 LST) bins and further binned in 36 (5° resolution)

mean latitudinal bins, 64 (5.625° resolution) mean longitudinal bins, and L_s bins at 5°

resolution: a resolution comparable to Mars general circulation model grids. Away from

the poles, MCS normally observes ~3:00 and ~15:00 LST. Mean latitude and longitude

refer to the coordinates at the tangent point observed by the center of the MCS detector

array at ~40 km above the surface. Opacity at pressures lower than the lowest pressure at

which opacity is reported is set to 0 to minimize the impact on the zonal average of rare

hazes detached from the bulk of the cloud.

6.3 Results

Figures 6.1a-h show nightside zonal average temperature (K) and q_{ice} for selected L_s bins

during northern summer and fall of Mars Year (MY) 29 (2008—2009) (by the

convention of *Clancy et al.* [2000]). (The latitude/longitude bins that contribute to the

zonal averages in Figure 6.1 are mapped in Figure 6.2). Sampling of longitudinal bins is

good in early summer and degrades as the summer progresses. I focus on nightside

profiles, because sampling is usually better during the night.
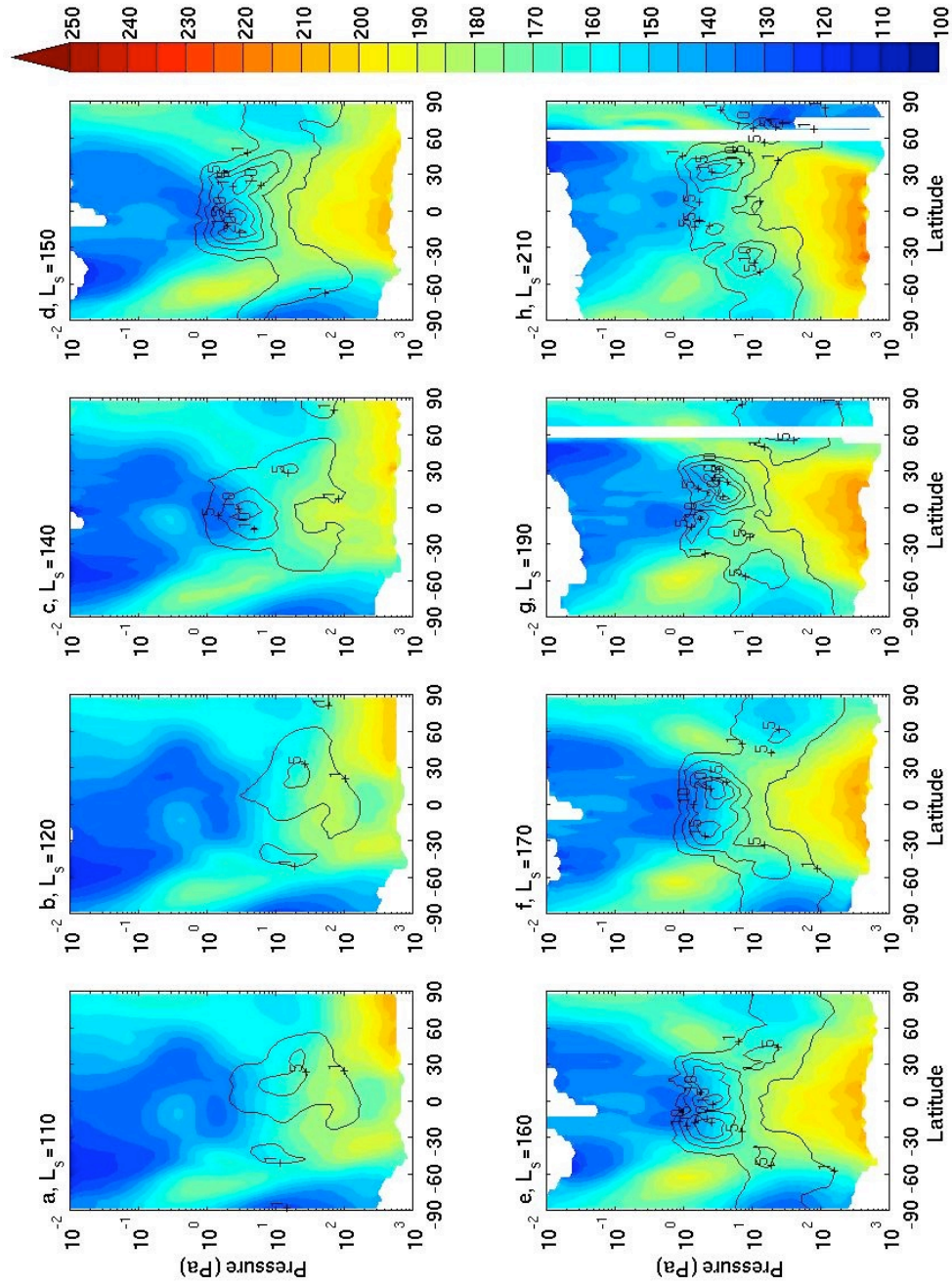
Figure 6.1. Nightside zonal average temperature (K) (color contours) and q_{ice} (ppm) (labeled contours) for selected L_s bins during MY 29 indicated by the labels at the top of each panel.
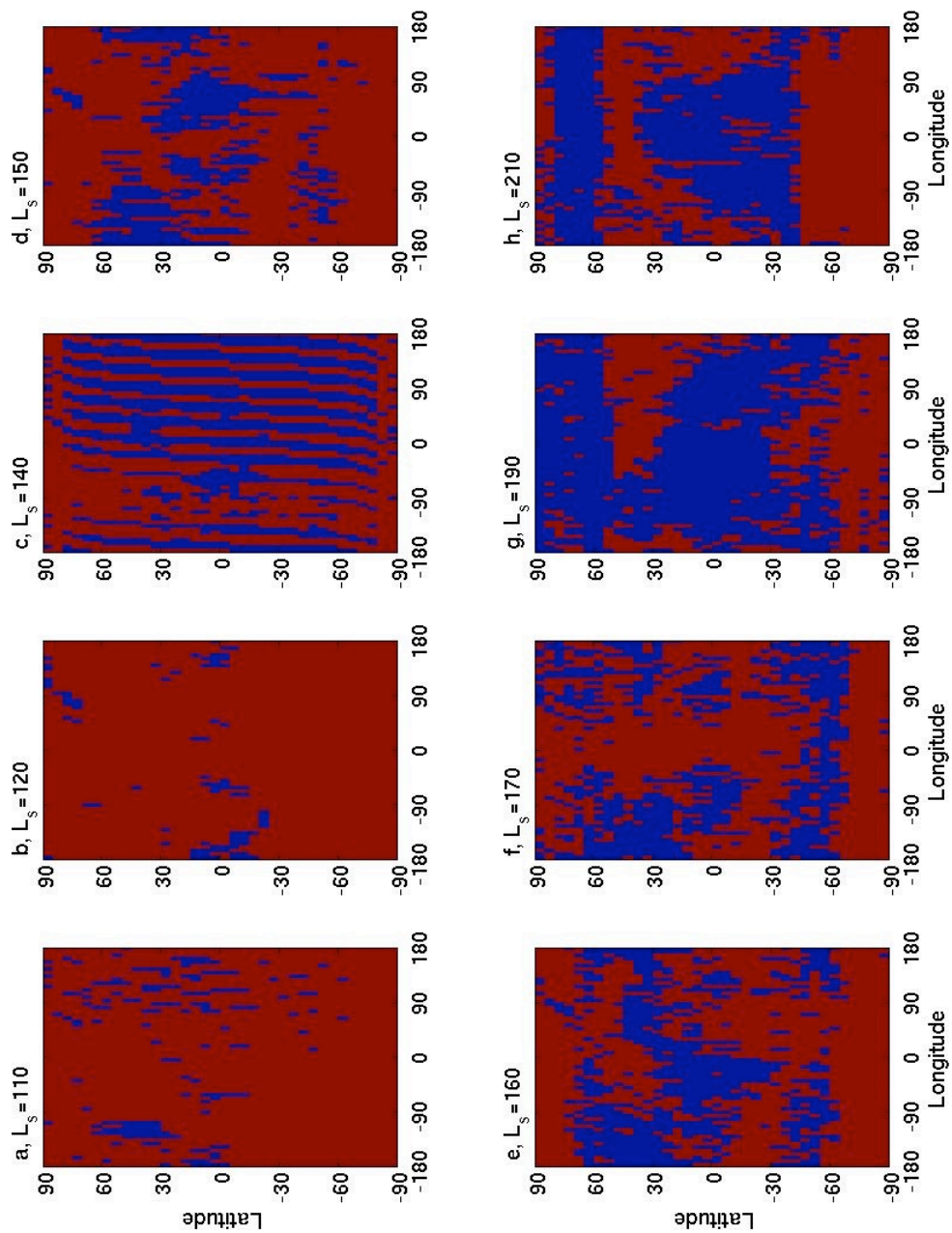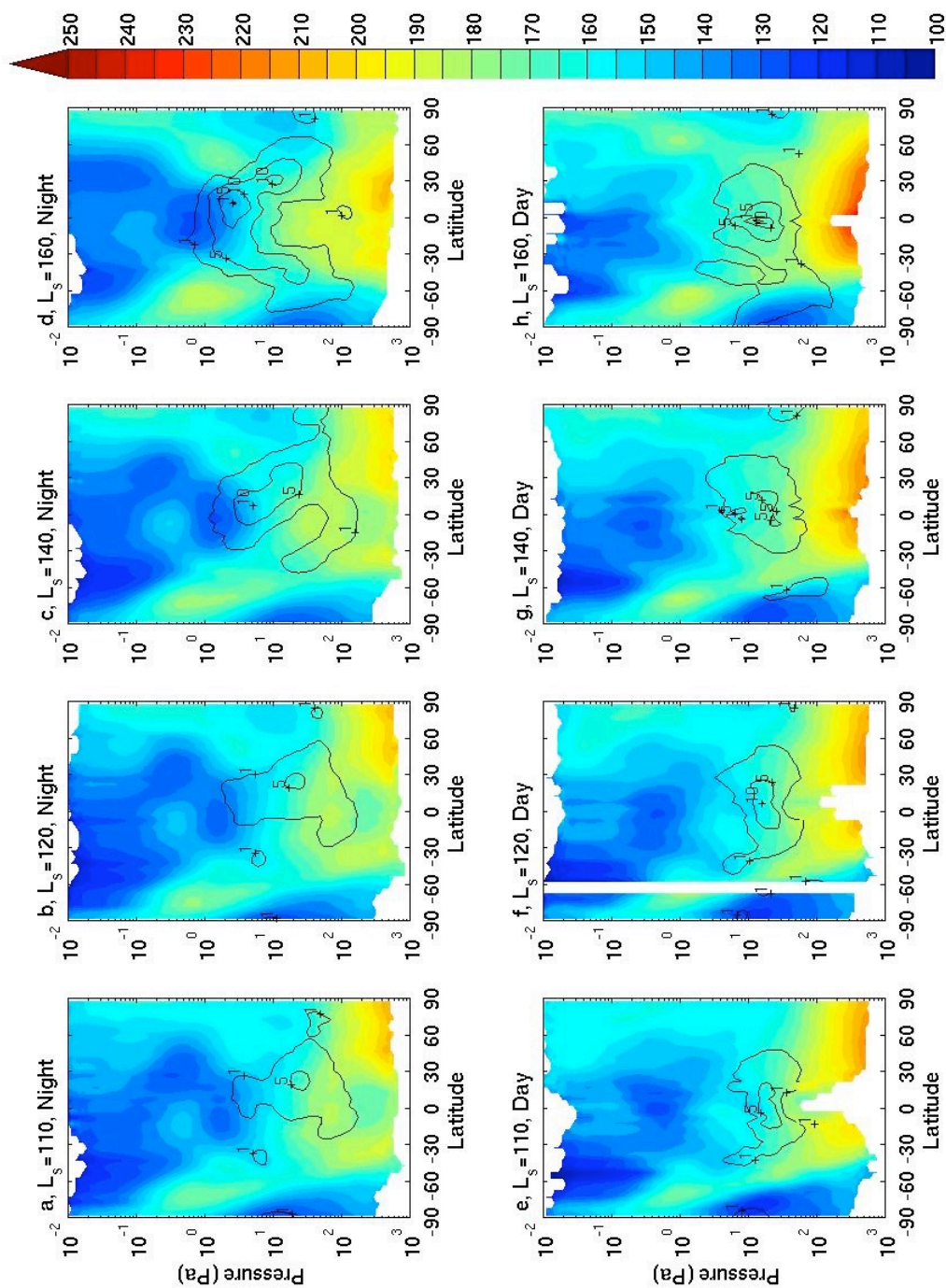
Figure 6.2. Map of latitude/longitude bins with at least one retrieval (red) for the L_s bins (used in Figure 6.1) indicated by the labels on the top of each panel.

In early summer, the highest zonal average nightside q_{ice} is 5 ppm over the northern tropics at ~20 Pa (Figures 6.1a-b). By L_s=140°, a layer of higher q_{ice} (up to 20 ppm) stretches across the tropics at ~4 Pa (Figure 6.1c), and this layer increases in q_{ice} throughout late summer as secondary maxima in q_{ice} of 5 ppm become apparent near 45° N and S at ~10-20 Pa (Figures 6.1e-f). The layer of high q_{ice} at ~4 Pa over the tropics begins to dissipate in early northern fall. Figures 6.3a-d show a similar transition in the distribution of water ice at night during the course of the summer of MY 28, during which longitudinal sampling is somewhat better later in the summer than during MY 29 (Figures 6.4a-d). On the dayside, a tropically symmetric layer of water ice with q_{ice}=5— 15 ppm is observed at ~20 Pa throughout northern summer (Figures 6.3e-h), though sampling is very poor (Figures 6.4e-h).

Figures 6.5a-b show longitudinal cross-sections of q_{ice} from a narrow latitude band roughly centered on the northern tropic and intersecting Lycus Sulci and the Elysium Montes. In the example from early summer of MY 29 (Figure 6.5a), there is a layer of high q_{ice} at ~20 Pa, which not vary much in q_{ice} or pressure level with longitude, even at longitudes that cross significant topography. This layer is vertically resolved by the retrievals. In the example from late summer of MY 28 (Figure 6.5b), q_{ice} is more longitudinally variable. There are layers of water ice with similar values of q_{ice} and at similar pressure levels as those in early summer, but there is also a layer at ~3 Pa with q_{ice} up to 65 ppm.

Figures 6.6a-b show longitudinal cross-sections of q_{ice} from a narrow latitude band at the equator that intersects the Tharsis Montes. In the example from early summer

Figure 6.3. Zonal average temperature (K) (color contours) and q_{ice} (ppm) (labeled contours) for selected L_s bins during MY 28 for dayside or nightside as indicated by the labels at the top of each panel.

Figure 6.4. Map of latitude/longitude bins with at least one retrieval (red) for the L_s bins (used in Figure 6.3) indicated by the labels on the top of each panel.
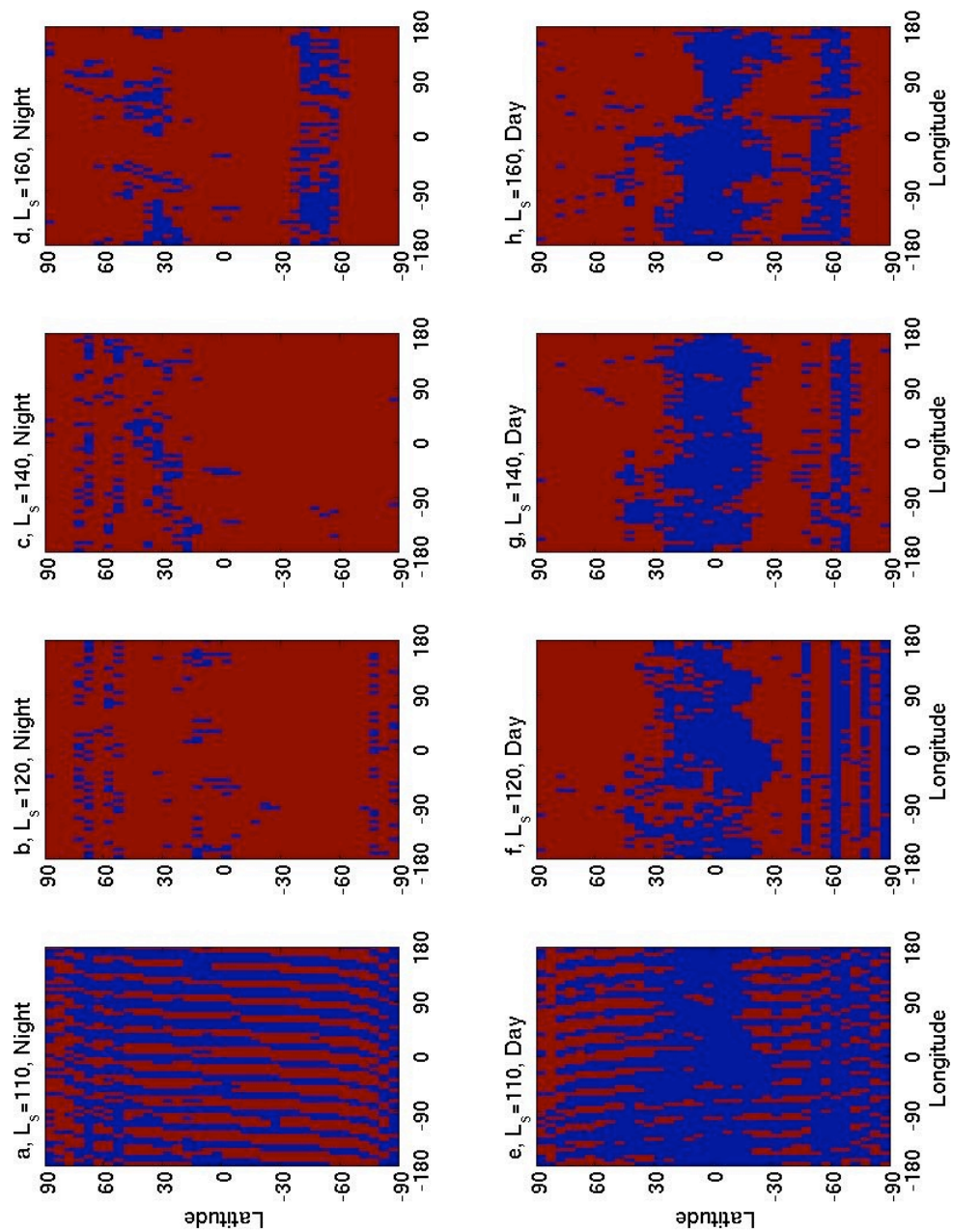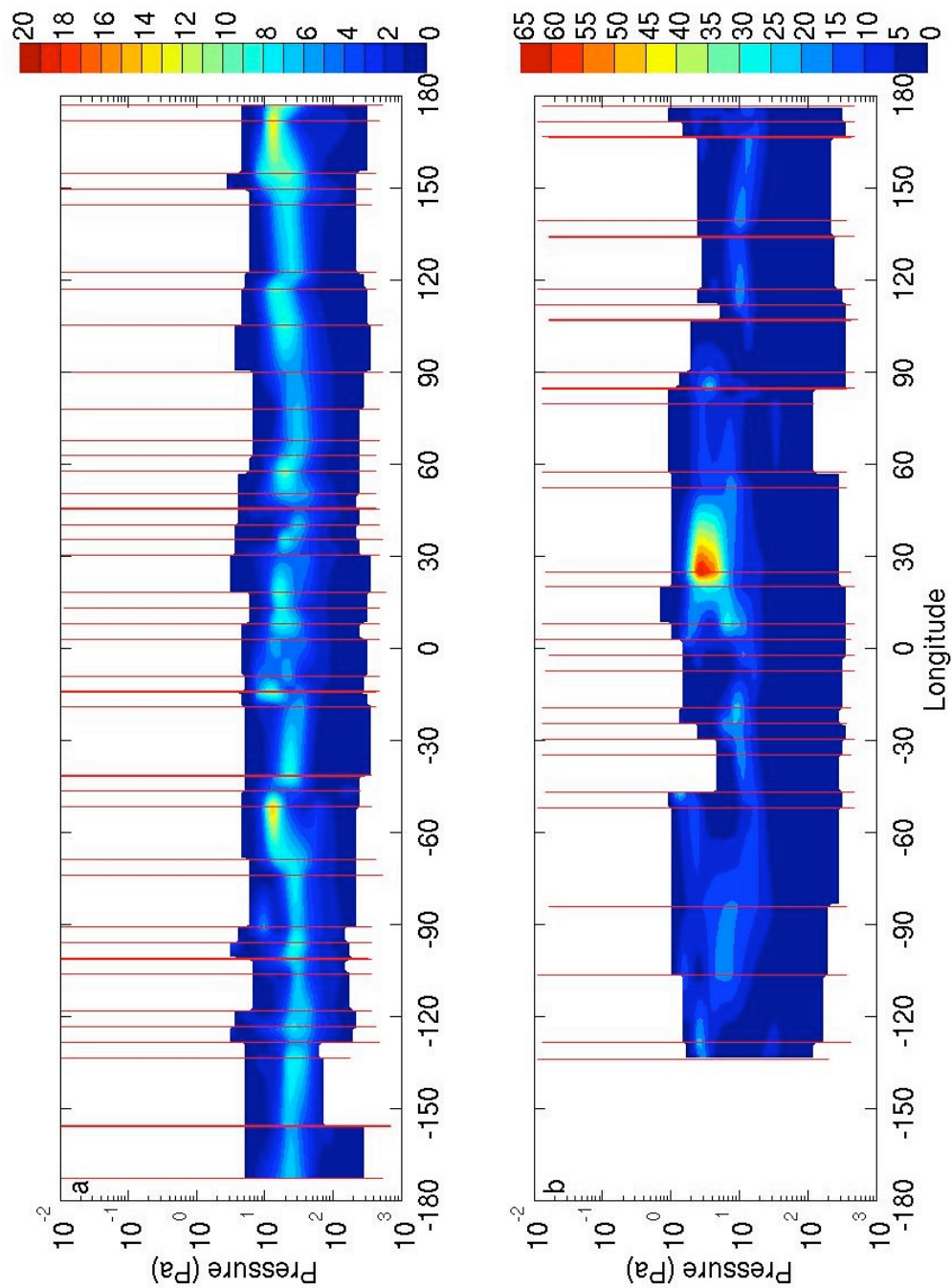
Figure 6.5. q_{ice} (ppm) for two longitudinal cross-sections interpolating retrievals from a narrow range of L_s and latitude: (a) L_s=119°—121°, 24°—26° N, nightside, MY 29; (b) L_s=159°—161°, 24°—26° N, nightside, MY 28. The red lines mark the mean longitude and vertical extent of each retrieval in the cross-section.
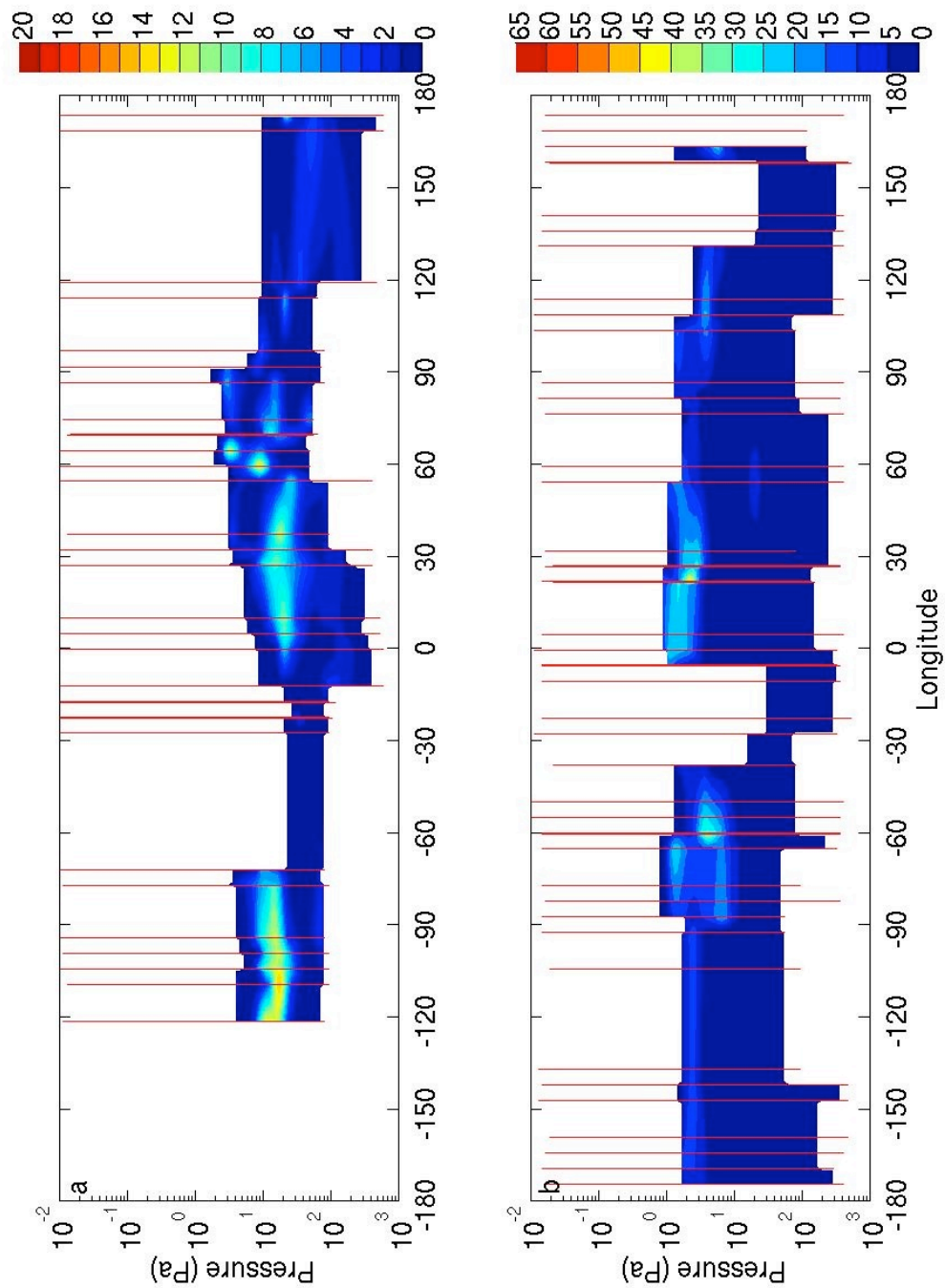
Figure 6.6. q_{ice} (ppm) for two longitudinal cross-sections interpolating retrievals from a narrow range of L_s and latitude: (a) L_s=119°—121°, 1° S—1° N, nightside, MY 29; (b) L_s=159°—161°, 1° S—1° N, nightside, MY 28. The red lines mark the mean longitude and vertical extent of each retrieval in the cross-section.

of MY 29 (Figure 6.4a), there are a couple of vertically resolved layers of

$q_{ice} \approx 10$ ppm at ~20 Pa. One layer is near and just east of the Tharsis Montes between

120° and 80° W, while the other is between 0° and 60° E. The longitudinal sampling is

not as complete as in Figure 6.5a, but the thick water ice clouds seem somewhat more

scattered. In the example from late summer, scattered cloudiness is now at a pressure

level between 2 and 10 Pa, while the q_{ice} of the thickest layers has increased by around a

factor of two.

6.4 Discussion

The tropical water ice distribution in early northern summer and the course of its

evolution during northern summer do not appear to be captured well by published

models. *Richardson et al.* [2002], *Montmessin et al.* [2004], *Wilson et al.* [2008], and

Nelli et al. [2009] all predict that the thickest clouds in early summer are mostly in the

northern tropics at ~100—300 Pa, a significantly lower level in the atmosphere than

where they are observed. (The first three studies present diurnal averages, while *Nelli et*

al. [2009] present longitudinal cross-sections for night.) The simulated q_{ice} for these

clouds in these published models is ~5 times higher than observed, a discrepancy too

great to be explain by an error in the grain size assumption used in Eq 6.1. *Richardson et*

al. [2002] does simulate a transition in the tropical water ice distribution during northern

summer, but this transition is from a tropically symmetric layer at a pressure level of

~200 Pa at L_s=110° to a thinner layer mainly over the northern tropics at a pressure level

of ~100 Pa at L_s=150°. Both of these layers are much lower than observed.

Part of the discrepancy in the pressure level of clouds may be due to the limited vertical range of the retrievals, which is dependent on altitude above the surface rather than pressure. Retrieval near the surface is inhibited by potentially large opacity in the instrument line-of-sight and substantial contributions of emission from the surface in the measured radiances, so the retrievals generally are cut off below ~5—15 km. Thus, the retrieved profiles will miss clouds near the surface, especially in the vicinity of topography, that could contribute high q_{ice} to model simulations at some pressure levels. In Figure 6.6a, for instance, the retrievals near the Tharsis Montes stop at ~80 Pa. This bias is likely intrinsic to limb observations in the thermal infrared at this season. These results agree well with TES limb retrieval results presented by McConnochie and Smith (Vertically Resolved Water Ice Aerosols Opacity From Mars Global Surveyor Thermal Emission Spectrometer (TES) Limb Sounding, Mars Water Cycle Workshop, 21—23 April 2008, Paris, France). But the vertical range bias cannot explain the entirety of the difference between the models and the observed water ice distribution. The vertical range of the retrievals reaches pressures as high as 300 Pa over most of the planet along the northern tropic (Figure 6.5a). Based on the simulations of *Wilson et al.* [2008], we would expect resolve a layer of cloud with q_{ice} 10—20 ppm centered at 100 Pa, but such a layer is not observed.

Lee et al. [2009] argues that the water ice distribution is controlled by the thermal tides. Water vapor is well-mixed to considerable depth in the atmosphere, and water ice condenses if the air temperature is below the saturation vapor pressure of water with respect to ice (and sufficient nuclei are available). Figures 6.5d and 6.5h very clearly support this hypothesis, since the tropical water ice layer on the dayside (nightside) is at a

level of the atmosphere that is warmer (cooler) in the night (day). Thus, a layer of

high q_{ice} moves up and down with the thermal tide during late summer.

Eqs. 6.1 and 6.2 permit calculation of the infrared heating due to such a layer. The

assumptions are: T_s=263 K (day) and 197 K (night) [*Schofield et al.*, 1997]; T_e=165 K

(day) and 145 K (night); β=1 (assumes infrared absorption equivalent to the value at ~12

μ); and c_p=756 J kg^{-1}. In this case, the daytime heating rate is 11.1 K sol^{-1} ppm^{-1} and the

nighttime heating rate is 2.9 K sol^{-1} ppm^{-1}. The zonal average diabatic heating/cooling

due to CO_2 at northern summer solstice was estimated to range from -20 to 10 K sol^{-1} in a

GCM simulation without aerosol by *Medvedev and Hartogh* [2007], so a zonal average of

10—20 ppm water ice cloud in the tropics should produce significant diabatic heating and

perturb the circulation. In addition, the heating due to the high q_{ice}, longitudinally

scattered clouds in Figure 6.53b and Figures 6.6a-b could be a significant asymmetric

forcing.

The most significant difference between the water ice cloud observations

presented here and published model results is the level at which water ice clouds are

found. *Rind and Rossow* [1984] observes that circulations are perturbed toward a

thermally direct state at a given pressure level if the equator to pole temperature gradient

is positive. Thus, neglecting eddy terms, radiative heating by water ice may drive a

thermally direct circulation like the Hadley cell on the Earth that effectively becomes part

of the equivalent to the Hadley cell on Mars: the principal meridional overturning cell

(PMOC). The higher the clouds, the deeper the cell. Therefore, the PMOC during

northern summer may be stronger at higher altitudes than simulated by both the published

models that simulate water ice clouds and by models that do not simulate such clouds.

Since the upwelling of the PMOC controls the tropical water vapor distribution

[*Richardson et al.*, 2002; *Richardson and Wilson*, 2002], water ice clouds also could have

a positive feedback (mainly limited by the water vapor supply) on the PMOC's height

and intensity.

Bibliography

Clancy, R. T., B. J. Sandor, M. J. Wolff, P. R. Christensen, M. D. Smith, J. C. Pearl, B. J. Conrath, and R. J. Wilson (2000), An intercomparison of ground-based millimeter, MGS TES, and Viking atmospheric temperature measurements: Seasonal and interannual variability of temperatures and dust loading in the global Mars atmosphere, *J. Geophys. Res.*, *105*(E4), 9553–9571.

Hinson, D. P., and R. J. Wilson (2004), Temperature inversions, thermal tides, and water ice clouds in the martian tropics, *J. Geophys. Res., 109*, E01002, doi:10.1029/2003JE002129.

Kleinböhl, A., J. T. Schofield, D. M. Kass, W. A. Abdou, C. R. Backus, B. Sen, J. H. Shirley, W. G. Lawson, M. I. Richardson, F. W. Taylor, N. A. Teanby, and D. J. McCleese (2009), Mars Climate Sounder limb profile retrieval of atmospheric temperature, pressure, dust, and water ice opacity, *J. Geophys. Res.*, *114*, E10006, doi: 10.1029/2009JE003358.

Lee, C., W.G. Lawson, M.I. Richardson, N.G. Heavens, A. Kleinböhl, D. Banfield, D.J. McCleese, R. Zurek, D. Kass, J.T. Schofield, C.B. Leovy, F.W. Taylor, A.D. Toigo, (2009), Thermal tides in the martian middle atmosphere as seen by the Mars Climate Sounder, *J. Geophys. Res.*, *114*, E03005, doi:10.1029/2008JE003285.

McCleese, D. J., J. T. Schofield, F. W. Taylor, S. B. Calcutt, M. C. Foote, D. M. Kass, C. B. Leovy, D. A. Paige, P. L. Read, and R. W. Zurek (2007), Mars Climate Sounder: An

investigation of thermal and water vapor structure, dust and condensate distributions in the atmosphere, and energy balance of the polar regions, *J. Geophys. Res.*, *112*, E05S06, doi:10.1029/2006JE002790.

Medvedev, A.S. and P. Hartogh (2007), Winter polar warmings and the meridional transport on Mars simulated with a general circulation model, *Icarus*, *186*(1), 97-110.

Montmessin, F., F. Forget, P. Rannou, M. Cabane, and R. M. Haberle (2004), Origin and role of water ice clouds in the martian water cycle as inferred from a general circulation model, *J. Geophys. Res.*, *109*, E10004, doi:10.1029/2004JE002284.

Nelli, S. M., J. R. Murphy, W. C. Feldman, and J. R. Schaeffer (2009), Characterization of the nighttime low-latitude water ice deposits in the NASA Ames Mars General Circulation Model 2.1 under present-day atmospheric conditions, *J. Geophys. Res.*, *114*, E11003, doi:10.1029/2008JE003289.

Richardson, M. I., and R. J. Wilson (2002), Investigation of the nature and stability of the martian seasonal water cycle with a general circulation model, *J. Geophys. Res.*, *107*(E5), 5031, doi:10.1029/2001JE001536.

Richardson, M. I., R. J. Wilson, and A. V. Rodin (2002), Water ice clouds in the martian atmosphere: General circulation model experiments with a simple cloud scheme, *J. Geophys. Res.*, *107*(E9), 5064, doi:10.1029/2001JE001804.

Rind, D., and W.B. Rossow (1984), The effects of physical processes on Hadley circulation, *J. Atmos. Sci.*, *41*, 479-507.

Schofield, J. T., J. R. Barnes, D. Crisp, R. M. Haberle, S. Larsen, J. A. Magalhães, J. R. Murphy, A. Seiff, and G. Wilson (1997), The Mars Pathfinder Atmospheric Structure Investigation/Meteorology (ASI/MET) Experiment, *Science*, *278*, 1752–1758.

Smith, M. D. (2004), Interannual variability in TES atmospheric observations of Mars during 1999– 2003, *Icarus*, *108*, 148– 165.

Wang, H., and A. P. Ingersoll (2002), martian clouds observed by Mars Global Surveyor Mars Orbiter Camera, *J. Geophys. Res.*, 107(E10), 5078, doi:10.1029/2001JE001815.

Wilson, R. J., G. A. Neumann, and M. D. Smith (2007), Diurnal variation and radiative influence of martian water ice clouds, *Geophys. Res. Lett.*, *34*, L02710, doi:10.1029/2006GL027976.

Wilson, R. J., S. R. Lewis, L. Montabone, and M. D. Smith (2008), Influence of water ice clouds on martian tropical atmospheric temperatures, *Geophys. Res. Lett.*, *35*, L07202, doi:10.1029/2007GL032405.

Chapter 7   Reflections on Martian Mesoscale Meteorology from a Global Climate Modeler

7.1 Introduction

At the First International Workshop on Mars atmosphere modeling and observations (Granada, Spain, 13—15 January 2003), Scot Rafkin of the Southwest Research Institute presented what he called, "an editorial designed to foster discussion," which was entitled, "Reflections on Mars Global Climate Modeling from a Mesoscale Meteorologist" (hereafter RMGCM3). RMGCM3 describes Rafkin as a "mesoscale meteorologist and modeler who is decidedly outside the general circulation modeling box (literally and figuratively)…a terrestrial mesoscale modeler, and…a classically trained Earth meteorologist." In effect, RMGCM3 claims a unique perspective within the martian meteorological community and asks whether mesoscale processes important for the forcing of the general circulation of the Earth are important on Mars and therefore should be included in Mars global climate models.

In some sense, this thesis has replied indirectly to RMGCM3 by breaking the most uncertain (and often mesoscale process-driven) forcings of the martian general circulation into their component parts. So I will conclude the thesis with a more direct reply to RMGCM3. The title of this Chapter is an inversion of RMGCM3 on the grounds that my primary training is as a climate scientist, a planetary historian, and a martian meteorologist. My first paper as a senior author [*Heavens et al.*, 2008] described possible

improvements to a martian global climate model and experiments with the model that

determined the effects of these improvements. Thus, my training and experience points

me toward Mars, the large-scale, and the long-term, just as Rafkin's experience (c. 2003)

pointed him toward Earth, the mesoscale, and short-term.

The significant questions raised by RMGCM3 are not only relevant to the study

of the martian atmosphere for purposes of weather prediction and comparative

planetology. The mesoscale processes we see today also may have some effect on the

formation of climate archives in the rock record and in the ice record, though this issue is

not considered in RMGCM3. Chapter 7.3 will very briefly discuss the significance of

mesoscale processes for interpreting the geological record of Mars.

7.2 A Review of Modern Mesoscale Phenomena

7.2.1 Hot Towers of Dust

RMGCM3 reviews current understanding of how the water vapor distribution in Earth's

tropics arises, emphasizing the significance of the tropical minimum in the moist static

energy (E_{moist}) in the middle troposphere:

$$E_{moist} = c_p T + gz + L_v q \tag{7.1}$$

where c_p is the isobaric heat capacity, T is the temperature, g is the acceleration due to

gravity, z is the altitude above the surface, and L_v is the latent heat of

vaporization/sublimation, and q is the water vapor mass mixing ratio. The significance of the moist static energy lies in its conservation under moist processes. If water is lost through condensation, the energy "loss" is compensated through latent heat release. The parcel either warms or gains gravitational potential energy. A minimum in moist static energy above the surface thus implies that the vertical distribution of water vapor (in an energetic rather than a physical sense) is not controlled by vertical eddy diffusion due to the overturning of Earth's Hadley cells, which would produce a moist static energy distribution that decays with height. In other words, the abundance of water vapor should decrease with distance from its source. Instead, numerically rare and areally insignificant deep convective cells preferentially transport water vapor into the upper troposphere. RMGCM3 then asks if such hot towers occur on Mars in the form of dust clouds and if they are significant for the transport of dust and volatiles.

These two questions can be answered hesitantly in the affirmative. The dust distribution of the martian atmosphere during much of northern spring and summer has a local maximum in mass mixing ratio high above the surface (at least on the nightside) (Chapters 4 and 5). Assuming conservation of dust, the tropical dust distribution of Mars around northern summer solstice is analogous to the moist static energy distribution of Earth's tropics and raises the same theoretical problem. The pseudo-moist dust convection described in Chapter 5 is a solution very similar to the idea of "hot towers," but Chapter 5 admits that this distribution also can be explained by invoking processes, such as scavenging by water ice particles, that violate the assumption of conservation of

dust and act on timescales faster than the large-scale vertical eddy diffusion timescale of the martian tropics.

In another instance described in Chapter 5, evidence was presented of a highly enriched layer of dust that likely originated from a regional dust storm near the southern tropic and then was advected across the equator against the likely direction of the cross-equatorial transport due to the PMOC at that season. This layer of dust likely carried water vapor concentrations typical of the surface during its ascent and thereby supported an unusually dense (five times the zonal average density-scaled opacity, see Figure 6.3c) water ice cloud at high altitude. Both the cause and effects of this top-heavy dust distribution have broad implications for radiative balance, dynamics, and atmospheric chemistry.

Enriched layers of dust above the surface are not restricted to northern spring and summer. They can occur during global dust storm activity as well. *Clancy et al.* [2009] report detection of such a layer at ~40 km above the surface in limb retrievals from the Thermal Emission Spectrometer (TES) on Mars Global Surveyor (MGS) during the 2001 dust storm. *Clancy et al.* [2009] also detect an enriched layer of scattering particles at 70-80 km, which they interpret as water ice. The enriched dust layer at 40 km is a clear contradiction to standard dynamical understanding. The heating of the atmosphere by the absorption of solar radiation by dust is thought to enhance the PMOC overturning, so dust storms would be expected to have uniformly mixed dust distributions. In addition, sedimentation is faster at lower densities than higher densities (Chapter 5), so a uniform dust distribution or a bottom-heavy dust distribution would be expected. *Newman et al.*
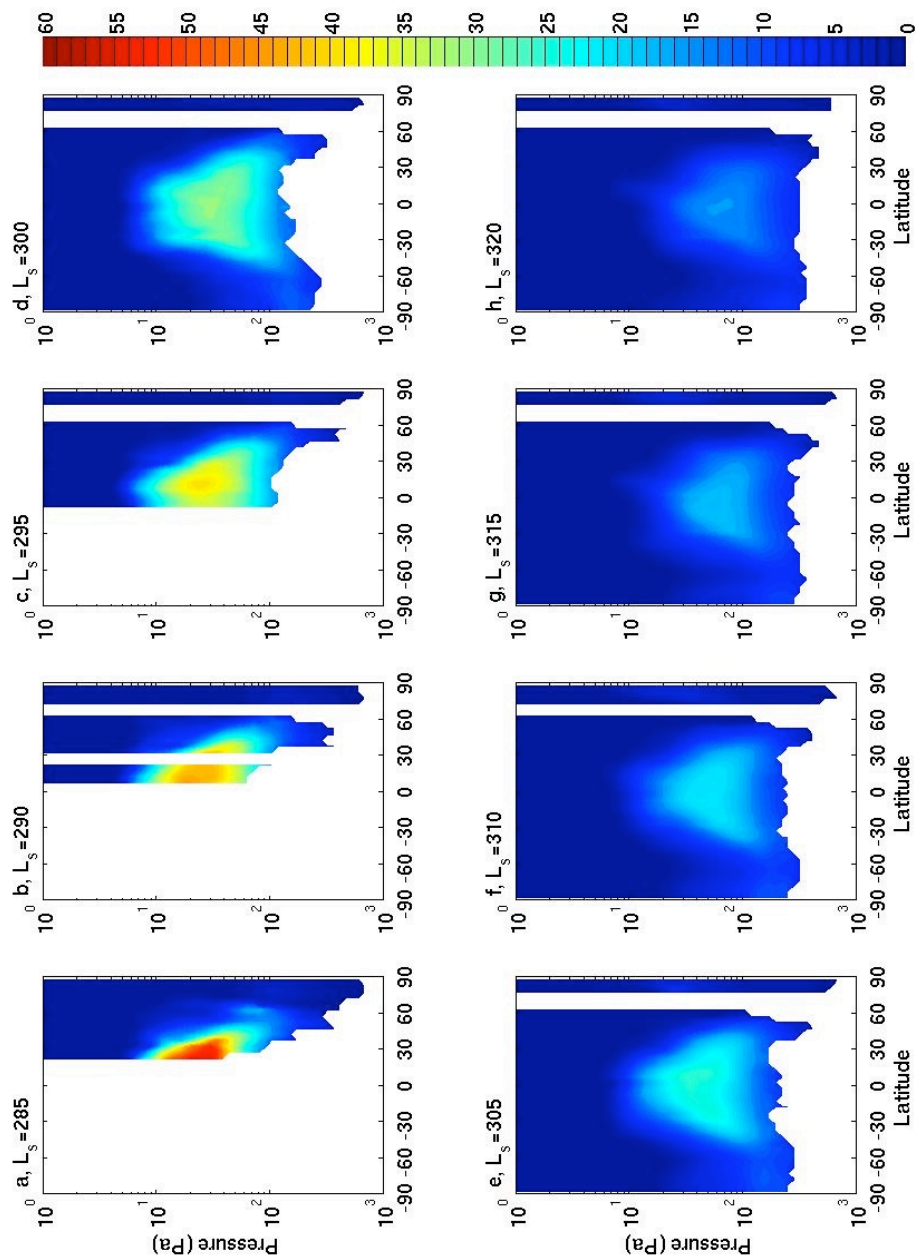
Figure 7.1: Estimated zonal average dust mass mixing ratio, nightside, MY 28, as labeled on the top of each panel.

[2002] and *Kahre et al.* [2008] have simulated enriched layers during large-scale dust storm activity, but *Clancy et al.* [2009] determined that the behavior they observed was "more extreme" than the simulations of *Kahre et al.* [2008].

Figures 7.1a-h show the zonal average dust mass mixing ratio (calculated as in Chapter 4) from MCS retrievals during the waning phases of the 2007 global dust storm (The nightside averages are shown, but the dayside averages are similar.) As retrieval coverage improves, a broad and enriched layer emerges and gradually decays over the course of 35° of L_s. While the observational biases described in Chapters 2 and 4 may have some quantitative effects on the zonal averages, the detection of an enriched layer by *Clancy et al.* [2009] similar to that implied by Figure 7.1b provides further confidence in this result. Thus, during the 2007 global dust storm, we infer that a zonal average layer of dust mass mixing ratio of >50 ppm was present over the martian tropics at a pressure level of ~30 Pa (or less).

While the observed dust distribution in the wake of the 2007 global dust storm looks extreme from the perspective of more modern models such as *Kahre et al.* [2008], it is consistent with the older three-dimensional model of the 1977b global dust storm by *Haberle et al.* [1982] and a simulation by *Newman et al.* [2002] of a synthetic dust storm near Hellas. *Haberle et al.* [1982] ran three experiments that evolved the dust distribution from a storm center in the southern mid-latitudes under three different sets of conditions: (1) dust was treated as a radiatively inert tracer; (2) dust was treated as radiatively active but a simple convective adjustment scheme was not applied; (3) dust was treated as radiatively active but a simple convective adjustment scheme was applied. In the case of

(1), the simulated dust distribution was confined very near to the surface in the
southern hemisphere. In the cases of (2) and (3), the simulated dust distribution was
relatively uniformly mixed over the southern tropics and mid-latitudes, while a highly
enriched layer was present at ~25 km above the surface over the northern tropics. In the
simulation of *Newman et al.* [2002], enriched layers of dust occur at 40 km above the
surface.

Since water ice clouds near the surface of the tropics are likely as rare during
global dust storms as they are during northern winter generally (Chapter 2), the enriched
layers of dust at high altitude observed during global dust storms most likely arise from
pseudo-moist dust convection on a horizontal scale that may be somewhat greater than
during northern summer. Such convective plumes may be partly resolved by the
simulations of *Haberle et al.* [1982] and *Newman et al.* [2002]. If the observed enriched
layer were supplied by pseudo-moist dust convection, the implied fractional area
occupied by the plumes would be around two to three orders of magnitude greater than
the high altitude tropical dust maximum (HATDM) (see Chapter 5), that is, between 0.1
and 1%, which is a reasonable estimate for the fractional area of active saltation in a
terrestrial dust storm [*Park and In*, 2003]. In addition (as noted in RMGCM3), dust
plumes with morphologies that resemble terrestrial cumuli have been observed in visible
imagery at the beginning of the 2001 dust storm [*Strausberg et al.*, 2005]. Thus, both the
morphologies of dust clouds and the vertical dust distribution during global dust storms
suggest that pseudo-moist dust convection occurs during seasons other than northern

spring and summer. Thus, the "hot towers" of dust proposed by RMGCM3 seem to

be a genuine atmospheric feature.

7.2.2 Mind the Water Ice!

The discussion of the vertical transport of dust in RMGCM3 begins by drawing an

analogy between the role of water in Earth's atmosphere and the role of dust in Mars's

atmosphere, which was discussed in far greater detail in Chapter 5. The importance of

dust in Mars's atmosphere and the very limited latent heating effect of water should not

encourage neglect of the significant infrared heating due to water ice clouds (discussed in

Chapter 6) and potential coupling between the dust and water cycles (discussed in

Chapter 5). The martian atmosphere is a thin atmosphere. Radiative heating terms due to

aerosol of any kind are comparable to latent heating in Earth's atmosphere.

7.2.3 Cold Towers of Carbon Dioxide Ice?

Carbon dioxide ice mostly has been mentioned in this thesis as a hindrance, either

because of its association with high hazes (equatorial mesospheric clouds) in Chapter 3 or

because of its tendency to be retrieved as dust in MCS retrievals (Chapter 4). Carbon

dioxide moist convection at the winter pole also was identified as potential source of

gravity waves in Chapter 3. The possible importance of carbon dioxide clouds at the

winter pole for polar energy balance and the large-scale circulation is definite excuse for

investigation of the mesoscale dynamics of these clouds. Promising work on this subject is ongoing at UCLA (P. Hayne and D.A. Paige, Snow Clouds and the Carbon Dioxide Cycle on Mars, paper presented at the American Geophysical Union Fall Meeting, San Francisco, CA, 14—18 December 2009).

Also of interest is the importance of carbon dioxide moist convection at high altitudes above the tropics (or possibly elsewhere), especially during global dust storms. *Leovy et al.* [1973] reports that there was a carbon dioxide cloud at about 70 km above the surface during the 1971 global dust storm, which *Leovy et al.* [1973] attributes to condensation of adiabatically cooled air over the strongly heated dust clouds of the storm. *Clancy et al.* [2009] observed some sort of scattering haze at 70 km during the 2001 dust storm, which *Clancy et al.* [2009] identifies as water ice. If such high hazes are widespread enough during global dust storms, they may be important for the thermodynamic control of dust storms (outlined in Chapter 3), since they broadly re-emit in the infrared at very cold temperatures and lower the effective emission temperature of the planet.

7.2.4 Gravity Waves

Gravity waves are almost an aside in RMGCM3, but they are a common occurrence in mesoscale simulations [*Rafkin et al.*, 2002; *Rafkin*, 2009; *Spiga and Forget*, 2009]. In all of these cases, the gravity wave source is non-orographic. While the analysis in Chapter 3 cannot make any definite attributions of the source of the middle atmospheric local

convective instabilities, a role for convective processes and higher wavenumber baroclinic disturbances remains likely, since: gravity wave energy above the tropics does not correlate with current simulations of wind stress [*Creasey et al.*, 2006], the strongest evidence for gravity wave drag in the extratropics is in Mars's flatter hemisphere (Chapter 3); and local convective instabilities in the middle atmosphere were detected in the tropics just before the 2007 dust storm (see Figure 3.10a). Yet specifically non-orographic gravity waves are not parameterized in present Mars GCMs.

7.2.5 Summary

The portrait that RMGCM3 painted of the martian atmosphere in 2003 was indeed prescient. Their temperature and pressure ranges of Earth's and Mars's atmospheres may differ. Solids and fluids may be present in them in differing proportions. But both of these atmospheres experience a variety of mesoscale and turbulent phenomena that are difficult to simulate in large-scale models of the general circulation but whose accurate representation may be critical to the predictive success of those models. Mars in fact seems to have at least five significant and genetically distinct forms of atmospheric convection: (1) dry convection in the planetary boundary layer; (2) dry convection in the middle atmosphere (Chapter 3); (3) pseudo-moist dust convection (Chapter 5); (4) carbon dioxide moist convection in polar night; and (5) high altitude carbon dioxide moist convection. Only the first type of convection is generally simulated in GCMs, though the

effects of the second type are sometimes included by means of a gravity wave drag parameterization.

Like RMGCM3, I look forward to the continued progress of martian mesoscale models as a means to develop routines for upscaling mesoscale phenomena into the GCMs. It will be important, however, for these models be carefully validated against the important observational record provided by Mars Climate Sounder and by other means described throughout this thesis, adapting techniques and approaches used in studies of Earth's atmosphere whenever possible and appropriate (as in Chapter 3 and Chapter 5.4.3).

7.3 Historical and Geological Significance

From the perspective of a planetary historian, the minutiae of processes that occur on timescales of minutes to days and on smaller than global scales seem intuitively irrelevant; at least in comparison with the grand orbital variations of Mars on timescales of thousands to millions of years that are hypothesized to drive cyclical deposition of ice and dust during the Amazonian era [e.g., *Milkovich and Head*, 2005; *Lewis et al.*, 2008]. This intuition is fundamentally wrong.

Mesoscale processes likely affect the most classic case of dust deposition on a polar cap. During some dust storms, the north polar vortex, which partially isolates the polar cap from the rest of the atmosphere, breaks apart. The disruption of the polar vortex

is signified by considerable warming in temperatures at a pressure of 10-100 Pa

above the pole (see discussion in Chapters 2 and 3). There is evidence for north polar

vortex disruption during the 2007 global dust storm (D.M. Kass et al., MCS Views of the

2007 Global Dust Storm, paper presented at the 39th Meeting of the Division for

Planetary Sciences of the American Astronomical Society, Orlando, FL, 7—12 October

2007), though Figures 7.1a-h show that the north pole still remained much clearer

throughout much of the storm than lower latitudes, consistent with past simulations

[*Haberle et al.*, 1982; *Barnes*, 1990]. It has been proposed that polar vortex breakdown

allows greater mixing with dusty air at lower latitudes and high rates of dust deposition

on the polar cap through water ice scavenging during a time in which CO_2 ice and water

ice are being deposited [*Barnes*, 1990 and references therein]. Since dust and water vapor

transport from the southern hemisphere may be controlled in part by the intensity of

pseudo-moist dust convection and polar vortex breakdown may require significant tidal

and/or gravity wave drag [*Wilson*, 1997; *Kuroda et al.*, 2009] but may not necessarily

require a global dust storm [*Wang*, 2007], even this relatively simple case of polar dust

deposition will be significantly affected by the poorly understood processes discussed in

Chapter 7.2 or discussed in greater detail in the previous Chapters. Therefore, it will be

important for future models to represent these processes with as generalized physics as

possible in order to understand changes in the frequency of polar vortex breakdown or the

intensity of pseudo-moist dust convection in different climate regimes.

Analogy with the dust cycle of the Earth confirms that the details of the

meteorological dynamics of dust transport in different climate regimes are important for

understanding the extant records of dust deposition. Dust concentrations in high-latitude ice cores on the Earth are 2-200 times greater during glacial periods than in interglacial periods such as the Holocene [*Mahowald et al.*, 1999 and references therein]. The best global modeling now can reproduce dust deposition rates consistent with these ice cores [*Mahowald et al.*, 2006], but the simulations suggest that the global increase in dust loading in the atmosphere only increases by a factor of 2.5 during glacials relative to interglacials, which is consistent with rates of dust deposition in tropical dust deposits [*Winckler et al.*, 2008]. The variability in ice core dust concentrations that exceeds this factor is mainly the combined effect of lower rates of snowfall at the high latitudes during glacials; enhanced transport of dust toward the poles due to a more vigorous atmospheric circulation during glacials; and the activation of additional dust source regions during glacials [*Mahowald et al.*, 2006; *Winckler et al.*, 2008]. In addition, there is sub-millennial variability in dust grain size among different ice cores in East Antarctica, which can be interpreted as resulting from sub-millennial variability in subsidence over ice core sites during times of high dust loading [*Delmonte et al.*, 2004]. Thus, the dust concentrations in high-latitude ice cores are controlled by climate variability on both the global and the local scales.

On Mars, the extreme cost of "coring" deposits at the north and south poles likely will limit the number of ice core records from Mars in the next couple of generations to one or two (hopefully one from each pole). This sampling density will preclude the perspective that multiple ice cores can provide about the role of local variability in dust deposition. So atmospheric modeling will be as necessary to provide perspective on the

sampling site as it will be to provide perspective on changes in polar dust deposition under variations in incident solar radiation and/or atmospheric density.

7.4 Conclusion

The most appropriate summary of this thesis would be a series of global climate model experiments that demonstrate that a proper representation of the forcings of the general circulation at least reproduced the observed thermal structure. While I hope to perform such experiments in the future, there is still considerable uncertainty about important elements of such experiments (e.g., the dayside aerosol distribution in the tropics during much of northern spring and summer), even if they were to use prescribed distributions of aerosol and gravity wave drag rather than more generalized physics. Instead, I have taken a new look at the broad significance of mesoscale processes for martian weather and climate.

The way forward in martian atmospheric science does not lie in better dynamical cores or new physics packages cribbed from Earth. It lies in realizing that the atmospheric dynamics of Mars is no less complex than the atmospheric dynamics of Earth, it is just different. It lies in being cognizant of those differences when determining the means of injecting dust into the boundary layer and beyond, the sources of gravity waves, and the dynamics of volatile clouds from the surface to the middle atmosphere. It lies in focusing on the little, the brief, and the shallow to understand the big, the long, and the deep.

Bibliography

Barnes, J.R. (1990), Transport of Dust to High Northern Latitudes in a martian Polar Warming, *J. Geophys. Res.*, *95*(B2), 1381-1400.

Clancy, R.T., M.J. Wolff, B.A. Whitney, B.A. Cantor, M.D. Smith, and T.H. McConnochie (2009), Extension of atmospheric dust loading to high altitudes during the 2001 Mars dust storm: MGS TES limb observations, *Icarus*, in press, doi: 10.1016/j.icarus.2009.10.011.

Creasey, J. E., J. M. Forbes, and D. P. Hinson (2006), Global and seasonal distribution of gravity wave activity in Mars' lower atmosphere derived from MGS radio occultation data, *Geophys. Res. Lett.*, *33*, L01803, doi:10.1029/2005GL024037.

Delmonte, B., J.R. Petit, K.K. Andersen, I. Basile-Doelsch, V. Maggi, and V. Ya. Lipenkov (2004), Dust size evidence for opposite regional atmospheric circulation changes over east Antarctica during the last climatic transition, *Clim. Dyn.*, *23*(3-4), 427-438.

Haberle, R.M., C.B. Leovy, and J.M. Pollack (1982), Some effects of global dust storms on the atmospheric circulation of Mars, *Icarus*, *50*, 322-367.

Heavens, N. G., M. I. Richardson, and A. D. Toigo (2008), Two aerodynamic roughness maps derived from Mars Orbiter Laser Altimeter (MOLA) data and their effects on

boundary layer properties in a Mars general circulation model (GCM), *J. Geophys. Res.*, *113*, E02014, doi:10.1029/2007JE002991.

Kahre, M.A., J.L. Hollingsworth, R.M. Haberle, and J.R. Murphy (2008), Investigations of the variability of dust particle sizes in the martian atmosphere using the NASA Ames General Circulation Model, *Icarus*, *195*(2), 576-597.

Kuroda, T., A.S. Medevedev, P. Hartogh, and M. Takahashi (2009), *J. Meteor. Soc. Japan*, *87*(5), 913-921.

Leovy, C.B., R.W. Zurek, and J.B. Pollack (1973), Mechanisms for Mars Dust Storms, *J. Atmos. Sci.*, *30*(5), 749-762.

Lewis, K.W., O. Aharonson, J.P. Grotzinger, R.L. Kirk, A.S. McEwen, and T.-A. Suer (2008), Quasi-Periodic Bedding in the Sedimentary Rock Record of Mars, *Science*, *322*(5907), 1532-1535.

Mahowald, N., K. Kohfeld, M. Hansson, Y. Balkanski, S. P. Harrison, I. C. Prentice, M. Schulz, and H. Rodhe (1999), Dust sources and deposition during the last glacial maximum and current climate: A comparison of model results with paleodata from ice cores and marine sediments, *J. Geophys. Res.*, *104*(D13), 15,895–15,916.

Mahowald, N. M., D. R. Muhs, S. Levis, P. J. Rasch, M. Yoshioka, C. S. Zender, and C. Luo (2006), Change in atmospheric mineral aerosols in response to climate: Last glacial period, preindustrial, modern, and doubled carbon dioxide climates, *J. Geophys. Res.*, *111*, D10202, doi:10.1029/2005JD006653.

Milkovich, S. M., and J. W. Head III (2005), North polar cap of Mars: Polar layered deposit characterization and identification of a fundamental climate signal, *J. Geophys. Res.*, *110*, E01005, doi:10.1029/2004JE002349.

Newman, C. E., S. R. Lewis, P. L. Read, and F. Forget (2002), Modeling the martian dust cycle 2. Multiannual radiatively active dust transport simulations, *J. Geophys. Res.*, *107*(E12), 5124, doi:10.1029/2002JE001920.

Park, S.-U., and H.-J. In (2003), Parameterization of dust emission for the simulation of the yellow sand (Asian dust) event observed in March 2002 in Korea, *J. Geophys. Res.*, *108*(D19), 4618, doi:10.1029/2003JD003484.

Rafkin, S. C. R. (2009), A positive radiative-dynamic feedback mechanism for the maintenance and growth of martian dust storms, *J. Geophys. Res.*, *114*, E01009, doi:10.1029/2008JE003217.

Rafkin, S. C. R., M. R. V. Sta. Maria, and T. I. Michaels (2002), Simulation of the atmospheric thermal circulation of a martian volcano using a mesoscale numerical model. *Nature*, *419*, 697-699.

Spiga, A., and F. Forget (2009), A new model to simulate the martian mesoscale and microscale atmospheric circulation: Validation and first results, *J. Geophys. Res.*, *114*, E02009, doi:10.1029/2008JE003242.

Strausberg, M. J., H. Wang, M. I. Richardson, S. P. Ewald, and A. D. Toigo (2005), Observations of the initiation and evolution of the 2001 Mars global dust storm, *J. Geophys. Res.*, *110*, E02006, doi:10.1029/2004JE002361.

Wang, H. (2007), Dust storms originating in the northern hemisphere during the third mapping year of Mars Global Surveyor, *Icarus*, *189*(2), 325-343, doi: 10.1016/j.icarus.2007.07.020.

Wilson, R. J. (1997), A general circulation model simulation of the martian polar warming, *Geophys. Res. Lett.*, *24*(2), 123–126.

Winckler, G., R.F. Anderson, M.Q. Fleisher, D. McGee, and N. Mahowald, Covariant Glacial-Interglacial Dust Fluxes in the Equatorial Pacific and Antarctica (2008), *Science 320* (5872), 93-96, doi: 10.1126/science.1150595.